Interaction between turbulent flow and saturated porous media

Mahesh Prakash

A thesis submitted in fulfillment of the requirements for the degree of Doctor of Philosophy

School of the Built Environment
Victoria University
Melbourne, Australia

June 2000

Declaration of candidate

This thesis contains no material that has been accepted at another university for the award of a degree, and to the best of the author's knowledge and belief, the thesis contains no material previously published by others, except where reference is made.

(Mahesh Prakash)

Melbourne, Australia
June, 2000

Abstract

In this thesis, the interaction between turbulent flow and saturated porous media has been investigated using computational fluid dynamics (CFD) simulations, flow visualisation experiments and laser Doppler velocimetry (LDV) measurements. In these systems, turbulence in the fluid layer may persist in the adjacent porous medium before it is attenuated at a rate that depends on the permeability and porosity of the porous medium. Synthetic reticulated foam of different permeabilities has been used as the porous medium for the experiments. Due the opaque nature of the porous foam, visualisations and measurements have been carried out in the fluid layer. The interaction between the turbulent fluid layer and the porous foam leads to changes in the flow pattern in the fluid layer. These changes have been recorded through the experiments for the purpose of evaluating the numerical model.

The flow visualisations have revealed that the permeability of the porous foam and the height of the fluid layer above the porous foam significantly affect the flow pattern, at least in the fluid layer. The thickness of the porous foam affects the flow pattern to a smaller extent. For low permeability porous foams, it has been found that there is little change in the flow pattern in the fluid layer from the cases without foam. It has been concluded that in such cases, the fluid layer and the porous medium can be regarded to be operating in the turbulent and laminar regimes, respectively. In case of the highest permeability foam tested, the flow pattern changes significantly in the fluid layer, indicating a strong interaction between the flow in the fluid layer and the adjacent foam.

Three different models were used to represent the flow in the porous foam, namely a laminar flow model and two turbulence models. The objective has been to infer the effect of the presence or absence of macroscopic turbulence in the porous medium by studying the changes in the flow pattern, mean velocities and turbulence kinetic energy in the fluid layer. The reason for such an indirect evaluation is the inability of using measurements made at point locations in the porous medium for comparison with simulations using volume averaged equations.

Of the two turbulence models used in this study, one has only Darcy damping in the turbulence transport equations for the porous foam. This model has been found to be qualitatively superior in predicting the gross flow patterns. The second

turbulence model has Darcy and Forchheimer modifications included in the turbulence transport equations for the foam. This model has been found to be qualitatively similar to the laminar flow model in its predictive capabilities. The reason for the similarity is the almost complete damping of turbulence at the interface between the foam and clear fluid due to the Darcy and Forchheimer modification terms. None of the three models used to represent flow in the foam can adequately predict the effect of changes in the thickness of the porous layer.

In order to consolidate on the flow visualisations, LDV measurements have been carried out for a quantitative comparison between the CFD simulations and the measurements. The vector plots obtained from the measurements confirmed that there is a significant change in the flow pattern in the fluid layer in the case of the highest permeability foam investigated. It has been further observed that the numerical simulations predict the mean axial velocity profiles better with the first turbulent flow model with only Darcy damping for the foam. For the radial velocity profiles, predictions with the laminar flow model and the second turbulence model with both Darcy and Forchheimer modification terms are better at the highest fluid height in a region close to the interface between the fluid layer and foam. On the other hand, the first turbulent flow model with Darcy damping gives results that are in better agreement with the measurements for the radial velocity with a decrease in the height of the fluid layer. The predicted turbulence kinetic energy profiles in the fluid layer using any of the three models for the foam have relatively good agreement with the experimental results.

After validating the numerical modelling of the interaction between a turbulent fluid flow overlying a saturated porous layer with experimental results, the numerical work has been extended to an industrially important case study concerning moisture migration in respiring agricultural produce. In this case study, a general procedure has been developed to simulate systems with a turbulent fluid layer overlying a saturated hygroscopic porous medium. Such a model is capable of predicting the moisture migration process more accurately than existing models, as it accounts for turbulence in the fluid layer.

Acknowledgements

I would like to take this opportunity to thank my supervisors, Associate Professor Graham Thorpe, Associate Professor Özden Turan and Dr. Yuguo Li who have guided and supported me throughout the course of my doctoral research. I wish to thank my postgraduate student colleagues who assisted me immensely, to make my stay in Australia as an overseas student, a very pleasant experience. Thanks are due to the Head of the School of the Built Environment, Associate Professor Michael Sek, for his words of wisdom and encouragement. I am grateful to the technical and secretarial staff of the school and the university who provided me with all the help needed, towards the successful completion of my doctoral research. I would like to acknowledge the School of the Built Environment for providing me with a departmental scholarship for pursuing my doctoral study in Australia. I would also like to acknowledge the Commonwealth Scientific and Industrial Research Organisation (CSIRO), Australia for allowing me to use their experimental facilities. Special thanks go to Mr. John Mahoney who provided me with technical assistance while performing my experiments at CSIRO, Building Construction and Engineering in Highett, Victoria, Australia.

I would like to dedicate this thesis to my parents in India who have throughout been extremely encouraging and supportive.

List of Symbols

a_E, a_W, a_N, a_S, a_P	coefficients associated with the final discretised equation
a_{vd}	dynamic specific surface area [m^{-1}]
b	discretised source term
c	speed of light [ms^{-1}]
c_μ	dimensionless coefficient in ν_t, eddy viscosity.
c_μ^*	new constant associated with the macroscopic k-ε turbulence model for flow through porous media
$c_{\varepsilon 1}$, $c_{\varepsilon 2}$, $c_{\varepsilon 3}$	coefficients associated with the rate of dissipation of turbulence kinetic energy
c_a	specific heat of air at constant pressure [$Jkg^{-1}°K^{-1}$]
c_b	bulk specific heat at constant pressure [$Jkg^{-1}°K^{-1}$]
c_F	Forchheimer coefficient
C_p, c_p	specific heat at constant pressure [$Jkg^{-1}°K^{-1}$]
c_w	specific heat of liquid water at constant pressure [$Jkg^{-1}°K^{-1}$]
D	inner diameter of the acrylic cylinder [m]
D	width of the system [m]
D_{as}	rate coefficient for moisture exchange between air and porous medium [s^{-1}]
D_j	jet diameter [m]
d_p	average pore diameter of the porous medium [m]
$\boldsymbol{e_1}$, $\boldsymbol{e_2}$, $\boldsymbol{l}$	unit vectors
f_1, f_2, f_μ	damping functions associated with the low Reynolds number k-ε turbulence model
f_l, f_{l1}, f_{l2}	frequencies of laser beams [Hz]
f_{lD}	approximate frequency difference between f_{l1} and f_{l2} [Hz]
g	acceleration due to gravity [ms^{-2}]
H	height of the fluid layer or height of the entire system [m]
h_p	thickness of the porous foam [m]
H_w	integral heat of wetting [Jkg^{-1}]
i, j, k	counters
K	permeability [m^2]
$\boldsymbol{K}$	permeability tensor [m^2]
k	turbulence kinetic energy [m^2s^{-2}]
k_b	thermal conductivity of the solid matrix [$Wm^{-1}°K^{-1}$]
k_f	thermal conductivity of the fluid [$Wm^{-1}°K^{-1}$]
n	number of samples taken per point in LDV measurements
p	pressure [Pa]
P_{atm}	atmospheric pressure [Pa]
p_{sat}	saturation pressure [Pa]
R	inner radius of the acrylic cylinder [m]
r, z	axi-symmetric co-ordinates [m]
R_N	radius of the nozzle [m]
T	temperature [°K]
t	time [s]
$\boldsymbol{u}$	velocity vector [ms^{-1}]
u, v	velocities [ms^{-1}]
U_b	bulk jet velocity [ms^{-1}]

u_p	pore velocity for flow through porous medium [ms^{-1}]
W	moisture content of the porous medium on a dry basis [kg of moisture/ kg of dry solid]
w	air moisture content on a dry basis [kg of moisture/ kg of dry air]
x, y	cartesian co-ordinates [m]
xu, yv	staggered locations in the cartesian co-ordinate system [m]

Greek symbols

β	coefficient of thermal expansion [$°K^{-1}$]
ρ	density [kgm^{-3}]
μ	dynamic viscosity of the fluid [Pas]
ν	kinematic viscosity of the fluid [m^2s^{-1}]
η	Kolmogorov length scale [m]
ϕ	porosity of the porous medium
ε	rate of dissipation of turbulence kinetic energy [m^2s^{-3}]
φ	representative scalar variable
τ	shear stress [$kgm^{-1}s^{-2}$]
Δ	symbol representing difference
σ	turbulent Prandtl number
κ	von Karman's constant
δ_{ij}	Kronecker's delta, $\delta_{ij} = 1$ for $i = j$ and $\delta_{ij} = 0$ for $i \neq j$
μ_t	absolute eddy or turbulent viscosity [Pas]
ν_t	kinematic eddy or turbulent viscosity [m^2s^{-1}]

Subscripts

pa	phase averaged quantity
va	volume averaged quantity
eff	effective value
i, j, k	vector components or counters
r, θ, z	vector components in cylindrical co-ordinates
w	value associated with the wall
imin, imax	minimum and maximum values
e, w, n, s	east, west, north and south control surfaces around a grid point
ref	reference value
avg	average value

Superscripts

E, W, N, S	east, west, north and south neighbours of a grid point
c	convective component
d	diffusive component
g	guess value
nd	non-dimensional value

List of Tables

List of Figures

Chapter 1

Introduction

1.1 Background of the research

There are few published studies on the interaction between turbulent flow and saturated porous media. Despite this lack of knowledge, such flows are encountered in several practical applications, such as grain storage systems, the cooling of nuclear reactors, cold-storage installations, air conditioning applications and the solidification of molten metals. The turbulence in such systems can arise from either forced or natural convection that results from temperature or concentration gradients. Any turbulence generated in the fluid layer may persist in an adjacent porous medium before it is attenuated at a rate that depends on the permeability and porosity of the porous medium. The research presented in this thesis is an attempt to elucidate, both experimentally and numerically, the nature of these important flows.

Previous studies on composite systems consisting of a fluid layer overlying a porous medium were carried out primarily on systems in which turbulence effects could be neglected. Most of these studies were carried out on systems in which the flow was generated due to a temperature gradient (natural convection flow). The numerical investigations of Poulikakos (1986) and Chen and Chen (1992) can be cited as examples of those in which the heating was from below, i.e. the Rayleigh-Bénard analogue of the single-phase fluid problem. The numerical investigation of Singh *et al.* (1993) and the experimental and numerical study of Song and Viskanta (1994) are examples of research in which the heating is from the side, i.e. the double glazing analogue of the natural convection problem.

As noted by Antohe and Lage (1997), the modelling of turbulence in porous media is a controversial topic. It is believed that due to the relatively low porosity and permeability of naturally occurring porous media, turbulence will not persist in the interstitial pores of the media. However, in the case of high porosity and/or high permeability porous media that are artificially produced, such as porous reticulated foams and metallic foams, turbulence can persist in the porous medium especially in

situations where there is an adjacent turbulent fluid layer. Antohe and Lage (1997) have provided a comprehensive review of instances where turbulence modelling has been used in porous media. These authors developed a general two-equation macroscopic turbulence model of a porous medium from the governing equations of fluid flow. However, they have not provided any numerical or experimental validation for their proposed model. Also, the large number of higher order terms arising in the turbulence transport equations makes their model difficult to implement especially in three-dimensional problems of industrial relevance.

A recently published paper by Getachew *et al.* (2000) extends the model developed by Antohe and Lage (1997) to include further higher order terms. However, this paper again suffers from the lack of experimental and numerical work supporting the model. Authors such as Lee and Howell (1987), Lim and Mathews (1993), Prescott and Incropera (1995) and Chen *et al.* (1998) accounted for turbulence in the porous medium by incorporating additional source/sink terms in the turbulence transport equations. The models adopted by these authors can be considered as simpler versions of the model developed by Antohe and Lage (1997). These modifications were, however, developed in an ad-hoc manner to suit specific experimental or physical scenarios.

There has been no published systematic attempt at studying the effect of turbulence modelling in a porous medium. There are two possible reasons for the lack of progress in this area. The first reason is that it is extremely difficult to derive the governing equations of turbulent flow from the axioms of continuum mechanics in a system that has complicated and essentially random geometry. Secondly, any model developed to represent turbulent flow in porous media needs to be validated with experimental data. Due to the opaque nature of most porous media, measurements or visualisations within the porous media are difficult to achieve. The lack of work in this area is highlighted by the concluding remarks made by Getachew *et al.* (2000), in which the authors write, "*In order to explain and gain deeper insight into the closure scheme and the final transport equations, further comprehensive numerical, analytical and experimental work remains to be done*".

In light of the above discussion, the research presented in this thesis:

1. Explicates the physics of the interaction between a turbulent fluid layer and an adjacent saturated porous layer by using flow visualisation experiments with streak photography and laser Doppler velocimetry (LDV) measurements, both complimented by computational fluid dynamics (CFD) simulations.

2. Examines the efficacy of modelling strategies that account for turbulence effects in the porous medium. There is evidence that turbulence in an adjacent fluid layer penetrates the porous medium especially when the porous medium has a high permeability and/or high porosity. The effect of the presence or absence of turbulence in the porous medium is inferred by studying the changes in the flow pattern and turbulence kinetic energy in the fluid layer. For this reason, porous reticulated foams (with porosity values greater than 0.9) of different permeabilities have been used in the experiments. Such an investigation sheds light into the treatment of turbulence in the porous medium for the purposes of numerical modelling. Also, it provides the scientific community with ideas to design future experiments for studying turbulence effects in the porous medium.

3. Applies the results obtained from the modelling of the interaction of turbulent flows and porous medium to an industrially important problem. The case study involves the behaviour of stored agricultural produce which has the additional property of being hygroscopic.

1.2 Outline of the research

To enable the effective presentation of the results of the present study, this thesis is organised as follows:

1. Chapter two provides the theoretical framework within which the research is developed. In particular, the basic governing equations of fluid flow are formally presented for the flow within a porous medium and an adjacent fluid layer.

Turbulence modelling for clear fluid flow is introduced. The numerical method used to construct the CFD code for the simulations is also developed in this chapter. Extensions to the basic governing equations of fluid flow are presented in subsequent chapters, along with the associated changes to the basic CFD code.

2. Preliminary validation of the numerical code described in chapter two is carried out in the third chapter. Such a benchmarking was essential in this study, because the present CFD code is an in-house developed one. Hence, the validation exercise determines any errors associated with the code development. The heating from the side or double glazing problem of natural convection flow is an established benchmark both numerically and experimentally. Therefore, it was decided to employ this benchmark as a preliminary validation tool for the numerical code written for two-dimensional systems. Air is used as the representative fluid for the validation exercise. As a result of the validation study, it has been concluded that the code can serve as a robust platform to implement further modifications. The benchmark problem is particularly relevant to the case study carried out in the present research, because it involves natural convection flow in a rectangular cavity.

3. Flow visualisation experiments using streak photography are described in detail in the fourth chapter. These experiments involve an axi-symmetric flow. A two-layer system consisting of a turbulent fluid flow adjacent to a saturated porous medium is used. The fluid and porous layer are housed in a cylindrical container. Water is used as the fluid, and synthetic reticulated foams of different gradations corresponding to different permeabilities and porosities are used as the porous media. A jet impinging on the foam was used to generate the turbulence.

4. The numerical code that is validated against the benchmark two-dimensional natural convection problem in chapter two is further extended to include an axi-symmetric geometry in the fifth chapter. The modified code is used to simulate the axi-symmetric experimental flow patterns of chapter four by using appropriate boundary and interface conditions. Two different modelling strategies are employed to account for the presence or absence of turbulence in the porous medium. In the first case, the fluid layer and the porous medium are assumed to

be in the turbulent and laminar regimes, respectively. In the second case, the fluid layer and the porous medium are assumed to be in the turbulent regime. For this case, the effect of including additional terms in the turbulence transport equations to damp turbulence in the porous medium is investigated. The resulting simulated flow patterns are compared with the experimental flow patterns obtained from the flow visualisations.

5. The streaklines observed from the flow visualisations (chapter four) highlight the flow regions where more detailed experimental investigations are required. Such detailed information has been gained from LDV measurements. These measurements are described in the sixth chapter. The LDV experiments have been carried out only for the important cases as determined from the flow visualisation experiments. The measurements are compared with the simulations presented in chapter five for a quantitative comparison between the experimental and numerical results.

6. After the thorough comparison of the modelling of the interaction of turbulent flows and porous medium with the present experiments, an industrially important problem has been chosen as a case study for further modelling. The case study is that of natural convection heat and mass transfer in respiring hyrgoscopic porous media. Chapter seven presents the numerical simulation of this application oriented problem using the model developed for a two-layer system consisting of a turbulent fluid flow overlying a saturated porous medium. Emphasis is placed on applying the model to simulate heat and mass transfer in respiring agricultural produce. Fluid flow and moisture migration occur only due to natural convection in the case study. A two-dimensional rectangular cavity is used as a representative geometry for simplicity. Boundary conditions typical of a grain storage system are used for the simulations.

A separate chapter on literature review has not been provided in this thesis. Instead, the review of the relevant literature is presented in the respective chapters.

Chapter 2

Governing equations and numerical methods

2.1 Introduction

The governing equations of fluid flow are a set of coupled non-linear partial differential equations. In their most basic form, they consist of the conservation of mass, or continuity, and the Navier-Stokes equations. The Navier-Stokes equations originally derived independently by Navier in 1822 and Stokes in 1845 (Bird *et al.*, 1960, pg. 81), describe the conservation of linear momentum. For problems involving heat and/or mass transfer, one needs to include additional transport equations for the conservation of thermal energy and species. When turbulence effects become important in a particular fluid flow problem, it is common practice to express the effect of turbulence on mean flow by using turbulence transport equations.

A porous medium essentially behaves as a resistance to fluid flow. Darcy's law represents the conservation of linear momentum for flow in a porous medium when inertial effects can be considered to be negligible. Henry Darcy in 1856 (Coulaud *et al.*, 1988) originally proposed Darcy's law as an empirical relationship. More recently, Whitaker (1986) was successful in theoretically deriving Darcy's law from first principles. Hsu and Cheng (1990) formally derived the equations governing flow in a porous medium by volume averaging the Navier-Stokes and thermal energy equations. The resultant equations representing conservation of linear momentum for flow in a porous medium resembled the original Navier-Stokes equations with additional terms (body forces) to account for the presence of the porous medium. The thermal energy equation also assumed a similar form to the analogous equation governing fluid flow without porous media. This form of the equations for flow in porous medium has been used by Chen and Chen (1992), Singh *et al.* (1993), Song and Viskanta (1994) and Chen *et al.* (1998) among other authors. Thus, the equations governing flow in porous media can be treated in the same way as those for fluid flow without porous media.

Other than for a few simplified problems, there is no analytical solution to these equations, and they need to be solved using numerical techniques. For the

numerical solution of the set of partial differential equations consisting of the Navier-Stokes, thermal energy, species transport and turbulence transport equations, computational fluid dynamics (CFD) is used. There are several commercially available packages such as CFX, COMPACT, FASTFLO and FLUENT that can be used to solve the set of partial differential equations. These packages use the finite difference, finite volume or finite element methods of discretising the governing partial differential equations. For the present research, a finite volume CFD code is developed for the geometries under consideration by modifying the TEACH[1] code that was originally developed by the Mechanical Engineering Group in what is now the Imperial College of Science, Technology and Medicine.

In the following sections, the set of partial differential equations consisting of the Navier-Stokes, thermal energy and turbulence transport equations is presented. Modifications to these equations to represent flow in a porous medium are developed. The numerical methods that are employed to solve the set of partial differential equations are described.

2.2 Governing equations

In the following description, the basic governing equations of fluid flow are described in the context of the natural convection benchmark problem that is presented in chapter three. Further developments in the model and consequently, the numerical code for the present thesis are considered as successive modifications to these basic equations. These modifications are presented in the respective chapters.

The governing equations for fluid flow are the mass continuity equation and the Navier-Stokes equations which consist of linear momentum balances for the three directions in space. In addition to these equations, the thermal energy balance needs to be fulfilled. Since the thesis involves only a two dimensional system, only two momentum equations are considered.

The governing equations can be written as follows:

[1] A copy of the modified code used for the present research is available from the author.

1. Equation of continuity:

$$\frac{\partial \rho}{\partial t}+\frac{\partial(\rho u)}{\partial x}+\frac{\partial(\rho v)}{\partial y}=0 \tag{2.1}$$

where ρ represents the fluid density, u and v are the velocity components in the x and y directions, respectively, and t is time.

2. Momentum equation in the x direction:

$$\frac{\partial(\rho u)}{\partial t}+\frac{\partial(\rho u u)}{\partial x}+\frac{\partial(\rho u v)}{\partial y}=-\frac{\partial p}{\partial x}+\frac{\partial}{\partial x}\left[\mu\left(2\frac{\partial u}{\partial x}\right)\right]+\frac{\partial}{\partial y}\left[\mu\left(\frac{\partial u}{\partial y}+\frac{\partial v}{\partial x}\right)\right]+f_x \tag{2.2}$$

where μ is the fluid viscosity, p is the fluid static pressure, and f_x is the body force in the x-direction. The body force f_x vanishes in the absence of an external force.

3. Momentum equation in the y direction:

$$\frac{\partial(\rho v)}{\partial t}+\frac{\partial(\rho v u)}{\partial x}+\frac{\partial(\rho v v)}{\partial y}=-\frac{\partial p}{\partial y}+\frac{\partial}{\partial y}\left[\mu\left(2\frac{\partial v}{\partial y}\right)\right]+\frac{\partial}{\partial x}\left[\mu\left(\frac{\partial u}{\partial y}+\frac{\partial v}{\partial x}\right)\right]+f_y \tag{2.3}$$

The body force f_y represents the buoyancy force, ρg, which arises from the co-ordinate choice of this thesis; g is acceleration due to gravity.

4. Thermal energy equation:

$$\frac{\partial(\rho T)}{\partial t}+\frac{\partial(\rho u T)}{\partial x}+\frac{\partial(\rho v T)}{\partial y}=\frac{\partial}{\partial x}\left(\frac{\mu}{\mathrm{Pr}}\frac{\partial T}{\partial x}\right)+\frac{\partial}{\partial y}\left(\frac{\mu}{\mathrm{Pr}}\frac{\partial T}{\partial y}\right)+c+d \tag{2.4}$$

where T is the fluid temperature, c represents compressibility and d represents viscous dissipation. Compressibility is neglected, because density is assumed to be a function of temperature alone. Viscous dissipation is neglected, as it has been shown to be small in comparison with the convective and diffusive terms in Equation (2.4) by Gebhart (1962) and Lankhorst (1991) for natural convection flows. The term $\mathrm{Pr}=\frac{C_p\mu}{k_f}$ is a dimensionless parameter called the Prandtl number (Pr=0.71 for air). Here, C_p represents the specific heat at constant pressure and k_f is the thermal conductivity of the fluid.

The continuity equation is not assumed to be satisfied apriori in the diffusion term of the Navier-Stokes equations, Equations (2.2) and (2.3). According to Henkes

(1990), this formulation makes the numerical solution of the natural convection problem more stable, as also observed in the present calculations

2.2.1 Treatment of the buoyancy term

Density is assumed to be a function of temperature alone, and this variation with temperature is invoked only in the buoyancy term according to the first Boussinesq approximation. This approximation is referred as the first Boussinesq approximation here, because there is another Boussinesq approximation which is invoked to represent eddy viscosity. The latter approximation is referred as the second Boussinesq approximation to avoid confusion. Further details of the fisrt Boussinesq approximation can be found in Gray and Giorgini (1976).

With the exception of the buoyancy term, density is assumed to be constant (at a characteristic temperature T_0). The density in the buoyancy term is linearised according to:

$$\frac{\rho(T)}{\rho(T_0)} = 1 - \beta(T - T_0) \tag{2.5}$$

where β is the coefficient of thermal expansion. The first Boussinesq approximation also treats the coefficients β, μ and Pr as constants, which are evaluated at the characteristic temperature T_0. This approximation is valid only for small temperature differences. For air, this approximation is valid for a temperature difference of around 30°C, and for water, it is valid for a temperature difference of around 2°C (Henkes 1990). In the present study, such small temperature differences are considered, and thus, the approximation is valid.

The governing equations are modified as follows:

1. Equation of continuity:

$$\frac{\partial u}{\partial x} + \frac{\partial v}{\partial y} = 0 \tag{2.6}$$

2. Momentum equation in the x-direction:

$$\rho\frac{\partial u}{\partial t}+\rho u\frac{\partial u}{\partial x}+\rho v\frac{\partial u}{\partial y}=-\frac{\partial p}{\partial x}+\frac{\partial}{\partial x}\left[\mu\left(2\frac{\partial u}{\partial x}\right)\right]+\frac{\partial}{\partial y}\left[\mu\left(\frac{\partial u}{\partial y}+\frac{\partial v}{\partial x}\right)\right] \tag{2.7}$$

3. Momentum equation in the y-direction:

$$\rho\frac{\partial v}{\partial t}+\rho u\frac{\partial v}{\partial x}+\rho v\frac{\partial v}{\partial y}=-\frac{\partial p}{\partial y}+\frac{\partial}{\partial y}\left[\mu\left(2\frac{\partial v}{\partial y}\right)\right]+\frac{\partial}{\partial x}\left[\mu\left(\frac{\partial u}{\partial y}+\frac{\partial v}{\partial x}\right)\right]+\rho g\beta(T-T_0) \tag{2.8}$$

4. Thermal energy equation:

$$\rho\frac{\partial T}{\partial t}+\rho u\frac{\partial T}{\partial x}+\rho v\frac{\partial T}{\partial y}=\frac{\partial}{\partial x}\left(\frac{\mu}{\mathrm{Pr}}\frac{\partial T}{\partial x}\right)+\frac{\partial}{\partial y}\left(\frac{\mu}{\mathrm{Pr}}\frac{\partial T}{\partial y}\right) \tag{2.9}$$

2.2.2 The Reynolds stress equations

The Navier-Stokes equations can be applied to a fluid flowing at any velocity relative to a given inertial frame of reference. However, at substantially large fluid velocities when the flow becomes turbulent, the size of the smallest eddies present in the flow becomes progressively smaller. The length scale of the smallest eddy present in the flow is called the Kolmogorov length scale (Tennekes and Lumley, 1972, pg. 20) given by:

$$\eta=\left(\frac{\nu^3}{\varepsilon}\right)^{1/4} \tag{2.10}$$

where ν is the fluid kinematic viscosity and ε is the rate of dissipation of turbulence kinetic energy per unit mass. $\varepsilon=\nu\overline{\frac{\partial u_i}{\partial x_k}\frac{\partial u_j}{\partial x_k}}$ where the over-bar represents a time average.

For resolving the smallest length scale, one will need to have a large number of computational grids for simulating turbulent flows. This need costs enormous computational resources that are not readily available at present. Since large eddies are responsible for most of the transport of momentum, heat and chemical species, one can represent all the variables in the governing equations in terms of average and fluctuating components, and then, average over time the resulting equations. The

averaging process gives rise to the Reynolds stress terms in the momentum equations. The need to solve for the smallest length scales is overcome by using a turbulence model that relates the average and fluctuating quantities. The averaged equations that result in the Reynolds stress and similar additional terms are presented below. Turbulence modelling is discussed later in Section 2.4.

Let $u = \bar{u} + u'$, $v = \bar{v} + v'$, $p = \bar{p} + p'$ and $T = \bar{T} + T'$ where the variables with an over-bar and prime denote average and fluctuating quantities, respectively. Upon substitution of the above terms in Equations (2.6) to (2.9) and on time averaging the resulting equations, one obtains the following equations for the mean flow:

1. Equation of continuity:

$$\frac{\partial \bar{u}}{\partial x} + \frac{\partial \bar{v}}{\partial y} = 0 \tag{2.11}$$

2. Momentum equation in the x direction:

$$\rho\frac{\partial \bar{u}}{\partial t} + \rho\bar{u}\frac{\partial \bar{u}}{\partial x} + \rho\bar{v}\frac{\partial \bar{u}}{\partial y} = -\frac{\partial \bar{p}}{\partial x} + \frac{\partial}{\partial x}\left[\mu\left(2\frac{\partial \bar{u}}{\partial x}\right)\right] + \frac{\partial}{\partial y}\left[\mu\left(\frac{\partial \bar{u}}{\partial y} + \frac{\partial \bar{v}}{\partial x}\right)\right] - \rho\frac{\partial \overline{u'v'}}{\partial y} - \rho\frac{\partial \overline{u'u'}}{\partial x} \tag{2.12}$$

3. Momentum equation in the y direction:

$$\rho\frac{\partial \bar{v}}{\partial t} + \rho\bar{u}\frac{\partial \bar{v}}{\partial x} + \rho\bar{v}\frac{\partial \bar{v}}{\partial y} = -\frac{\partial \bar{p}}{\partial y} + \frac{\partial}{\partial y}\left[\mu\left(2\frac{\partial \bar{v}}{\partial y}\right)\right] + \frac{\partial}{\partial x}\left[\mu\left(\frac{\partial \bar{u}}{\partial y} + \frac{\partial \bar{v}}{\partial x}\right)\right] + \rho g\beta\left(\bar{T} - T_0\right) - \rho\frac{\partial \overline{u'v'}}{\partial x} - \rho\frac{\partial \overline{v'v'}}{\partial y} \tag{2.13}$$

4. Thermal energy equation:

$$\rho\frac{\partial \bar{T}}{\partial t} + \rho\bar{u}\frac{\partial \bar{T}}{\partial x} + \rho\bar{v}\frac{\partial \bar{T}}{\partial y} = \frac{\partial}{\partial x}\left(\frac{\mu}{\mathrm{Pr}}\frac{\partial \bar{T}}{\partial x}\right) + \frac{\partial}{\partial y}\left(\frac{\mu}{\mathrm{Pr}}\frac{\partial \bar{T}}{\partial y}\right) - \rho\frac{\partial \overline{u'T'}}{\partial x} - \rho\frac{\partial \overline{v'T'}}{\partial y} \tag{2.14}$$

The additional terms arising from time averaging, in Equations (2.12) and (2.13) are called the Reynolds stress terms, because Reynolds in 1895 (Tennekes and Lumley,

1972, pg. 27), was the first to give the equations for turbulent flow in the above form. In Equation (2.14), the additional terms are the Reynolds stress analogues for thermal energy. The transport equations governing the second order terms involve third order correlations. Similarly, the transport equations for third order correlations lead to fourth order terms, and so on. Hence, the number of unknowns will always exceed the number of equations. This is the closure problem of turbulence. To form a closed set of equations, a decision has to be made to model the correlation terms at a certain order. Usually, turbulence modelling starts at the level of the second order correlations as shown in Equations (2.12) to (2.14). The resulting method of solving this problem using turbulence modelling is discussed in Section 2.4.

As mentioned earlier, it is necessary to model these additional terms. This is the closure problem of turbulence and the method of solving this problem using turbulence modelling is discussed in Section 2.4.

Having presented the equations that govern fluid flow, attention is now focussed on the equations that govern single-phase fluid flow in porous media.

2.2.3 Flow in porous media

In the case of flow in porous media, one is interested in macroscopic (spatially averaged) quantities which render the governing equations more tractable. The usual method of deriving the laws that govern macroscopic variables is to begin with the equations that determine the microscopic behaviour of the fluid and obtain macroscopic equations by averaging over the volumes or areas that contain many pores. A continuum model for a porous medium based on the representative elementary volume (r.e.v.) concept is adopted for the present research. The concepts of a r.e.v. and volume averaging have been discussed by Whitaker (1967).

By definition, one can have two types of averaged variables of the fluid in a porous medium. These are the volume averaged variable, Ψ_{va}, and the intrinsic phase averaged variable, Ψ_{pa}. These two averages are related by the porosity of the porous medium according to the relation:

$$\Psi_{va} = \phi \Psi_{pa} \tag{2.15}$$

where ϕ represents the porosity of the porous medium. The above relationship is called the Dupuit-Forchheimer relationship.

Once there is a continuum to deal with, one can apply the usual arguments and derive differential equations expressing conservation laws as in the case of the clear fluid. The equation for conservation of mass (the equation of continuity) in two dimensions can be written as:

$$\frac{\partial(\rho u_{va})}{\partial x} + \frac{\partial(\rho v_{va})}{\partial y} = 0 \tag{2.16}$$

The momentum equation for flow through porous media is, however, not straight forward, and it has been given in different forms by various authors as discussed below.

2.2.3.1 Darcy's law

The basic governing equation for conservation of linear momentum in porous media is Darcy's law developed by Henry Darcy in 1856 (Coulaud *et al.*, 1988). It expresses the proportionality between the flow rate and the applied pressure difference:

$$\boldsymbol{u}_{va} = -\frac{\boldsymbol{K}}{\mu} \vec{\nabla} P_{pa} \tag{2.17}$$

where $\boldsymbol{u}_{va}$ is the fluid velocity, $\boldsymbol{K}$ is the permeability tensor and $\vec{\nabla} P_{pa}$ represents the pressure gradient. In the case of single-phase flows (i.e. the present system), $\boldsymbol{K}$ is normally referred to as the permeability of the porous medium. The velocity $\boldsymbol{u}_{va}$ in the original Darcy equation is the seepage velocity or the filter velocity, more commonly know as the volume averaged velocity. The pressure P_{pa} is the measured pressure or the intrinsic phase average pressure.

Reviews of the extensions to Darcy's law have been given by Scheidegger (1963), Bear (1972) and Nield and Bejan (1992). Among these, Forchheimer's

equation (1901) and Brinkman's equation (1947) are the most significant extensions, and these are discussed next.

2.2.3.2 Forchheimer's equation

Darcy's equation is linear in the volume average velocity, and it holds when the pore Reynolds number, Re_p, is of the order of one or smaller. The pore Reynolds number for flow through porous media is defined as:

$$\mathrm{Re}_p = \frac{\rho u_{va} d_p}{\mu} \tag{2.18}$$

where d_p is the average pore diameter of the porous medium.

As the velocity increases, the transition from linear to non-linear drag is quite smooth. This transition occurs in the range of Re_p from 1 to 10, and it is not a transition from laminar to turbulent flow. As pointed out by Nield and Bejan (1992) and by many other authors, the breakdown in linearity is due to the fact that the form drag due to solid obstacles is now comparable with the surface drag due to friction.

Forchheimer's equation was originally proposed as a heuristic relationship by Dupuit in 1863 (see, Lage, 1998) and later by Forchheimer (1901) where the authors included a quadratic term in addition to the linear term in velocity in Equation (2.17) to account for inertial effects. This additional term is called the Forchheimer term. The Forchheimer term has been obtained from a closure modelling of the drag force due to solid particles by Hsu and Cheng (1990). Forccheimer's equation can be expressed as:

$$\vec{\nabla} P_{p\alpha} = -\frac{\mu}{\boldsymbol{K}} \boldsymbol{u}_{v\alpha} - \frac{c_F}{\sqrt{\boldsymbol{K}}} \rho |\boldsymbol{u}_{v\alpha}| \boldsymbol{u}_{v\alpha} \tag{2.19}$$

where c_F is a dimensionless form drag constant. The Ergun equation whose derivation is given in Bird *et al.* (1960, pg. 200), has a form similar to the Forchheimer equation, but it has been derived specifically for a packed bed of spheres. Therefore it is not as general as Equation (2.19).

2.2.3.3 Brinkman's equation

Another alternative to Darcy's equation is what is commonly known as Brinkman's equation. It can be expressed as follows:

$$\vec{\nabla} P_{pa} = -\frac{\mu}{\boldsymbol{K}} \boldsymbol{u}_{va} + \mu_{eff} \vec{\nabla}^2 \boldsymbol{u}_{va} \tag{2.20}$$

where μ_{eff} is an effective viscosity. This effective viscosity is only approximately equal to the fluid viscosity μ, and its exact quantification is still a matter of speculation. Recently, Givler and Altobelli (1994) determined the value of this effective viscosity for a porous medium of high porosity with water as the fluid. However, such an experiment can provide the value of effective viscosity only for the specific porous medium and the fluid under consideration. The second term on the right hand side of Equation (2.20) is called the Brinkman term. This term is valid for only high porosity porous media according to some authors such as Nield (1991), and it might not be valid for natural porous media which do not have porosities higher than 0.6. In situations such as in the present research, there is an interface between a clear fluid and porous medium. In such cases, a mismatch exists between the Navier-Stokes equation for fluid flow (which has a Laplacian term) and the equation for flow through the adjacent porous medium if Darcy's law (Equation (2.17)) is applied. This mismatch at the interface between the fluid layer and porous medium is overcome by the addition of the Brinkman term in the original Darcy's law.

Several authors, such as Beckermann *et al.* (1987), Chen and Chen (1992), Song and Viskanta (1994) and Chen *et al.* (1998), have used a combination of Equations (2.19) and (2.20) to form what is established as the Brinkman-Forchheimer extended Darcy (BFD) flow model for porous media. The BFD model allows the numerical treatment of a composite system, such as the present one, as a continuum. The change from the fluid layer to a porous layer is taken care by just a change of the parameters, ϕ and K, of the porous medium.

Hsu and Cheng (1990) formally derived the BFD model for macroscopic flow through porous media by assuming that the microscopic momentum equation for incompressible flow in a porous medium is given by the Navier-Stokes equation. The final form of this equation after volume averaging the Navier-Stokes equation in vector form is:

$$\rho\frac{\partial \boldsymbol{u}_{va}}{\partial t}+\vec{\nabla}\left(\frac{\boldsymbol{u}_{va}.\boldsymbol{u}_{va}}{\phi}\right)=-\vec{\nabla}p_{va}+\mu_{eff}\vec{\nabla}^{2}\boldsymbol{u}_{va}-\left[\frac{\mu\phi\boldsymbol{u}_{va}}{\boldsymbol{K}}+\rho\frac{c_F\phi\boldsymbol{u}_{va}|\boldsymbol{u}_{va}|}{\sqrt{\boldsymbol{K}}}\right] \tag{2.21}$$

The first and second terms in the square bracket on the right hand side of the equation are the Darcy and Forchheimer terms, respectively. These terms were derived after closure modelling of the total drag force per unit volume (body force) due to the presence of the solid particles. The effective viscosity, μ_{eff}, associated with the Brinkman term (second term on the right hand side of the equation) is equal to the fluid viscosity, μ, in the derivation of Hsu and Cheng (1990). It has also been shown by Neale and Nader (1974) that taking $\mu_{eff}=\mu$ provides good agreement with experimental data. All variables in Equation (2.21) are volume averaged. The conversion from intrinsic phase averaged value to the volume averaged value is carried out by using the relationship given in Equation (2.15).

2.2.3.4 Heat transfer in porous media

The thermal energy equation for porous media is fairly straightforward, and it is similar to the thermal energy equation for a clear fluid. The thermal energy equation can be written as:

$$\frac{\partial T_{va}}{\partial t}+u_{va}\frac{\partial T_{va}}{\partial x}+v_{va}\frac{\partial T_{va}}{\partial y}=\frac{\partial}{\partial x}\left(\alpha_{eff}\frac{\partial T_{va}}{\partial x}\right)+\frac{\partial}{\partial y}\left(\alpha_{eff}\frac{\partial T_{va}}{\partial y}\right) \tag{2.22}$$

where α_{eff} is the effective thermal diffusivity of the fluid and porous medium system. Thermal diffusivity for a fluid is defined as the ratio of the kinematic viscosity ν and the Prandtl number Pr of the fluid. In other words, the thermal diffusivity of the fluid can be written as:

$$\alpha=\frac{k_f}{\rho c_{p,f}} \tag{2.23}$$

where k_f is the thermal conductivity of the fluid, and $c_{p,f}$ is the specific heat of the fluid at constant pressure.

Beckermann *et al.* (1988), have suggested the following form of the effective diffusivity for the porous medium:

$$\alpha_{eff} = \frac{k_{eff}}{\rho c_{p,f}} \tag{2.24}$$

where $k_{eff} = k_f^{\phi} k_b^{(1-\phi)}$, k_b being the thermal conductivity of the solid matrix. Although Nozad *et al.* (1984) have derived a more sophisticated form of k_{eff}, the above formulation is simple, and it has been shown to give reasonably accurate results by Beckermann *et al.* (1988) and Chen *et al.* (1998).

2.2.4 Summary

The governing equations for fluid flow without the porous medium are well established. From the point of view of representation of turbulence, discussed in Section 2.4, they pose several difficulties. However, in the case of flow through porous media, there is still some controversy regarding the exact nature of the equations to be used especially to represent the conservation of linear momentum. To summarise, Equations (2.6) to (2.9) represent the basic equations governing fluid flow and heat transfer without porous media. The time-averaged forms of these equations are given by Equations (2.11) to (2.14). Equation (2.21) is the Navier-Stokes analogue of the conservation of linear momentum for flow in porous media and is commonly referred to as the Brinkman-Forchheimer extended Darcy flow (BFD) model. The continuity and thermal energy equations, Equations (2.16) and (2.22) respectively, for flow in porous media have a form that is similar to that in fluid flow without porous media.

2.3 Treatment of boundary and interface conditions

One of the important aspects of modelling flows in a system such as the one being studied, is the treatment of the boundary and interface between the porous medium and the clear fluid. For the clear fluid region, the linear momentum balance for fluid flow is the Navier-Stokes equation. Thus, the usual symmetry and no-slip or free slip boundary conditions can be applied. Parts of the walls attached to the porous medium can have either a no-slip boundary condition or a slip boundary condition for velocities depending on whether the Brinkman extended Darcy formulation (Section 2.2.3.3) or the Darcy formulation (Section 2.2.3.1) is used.

The treatment of the interface between the fluid and fluid saturated porous medium is, however, difficult. The temperature boundary condition is straightforward, and one simply needs the temperature to be varying continuously across the interface. However, for the velocity boundary condition, there are four different approaches that could be adopted. These are:

2.3.1 The Beavers and Joseph boundary condition

If the Brinkman term is excluded from the governing equations for the porous medium, there is a difficulty of matching up the Navier-Stokes equation for the clear fluid and the Darcy type equation for the porous medium at the interface. This difficulty arises because of the fact that the Navier-Stokes equation has a Laplacian term which the Darcy type equation lacks. In order to overcome this difficulty, Beavers and Joseph (1967) proposed an interface condition. It assumes that the interface is permeable, and it takes the vertical velocity component to be continuous across the interface. It also relates the tangential shear experienced by the fluid along the permeable surface to the velocity difference between the tangential velocity of the fluid in the clear fluid region and the volume averaged tangential velocity in the porous bed close to the interface. This relationship can be expressed as:

$$\left.\frac{\partial u}{\partial y}\right|_{y=0_+} = \alpha_{bj}\left(u_+ - u_{av+}\right) \tag{2.25}$$

where α_{bj} is the Beavers and Joseph constant, u_+ is the fluid side tangential velocity close to the interface and u_{av+} is the porous medium side tangential velocity close to the interface.

This boundary condition was employed by Poulikakos *et al.* (1986), in their study of natural convection in a fluid overlying a porous bed. Although these authors study a system similar to the present one, the range of Rayleigh numbers considered is low, and it does not encompass the turbulent regime, the investigation of which is a key objective of this thesis.

2.3.2 Stress jump condition proposed by Ochoa-Tapia and Whitaker

Ochoa-Tapia and Whitaker (1995a) proposed a stress jump condition in which a set of equations is suggested for the interface, which incorporates the Brinkman term. The Stokes equation (i.e. the Navier-Stokes equation without the temporal and inertial terms) is used as the basis for the derivation. The excess stress terms that appear in the jump condition are represented in a manner that leads to a tangential stress boundary condition containing a single adjustable coefficient of order one. These authors also compared the theory with the experimental findings of Beavers and Joseph (1967), and they found good agreement.

2.3.3 Variable porosity model of Ochoa-Tapia and Whitaker

Ochoa-Tapia and Whitaker (1995b) also suggested a variable porosity model for the boundary as a substitute for the jump condition (1995a). They found that although the variable porosity model does not lead to a successful representation of all the experimental data, it does provide some insight into the complexities of the interface between the porous medium and a homogeneous fluid.

2.3.4 Treatment of the interface as a continuum

A particularly pragmatic approach to treating the boundary is to assume that the composite system is essentially a single medium with varying properties, ϕ and K. For the fluid layer, ϕ assumes a value of one, and for the porous medium, it assumes the value of the porosity of the porous medium. Similarly, for the fluid layer, K tends to infinity, and for the porous medium, it assumes the value of the permeability of the porous medium. As mentioned earlier, this approach is made possible by using the Brinkman term in the Darcy type equation for the porous medium, so that it matches the Navier-Stokes equation. The extra terms, namely, the Forchheimer term and the Darcy term, vanish for the clear fluid, whereas the Brinkman term is equivalent to the Laplacian in the Navier-Stokes equation. This approach has been adopted

successfully by Song and Viskanta (1994) and Chen *et al.* (1998) among other authors.

2.3.5 Summary

There is no universally acceptable treatment of the interface between the fluid layer and a porous medium. However, the treatment of the composite system as a single medium seems to be the most pragmatic among the four different approaches. Also, there is no evidence to suggest that this approach is inferior to the other approaches. Thus, in the present research, this approach of treating the interface is employed.

2.4 Turbulence modelling

2.4.1 Turbulence modelling of fluid flow in the absence of porous media

The Reynolds stress terms that arose out of the averaging process in Section 2.2.2 can be dealt with in two ways, namely, either by using an eddy viscosity model or by using a Reynolds stress model. The former uses a model for the turbulent viscosity, μ_t, whereas the latter uses transport equations for all the Reynolds stresses. The former closure approach is preferred firstly because of the significantly lower computing time required for solving the governing equations. Also, the latter approach leads to significantly larger number of terms that need modelling.

In the eddy viscosity model, the Reynolds stress and analogous terms are defined as follows:

$$-\rho\overline{u_i'u_j'} = \mu_t\left(\frac{\partial\overline{u_i}}{\partial x_j}+\frac{\partial\overline{u_j}}{\partial x_i}\right)-\frac{2}{3}\delta_{ij}\left(k\rho+\mu_t\frac{\partial\overline{u_k}}{\partial x_k}\right) \tag{2.26}$$

$$-\rho\overline{u_j'T'} = \frac{\mu_t}{\sigma_T}\frac{\partial\overline{T}}{\partial x_j} \tag{2.27}$$

where, $i = 1, 2$ and $j = 1, 2$

In the above equations, $k = \frac{\overline{u_k u_k}}{2}$ is the turbulence kinetic energy. δ_{ij} is Kronecker's delta. $\delta_{ij} = 1$ for $i = j$, and $\delta_{ij} = 0$ for $i \neq j$. σ_T is the turbulent Prandtl number for temperature, $\sigma_T = 0.9$. μ_t represents eddy viscosity.

In general, the eddy viscosity, μ_t, satisfies the identity,

$$\mu_t = \rho c_\mu V L \tag{2.28}$$

where V and L are the characteristic velocity and length scales, of turbulence, respectively. c_μ is a model constant. In general c_μ, V and L can be functions of time and space.

Depending on the treatment of the various parameters in Equation (2.28), one obtains different turbulence models.

1. The simplest eddy viscosity model is the Boussinesq model which can be expressed as:

$$-\rho\overline{u_i' u_j'} = \mu_t\left(\frac{\partial \overline{u_i}}{\partial x_j} + \frac{\partial \overline{u_j}}{\partial x_i}\right) \tag{2.29}$$

This model treats μ_t as a constant, and it is called the Boussinesq approximation which is referred here as the second Boussinesq approximation (Section 2.2.1 contains details of the first Boussinesq approximation). It was proposed first by Boussinesq in 1877 (Launder and Spalding, 1972, pg. 9).

2. Zero equation models (or algebraic models):

These models use an algebraic relationship between eddy viscosity and other variables. The most famous zero equation model is Prandtl's mixing length model. An extension of this model is the Cebeci and Smith model (1974).

3. One equation models:

These models solve one partial differential equation for a μ_t-related variable in addition to the continuity, momentum and energy equations. For example, in

Equation (2.28), the model can use an algebraic expression for V and a differential equation for L.

4. Two equation models:

These models solve two partial differential equations for two μ_t-related variables. The most widely used class of two equation models is the k-ε model which results in transport equations for k, the turbulence kinetic energy, and ε, the rate of dissipation of k. With reference to Equation (2.28), the model uses a constant c_μ and sets $V = k^{0.5}$ and $L = k^{1.5}/\varepsilon$. The k-ε model is perhaps the most versatile of all the turbulence models. In the present research, all calculations for the turbulent regime use the k-ε model. A detailed description of the various turbulence models can be found in Wilcox (1993).

2.4.1.1 The standard k-ε model

The k-ε model in its standard form was originally proposed by Harlow and Nakayama (1967). Details of the derivation of this model can be found in the original paper. The final forms of the modelled momentum, thermal energy and the two additional transport equations for k and ε are presented below:

1. Momentum equation in the x direction:

$$\rho\frac{\partial u}{\partial t}+\rho u\frac{\partial u}{\partial x}+\rho v\frac{\partial u}{\partial y}=-\frac{\partial p}{\partial x}+\frac{\partial}{\partial x}\left[(\mu+\mu_t)\left(2\frac{\partial u}{\partial x}\right)\right]+\frac{\partial}{\partial y}\left[(\mu+\mu_t)\left(\frac{\partial u}{\partial y}+\frac{\partial v}{\partial x}\right)\right] \quad (2.30)$$

2. Momentum equation in the y direction:

$$\rho\frac{\partial v}{\partial t}+\rho u\frac{\partial v}{\partial x}+\rho v\frac{\partial v}{\partial y}=-\frac{\partial p}{\partial y}+\frac{\partial}{\partial y}\left[(\mu+\mu_t)\left(2\frac{\partial v}{\partial y}\right)\right]+\frac{\partial}{\partial x}\left[(\mu+\mu_t)\left(\frac{\partial u}{\partial y}+\frac{\partial v}{\partial x}\right)\right] \quad (2.31)$$
$$+\rho g\beta(T-T_0)$$

3. Thermal energy equation:

$$\rho\frac{\partial T}{\partial t}+\rho u\frac{\partial T}{\partial x}+\rho v\frac{\partial T}{\partial y}=\frac{\partial}{\partial x}\left[\left(\frac{\mu}{\mathrm{Pr}}+\frac{\mu_t}{\sigma_T}\right)\frac{\partial T}{\partial x}\right]+\frac{\partial}{\partial y}\left[\left(\frac{\mu}{\mathrm{Pr}}+\frac{\mu_t}{\sigma_T}\right)\frac{\partial T}{\partial y}\right] \tag{2.32}$$

where σ_T is the turbulent Prandtl number for temperature.

The above equations are modified forms of Equations (2.12) to (2.14) after applying the eddy viscosity closure model (Equations (2.26) and (2.27)) to the Reynolds stress terms in the respective equations. The eddy viscosity, μ_t, is given by the relationship:

$$\mu_t=\rho c_\mu f_\mu\frac{k^2}{\varepsilon} \tag{2.33}$$

where f_μ is a damping function associated with low Reynolds number k-ε turbulence models discussed in Section 2.4.1.2. All variables in these equations are the averaged variables. The over-bar signs have been removed from these variables for convenience of representation. The k and ε equations that convert the above equations into a closed set are presented below.

4. Turbulence kinetic energy equation:

$$\rho\frac{\partial k}{\partial t}+\rho u\frac{\partial k}{\partial x}+\rho v\frac{\partial k}{\partial y}=\frac{\partial}{\partial x}\left[\left(\mu+\frac{\mu_t}{\sigma_k}\right)\frac{\partial k}{\partial x}\right]+\frac{\partial}{\partial y}\left[\left(\mu+\frac{\mu_t}{\sigma_k}\right)\frac{\partial k}{\partial y}\right] \tag{2.34}$$
$$+P_k+G_k-\rho\varepsilon+\rho D$$

where k is the turbulence kinetic energy, σ_k is the turbulent Prandtl number for k, and ε is the rate of turbulence kinetic energy dissipation. D is a damping term, and it is equal to zero for the standard k-ε model. The terms P_k and G_k are defined after Equation (2.35).

5. Equation for the rate of energy dissipation:

$$\rho\frac{\partial \varepsilon}{\partial t}+\rho u\frac{\partial \varepsilon}{\partial x}+\rho v\frac{\partial \varepsilon}{\partial y}=\frac{\partial}{\partial x}\left[\left(\mu+\frac{\mu_t}{\sigma_\varepsilon}\right)\frac{\partial \varepsilon}{\partial x}\right]+\frac{\partial}{\partial y}\left[\left(\mu+\frac{\mu_t}{\sigma_\varepsilon}\right)\frac{\partial \varepsilon}{\partial y}\right] \tag{2.35}$$
$$+\left(c_{\varepsilon 1}f_1\left(P_k+c_{\varepsilon 3}G_k\right)-\rho c_{\varepsilon 2}f_2\varepsilon\right)\frac{\varepsilon}{k}+\rho E$$

with

$$P_k=\mu_t\left(2\left(\frac{\partial u}{\partial x}\right)^2+2\left(\frac{\partial v}{\partial y}\right)^2+\left(\frac{\partial u}{\partial y}+\frac{\partial v}{\partial x}\right)^2\right) \tag{2.36}$$

$$G_k=-\frac{\mu_t}{\sigma_T}g\beta\frac{\partial T}{\partial y}$$

The terms P_k and G_k represent the production of turbulence kinetic energy due to shear and buoyancy, respectively. E is a damping term, and it is equal to zero for the standard k-ε model. σ_ε is the turbulent Prandtl number for ε. The following values are empirical constants used in the standard k-ε model:

$c_\mu = 0.09$, $c_{\varepsilon 1} = 1.44$, $c_{\varepsilon 2} = 1.92$, $\sigma_T = 0.9$, $\sigma_k = 1.0$, $\sigma_\varepsilon = 1.3$, $f_\mu = f_1 = f_2 = 1.0$.

The constant $c_{\varepsilon 3}$ does not have a universally accepted value for natural convection flow calculations. Rodi (1980) suggests that the coefficient assumes a value close to 1 in vertical boundary layers and close to 0 in horizontal boundary layers. For all turbulent natural convection flow calculations in the present study, the form suggested by Henkes (1990) is used, which satisfies both limits:

$$c_{\varepsilon 3} = \tanh|v/u| \tag{2.37}$$

2.4.1.1.1 Wall functions for the standard k-ε model

Close to a fixed wall, velocity and temperature profiles in a forced-convection boundary layer, with zero or negligible pressure gradient, can be approximated by logarithmic wall functions (Tennekes and Lumley, 1972, pg. 186) given by,

$$\begin{aligned} v^+ &= \frac{1}{\kappa}\ln(9x^+) \quad (\kappa = 0.41) \\ T^+ &= 2.195\ln(x^+) + 13.2\,\mathrm{Pr} - 5.66 \end{aligned} \tag{2.38}$$

with

$$\begin{aligned} x^+ &= \frac{xv^*}{\nu}, v^+ = \frac{v}{v^*}, T^+ = \frac{T_w - T}{T^*} \\ v^* &= \sqrt{\frac{\tau_w}{\rho}} = \sqrt{\nu\left(\frac{\partial v}{\partial x}\right)_w}, T^* = -\frac{\nu}{\mathrm{Pr}\,v^*}\left(\frac{\partial T}{\partial x}\right)_w \end{aligned} \tag{2.39}$$

where x is the distance along a normal to the wall, and τ represents the shear stress. The subscript w refers to the value at the wall. The wall functions in Equation (2.38) are used in the fully turbulent inertial sublayer at $x^+ \geq 11.63$. In the viscous sublayer close to the wall, at $x^+ < 11.63$, turbulence is neglected (and the relationship $v^+ = x^+$ is used). These are the assumptions made in the standard k-ε model.

Wall functions for k and ε can be derived from Equation (2.38) as follows (Henkes, 1990). By assuming that the convection and diffusion of k is negligible in the inertial sublayer, Equation (2.34) reduces to:

$$P_k = \rho\varepsilon \tag{2.40}$$

Note that P_k in Equation (2.36) is reduced to its boundary layer form:

$$P_k = \mu_t \left(\frac{\partial v}{\partial x}\right)^2 \tag{2.41}$$

Prandtl's mixing length model is also invoked:

$$\mu_t = \rho(\kappa x)^2 \frac{\partial v}{\partial x} \qquad (\kappa = 0.41) \tag{2.42}$$

Using Equations (2.33), (2.40) and (2.41), wall functions for k and ε are formulated as:

$$k = \frac{(v^*)^2}{\sqrt{c_\mu}} \tag{2.43}$$

$$\varepsilon = \frac{(v^*)^3}{\kappa x} \tag{2.44}$$

These wall functions are used while employing the standard k-ε model.

2.4.1.2 Low Reynolds number k-ε models

The use of wall functions in the standard k-ε model for calculating variables close to the wall is not acceptable for forced-convection flows where there may be an adverse pressure gradient, or for natural convection flows. The reason is that these wall functions do not represent the correct behaviour in such flows in the vicinity of the wall. In order to overcome this problem, various authors have suggested modifications to the standard k-ε model. The models of Jones and Launder (JL, 1972), Launder and Sharma (LS, 1974), Lam and Bremhorst (LB, LB1 1981), Chien (CH, 1982) and To and Humphrey (TH, 1986) represent examples of such modifications. A review of some of these models has been given in Patel *et al.* (1985) for wall bounded forced convection shear flows. These modified models are also referred as low Reynolds number k-ε models, as they have the correct wall behaviour

where viscous effects predominate (when the local Reynolds number is low). Unlike the standard k-ε model, simulations using the low Reynolds number models solve for velocities and turbulent quantities right up to the wall. In order to account for the no-slip wall boundary conditions, the low Reynolds number models incorporate either a wall damping effect or a direct effect of molecular viscosity, or both, on the empirical constants and functions in the turbulence transport equations. Some low Reynolds number models are provided as examples in Table 2.1.

2.4.2 Turbulence modelling for fluid flow within porous media

Turbulence modelling of flows within porous media is a recently emerging and controversial topic. Masuoka and Takatsu (1996) have developed a zero equation turbulence model for flow through porous media by assuming the deviation from Darcy's law to be caused by turbulence. However, this is contrary to the investigation of Hsu and Cheng (1990) and the arguments of Nield (1997) that the deviation from Darcy's law actually gives rise to the Forchheimer flow resistance.

Theoretical developments in the field of modelling turbulent flow in porous media have primarily used the k-ε model for clear fluid flow as the basis. The reason might be the versatility and the simplicity of the k-ε class of turbulence models. Without a formal derivation of a two-equation turbulence model for porous media, authors such as Lee and Howell (1987), Lim and Mathews (1993) and Prescott and Incropera (1995) have used modified forms of the k-ε model to represent turbulent flow in porous media. Since a porous medium acts as a resistance to flow, these authors introduced additional sink terms in the turbulence transport equations to account for the damping of turbulence by the porous medium. In formally deriving a k-ε model for flow in porous media, one can adopt two approaches:

One approach is to start with the k-ε model for clear fluid flow and use the volume averaging technique given in Section 2.2.3 to obtain a macroscopic model for turbulent flow in porous media. Wang and Takle (1995) discouraged the adoption of such an approach by stating that, " *time averaging followed by spatial averaging*

implies that obstacle elements interact only with time-averaged flow.....turbulence energy-cascade process is precluded under these assumptions".

A second approach is to start with the volume averaged equations for flow through porous media and to apply time averaging to this set of equations. Closure modelling of the extra terms arising out of time averaging leads to the modified k-ε model for the porous medium. Antohe and Lage (1997) have adopted this approach by using the BFD model (Equation (2.21)) as the governing equation for conservation of linear momentum in porous media.

The main problem with both approaches is the loss of information occurring due to the closure modelling after the second averaging procedure. However, it seems reasonable to assume that this loss of information would be similar irrespective of the method adopted. Therefore, in the present study, it was decided to use the form of the model developed by Antohe and Lage (1997) and to compare the simulations using the model with the experimental results. A detailed derivation of the model is not presented here as it can be found in the original paper. The model has been used here in the numerical simulations of the experiments given in chapters four and six. Hence, the model is presented with the simulations in chapter five.

Table 2.1 Examples of low Reynolds number turbulence models.

Model Code	ε_w	C_μ	$c_{\varepsilon 1}$	$c_{\varepsilon 2}$	σ_k	σ_ε	f_μ	f_1	f_2	D	E
Std. k-ε	Wall Function	0.09	1.44	1.92	1.0	1.3	1.0	1.0	1.0	0.0	0.0
JL	$\varepsilon = 0$	0.09	1.44	1.92	1.0	1.3	$\exp\left(\frac{-2.5}{1+\mathrm{Re}_t/50}\right)$	1.0	$1-0.3\exp\left(-\mathrm{Re}_t^2\right)$	$-2\nu\left(\frac{\partial\sqrt{k}}{\partial x}\right)^2$	$2\nu\nu_t\left(\frac{\partial^2 v}{\partial x^2}\right)^2$
LB	$\varepsilon = \nu\frac{\partial^2 k}{\partial x^2}$	0.09	1.44	1.92	1.0	1.3	$\left(1-\exp\left(-0.0165\,\mathrm{Re}_k\right)\right)^2\left(1+20.5/\mathrm{Re}_t\right)$	$1+\left(\frac{0.05}{f_\mu}\right)^3$	$1-\exp\left(-\mathrm{Re}_t^2\right)$	0.0	0.0
LBI	$\frac{\partial\varepsilon}{\partial x} = 0$	0.09	1.44	1.92	1.0	1.3	$\left(1-\exp\left(-0.0165\,\mathrm{Re}_k\right)\right)^2\left(1+20.5/\mathrm{Re}_t\right)$	$1+\left(\frac{0.05}{f_\mu}\right)^3$	$1-\exp\left(-\mathrm{Re}_t^2\right)$	0.0	0.0
CH	$\varepsilon = 0$	0.09	1.35	1.8	1.0	1.3	$1-\exp\left(-0.0115x^+\right)$	1.0	$1-\frac{2}{9}\exp\left(-\left(\frac{\mathrm{Re}_t}{6}\right)^2\right)$	$-2\nu\frac{k}{x^2}$	$-2\frac{\nu\varepsilon}{x^2}\exp\left(-0.5x^+\right)$
TH	$\varepsilon = 2\nu\left(\frac{\partial\sqrt{k}}{\partial x}\right)^2$	0.09	1.44	1.92	1.0	1.3	$\exp\left(\frac{-2.5}{1+\mathrm{Re}_t/50}\right)$	1.0	$1-0.3\exp\left(-\mathrm{Re}_t^2\right)f_3$ $f_3 = \begin{cases} 1 & \text{if } x^+ \geq 5 \\ 1-\exp\left(-\mathrm{Re}_t^2\right) & \text{if } x^+ < 5 \end{cases}$	0.0	0.0

$$\mathrm{Re}_k = \frac{x\sqrt{k}}{\nu}, \quad \mathrm{Re}_t = \frac{k^2}{\nu\varepsilon}, \quad x^+ = \frac{xv^*}{\nu}$$

2.4.3 Summary

The k-ε model has been found to be quite successful in predicting flows without porous media. However, the form of the model which suits flow in porous media is uncertain. The main difficulty in ascertaining the validity of a turbulence model for porous media is the lack of experimental data available in literature. As mentioned earlier, turbulence in a porous medium may not exist if it has low porosity and permeability. Even for high porosity/permeability porous media, measurements made within the porous medium may not be useful to quantify macroscopic turbulence that is essential from a modelling point of view. Therefore, in the present thesis, a two-layer system has been chosen to be studied. The system consists of a turbulent fluid layer overlying a porous medium. The effect of turbulence penetrating the porous medium can be inferred by investigating the change in the flow patterns in the fluid layer for such systems. The validity of the turbulence model can then be ascertained by comparing the simulations for the same system with the experimental results.

The next section deals with the numerical methods adopted to solve the set of partial differential equations.

2.5 Numerical methods

2.5.1 Discretisation of the governing equations

Since the governing equations for fluid flow form a set of coupled non-linear partial differential equations, these have to be solved using a numerical scheme for complicated problems, such as that considered in the present work. Numerical schemes can be broadly classified into four categories in terms of the type of discretisation used. These are the spectral, finite element, finite difference and the finite volume methods. The last two methods are used extensively for fluid flow problems. The present study employs the finite volume method described by Patankar (1980) using the primitive variable formulation. In this formulation, the calculation of all variables (i.e., vectors u and v and scalars p, T, k and ε) at one point

leads to a non-uniform pressure field being represented as a uniform pressure field. Also, a physically unrealistic velocity field seems to satisfy the discretised continuity equation. These problems are overcome by using a different set of points to calculate vectors and scalars. This approach is called the staggered grid concept where the points at which vectors are calculated are staggered with respect to the points at which scalars are evaluated. Such a staggered grid for velocity components was first used by Harlow and Welch (1965).

In the staggered grid, the velocity components are calculated for the points that lie on the faces of a control volume. Thus, the x-component of velocity u is calculated at the faces that are normal to the x-direction. The locations of u are indicated in Figure 2.1 by short arrows, while the grid points (hereafter called the main grid points) are located at the intersections of the solid lines. The dashed lines indicate the faces of the control-volume.

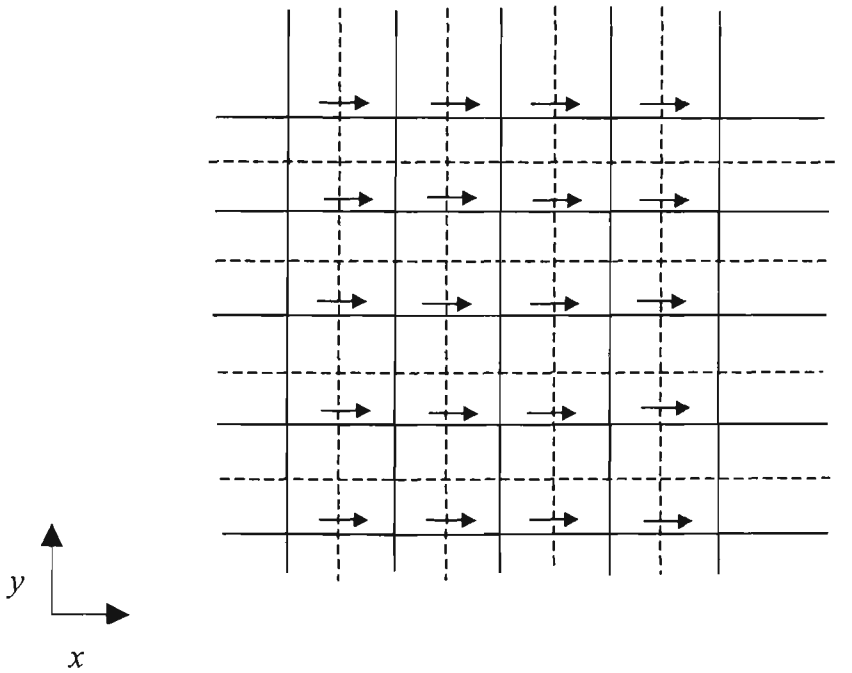

Figure 2.1: Staggered locations for u

Note that with respect to the main grid points, the u locations are staggered only in the x direction. Similarly, the v locations are staggered only in the y direction. Scalar variables like T, p, k and ε are calculated at the main grid points.

The finite volume method can be explained by considering a two-dimensional convection-diffusion equation for an unknown scalar, φ (=T, k or ε):

$$\frac{\partial \varphi}{\partial t} + \mathrm{div}\xi = S \tag{2.45}$$

where, ξ is the flux vector and S is a source term. ξ is the sum of a convection component $\xi^c = \rho u \varphi$ and a diffusion component $\xi^d = -\mu^\varphi \nabla \varphi$. Note that the extra terms in the momentum equations occurring due to the presence of the porous medium (the Darcy and Forchheimer terms in Equation (2.21)) are part of the source term. Equation (2.45) is integrated over the finite volume around grid point (i, j). In Figure 2.2, an example of a control volume for a scalar quantity, is given to illustrate the discretisation process.

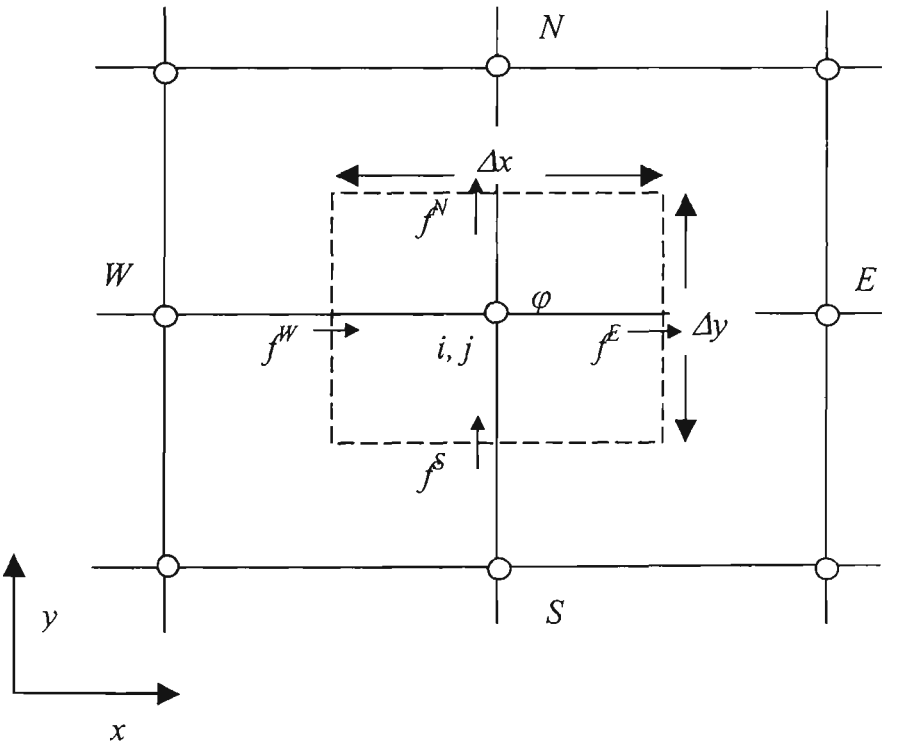

Figure 2.2: Shaded area representing a scalar control volume.

Rewriting div ξ as fluxes, f, through the sides of the (i, j)-volume with the help of Gauss' divergence theorem one obtains:

$$\int_{\mathrm{vol.}(i,j)} \frac{\partial \varphi}{\partial t} dxdy + \int_{\mathrm{side}} \left[f^E - f^W\right] dy + \int_{\mathrm{side}} \left[f^N - f^S\right] dx = \int_{\mathrm{vol.}(i,j)} S dxdy \tag{2.46}$$

The superscripts E, W, N and S refer to the east, west, north and south sides of the volume respectively. The integrals are approximated as follows:

$$\left[\frac{\partial \varphi}{\partial t}\right]_{i,j} \Delta x \Delta y + \left[f_{i+1/2,j} - f_{i-1/2,j}\right] \Delta y + \left[f_{i,j+1/2} - f_{i,j-1/2}\right] \Delta x = S_{i,j} \Delta x \Delta y \tag{2.47}$$

Note that the integration is performed over finite volumes around the staggered grid points for the velocities u and v if the momentum equations are considered.

The integration of Equation (2.47) with respect to time is carried out fully implicitly (unless otherwise mentioned) by evaluating all spatial derivatives at the new time level n. The unsteady term, fluxes and source are further discretised using finite differences. The unsteady term at the time level n is discretised with two time levels giving a first-order truncation error in time as follows:

$$\left[\frac{\partial \varphi}{\partial t}\right]_{i,j} = \frac{\varphi_{i,j}^{n} - \varphi_{i,j}^{n-1}}{\Delta t} + O(\Delta t) \tag{2.48}$$

The source term and the diffusion part of the flux are discretised with a second order truncation error as follows:

$$f_{i+1/2,j}^{d} = -\frac{1}{2}\left(\mu_{i,j}^{\varphi} + \mu_{i+1,j}^{\varphi}\right)\frac{\varphi_{i+1,j} - \varphi_{i,j}}{x_{i+1} - x_{i}} + O(\Delta x^{2}) \tag{2.49}$$

The convection flux can be rewritten as:

$$f_{i+1/2,j}^{c} = (\rho u)_{i+1/2,j}\varphi^{E} \tag{2.50}$$

where φ^{E} is an approximation for φ at the east side of the volume (i, j). Different approximations for φ^{E} are proposed in the literature. Three examples are given below:

1. Second-order central scheme

$$\varphi^{E} = \left(\varphi_{i,j} + \varphi_{i+1,j}\right)/2 \tag{2.51}$$

2. First-order upwind scheme

$$\varphi^{E} = \begin{cases} \varphi_{i,j} & \text{if } u_{i+1/2,j} \geq 0 \\ \varphi_{i+1,j} & \text{if } u_{i+1/2,j} < 0 \end{cases} \tag{2.52}$$

3. QUICK scheme (Quadratic Upstream Interpolation for Convection Kinematics) introduced by Leonard (1979a)

$$\varphi^{E} = \begin{cases} \left(\varphi_{i,j} + \varphi_{i+1,j}\right)/2 - \left(\varphi_{i-1,j} - 2\varphi_{i,j} + \varphi_{i+1,j}\right)/8 & \text{if } u_{i+1/2,j} \geq 0 \\ \left(\varphi_{i,j} + \varphi_{i+1,j}\right)/2 - \left(\varphi_{i,j} - 2\varphi_{i+1,j} + \varphi_{i+2,j}\right)/8 & \text{if } u_{i+1/2,j} < 0 \end{cases} \tag{2.53}$$

There are several other schemes such as the Leonard difference scheme, the power law scheme (Patankar, 1980), the fourth order central scheme and the second order upwind scheme which have been used to discretise the convection term. The

choice of a particular scheme depends on the numerical accuracy required and the stability offered by the discretisation scheme. For example, schemes 1 and 3 above lead to a second order truncation error in the approximation of div ξ^{φ}, whereas scheme 2 gives only a first order accuracy. Strictly speaking, this truncation error holds true only when a uniform grid spacing is used. Solutions obtained by using the central scheme exhibit local oscillations if the grid Peclet (or Reynolds) number, ($Pe = \rho|u|\Delta x / \mu^{\varphi}$) becomes larger than two. These oscillations can be suppressed by using an upwind scheme such as 2 or 3. The first order upwind scheme most effectively damps oscillations albeit with an increase in the truncation error. This scheme also suffers from a large artificial numerical diffusion.

The hybrid scheme uses a combination of the central and first order upwind schemes. It is more stable than the central scheme, at the same time being more accurate than the upwind scheme. If the grid Peclet number exceeds the value of two, the hybrid scheme locally switches from the second order central scheme to the first order upwind scheme, and hence, the diffusion contribution is set to zero. The second order central, first order upwind and the hybrid schemes are used throughout this thesis.

2.5.2 Grid distribution

In this thesis, grids are generated using algebraic functions. These grids can either be uniformly or non-uniformly spaced. The staggered grid points are first developed. They are represented as *xu(i)* and *yv(j)* in the x and y directions, respectively. The main grid points are then calculated by using the staggered grid locations. Figure 2.3 shows the staggered and main grid locations *xu(i)* and *x(i)*, respectively, for the x direction on a 7x7 grid. For discretising the boundary conditions, the grid is extended across the boundaries, introducing virtual grid points. In Figure 2.3 the heavy solid lines represent the virtual grid, whereas the heavy dashed line represent the physical boundary. The use of virtual grid points has the advantage that no modification of the discretisation of the equations is required in the volumes along the boundaries.

A Dirichlet boundary condition for u velocity on the west or east boundary is treated by assigning the value to the unknown at the boundary. Similarly, the value for v is assigned to the unknown at the north and south boundary. Dirichlet boundary conditions for the scalars are discretised with second order accuracy by using the virtual point. For example:

$$\varphi_{Dir} = \frac{\varphi_{i\max,j} + \varphi_{i\max+1,J}}{2} + O(\Delta x^2) \tag{2.54}$$

where $i$max+1 denotes the virtual point.

The discretisation of Neumann boundary conditions with virtual points is straightforward, and it can be written as:

$$\varphi'_{Neu} = \frac{\varphi_{i\max+1,j} - \varphi_{i\max,j}}{\Delta x} + O(\Delta x^2) \tag{2.55}$$

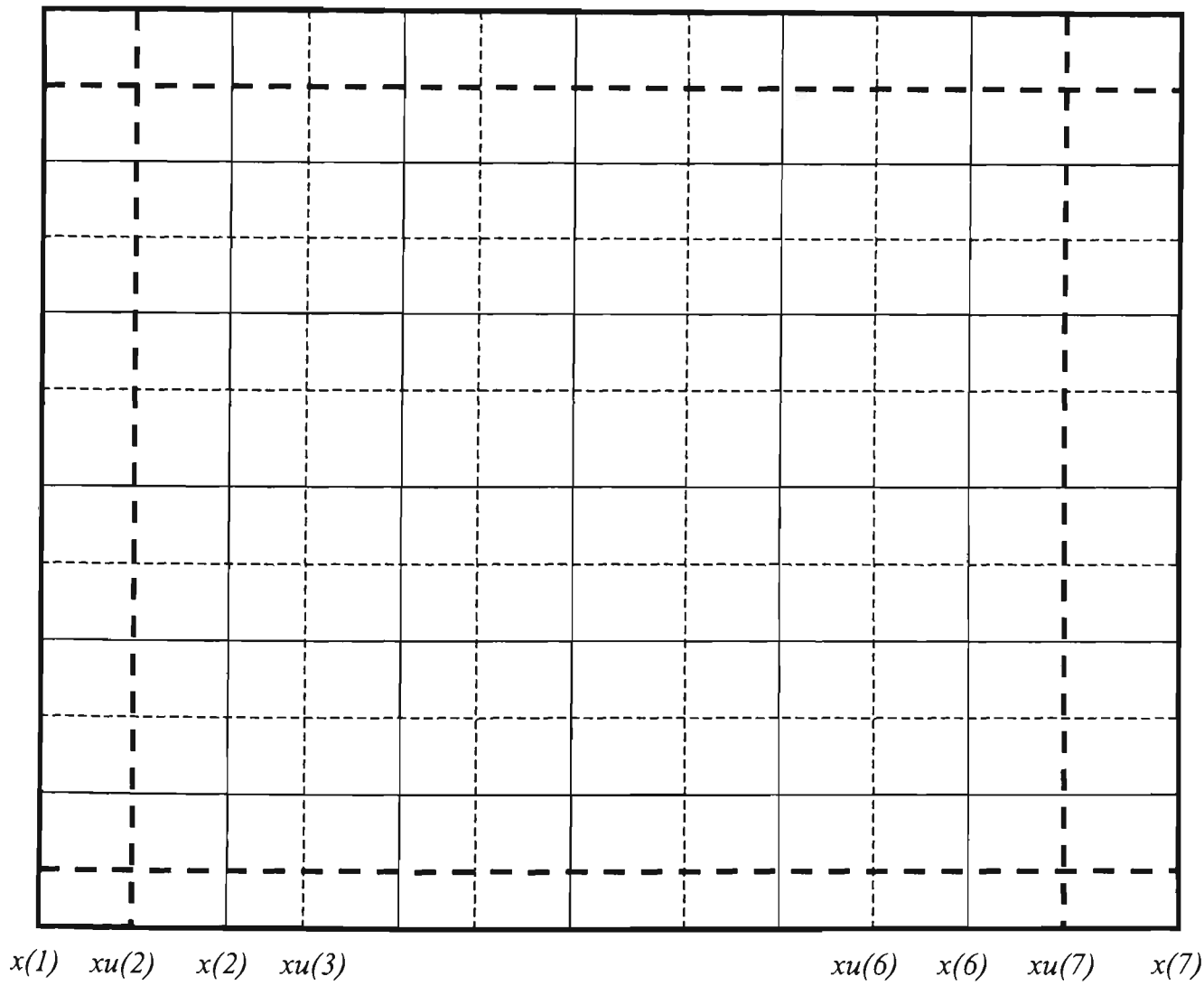

Figure 2.3: Main and Staggered grid locations for a 7x7 grid

2.5.3 Solution of the discretised equations

The discretised partial differential equations represent a non-linear system of algebraic equations. Because of the non-linear nature of the equations, a direct method of solving the equations entails large computer storage, and it is not preferred. There are several iterative methods to solve the system of equations such as the Gauss-Seidel method, the *Alternating Direction Implicit* (ADI) method introduced by Peaceman and Rachford (1955) and the *Strongly Implicit Procedure* (SIP) described by Stone (1968). For the present study, the line by line Gauss-Seidel method is used that employs a combination of the *Tri-Diagonal-Matrix Algorithm* (TDMA) for one-dimensional situations and the point by point Gauss-Seidel iterative method.

2.5.3.1 The *Tri-Diagonal-Matrix Algorithm* (TDMA)

The following is a description of the TDMA for the one dimensional case:
The discretised form of the equation that governs the variable φ in one dimension is written as,

$$d_i\varphi_i = a_i\varphi_{i+1} + b_i\varphi_{i-1} + c_i \tag{2.56}$$

in which *a, b, c* and *d* represent coefficients of the discretised equation for variable φ. Subscript *i* represents a counter for space, *i=imin, imax.* The TDMA algorithm consists of a recurrence formula for the variable in question so that one can obtain the new value for φ with the help of the boundary conditions.

For the forward substitution process, one seeks a relation, of the form

$$\varphi_i = P_i\varphi_{i+1} + Q_i \tag{2.57}$$

With *i=i-1* in the above relationship one can arrive at an equation for φ_{i-1},

$$\varphi_{i-1} = P_{i-1}\varphi_i + Q_{i-1} \tag{2.58}$$

Substitution of Equation (2.58) into Equation (2.56) leads to,

$$d_i\varphi_i = a_i\varphi_{i+1} + b_i(P_{i-1}\varphi_i + Q_{i-1}) + c_i \tag{2.59}$$

If Equation (2.59) is rearranged to take the form of Equation (2.57) and the coefficients are compared, one arrives at a recurrence relationship of the form,

$$P_i = \frac{a_i}{d_i - b_i P_{i-1}} \tag{2.60}$$

$$Q_i = \frac{c_i + b_i Q_{i-1}}{d_i - b_i P_{i-1}} \tag{2.61}$$

For $i=imin$, the recurrence relations (2.60) and (2.61) give definite values for P_{min} and Q_{min}. Similarly for $i=imax$, the recurrence relations give definite values for P_{max} and Q_{max}. An explanation for a specific boundary condition with temperature as the variable is given in Patankar (1980).

Summary of the algorithm

1. Calculate P_{min} and Q_{min} using the left boundary conditions (i.e. for $i=i_{min}$)
2. Use the recurrence relations (2.60) and (2.61) to obtain P_j and Q_j for $i=imin+1$, $imax$.
3. Equate the right boundary conditions (i.e. for $i=i_{max}$) with P_{max} and Q_{max}.
4. Use Equation (2.57) for $i=imax-1$, $imin$ to obtain φ_{imax-1}, φ_{imin}.

For the two dimensional situation, one needs to use the Gauss-Seidel point by point method along with the TDMA. The general discretized equation in two dimensions can be written as:

$$a_P\varphi_P = a_E\varphi_E + a_W\varphi_W + a_N\varphi_N + a_S\varphi_S + b \tag{2.62}$$

where a_P, a_E, a_W, a_N and a_S represent coefficients associated with the variable φ, and b represents the discretised source term. In order to be able to use the TDMA, one has to choose a particular direction for one sweep and assume the other direction to be a constant. For the present simulations, the *S-N* direction is chosen for calculations, and the *W-E* direction is assumed to be constant for every sweep. Thus, a new source term

b_0 is introduced which contains the terms in the *W-E* direction. Equation (2.62) is thus modified to become,

$$a_P\varphi_P = a_N\varphi_N + a_S\varphi_S + b_0 \tag{2.63}$$

where $b_0 = a_E\varphi_E + a_W\varphi_W + b$.

2.5.3.2 The line by line Gauss-Seidel method

The line by line scheme can be visualized with reference to Figure 2.4. The discretization equations for the grid points along a chosen line are considered first. These contain the values of φ at the grid points (shown by squares) along two adjacent lines. If these φ's are substituted from their latest values, the equations for the grid points (shown by circles) along the chosen line would look like one-dimensional equations, and they could be solved by the TDMA. This procedure is carried out for all the lines in the *S-N* direction.

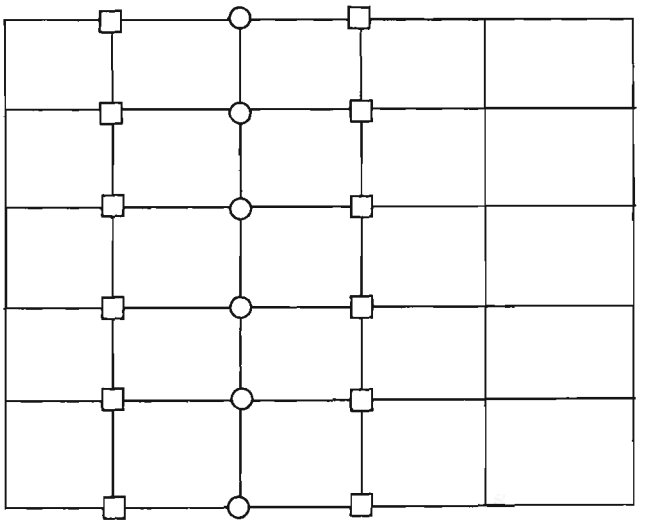

Figure 2.4: Representation of the line by line Gauss-Seidel method.

2.5.3.3 The SIMPLE algorithm

The pressure does not appear explicitly in the continuity equation, Equation (2.11). This means that the continuity equation acts as a constraint on the velocity field, and the pressure has to be determined such that the velocity field in the momentum equation satisfies the continuity equation. The SIMPLE (which stands for *Semi-Implicit Method for Pressure-Linked Equations*) class of algorithms uses a

pressure-velocity coupling to overcome this problem. A pressure correction equation is developed which incorporates the continuity equation in the solution procedure of the Navier-Stokes equation. The main steps in the derivation of the pressure correction equation are given here (details can be found in Patankar, 1980)

Let p^g be the guessed pressure, p the corrected pressure and p' the pressure correction in an iterative solution procedure. Then, one can write:

$$p = p^g + p' \tag{2.64}$$

A similar equation can be written for the corrected velocities, u and v:

$$u = u^g + u', \quad v = v^g + v' \tag{2.65}$$

where u^g and v^g are the guessed velocities, and u' and v' are the velocity corrections.

The velocity correction formulae can be written as:

$$u' = d_w(p'_W - p'_P), \quad v' = d_s(p'_S - p'_P) \tag{2.66}$$

where,

$$d_w = \frac{A_{ew}}{a_P} \text{ and } d_s = \frac{A_{ns}}{a_P}.$$

A_{ew} and A_{ns} represent areas associated with the East-West and North-South directions, respectively. In Patankar (1980), a slightly different formulation is given for the velocity correction formulae, but both formulations have the same meaning. Equation (2.66) gives a relationship between the velocity correction and pressure correction. One can now write Equation (2.65) as follows:

$$u = u^g + d_w(p'_W - p'_P), \; v = v^g + d_s(p'_S - p'_P) \tag{2.67}$$

The continuity equation can be written as:

$$\frac{\partial \rho}{\partial t} + \frac{\partial(\rho u)}{\partial x} + \frac{\partial(\rho v)}{\partial y} = 0 \tag{2.68}$$

This equation is integrated over the shaded control volume in Figure 2.5.

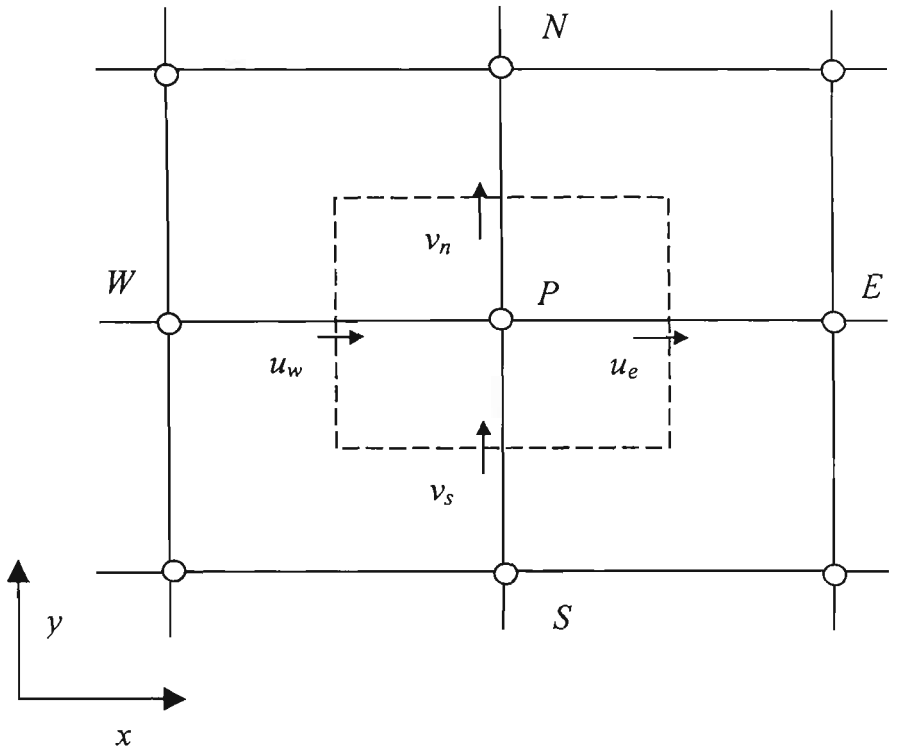

Figure 2.5: Control volume for the continuity equation.

For the integration of the term $\frac{\partial \rho}{\partial t}$, the density, ρ_P, is assumed to prevail over the control volume. Since a fully implicit procedure is used for time, the new values of velocity and density at time $t + \Delta t$ are assumed to prevail over the time step; the old density, ρ_P^o at time t, will appear only through the term $\frac{\partial \rho}{\partial t}$. Thus the integrated form of Equation (2.68) becomes

$$\frac{(\rho_P - \rho_P^o)\Delta x \Delta y}{\Delta t} + [(\rho u)_e - (\rho u)_w]\Delta y + [(\rho v)_n - (\rho v)_s]\Delta x = 0 \qquad (2.69)$$

Equation (2.69) is now converted to the pressure correction equation, using Equation (2.67). The final discretized form of the pressure correction equation can be written as:

$$a_P p_P' = a_E p_E' + a_W p_W' + a_N p_N' + a_S p_S' + b \qquad (2.70)$$

where

$a_E = \rho_e d_e \Delta y$,

$a_W = \rho_w d_w \Delta y$,

$a_N = \rho_n d_n \Delta x$,

$a_S = \rho_s d_s \Delta x$,

$a_P = a_E + a_W + a_N + a_S$,

$$b = \frac{(\rho_P^o - \rho_P)\Delta x \Delta y}{\Delta t} + [(\rho u^g)_w - (\rho u^g)_e]\Delta y + [(\rho v^g)_s - (\rho v^g)_n]\Delta x . \qquad (2.70a)$$

There are several variations on the basic SIMPLE algorithm such as SIMPLER, SIMPLEC, SIMPLEST and PISO that enhance the rate of convergence of the solution for particular flow problems. The SIMPLE algorithm has been found to be adequate for the present study. A detailed explanation of this algorithm can be found in Patankar and Spalding (1972). A flow chart explaining the solution procedure for an unsteady incompressible flow problem using the SIMPLE algorithm is presented in Figure 2.6.

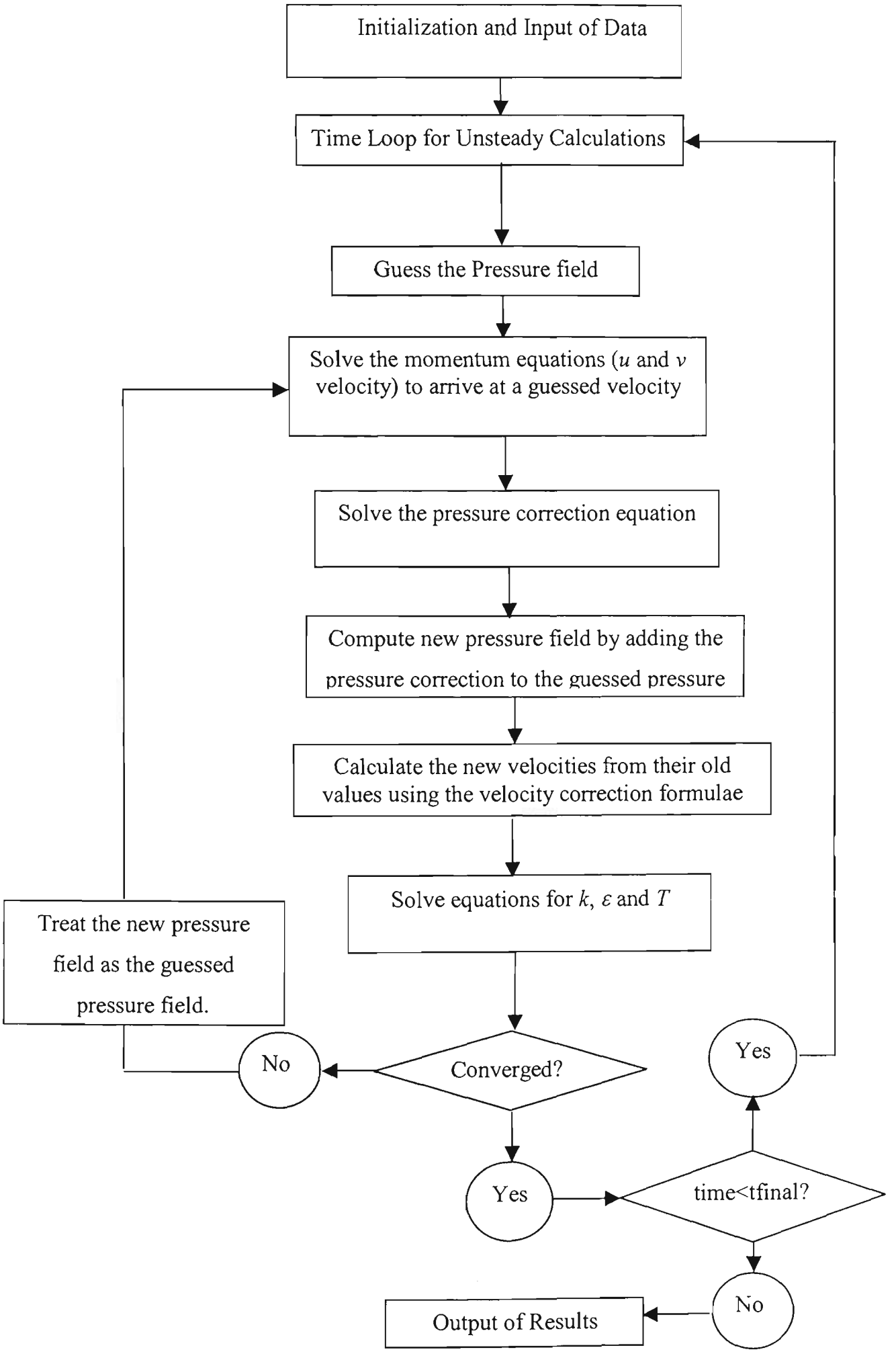

Figure 2.6: Flow chart of the SIMPLE algorithm.

2.5.3.4 Convergence

Since an iterative procedure is used to solve the discretised set of equations, a relaxation process is required to prevent the solution from diverging, or to speed up the process of convergence. In the present thesis, this is achieved by using two methods:

1. Application of a relaxation factor to the variables (such as u, v, T, k and ε)

The solution at the new iteration level is found as:

$$\varphi^n = \alpha\varphi^{gn} + (1-\alpha)\varphi^{n-1} \tag{2.71}$$

where α is the relaxation factor: $\alpha < 1$ leads to under-relaxation, $\alpha = 1$ gives no relaxation and $\alpha > 1$ leads to over-relaxation. φ^{gn} is the solution without any relaxation.

2. Relaxation with a false time step

The use of an unsteady solution procedure is akin to using under-relaxation. The term Δt_F in the unsteady part of the transport equations, $\left(\varphi^n_{i,j} - \varphi^{n-1}_{i,j}\right)/\Delta t_F$, serves as the under-relaxation.

In order to check whether the solution obtained is a converged solution, adequate convergence criteria need to be applied (given as the 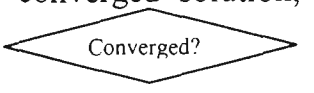

symbol in Figure 2.6). For the present study, this is achieved by checking whether the residual source terms in the discretised equations are below a small stop criterion. As an example, for the mass sources, the following convergence criterion is applied:

$$\left| \frac{\sum_{i=2}^{NI-1}\sum_{j=2}^{NJ-1}\left[(\rho u)_{i+1/2,j}A_e - (\rho u)_{i-1/2,j}A_w + (\rho v)_{i,j+1/2}A_n - (\rho v)_{i,j-1/2}A_s\right]}{(NI-2)(NJ-2)} \right| \le 10^{-8} \tag{2.72}$$

where NI and NJ represent the number of grids in the x and y directions respectively. Similar convergence criteria, but including the source terms, are applied to the momentum and thermal energy equations. In addition to the stop criterion, convergence was also verified by checking the changes in the variables at specific monitoring locations between successive iterations

2.5.4 Summary

The numerical methods chosen to solve the set of partial differential equations governing fluid flow are discussed in this section. Major aspects involved in the development of the CFD code, including the discretisation of the partial differential equations, grid distribution and solution of the discretised set of equations, are explained for a two-dimensional system. In the following chapters, the governing equations and the numerical methods developed in this chapter are used with minor modifications to suit the appropriate physical conditions, geometry and boundary conditions. These modifications are explicitly stated as they are implemented in the solution procedure.

Preliminary validation of the CFD code developed for two-dimensional natural convection flows is presented in the next chapter.

Chapter 3

Preliminary validation of the CFD code

3.1 Introduction

To ascertain the robustness and to check the accuracy of a CFD code it is desirable to validate the code against established benchmark numerical and/or experimental results. When a code is developed in-house, such as in the present research, this validation exercise becomes essential. The heating from the side or double glazing problem of natural convection flow has established benchmarks, both numerical and experimental. Also, the case study of chapter seven involves natural convection flow in a rectangular cavity. Therefore, it was decided to employ this benchmark as a preliminary validation tool for the numerical code written for two-dimensional systems. The code thus developed can serve as a robust platform to implement further modifications.

Firstly, the problem of laminar natural convection flow in a side-heated cavity is revisited. Air is used as the fluid for all calculations. Comparisons are made with the benchmark numerical solutions of De Vahl Davis (1983), the revisited benchmark numerical solutions of Le Quéré (1990) and the solutions obtained by Henkes (1990). De Vahl Davis used a finite difference method of discretisation with a stream function-vorticity based formulation in his benchmark study. Solutions were obtained with Rayleigh numbers up to 10^6. Due to the lack of computational resources, benchmark solutions for higher Rayleigh numbers for air, could not be established by De Vahl Davis. Le Quéré used a psuedo-spectral method of discretisation based on an expansion in Chebyshev polynomials in his benchmark study. This method of discretisation is known to give more accurate results than the finite difference or finite volume methods, and thus, the results can be used as a more accurate benchmark. Le Quéré obtained solutions up to a Rayleigh number of 10^8 and thus extended the benchmark solutions of De Vahl Davis.

Henkes (1990) used a finite volume method in his investigations as in the present study. Calculations were carried out for three different discretisation schemes for the convection flux, namely, second-order central difference scheme, hybrid

scheme and first-order upwind scheme. The central difference scheme was found to give the most accurate solutions. However, the central scheme was also found to be the stiffest scheme as far as convergence was concerned. The finest grid used was a 120x120 grid with a non-uniform grid distribution. Janssen (1994) extended these calculations to a 360x360 grid with several discretisation schemes which included a second-order central difference scheme, fourth-order central difference scheme, first-order upwind scheme, second-order upwind scheme, QUICK scheme and the Leonard Difference Scheme (LDS). Janssen (1994) found that for the highest Rayleigh number calculated in the steady flow regime, $1x10^8$, the fourth order central difference scheme on a 240x240 grid gave results comparable with the pseudo-spectral results of Le Quéré (1991). The spectral solutions were however obtained on an 80x80 grid. This result shows the higher accuracy of spectral methods over finite difference or finite volume methods. However, finite volume and finite difference methods are easier to implement, and they can be used for complex geometries with relative ease. At a Rayleigh number of around $1.7x10^8$, the flow no longer converges to a steady flow but oscillates with a definite frequency. This regime has been described by various authors such as, Paolucci and Chenoweth (1989), Henkes (1990), Janssen (1994) and Le Quéré and Behnia (1998), as the transition regime. Thus, all calculations for the steady, laminar, natural convection problem are carried out up to a Rayleigh number of 10^8 in the present investigation. The finest grid used in the present study is 120x120, although sufficiently grid independent solutions were obtained even on an 80x80 grid.

The present investigation is further extended to the turbulent regime for the same problem for determining the accuracy of implementation of the k-ε model in the code. In a seminar series organised at the J. M. Burgers Centre for Fluid Mechanics in 1992 at Delft, Netherlands (Henkes and Hoogendoorn, 1992), benchmark numerical solutions for the turbulent natural convection problem in a side heated square cavity were sought. The Rayleigh number for the benchmark problem was fixed at $5x10^{10}$. The experimentally determined turbulent natural convection results of Cheesewright and his co workers (described in Cheesewright *et al.*, 1986a; Cheesewright and Ziai, 1986b and King, 1989) at $Ra=4.41x10^{10}$ (which is close to $Ra=5x10^{10}$) in a cavity with an aspect ratio of five, $A=5$, were used for comparison with the benchmark results as this was the most relevant experiment at that point of

time. According to Henkes and Hoogendoorn (1992), calculations for different aspect ratios at the same Rayleigh number $5x10^{10}$ presented in the seminar showed that differences in the results for A=1 and A=5 cavities are very small, provided that the results are scaled using the enclosure height H as the length scale. For the present study, the same numerical problem is used, since it is a well established benchmark problem for turbulent natural convection. The standard k-ε model with modifications for natural convection flows as suggested by Henkes (1990) and Lankhorst (1991) has been used for the computations.

3.2 Problem definition and governing equations

Figure 3.1 shows the side heated square cavity used for the simulations. In the

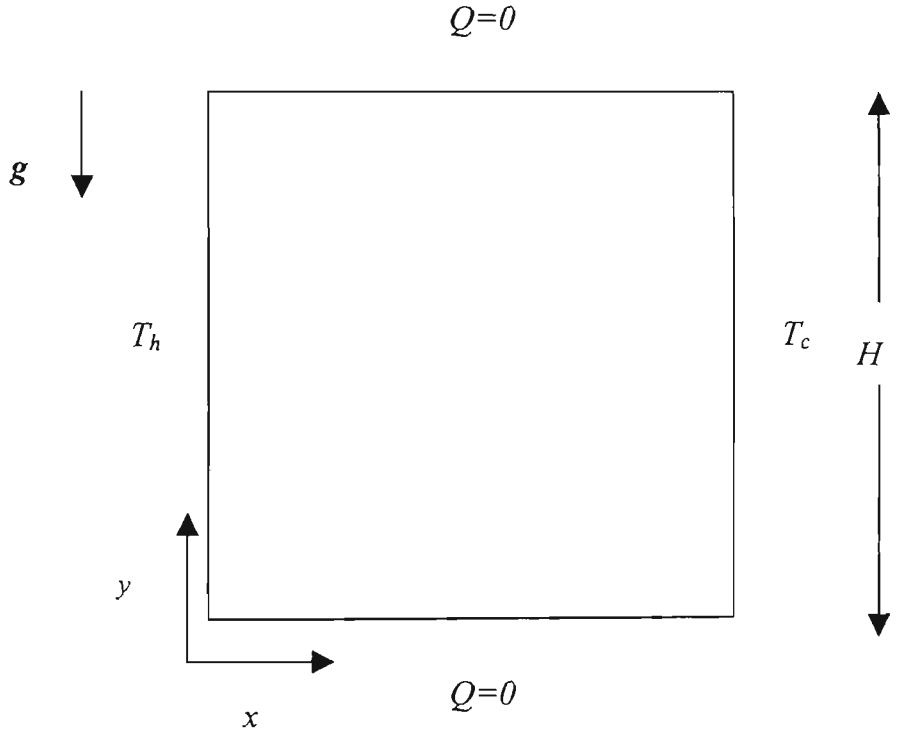

Figure 3.1: Square cavity that has vertical walls maintained at different temperatures and the top and bottom walls are adiabatic.

figure, Q is the heat flux, and it is zero for the adiabatic horizontal walls. T_h represents the temperature of the hot wall. T_c represents the temperature of the cold wall, and H is the length and height of the square cavity. Vector $\boldsymbol{g}$ represents acceleration due to gravity. Since the heat flux Q involves the first derivative of temperature with respect to space, the adiabatic condition can be mathematically represented as $\frac{\partial T}{\partial y} = 0$ at y=0 and H.

3.2.1 Non-dimensional equations

For the present problem, the Rayleigh number is defined as $Ra = \frac{g\beta\Delta T H^3 \,\mathrm{Pr}}{\nu^2}$, where $\Delta T = T_h - T_c$ is the temperature difference between the hot and cold walls and $\mathrm{Pr} = \frac{C_p \mu}{k_f}$ is the fluid Prandtl number (Pr=0.71 for air). In the case of natural convection flows, for low Prandtl number fluids such as gases as well as low viscosity liquids, the convective acceleration term is balanced by the buoyancy term in the momentum equation. The governing equations for buoyancy driven flow in a two-dimensional system presented in Section 2.4.1.1 of chapter two are non-dimensionalised in the following manner.

Let the subscript *ref* represent a reference value for all variables and superscript *nd* represent the non-dimensional variable. As a result, one can write:

$$u^{nd} = \frac{u}{u_{ref}},\quad v^{nd} = \frac{v}{u_{ref}},\quad T^{nd} = \frac{T - T_{ref}}{T_h - T_c},\quad x^{nd} = \frac{x}{H},\quad y^{nd} = \frac{y}{H},\quad p^{nd} = \frac{p}{p_{ref}},$$

$$\varepsilon^{nd} = \frac{\varepsilon}{\varepsilon_{ref}},\ k^{nd} = \frac{k}{k_{ref}},\ \rho^{nd} = \frac{\rho}{\rho_{ref}},\ \mu^{nd} = \frac{\mu}{\mu_{ref}},\ \mu_t^{nd} = \frac{\mu_t}{\mu_{ref}},\ t^{nd} = \frac{t}{t_{ref}}\quad .$$

Using the above non-dimensional variables, one can equate the convective acceleration and buoyancy terms in Equation (2.31) and arrive at: $u_{ref} = \sqrt{g\beta\Delta T H}$. By equating the convective acceleration term with the pressure term, one then obtains: $p_{ref} = \rho u_{ref}^2$. The reference temperature is taken as $T_0=(T_c+T_h)/2$. The reference density and viscosity are taken as the fluid density and viscosity, respectively. The reference time t_{ref}, is taken as the ratio of the reference length scale and the reference velocity scale, i.e. $t_{ref} = \frac{H}{\sqrt{g\beta\Delta T H}}$.

The reference values for turbulence kinetic energy and the rate of energy dissipation are derived with the aid of perturbation theory as described in Wilcox (1993). k_{ref} and ε_{ref} are given as:

$$k_{ref} = u_{ref}^2,\ \varepsilon_{ref} = \frac{u_{ref}^3}{H}.$$

Using the non-dimensional parameters and dropping the superscript *nd* from all the variables, the equations given in Section 2.4.1.1 can be rewritten as:

1. Equation of continuity:

$$\frac{\partial(\rho u)}{\partial x}+\frac{\partial(\rho v)}{\partial y}=0 \tag{3.1}$$

2. Momentum equation in the x direction:

$$\rho\frac{\partial u}{\partial t}+\rho u\frac{\partial u}{\partial x}+\rho v\frac{\partial u}{\partial y}=-\frac{\partial p}{\partial x}+\sqrt{\frac{\mathrm{Pr}}{Ra}}\frac{\partial}{\partial x}\left[(\mu+\mu_t)\left(2\frac{\partial u}{\partial x}\right)\right]+\sqrt{\frac{\mathrm{Pr}}{Ra}}\frac{\partial}{\partial y}\left[(\mu+\mu_t)\left(\frac{\partial u}{\partial y}+\frac{\partial v}{\partial x}\right)\right] \tag{3.2}$$

3. Momentum equation in the y direction:

$$\rho\frac{\partial v}{\partial t}+\rho u\frac{\partial v}{\partial x}+\rho v\frac{\partial v}{\partial y}=-\frac{\partial p}{\partial y}+\sqrt{\frac{\mathrm{Pr}}{Ra}}\frac{\partial}{\partial y}\left[(\mu+\mu_t)\left(2\frac{\partial v}{\partial y}\right)\right]+\sqrt{\frac{\mathrm{Pr}}{Ra}}\frac{\partial}{\partial x}\left[(\mu+\mu_t)\left(\frac{\partial u}{\partial y}+\frac{\partial v}{\partial x}\right)\right]+(T-T_0) \tag{3.3}$$

2. Thermal energy equation:

$$\rho\frac{\partial T}{\partial t}+\rho u\frac{\partial T}{\partial x}+\rho v\frac{\partial T}{\partial y}=\frac{1}{\sqrt{\mathrm{Pr}\,Ra}}\frac{\partial}{\partial x}\left[\left(\mu+\frac{\mu_t\,\mathrm{Pr}}{\sigma_T}\right)\frac{\partial T}{\partial x}\right]+\frac{1}{\sqrt{\mathrm{Pr}\,Ra}}\frac{\partial}{\partial y}\left[\left(\mu+\frac{\mu_t\,\mathrm{Pr}}{\sigma_T}\right)\frac{\partial T}{\partial y}\right] \tag{3.4}$$

3. Turbulence kinetic energy equation:

$$\rho\frac{\partial k}{\partial t}+\rho u\frac{\partial k}{\partial x}+\rho v\frac{\partial k}{\partial y}=\sqrt{\frac{\mathrm{Pr}}{Ra}}\frac{\partial}{\partial x}\left[\left(\mu+\frac{\mu_t}{\sigma_k}\right)\frac{\partial k}{\partial x}\right]+\sqrt{\frac{\mathrm{Pr}}{Ra}}\frac{\partial}{\partial y}\left[\left(\mu+\frac{\mu_t}{\sigma_k}\right)\frac{\partial k}{\partial y}\right]+P_k+G_k-\rho\varepsilon \tag{3.5}$$

4. Equation for the rate of energy dissipation:

$$\rho\frac{\partial\varepsilon}{\partial t}+\rho u\frac{\partial\varepsilon}{\partial x}+\rho v\frac{\partial\varepsilon}{\partial y}=\sqrt{\frac{\mathrm{Pr}}{Ra}}\frac{\partial}{\partial x}\left[\left(\mu+\frac{\mu_t}{\sigma_\varepsilon}\right)\frac{\partial\varepsilon}{\partial x}\right]$$
$$+\sqrt{\frac{\mathrm{Pr}}{Ra}}\frac{\partial}{\partial y}\left[\left(\mu+\frac{\mu_t}{\sigma_\varepsilon}\right)\frac{\partial\varepsilon}{\partial y}\right] \qquad (3.6)$$
$$+\left(c_{\varepsilon 1}f_1\left(P_k+c_{\varepsilon 3}G_k\right)-\rho c_{\varepsilon 2}f_2\varepsilon\right)\frac{\varepsilon}{k}$$

with

$$P_k=\mu_t\sqrt{\frac{Pr}{Ra}}\left(2\left(\frac{\partial u}{\partial x}\right)^2+2\left(\frac{\partial v}{\partial y}\right)^2+\left(\frac{\partial u}{\partial y}+\frac{\partial v}{\partial x}\right)^2\right)$$

$$G_k=-\frac{1}{\sqrt{Pr\,Ra}}\frac{\mu_t}{\sigma_T}\frac{\partial T}{\partial y}$$

$$\mu_t=\sqrt{\frac{Ra}{Pr}}\rho c_\mu f_\mu\frac{k^2}{\varepsilon}$$

For laminar solutions, Equations (3.5) and (3.6) are not used in the calculations, and the eddy viscosity, μ_t, is taken as zero. Variables, u, v, p and T are instantaneous quantities for laminar calculations. One can use either a steady or transient approach for laminar calculations. In the former case, the time derivatives in the equations are set to zero.

For turbulent solutions, Equations (3.5) and (3.6) are solved simultaneously with Equations (3.1) to (3.4). Variables, u, v, p and T are time-averaged quantities of calculations that involve turbulence. Here again, one can either use a steady approach or approach the steady state solution by integrating through time. The time derivatives in the time averaged Navier-Stokes equation represent the large time behaviour according to Henkes (1990). The nature of the transient solution depends on the type of turbulence model used. Thus, the transient solution may not approach a true transient for turbulent flow calculations.

In the present simulations, a steady approach is adopted for laminar and turbulent calculations.

3.2.2 Boundary conditions

For calculations that involve laminar flow, natural boundary conditions are applied for u, v and T. The boundary conditions can be summarised as follows:

$$\begin{aligned} &u = v = 0 \quad \text{at} \quad x = 0 \text{ and } H \\ &u = v = 0 \quad \text{at} \quad y = 0 \text{ and } H \\ &T = T_h \quad \text{at} \quad x = 0 \\ &T = T_c \quad \text{at} \quad x = H \\ &\frac{\partial T}{\partial y} = 0 \quad \text{at} \quad y = 0 \text{ and } H \end{aligned} \tag{3.7}$$

For calculations involving turbulent flow, using the standard k-ε model, wall functions presented in Section 2.4.1.1.1 of chapter two are not used. As mentioned in Section 2.4.1.2 of chapter two, standard wall functions, (Equations (2.38) and (2.39)), developed from simple forced convection flow experiments cannot be used for natural convection flows. In order to alleviate this problem Henkes (1990) and Lankhorst (1991) suggested the modification of the standard k-ε model near walls. These authors solved for the mean quantities (u, v and T) right up to the wall, which is similar to the treatment adopted in the case of low-Reynolds number k-ε models. However, for the turbulent quantities, k and ε, wall functions such as in Equations (2.43) and (2.44) were used. These wall functions are applied at the first inner grid point. Since the region close to the wall is extremely important in calculating heat transfer rates within the boundary layers, the first grid point has to be located extremely close to the wall. When this is done, it is reasonable to assume that the values of k and ε at the first inner grid point might be obeying the law of the viscous sublayer ($v^+ = x^+$ for $x^+ < 11.63$). Therefore, in addition to the wall functions in Equations (2.43) and (2.44) for k and ε obtained from the inertial law ($x^+ \geq 11.63$), Lankhorst (1991) developed wall functions for these turbulent quantities within the viscous sublayer. By differentiating the linear velocity profile for the inertial sublayer and using it together with the defining equation for μ_t, one obtains alternative wall functions for k and ε as follows (for $x^+ < 11.63$):

$$k = \frac{\left(\kappa x^+ v^*\right)^2}{\sqrt{c_\mu}} \tag{3.8}$$

$$\varepsilon = \frac{\left(k x^{+}\right)^{2}\left(v^{*}\right)^{4}}{v} \tag{3.9}$$

For the present calculations, these two forms of the wall functions are used and compared with the results obtained by Lankhorst (1991) and the experiments of Cheesewright and his co workers. The mean variables (u, v and T) are solved right up to the wall. Note that all boundary conditions are used in their respective non-dimensional forms.

3.3 Numerical methods

The governing equations are solved using the finite-volume method on a staggered grid as described in Section 2.5.1 of chapter two. The convection-diffusion terms are discretised using a second order central difference scheme and a hybrid scheme for comparison. Pressure and velocity are coupled using the SIMPLE algorithm, and the line by line Gauss Seidel method is used for solving the discretised equations. Details of the numerical methods can be found in Section 2.5 of chapter two. The under-relaxation factors for the variables u, v, T and p were assigned different values depending on the Rayleigh numbers calculated. As the Rayleigh number was increased, lower under-relaxation factors had to be assigned to avoid divergence of the solution. The specific values are provided in Section 3.4.

3.3.1 Grid distribution

Non-uniform grid spacing is used for all calculations with fine grids close to the wall and progressively coarse grids towards the centre of the cavity. At low Rayleigh numbers, non-uniform grid spacing is not essential. At higher Rayleigh numbers, one encounters steep velocity and temperature gradients. Fine grid spacing is required close to the wall to resolve these gradients. The use of non-uniform grid spacing allows an economical distribution of grids in the calculation domain. For laminar calculations, a sine function distribution for the x and y directions is used:

$$\frac{xu(i)}{H} = \frac{i}{i\max} - \frac{1}{2\pi}\sin\left(2\pi\frac{i}{i\max}\right) \qquad i = i\min, i\max \tag{3.10}$$

$$\frac{yv(j)}{H} = \frac{j}{j\max} - \frac{1}{2\pi}\sin\left(2\pi\frac{i}{i\max}\right) \qquad j = j\min, j\max \tag{3.11}$$

At the highest Rayleigh number ($1x10^8$) in the laminar regime and for all calculations in the turbulent regime, a hyperbolic tangent function is employed for grid distribution in the x direction. This function enables a finer refinement close to the wall.

$$xu(i) = \frac{1}{2}\left(1 + \frac{\tanh\{\alpha_1[i/i\max - 1/2]\}}{\tanh(\alpha_1/2)}\right) \qquad i = i\min, i\max \tag{3.12}$$

where α_1 represents a grid refinement parameter given by:

$$\alpha_2 = \frac{\alpha_1}{\sinh(\alpha_1)} \tag{3.13}$$

With a low value of α_2, one can obtain a fine grid close to the wall. A range of values of this parameter, $1.0\times10^{-5} \le \alpha_2 \le 1.0\times10^{-1}$, is used to study the effect of grid refinement close to the wall. A representative non-uniform mesh using the sine functions (3.10) and (3.11) for grid distribution in the x and y directions is shown in Figure 3.2. In general, the results obtained with an 80x80 grid were found to be sufficiently grid independent for both laminar and turbulent cases. However, calculations are done up to a grid size of 120x120 for the sake of comparison with the result obtained by Henkes (1990) on the same grid.

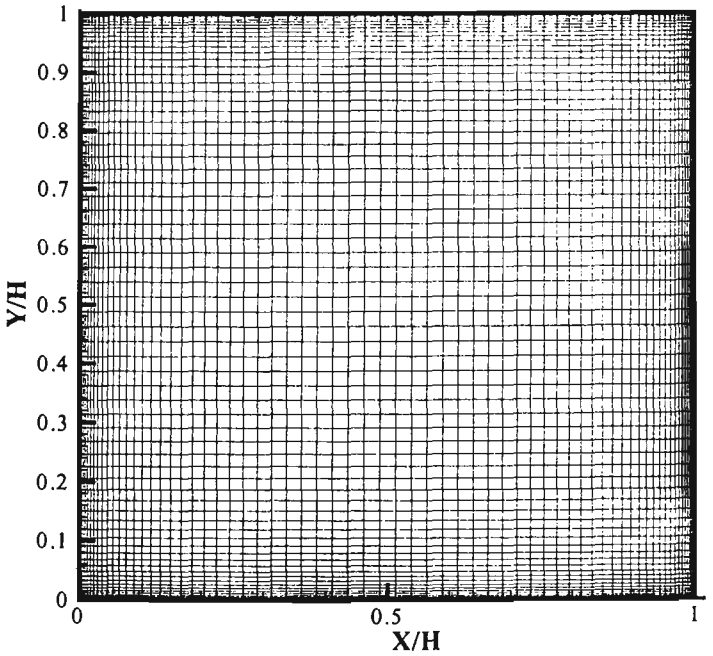

Figure 3.2: Representative non-uniform mesh using a sine function for grid distribution in the x and y directions.

3.4 Results and discussion

In order to verify the accuracy of the solutions some important parameters are monitored for each calculation. These are:

1. Non-dimensionalised heat transfer from the hot wall which is referred as the Nusselt number.

$$Nu = -\frac{H}{\Delta T}\left(\frac{\partial T}{\partial x}\right)_{hotwall} \tag{3.14}$$

2. Stratification at the centre of the cavity.

$$S_c = \frac{H}{\Delta T}\left(\frac{\partial T}{\partial y}\right)_c \tag{3.15}$$

3. Non-dimensionalised maximum of the vertical velocity at the horizontal mid-plane of the cavity.

$$\frac{v_{max}}{\sqrt{g\beta\Delta TH}} \tag{3.16}$$

4. Non-dimensionalised maximum of the horizontal velocity at the vertical mid-plane of the cavity.

$$\frac{u_{max}}{(g\beta\Delta T\nu)^{1/3}} \text{ (laminar flow)}, \quad \frac{u_{max}}{\sqrt{g\beta\Delta TH}} \text{ (turbulent flow)} \tag{3.17}$$

3.4.1 Laminar flow solutions

3.4.1.1 Streamlines and isotherms

In Figure 3.3, simulations are presented for increasing Rayleigh (Ra) numbers for air in the laminar regime, starting from $Ra=10^3$ up to 10^8. Frames (a), (c), (e), (g), (i) and (k) in the figure represent isotherms, whereas frames (b), (d), (f), (h), (j) and (l) represent the corresponding streamlines for $Ra=10^3$, 10^4, 10^5, 10^6, 10^7 and 10^8, respectively. As the Rayleigh number is increased from very low values (almost stagnant fluid for $Ra < 10^3$), natural convection flow in the square cavity begins. At $Ra=10^3$ and 10^4 (Figures 3.3(a) to (d)), one can see a bending of the isotherms from a vertical position indicating the effect of natural convection on the temperature

patterns in the cavity. A single clockwise rotating cell is formed at these Rayleigh numbers as seen from the streamlines (Note that the left wall is hot and the right wall is cold, and therefore, the motion is in the clockwise direction). The under-relaxation factors used for this set of simulations were: u_{urf} = 0.5, v_{urf} = 0.5, T_{urf} = 0.5 and p_{urf} = 0.8.

As the Rayleigh number is increased to Ra=10^5 and 10^6 (Figures 3.3(e) to (h)), the bending of the isotherms is enhanced further. At Ra=10^6, the originally vertical isotherms are almost horizontal in the central portion of the cavity as seen in Figure 3.3(g), indicating strong natural convection currents. The isotherms are closely spaced near the vertical walls indicating steep gradients close to these walls. The streamlines for Ra=10^5, Figure 3.3(f), show the splitting of the single clockwise cell to a two cell pattern with a saddle (or no flow) point at the centre of the cavity. At Ra=10^6, the streamline pattern again changes, now showing three clockwise rotating cells with two saddle points, as seen in Figure 3.3(h). The closeness of the streamlines near the vertical walls again indicates steep velocity gradients near these walls. The under-relaxation factors used for this set of simulations were: u_{urf} = 0.3, v_{urf} = 0.3, T_{urf} = 0.3 and p_{urf} = 0.5.

With a further increase in Rayleigh number to Ra=10^7 and 10^8 (Figures 3.3(i) to (l)), the streamlines and isotherms become very closely spaced near the vertical walls. The centre of the cavity is, however, quite stagnant with an almost no flow region. At these high Rayleigh numbers, the streamlines have split into several clockwise rotating cells as seen from Figures 3.3(j) and (l). The central portion of the cavity still has three clockwise cells and two saddle points. However, the upper left and lower right corners of the cavity have developed strong rotating cells or vortices. Similar flow patterns were observed by Henkes (1990) in his calculations with air as the fluid. At these Rayleigh numbers, significantly low under-relaxation factors had to be used to allow the solutions to reach a final converged steady state result. These were: u_{ref} = 0.1, v_{ref} = 0.1, T_{ref} = 0.05, p_{ref} = 0.1. This was particularly the case with the central difference scheme of discretising the convection-diffusion terms.

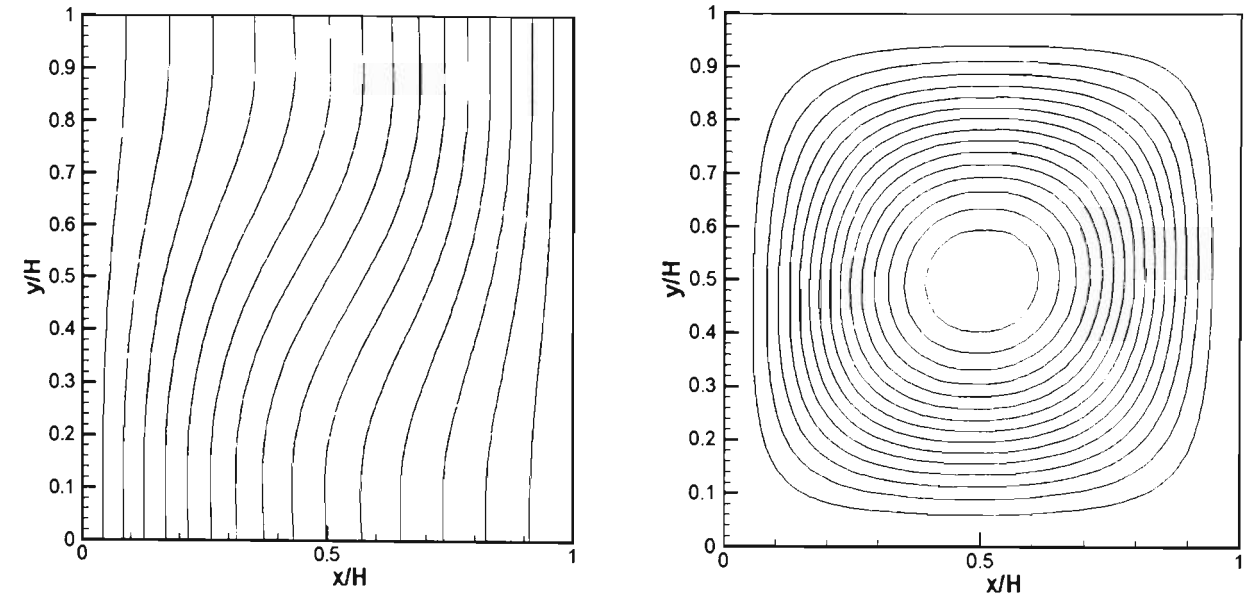

(a) (b)

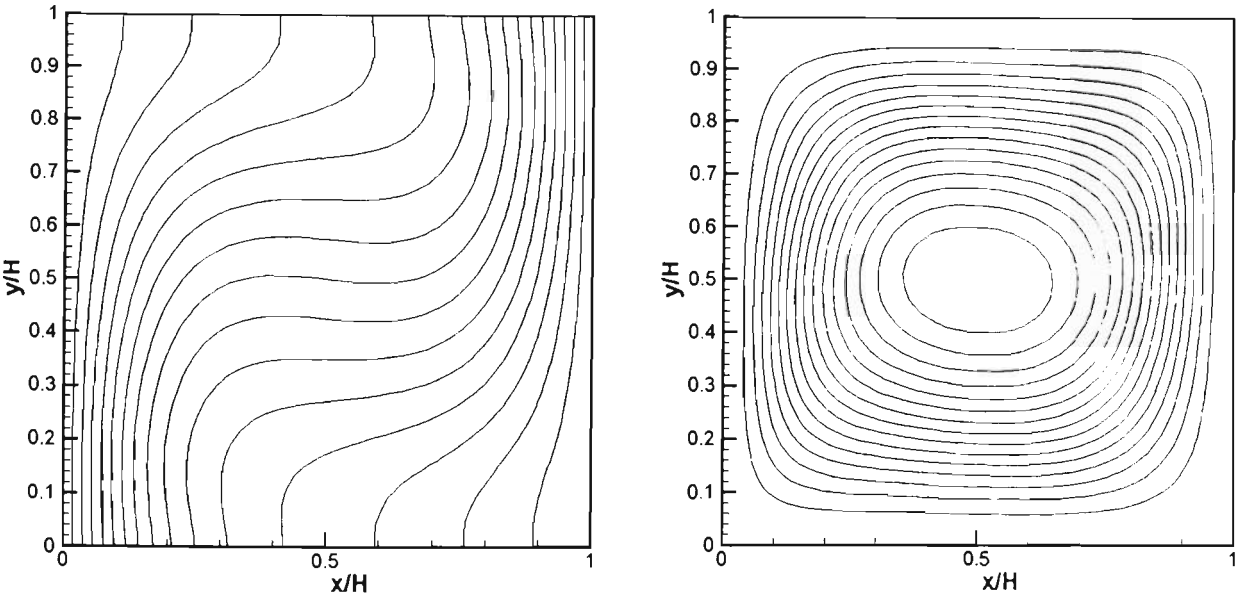

(c) (d)

Figure 3.3 (For caption, see page 57)

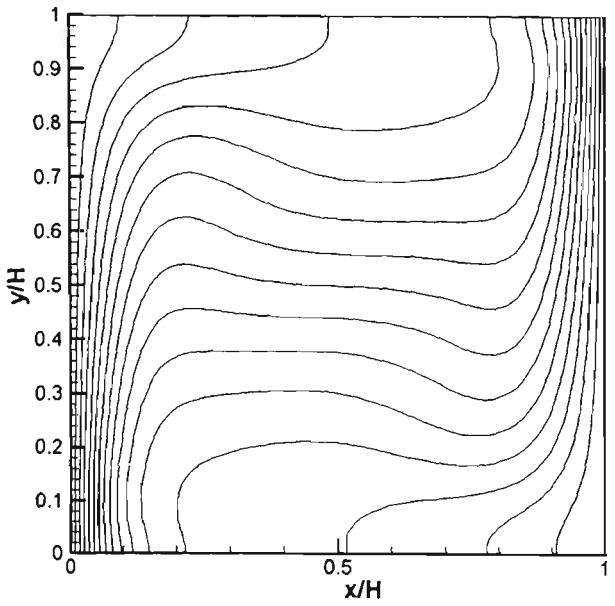

(e)

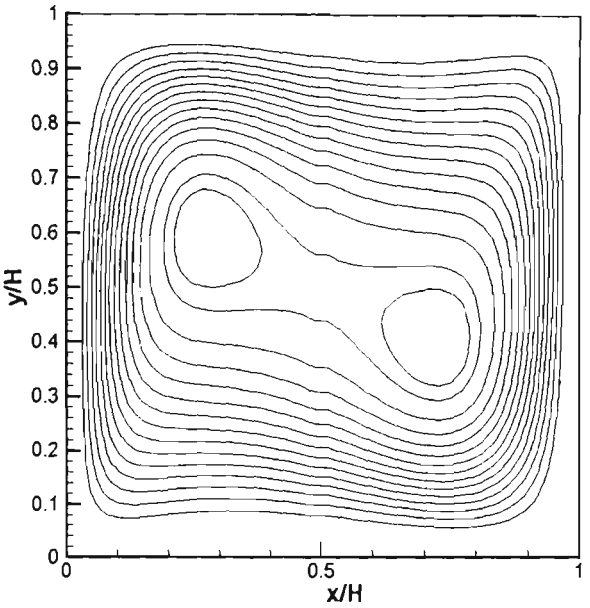

(f)

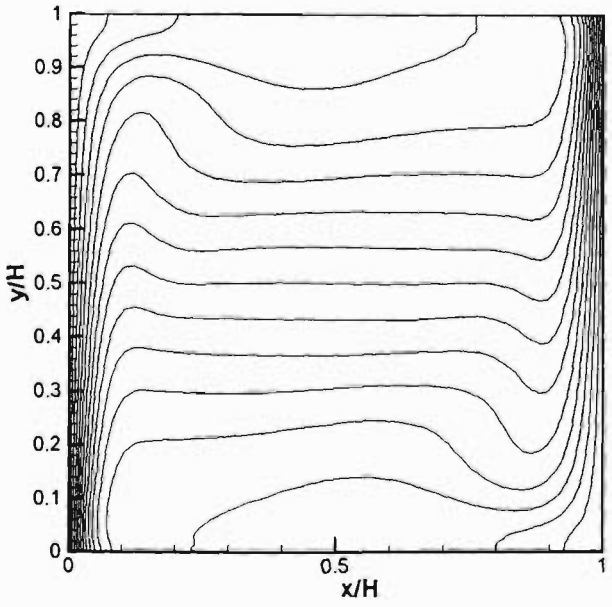

(g)

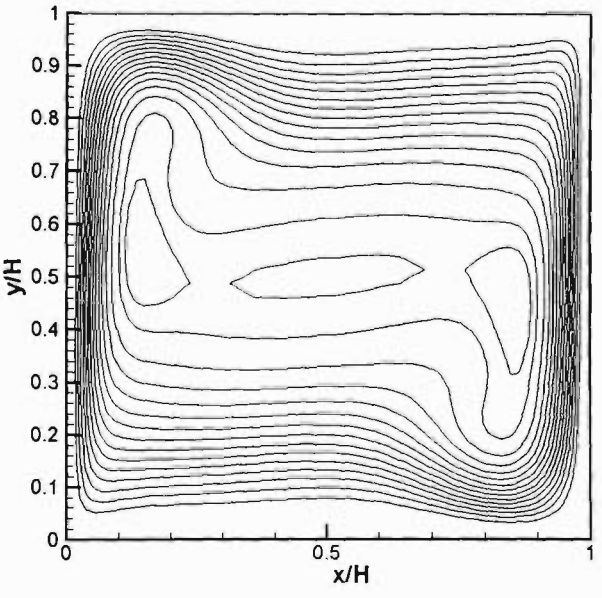

(h)

Figure 3.3 contd. (For caption, see next page)

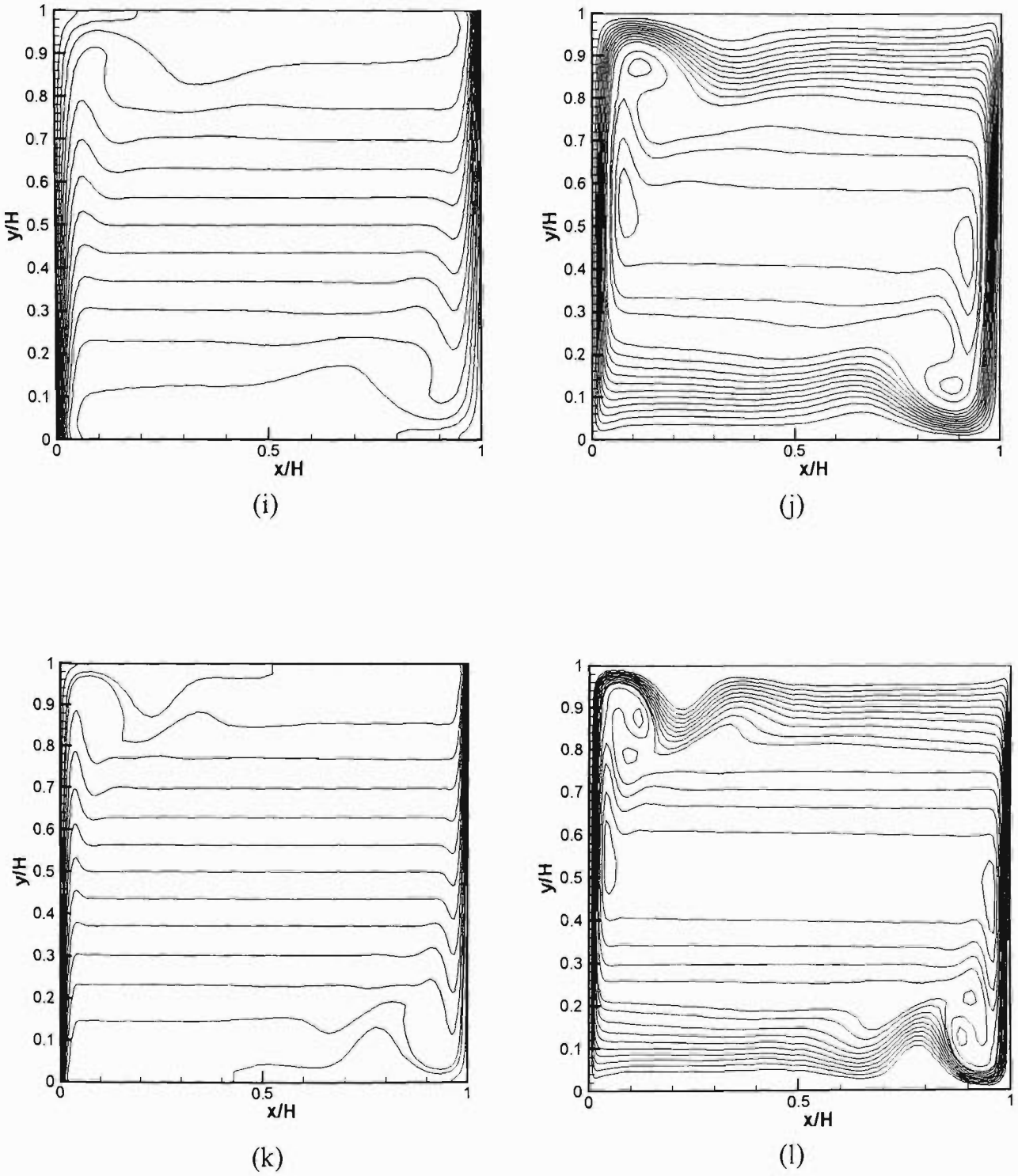

Figure 3.3: Numerical prediction of the flow field for increasing Rayleigh numbers for air in the laminar regime. Frames (a), (c), (e), (g), (i) and (k) represent isotherms whereas frames (b), (d), (f), (h), (j) and (l) represent streamlines for Ra=10^3, 10^4, 10^5, 10^6, 10^7 and 10^8 respectively.

3.4.1.2 Accuracy of the solutions

Table 3.1 indicates the accuracy of the solution for air at $Ra=10^3$, 10^4 and 10^5. Non-uniform grids were used for all these Rayleigh numbers, although it is not essential to do so at lower Rayleigh numbers. Parameters given in Equations (3.14) to (3.17) were monitored for all Rayleigh numbers. For the simulations, 30x30, 40x40, 60x60 and 80x80 grids were employed for each Rayleigh number. The convection-diffusion terms were discretised by using the second order central scheme. Results have been compared with the benchmark numerical solutions of De Vahl Davis (1983), (referred to as DVD in the tables). As seen from the Table, the present solutions compare well with the results of De Vahl Davis. If one compares the present results at the largest grid size to the benchmark, the maximum deviation in Nu is 0.17% (for $Ra = 10^4$), in u_{max} is 0.20% (for $Ra = 10^4$) and in v_{max} is 0.52% (for $Ra = 10^4$). De Vahl Davis does not provide values for the stratification, and therefore, a comparison could not be made. One can also see from Table 3.1 that as the grid size is increased, the solutions tend to a grid independent result.

Table 3.2 presents the accuracy of the solution for air at $Ra=10^6$. The central difference scheme is again used for all simulations. Calculations are performed up to 120x120 grids. The results obtained are compared with the benchmarks of De Vahl Davis (1983), Le Quéré (1990), (referred to as LQ in the tables) and the results of Henkes (1990) at the highest, 120x120, grid calculated by the author. From the tables, it can be seen that the present results are in general close to the results obtained in all previous studies. In particular, the present solution with the 120x120 grid is closer to the benchmark of Le Quéré who used a more accurate pseudo-spectral method. The present results are also in close agreement with the results obtained by Henkes (1990) who used a finite volume method as in the present thesis. With the finest grid, the present results have the following deviations from the results of Le Quéré and Henkes:

in Nu_{avg}, 0.07% (LQ), 0.11% (Henkes),

in u_{max}, 0.32% (LQ), 0.34% (Henkes),

in v_{max}, 0.11% (LQ), 0.00% (Henkes),

in S_c, not available (LQ), 0.04% (Henkes).

Table 3.1: Accuracy of the Solution for air at $Ra=10^3$, 10^4 and 10^5

Rayleigh Number	Scheme	Grid	Nu_{avg}	$\frac{Nu_{avg}}{Ra^{1/4}}$	$\frac{u_{max}}{(g\beta\Delta T\nu)^{1/3}}$	$\frac{v_{max}}{\sqrt{g\beta\Delta TH}}$	$S_c=\frac{H}{\Delta T}\left(\frac{\partial T}{\partial y}\right)_c$
$1x10^3$	Central	30x30	1.118	0.1988	0.4587	0.1381	0.5289
$1x10^3$	Central	40x40	1.118	0.1988	0.4600	0.1390	0.5298
$1x10^3$	Central	60x60	1.118	0.1988	0.4580	0.1390	0.5266
$1x10^3$	Central	80x80	1.118	0.1988	0.4593	0.1388	0.5228
$1x10^4$	Central	30x30	2.247	0.2247	0.9298	0.2348	0.8477
$1x10^4$	Central	40x40	2.246	0.2246	0.9391	0.2343	0.8418
$1x10^4$	Central	60x60	2.242	0.2242	0.9426	0.2325	0.8377
$1x10^4$	Central	80x80	2.239	0.2239	0.9436	0.2335	0.8344
$1x10^5$	Central	30x30	4.526	0.2545	0.9363	0.2571	1.055
$1x10^5$	Central	40x40	4.524	0.2544	0.9377	0.2592	1.061
$1x10^5$	Central	60x60	4.520	0.2542	0.9387	0.2570	1.065
$1x10^5$	Central	80x80	4.516	0.2540	0.9408	0.2580	1.065
$1x10^3$ (DVD)	-----	-----	1.118	0.1988	0.4585	0.1387	------
$1x10^4$ (DVD)	-----	-----	2.243	0.2243	0.9417	0.2323	------
$1x10^5$ (DVD)	-----	-----	4.519	0.2541	0.9400	0.2574	------

Table 3.2: Accuracy of the Solution for air at $Ra=10^6$

Rayleigh number	Scheme	Grid	Nu_{avg}	$\frac{Nu_{avg}}{Ra^{1/4}}$	$\frac{u_{max}}{(g\beta\Delta T\nu)^{1/3}}$	$\frac{v_{max}}{\sqrt{g\beta\Delta TH}}$	$S_c=\frac{H}{\Delta T}\left(\frac{\partial T}{\partial y}\right)_c$
$1x10^6$	Central	20x20	8.766	0.2772	0.7900	0.2567	0.9639
$1x10^6$	Central	30x30	8.792	0.2780	0.7965	0.2546	0.9397
$1x10^6$	Central	40x40	8.808	0.2785	0.8067	0.2595	0.9281
$1x10^6$	Central	60x60	8.817	0.2788	0.8129	0.2627	0.9193
$1x10^6$	Central	80x80	8.822	0.2790	0.8139	0.2618	0.9164
$1x10^6$	Central	120x120	8.835	0.2793	0.8172	0.2621	0.9140
$1x10^6$ (DVD)	-----	-----	8.800	0.2783	0.8121	0.2603	------
$1x10^6$ (LQ)	-----	-----	8.826	0.2791	0.8146	0.2618	------
$1x10^6$ (Henkes)	Central	120x120	8.822	0.2790	0.8144	0.2621	0.9144

Thus, the maximum deviation in the results is less than 0.5% for all parameters. The stratification value was not provided by either Le Quéré or De Vahl Davis. Therefore, the present results for stratification were compared with those of Henkes, only.

Table 3.3 presents the results obtained for $Ra=10^8$. The central and hybrid differencing schemes were used to discretise the convection-diffusion terms in this case. Since De Vahl Davis (1983) has not provided any results for this case, comparisons have been made only with the results of Le Quéré (1990) and Henkes (1990). From the table, it is clear that the central scheme is superior to the hybrid scheme in terms of accuracy. However the central scheme was found to be extremely stiff at such high Rayleigh numbers, and significantly low under-relaxation factors had to be employed to arrive at a steady converged solution. Following are the deviations calculated with the central and hybrid schemes for the finest grid in comparison with the benchmark of Le Quéré and the finite volume solutions of Henkes.

Central scheme:	Hybrid Scheme:
in Nu_{avg}, 0.30% (LQ), 0.20% (Henkes),	Nu_{avg}, 0.53% (LQ), 0.10% (Henkes)
in u_{max}, 0.95% (LQ), 4.86% (Henkes),	u_{max}, 7.57% (LQ), 1.47% (Henkes)
in v_{max}, 0.30% (LQ), 0.04% (Henkes),	v_{max}, 0.4171 (LQ), 0.04% (Henkes)
in S_c not available (LQ), 0.05% (Henkes),	S_c not available (LQ), 0.05% (Henkes).

The maximum error between the benchmark and present solution occurs for the maximum of the u velocity, and it is as much as 7.57% for the hybrid scheme. For the central scheme, all errors are below 1% compared to the benchmark of Le Quéré (1990). Although the present results for the maximum of the u velocity deviate significantly from the benchmark for the hybrid scheme, these results are more accurate than those of Henkes (1990). To put it in context, the results of Henkes deviate by as much as 5.54% for the central scheme and 8.92% for the hybrid scheme (for the maximum of the u velocity) from the benchmark. Further calculations were not carried out in the laminar regime, since a converged solution could not be obtained beyond a $Ra=10^8$ with the central scheme. Previous studies have also found that a Rayeligh number of approximately $Ra=10^8$ represents the limit of the laminar flow regime for air in a side heated square cavity.

Table 3.3: Accuracy of the solution for air at $Ra=10^8$

Rayleigh number	Scheme	Grid	Nu_{avg}	$\frac{Nu_{avg}}{Ra^{1/4}}$	$\frac{u_{max}}{(g\beta\Delta T\nu)^{1/3}}$	$\frac{v_{max}}{\sqrt{g\beta\Delta TH}}$	$S_c=\frac{H}{\Delta T}\left(\frac{\partial T}{\partial y}\right)_c$
$1x10^8$	Central	20x20	28.60	0.2860	0.7053	0.2221	0.9332
$1x10^8$	Central	40x40	29.99	0.2999	0.7262	0.2694	0.9922
$1x10^8$	Central	60x60	30.13	0.3013	0.7480	0.2614	0.9941
$1x10^8$	Central	80x80	30.15	0.3015	0.7941	0.2651	0.9942
$1x10^8$	Central	120x120	30.14	0.3014	0.8631	0.2645	0.9938
$1x10^8$ (Henkes)	Central	120x120	30.20	0.3020	0.8231	0.2646	0.9943
$1x10^8$	Hybrid	20x20	27.43	0.2743	0.8676	0.2243	0.8303
$1x10^8$	Hybrid	40x40	29.59	0.2959	0.7528	0.2702	0.9521
$1x10^8$	Hybrid	60x60	29.88	0.2988	0.7773	0.2629	0.9712
$1x10^8$	Hybrid	80x80	29.91	0.2991	0.7988	0.2658	0.9757
$1x10^8$	Hybrid	120x120	30.07	0.3007	0.8054	0.2648	0.9803
$1x10^8$ (Henkes)	Hybrid	120x120	30.10	0.3010	0.7937	0.2649	0.9808
$1x10^8$ (LQ)	-----	-----	30.23	0.3023	0.8714	0.2637	------

3.4.1.3 Effect of grid distribution on accuracy

In order to present the effect of grid distribution on the accuracy of the solution, further calculations were carried out at $Ra=10^8$ by using the hyperbolic tangent function in Equation (3.12) as the grid distribution function in the x direction. For the y direction, the sine function (Equation (3.11)) was maintained. The hybrid scheme was used to discretise the convection-diffusion terms. As mentioned earlier, with a low value of α_2 in Equation (3.13), one can obtain a fine grid close to the vertical walls. Therefore, the value of α_2 was varied between $1.0\text{x}10^{-1}$ and $1.0\text{x}10^{-5}$ for the present study. The grid size is maintained at 80x80 for all calculations. Comparisons are made with the benchmark results of Le Quéré (1990) for all parameters except the stratification. For stratification, the results obtained in the present study with the 120x120 grid and the central scheme are used as a benchmark. The results are summarised in Table 3.4. For $\alpha_2=1.0\text{x}10^{-1}$, the results obtained are closest to the benchmark for Nu_{avg}, u_{max} and S_c, but not for v_{max}. As the value of α_2 is decreased, the results show an improvement for v_{max} with a slight deterioration in the predictions for the other parameters up to $\alpha_2=1.0\text{x}10^{-3}$. With a further decrease in the value of α_2, however, the predictions begin to deteriorate significantly as seen from the results for $\alpha_2=1.0\text{x}10^{-4}$ and $1.0\text{x}10^{-5}$. These results clearly show that the accuracy of the solution depends greatly on the grid distribution in addition to the total number of grid points.

3.4.1.4 Variation of wall heat transfer and stratification

Henkes (1990) calculated the variation of wall heat transfer and stratification for air using the boundary layer equations as well as the full Navier-Stokes and thermal energy equations. Henkes (1990) found that for the laminar regime the stratification asymptotes to a value of 0.99 (at $Ra = 10^8$) with the boundary layer and Navier-Stokes solutions. The average wall heat transfer asymptotes to the relation: $Nu_{avg} = cRa^{1/4}$ where $c = 0.30$ and 0.31 with the Navier-Stokes and boundary layer equations, respectively. As seen from Table 3.3, the results for $Ra = 10^8$ indicate the same asymptotic behaviour for the present simulations. This asymptotic behaviour

for stratification and average wall heat transfer with Rayleigh number in the laminar regime for air is also seen in Figures 3.4(a) and (b), respectively.

Table 3.4: Effect of grid distribution on accuracy (an 80x80 grid is used for all calculations).

Scheme	$\alpha_2 = \frac{\alpha_1}{\sinh(\alpha_1)}$	Nu_{avg}	$\frac{Nu_{avg}}{Ra^{1/4}}$	$\frac{u_{max}}{(g\beta\Delta T\nu)^{1/3}}$	$\frac{v_{max}}{\sqrt{g\beta\Delta TH}}$	$S_c = \frac{H}{\Delta T}\left(\frac{\partial T}{\partial y}\right)_c$
Hybrid	$1.0\text{x}10^{-1}$	30.07	0.3007	0.7958	0.2651	0.9786
Hybrid	$1.0\text{x}10^{-2}$	29.96	0.2996	0.7918	0.2650	0.9749
Hybrid	$2.0\text{x}10^{-3}$	29.90	0.2990	0.7902	0.2645	0.9735
Hybrid	$1.5\text{x}10^{-3}$	29.90	0.2990	0.7892	0.2647	0.9744
Hybrid	$1.0\text{x}10^{-3}$	29.87	0.2987	0.7888	0.2655	0.9733
Hybrid	$1.0\text{x}10^{-4}$	30.55	0.3055	0.7868	0.2640	0.9732
Hybrid	$1.0\text{x}10^{-5}$	48.05	0.4805	0.7852	0.2671	0.9667
Ref. (LQ)	------	30.23	0.3023	0.8714	0.2637	0.9938 (present)

In Figure 3.5, the variation in the local wall heat transfer, for the hot wall, is presented for different Rayleigh numbers for air. In this figure, y/H = 0 and 1, respectively represent the bottom and top of the square cavity. It is seen from this figure that with an increase in the Rayleigh number, the heat transfer from the bottom half of the hot wall progressively increases. This increase consequently leads to an enhancement in the average wall heat transfer with Rayleigh number.

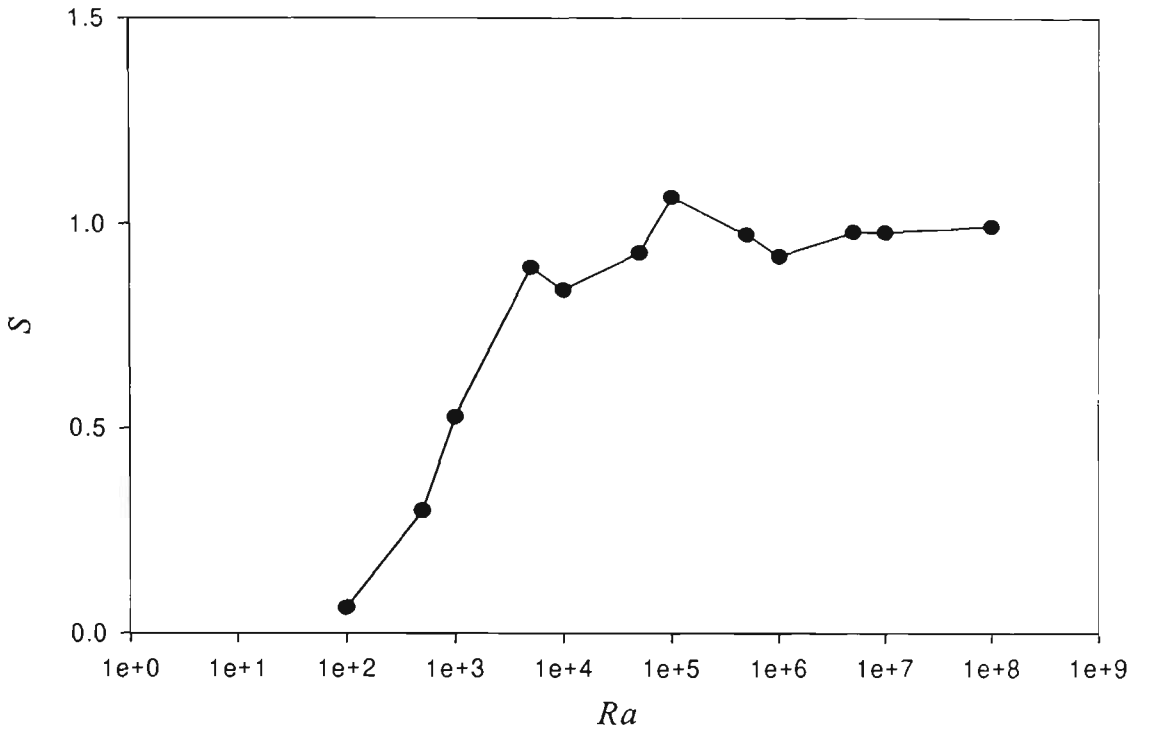

(a)

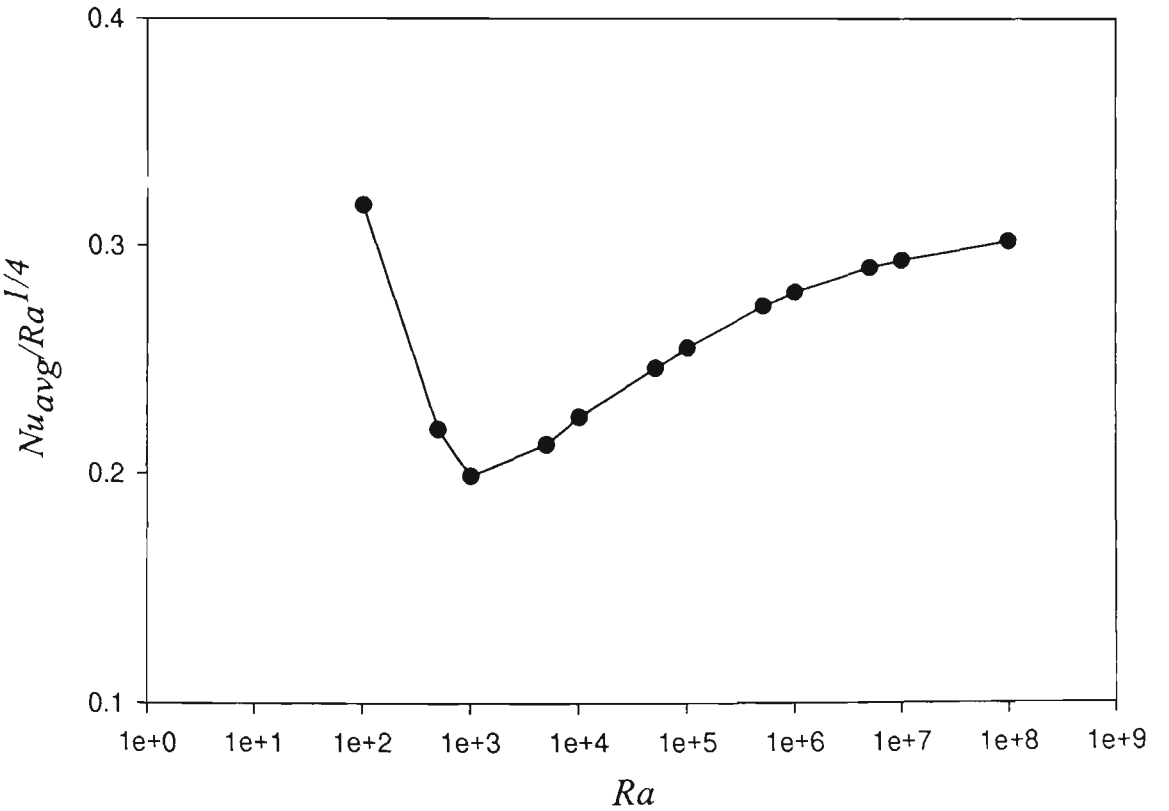

(b)

Figure 3.4: Variation in the (a) core stratification (b) average wall heat transfer with Rayleigh number for air in the laminar regime.

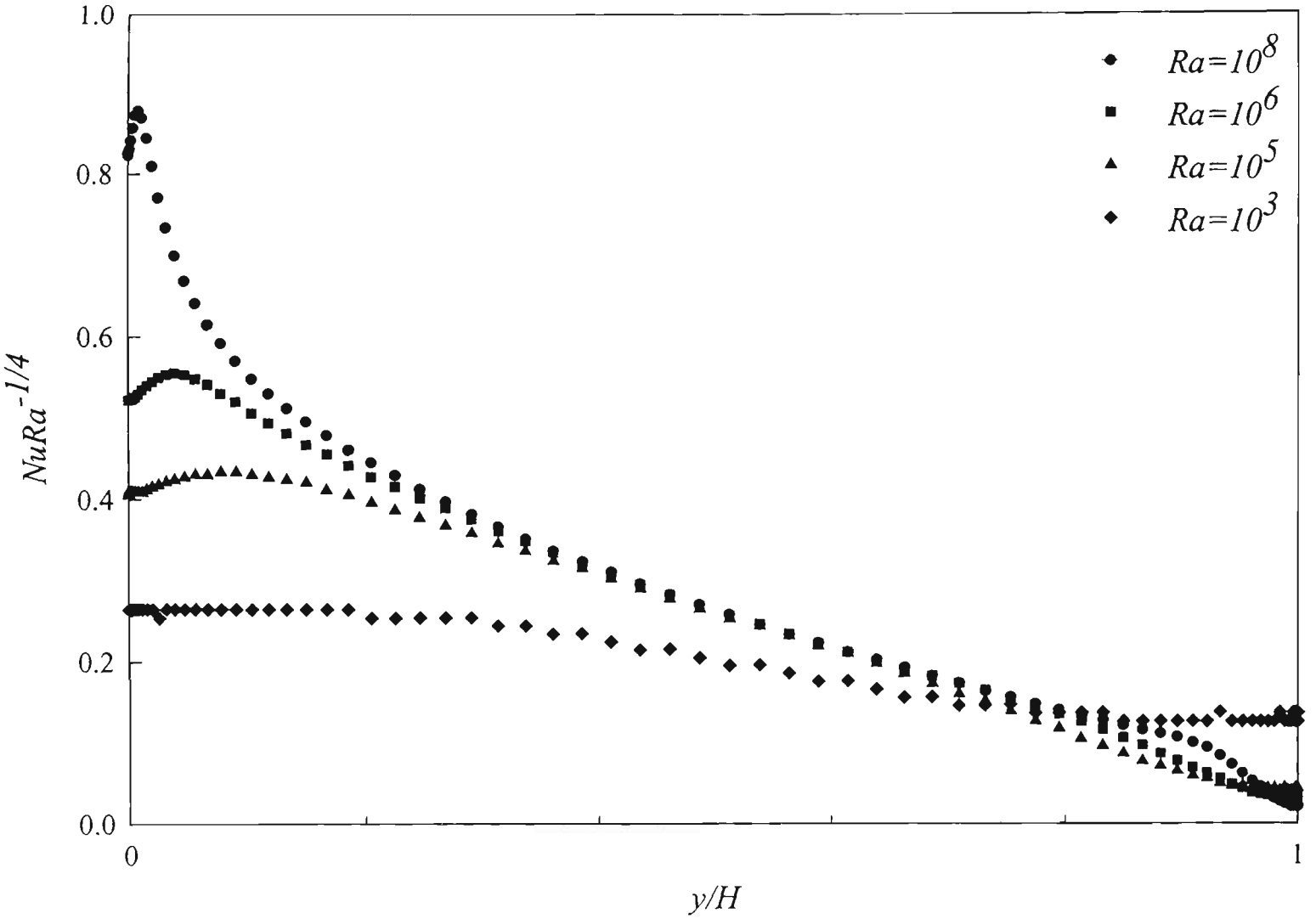

Figure 3.5: Variation of local wall heat transfer for air at different Rayleigh numbers in the laminar regime.

3.4.2 Turbulent flow solutions

Turbulent natural convection flow is still an active research area from both experimental and computational points of view. Experimentally, it is difficult to construct a setup which can be used to study high Rayleigh number natural convection especially with air at atmospheric pressure. Such an experimental setup needs to be at least as large as the size of a standard room. In order to overcome this problem, some authors have studied natural convection either at high pressures or by using a high Prandtl number fluid. Even when such experiments are conducted, the application of boundary conditions, such as the adiabatic boundary condition, is not a trivial task. Therefore, it is difficult to compare the experimental results with a numerical simulation that uses ideal boundary conditions. In order to overcome such difficulties, a standard test case was suggested by Henkes and Hoogendoorn (1992), to test the accuracy of turbulence models for natural convection flows. The standard test case involves the study of a side heated square cavity with air at $Ra=5\text{x}10^{10}$ by using the standard k-ε model. Several authors provided their numerical results for this test case, and the results were compared with the experimental results of Cheesewright and his co workers. For the present calculations, this test case is used as a validation exercise for the implementation of the turbulent flow model. It should be emphasised here that since the implementation of a turbulence model and the associated boundary conditions can vary significantly from one study to another, the validation exercise with turbulent flow calculations is not as rigorous as that with laminar flow calculations. Nevertheless, the validation still provides sufficient confidence while using the code for future turbulent flow calculations.

Turbulent natural convection flow problems, such as the present one, have been known to have numerical problems with convergence. In the present case, initially, an unsteady procedure was adopted to arrive at the converged solution. The unsteady solution was found to be more stable due to the use of false time stepping which acts as an under relaxation. However, a significant amount of time was taken to arrive at a final converged steady solution. In order overcome this problem, a steady solution procedure was adopted starting with relatively high under-relaxation

factors to induce turbulent flow with u_{urf} = 0.5, v_{urf} = 0.5, T_{urf} = 0.5 and p_{urf} = 0.5. The number of Gauss-Seidel sweeps between each iteration was also increased to 10 sweeps for the velocities and temperature (from one for laminar calculations) and 30 sweeps for the pressure (from three for laminar calculations). For the turbulent quantities, k and ε, again 10 Gauss-Seidel sweeps were employed. The required number of Gauss-Seidel sweeps were ascertained after a trial and error procedure, and the above number of sweeps were found to be the lowest to obtain a converged solution. After approximately 500 iterations, when the solution stopped converging, but started giving oscillatory behaviour, the under relaxation factors were decreased significantly to u_{urf}= 0.1, v_{urf}= 0.1, T_{urf}= 0.1 and p_{urf}= 0.2. The Gauss-Seidel sweeps were kept constant for the entire period. This procedure ensured a converged steady solution.

For the test case of Ra=5x10^{10}, square cavity, the boundary conditions for the mean and turbulent quantities were modified for natural convection. Henkes and Hoogendoorn (1992) suggested that the mean and turbulent quantities be solved right up to the wall without the use of any wall functions. For the mean quantities, the boundary conditions given in Equation (3.7) were used. Instead of using wall functions for k and ε such as in Equations (2.43), (2.44), (3.8) and (3.9), these authors used k = 0 and $\varepsilon \rightarrow \infty$ at the wall for the test case (here, ∞ implies the use of a large value of ε at the wall). In the present computations, however, the use of $\varepsilon \rightarrow \infty$ at the wall did not lead to a converged solution. Therefore, it was decided to use two sets of wall functions for k and ε provided by Equations (2.43) and (2.44) (hereafter referred as SBC1) and (3.8) and (3.9) (hereafter referred as SBC2) at the first inner grid point in conjunction with the boundary conditions given by Equation (3.7) for the mean quantities. These wall functions were also used by Lankhorst (1991) in his calculations.

3.4.2.1 Nature of the solutions for turbulent flow

Figure 3.6 represents the structure of the solutions obtained for turbulent flow with air. Frames (a), (b) and (c) in the figure represent the streamlines, isotherms and eddy viscosity contours, respectively. The solutions are identical to the results

presented in Henkes and Hoogendorn (1992). Therefore, only the presents results are shown here. In the turbulent regime, the streamlines in Figure 3.6(a) indicate that the centre of the cavity is an almost stagnant zone with most of the flow occurring along the vertical sides of the cavity. The streamlines and isotherms in Figures 3.6(a) and (b) indicate that the temperature and velocity gradients have become steeper close to the vertical walls. This necessitated the use of the hyperbolic tangent function (Equation (3.12)) in the x-direction. The parameter α_2 was assigned a value of $1.5\text{x}10^{-3}$ for all turbulent flow computations. The eddy viscosity contours in Figure 3.6(c) clearly show that the turbulence is restricted to regions close to the vertical walls with a central core that is essentially laminar.

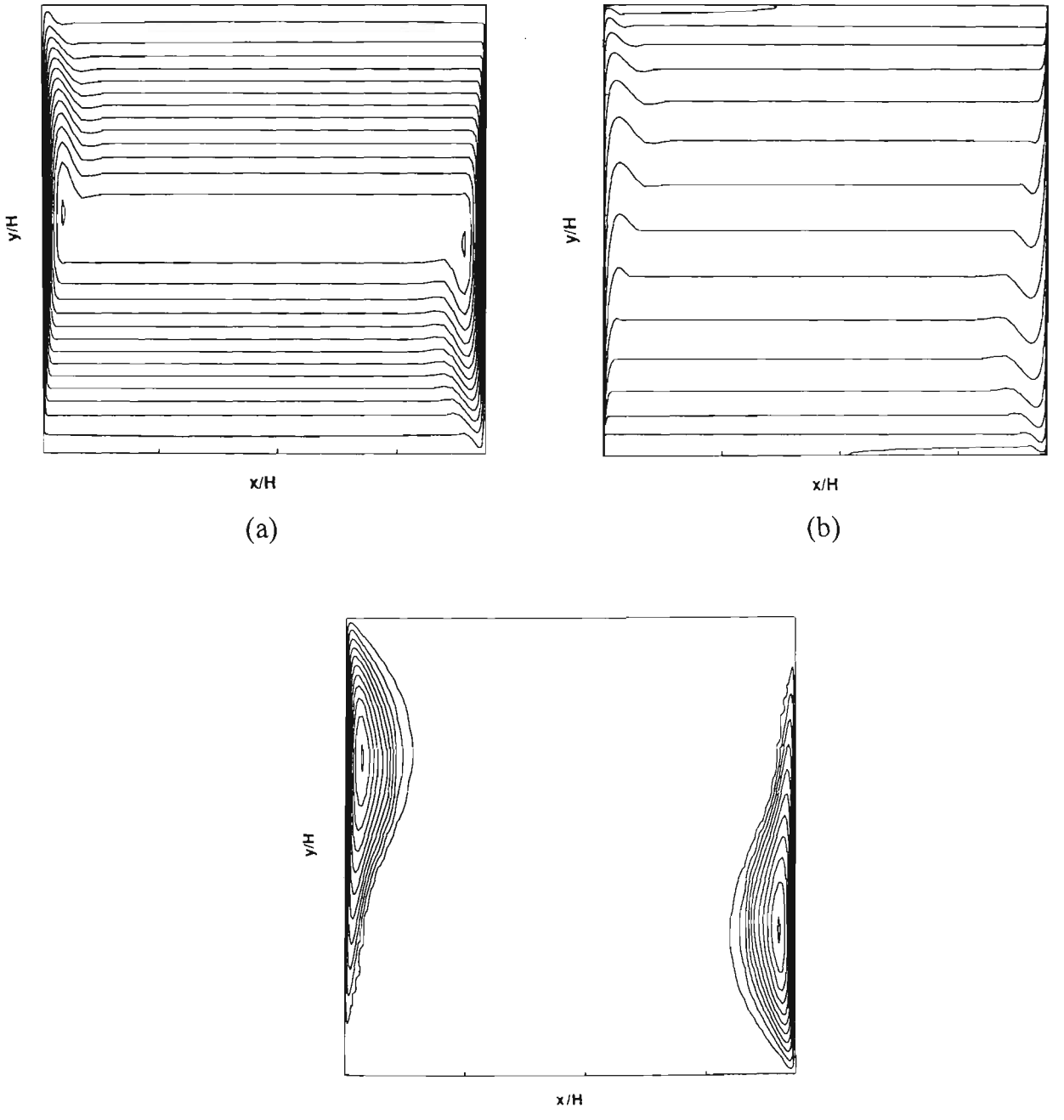

Figure 3.6: Nature of the solutions for turbulent flow (Ra=$5\text{x}10^{10}$) for air.
(a) streamlines, (b) isotherms (c) eddy viscosity contours.

3.4.2.2 Comparisons with previously obtained numerical and experimental results

For the turbulent flow computations, 40x40, 60x60 and 80x80 grids were used. The grid independence of the turbulent results is demonstrated in Figure 3.7. The horizontal axis in the figure represents the non-dimensionalised vertical distance. The vertical axis is the wall heat transfer given in the form $Nu/Ra^{1/3}$. The choice of the vertical axis is due to scaling law suggested for the Nusselt number to Rayleigh number relationship: $Nu_{avg}=cRa^{1/3}$ for turbulent flow where c is a constant (Henkes 1990). The figure shows that the computed vertical hot wall heat transfer which is one of the most critical parameters, gives an almost grid independent solution. The results obtained with the 80x80 grid are therefore used for comparisons with the experimental results of Cheesewright and his co workers.

Figure 3.8 represents a comparison of the experimental and computed wall heat transfer rates with two different sets of wall functions for k and ε, SBC1 (wall function derived from inertial law) and SBC2 (wall function derived from viscous law). The x and y axes have the same meaning as in Figure 3.7. Note that the experimental results show two different wall heat transfer rates for the hot and cold walls, since ideal boundary conditions cannot be applied in the experiments. The numerical results obtained with the two sets of wall functions have wall heat transfer values that are between the experimental results for the hot and cold walls, but they are closer to the results for the hot wall. Therefore, on the average, the numerical results over predict the wall heat transfer values. Henkes (1990) established an average value for the coefficient c in $Nu_{avg}=cRa^{1/3}$ for turbulent flow after comparing the results of the experiments conducted by MacGregor and Emery (1969), Cowan *et al.* (1982) and Betts and Dafa'Alla (1986) who reported values of 0.046, 0.043 and 0.053, respectively. The averaged value was found to be 0.047. Paolucci (1990) obtained a value of 0.046 for c after carrying out a direct numerical simulation (DNS) in a square cavity for air with $Ra=10^{10}$. Results obtained from the present simulations indicate that the predicted value of c (or the average wall heat transfer) is approximately 22% too high with SBC1 and 33% too high with SBC2 for the 80x80 grid calculations. These results are summarised in Table 3.5. Lankhorst (1991) found

the corresponding errors with SBC1 and SBC2 to be approximately +20% and +50%, respectively.

Further comparisons with the experimental results of Cheesewright and his co workers and the present computational results for turbulent flow are presented in Figure 3.9. In Figure 3.9(a), the comparison is given for the non-dimensionalised vertical velocity $\left(\frac{v}{\sqrt{g\beta\Delta TH}}\right)$ profile at $y=H/2$. The experimental hot and cold wall results are closer to each other for the vertical velocity profile inspite of the non-ideal boundary conditions. The numerically obtained vertical velocity profiles are not significantly affected by the boundary conditions, and they are between the hot and cold wall results. In Figure 3.9(b), the comparison is presented for the non-dimensionalised turbulent shear stress $\left(\frac{\overline{u'v'}}{g\beta\Delta TH}\right)$ profile at $y=H/2$. The experimentally obtained turbulent shear stresses for the hot and cold walls are significantly different with the difference in the peak value for each wall being as much as 50% based on the cold wall value. The numerical results are again similar with both boundary conditions, and they are closer to the experimental hot wall results.

Figure 3.9(c) presents a comparison for the non-dimensionalised turbulence kinetic energy profile at $y=H/2$. For this purpose, the turbulence was assumed to be isotropic. The numerically obtained values of the parameter, $\frac{\sqrt{2k/3}}{\sqrt{g\beta\Delta TH}}$, are compared with the experimentally obtained values of the parameter, $\frac{\sqrt{\overline{v'^2}}}{\sqrt{g\beta\Delta TH}}$. The experimental hot and cold wall results are close to each other for the turbulence kinetic energy. The numerical results show a significant under prediction of the peak value. The deviation is approximately -22% for both boundary conditions. This error can be partly attributed to the assumption of isotropy for the comparison.

In Figure 3.9(d) the results are presented for the non-dimensionalised eddy viscosity $\left(\frac{\nu_t}{\nu}\right)$ at $y=H/2$. Comparison with experiments was not possible in this case, since results for the eddy viscosity could not be obtained from the experiments. Nonetheless, the result gives an indication of the strength of turbulence for such flows. The eddy viscosity is independent of the boundary conditions used for k and ε with a maximum value of approximately 45 times the fluid viscosity.

Henkes and Hoogendoorn (1992) compiled a table of the numerical results obtained from various authors which fell in the 50% range of agreement with each other. An average for each of the parameters studied was then obtained. The average of the eddy viscosity thus obtained was found to be 51.7 times the fluid viscosity which is in the range of the results obtained from the present simulations. Other average results have been presented in Table 3.5 as HH (mean). Also, the experimental hot and cold wall and their average results from the experiments of Cheesewright and his co workers are presented in Table 3.5 for comparison. From Table 3.5, it is clear that the present numerical results are in better agreement with the experimental averages for the Nusselt number and the core stratification than the average numerical results of Henkes and Hoogendorn. For example, with SBC1 and the finest grid used, the present results over predict the heat transfer by approximately 16%, and the core stratification is under predicted by 1.6%. The average result of Henkes and Hoogendoorn (1992), on the other hand, over predicts the heat transfer by approximately 41% and under predicts the core stratification by approximately 12%. The vertical velocity maximum at $y=H/2$, however, is under predicted in the present simulations (an under prediction of approximately 18% with SBC1 and the 80x80 grid in comparison with an almost error free solution for the average of Henkes and Hoogendorn). Overall, the present numerical results show good agreement with the experiments and previous numerical simulations.

The results obtained with boundary conditions for k and ε through the inertial law (the SBC1 boundary condition) are consistently better than the ones with viscous law (the SBC2 boundary condition) irrespective of grid refinement. With an 80x80 grid and the present grid distribution, the first inner grid point was found to be well

within an x^+ value of 10. Therefore, the SBC1 boundary condition is chosen as the preferred boundary condition for the application oriented case study in chapter seven.

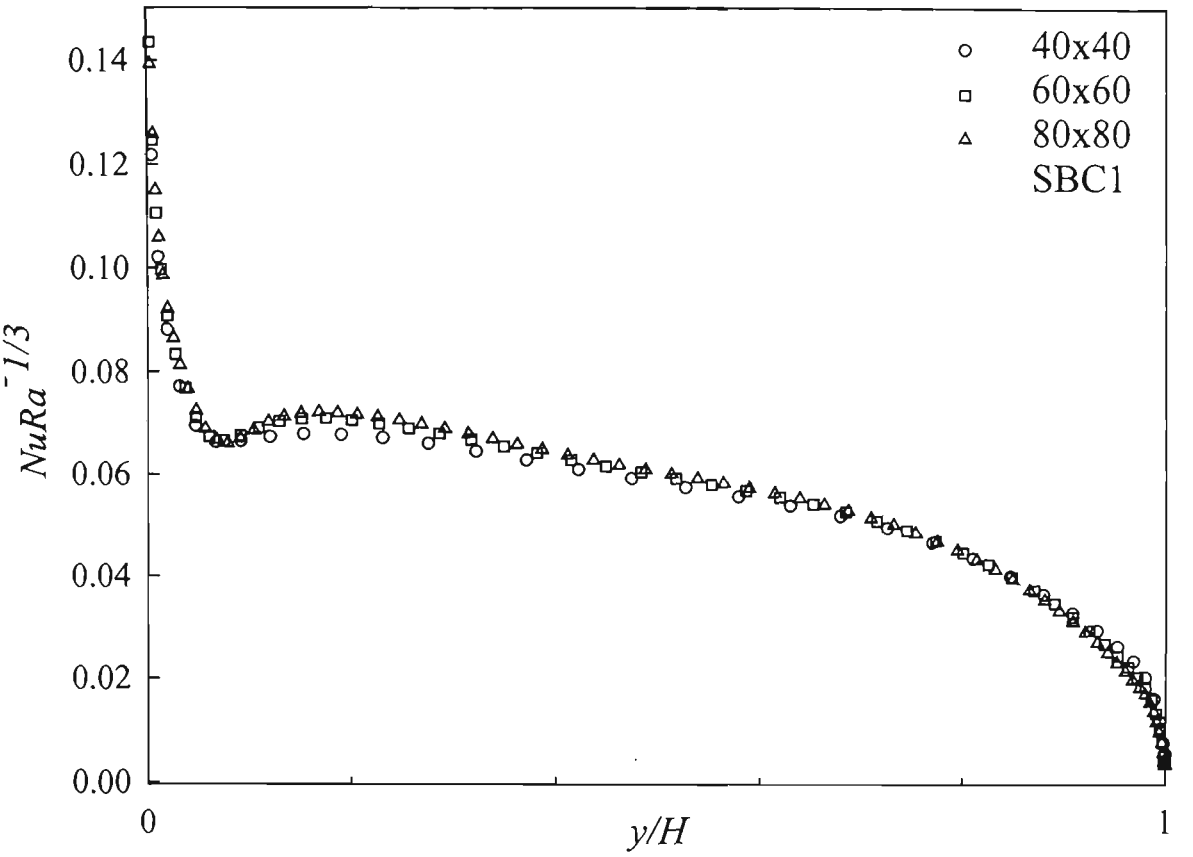

Figure 3.7: Grid independence for turbulent flow

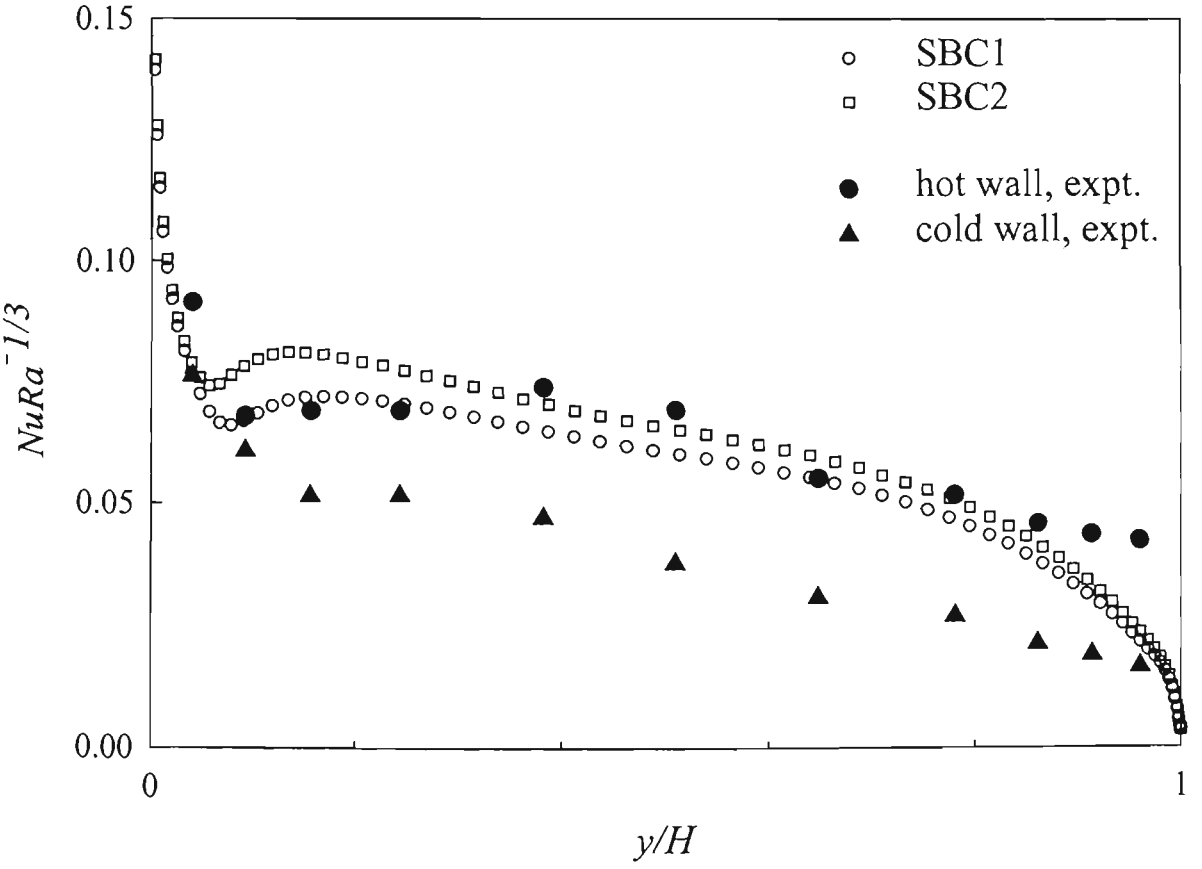

Figure 3.8: Comparison of wall heat transfer for turbulent flow. Experimental results are from Cheesewright and co workers.

Table 3.5: Summary of solutions for turbulent flow with Ra=5x10^{10}

Model	Grid	Nu_{avg}	$\frac{Nu_{avg}}{Ra^{1/3}}$	$\frac{u_{max}}{\sqrt{g\beta\Delta TH}}$	$\frac{v_{max}}{\sqrt{g\beta\Delta TH}}$	$S_c = \frac{H}{\Delta T}\left(\frac{\partial T}{\partial y}\right)_c$
SBC1	40x40	205.4	0.0557	0.009017	0.1394	0.4404
SBC1	60x60	210.1	0.0570	0.009137	0.1369	0.4750
SBC1	80x80	211.6	0.0574	0.009394	0.1363	0.4721
SBC2	40x40	231.8	0.0629	0.009309	0.1427	0.4612
SBC2	60x60	231.5	0.0628	0.009400	0.1403	0.4947
SBC2	80x80	230.8	0.0626	0.009441	0.1392	0.4899
HH (mean)	------	256.0	0.0695	0.0124	0.167	0.5390
Expt. (cold wall)	------	154.0	0.0418	------	0.144	0.48
Expt. (hot wall)	------	210.0	0.0570	------	0.190	0.48
Expt. (Average)	------	182.0	0.0494	------	0.167	0.48

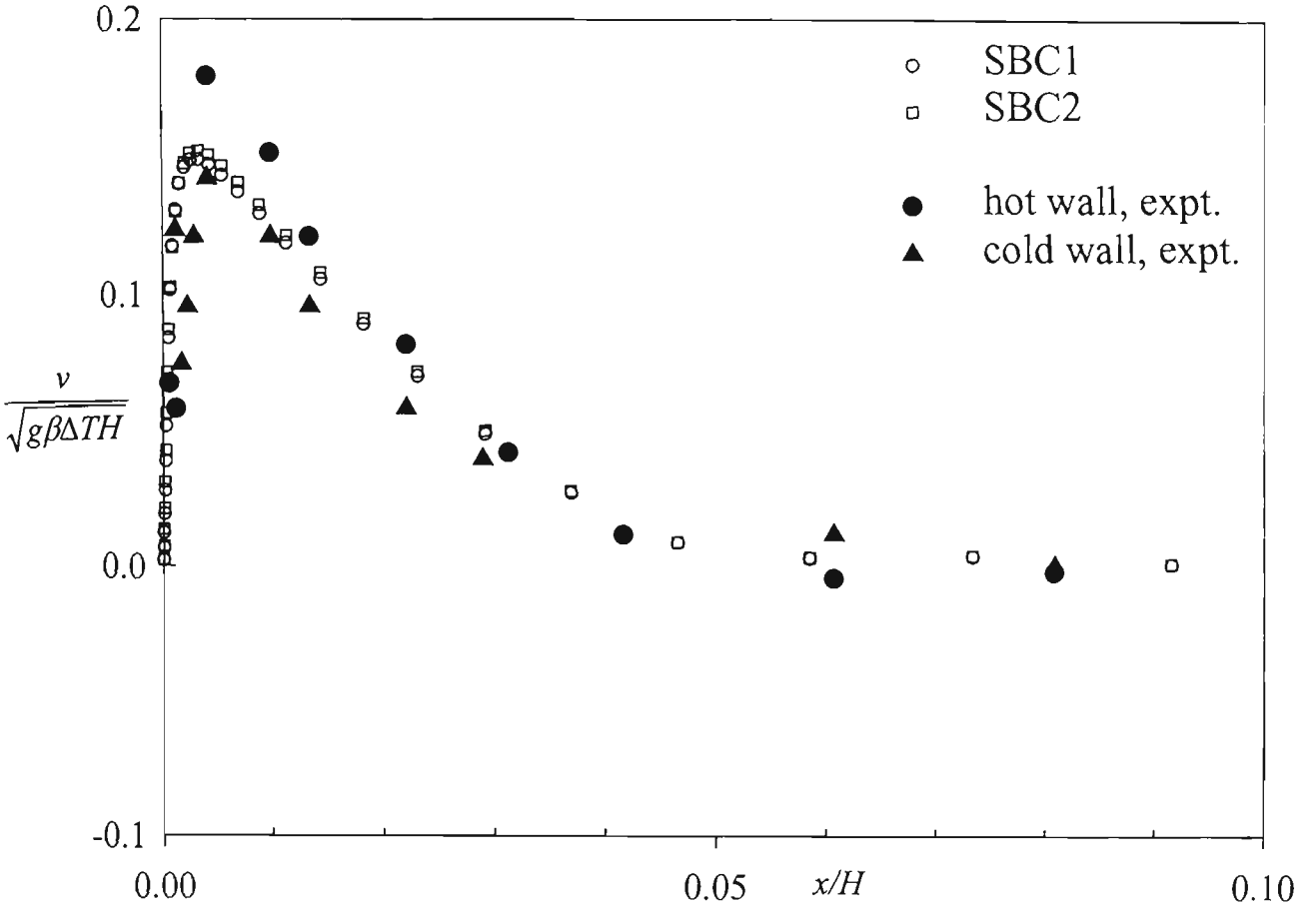

(a)

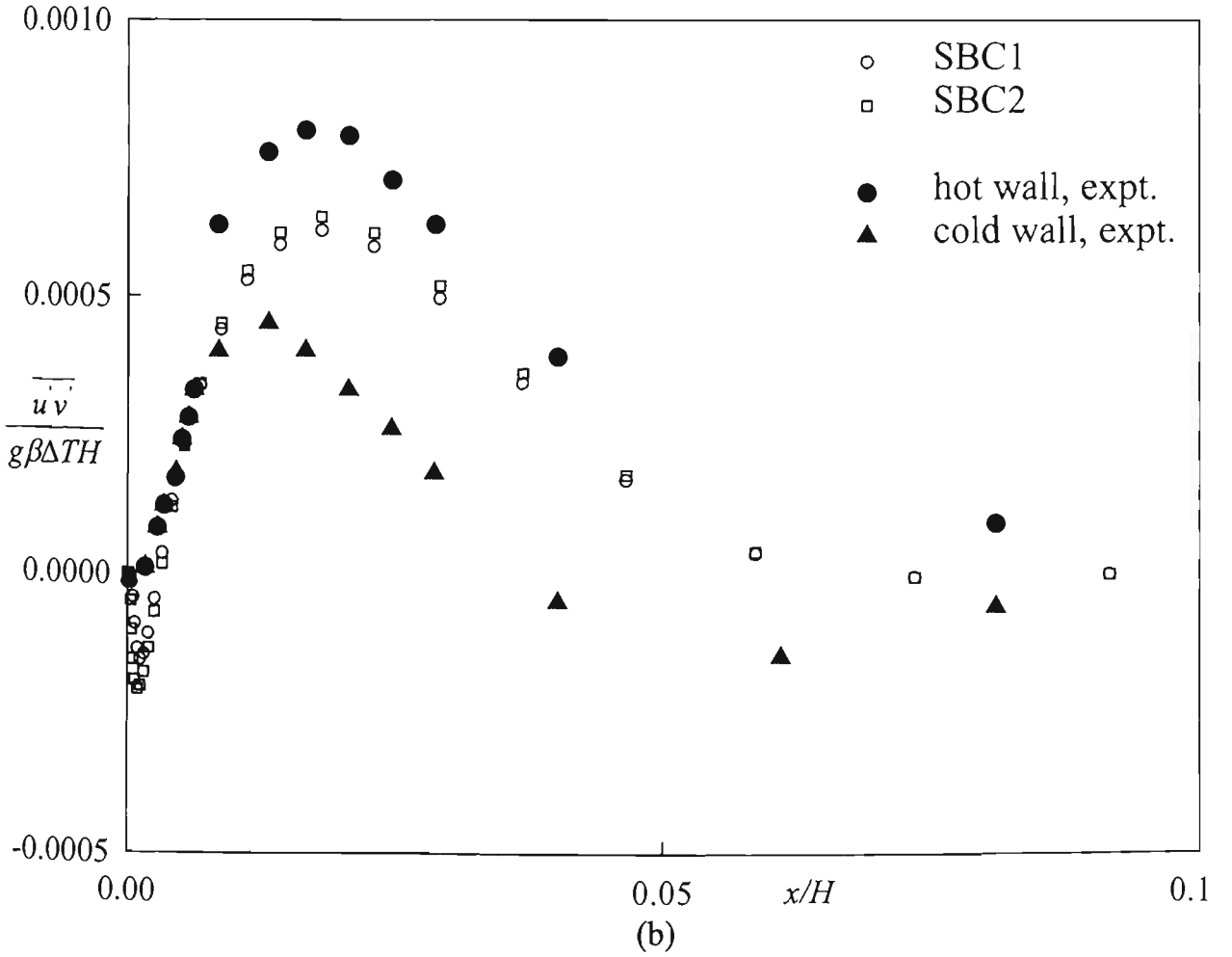

(b)

For caption, see next page

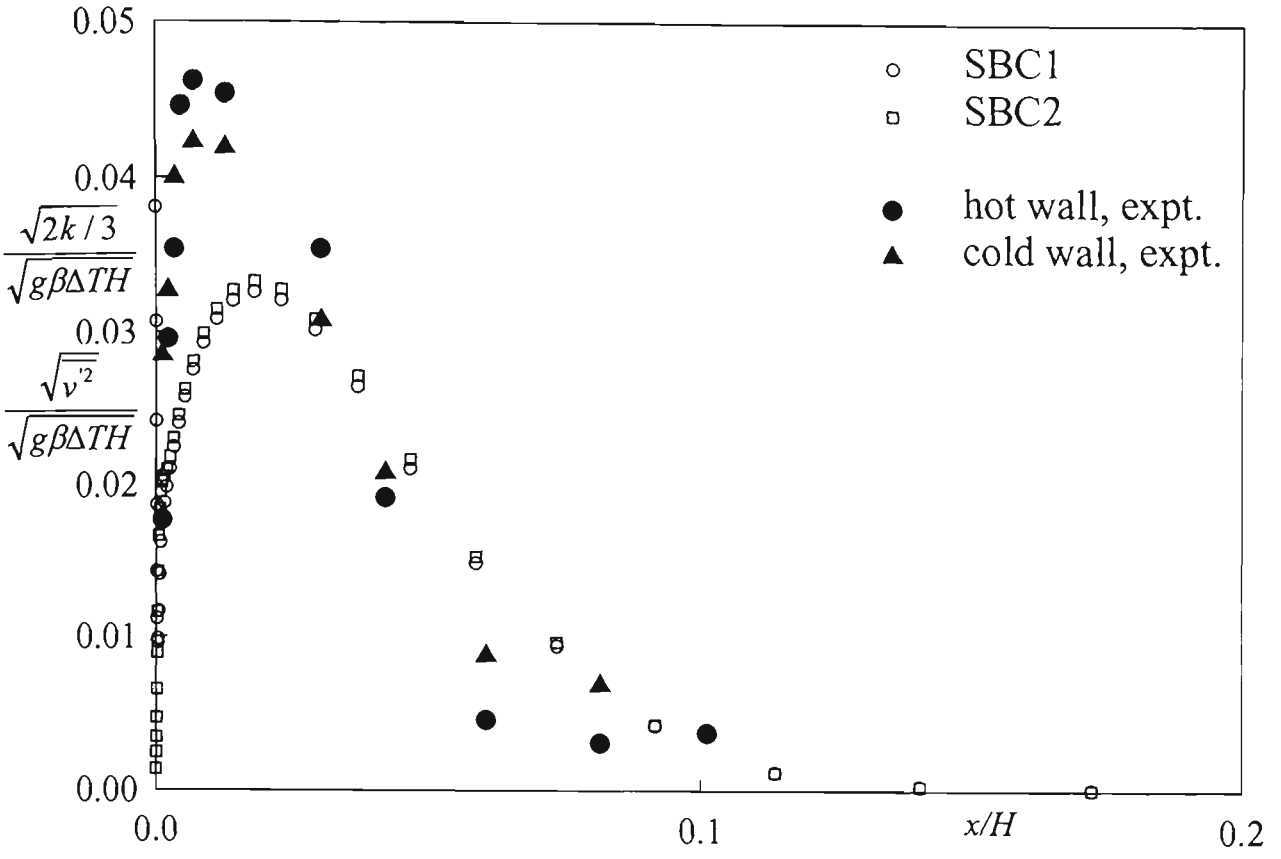

(c)

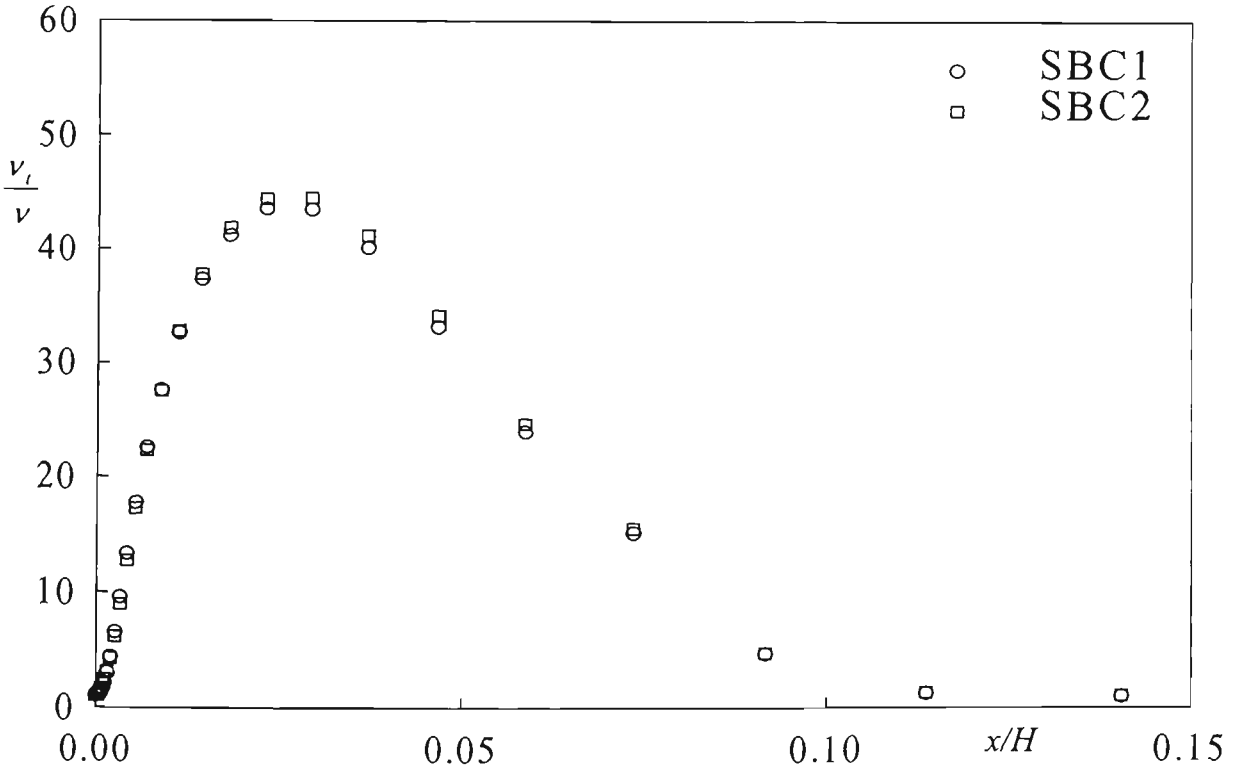

(d)

Figure 3.9: Further comparison between present numerical solutions and the experiments of Cheesewright and his co workers (a) vertical velocity at $y=H/2$, (b) turbulent shear stress at $y=H/2$, (c) turbulence kinetic energy at $y=H/2$, (d) eddy viscosity at $y=H/2$ (note that there are no experimental results available for the eddy viscosity).

3.5 Conclusions

The CFD code developed in-house to solve problems involving laminar and turbulent fluid flow and heat transfer has been validated by using the heating from the side or double glazing problem of natural convection. The code can be considered to be accurate for solving two-dimensional laminar natural convection flows. The results obtained for all parameters have an error of less than 1% compared to benchmark numerical results. The asymptotic value of the core stratification, $\left(\frac{H}{\Delta T}\left(\frac{\partial T}{\partial y}\right)_c = 0.99\right)$, and the heat transfer scaling in a cavity for laminar natural convection flow with air, $\left(Nu_{avg} = 0.30Ra^{1/4}\right)$, are predicted accurately by the model. The code is also able to predict flow transition from laminar to a transition regime accurately, which happens at a Rayleigh number of approximately 10^8 for air.

Turbulent natural convection flows are still an active research area, and the benchmark studies carried out for this problem do not have precise solutions as in the case of laminar natural convection problems. The present computations with the standard k-ε model showed good agreement with previous numerical simulations. The difference between the present numerical and benchmark experimental results is comparable to those of previous numerical studies. In particular, the results obtained with the wall functions for k and ε obtained through the inertial law were found to be superior to those obtained with viscous law.

Chapter 4

Flow visualisation experiments

4.1 Introduction

After preliminary validation with benchmark numerical and experimental results, the CFD code is modified for simulating a system consisting of a turbulent fluid layer overlying a porous medium. Flow visualisation and LDV measurements for this system have been carried out for the purpose of comparison with the CFD simulations. The flow visualisation experiments are described in detail in the present chapter. The simulations of this set of experiments are presented in chapter five.

In recent years, there has been renewed interest in high-speed flows in porous media because of their potential industrial applications. In the chemical industry, for example, fixed bed reactors often have velocities that are higher than the regime in which Darcy's law is valid. Other areas where an understanding of high-speed flow in porous media has become essential are, in the modelling of transport processes in stored agricultural produce carried out by Chen and Li (1998) and Prakash *et al.* (1999a), and simulation of metal solidification such as in Prescott and Incropera (1995). A comprehensive review of other applications of such flows is given in Antohe and Lage (1997). Due to the development of advanced computer modelling techniques such as CFD and the availability of measurement techniques such as laser Doppler velocimetry (LDV) and particle image velocimetry (PIV), such flows can be studied in much greater detail than was possible before.

Originally, the studies of flows in porous media were limited to soil mechanics where one did not normally encounter large velocities. Darcy's law could therefore be applied. Several modifications to Darcy's law have been proposed to account for non-Darcian effects. Reviews of these can be found in Scheidegger (1963) and Nield and Bejan (1992). The most important among these were the modifications suggested by Forchheimer (1901) and Brinkman (1947). As described in Section 2.2.3 of chapter two, the Forchheimer modification incorporated the inertial term in the original Darcy equation, which becomes significant only when one encounters high velocities in the porous medium. The Brinkman term, on the other hand, is a viscous

drag term that becomes significant in regions in the porous medium close to walls, or at the interface between a porous medium and clear fluid. To accommodate these conditions, the original Darcy equation was modified to resemble the familiar Navier-Stokes equation. This extended model of non-Darcian flow in porous medium is commonly referred to as the Brinkman Forchheimer extended Darcy model or the BFD model (Equation (2.21)).

As pointed out by Antohe and Lage (1997), theories of the physics of turbulence in porous media give rise to considerable controversy in the fluid mechanics community. It has been shown through experimental studies (Lage *et al.*, 1997) that the Forchheimer term cannot account for very high Reynolds number flows. Thus, in the case of flow in porous media, one might have three different regimes: the Darcy flow regime, the Forchheimer flow regime and a turbulent flow regime. Experimental work in this area has been relatively sparse due to difficulties of taking measurements in the porous medium. The experimental works of Mickley *et al.* (1965), Jolls and Hanratty (1966) and Van Der Merwe and Gauvin (1971) were some of the earliest in this category. All three experiments were carried out using a packed bed of spheres either in a regular arrangement (Van Der Merwe and Gauvin, 1971 and Mickley *et al.*, 1965) or in a random arrangement (Jolls and Hanratty, 1966). These experiments were directed at investigating flow regimes that occur in packed bed reactors, an issue which is of relevance in the chemical industry.

Seguin *et al.* (1998a and b) have shown recently that there is a significant difference in the behaviour of fluids flowing in different types of porous media. These authors used porous media that consisted of packed beds of spheres, packed beds of square-based parallelepipedal plates of different height to side ratios and synthetic reticulated foams of different grades (given in pores per inch, ppi). They used electrochemical micro-probes to measure local instantaneous values of the current intensity. The electrolyte solution used had a density and viscosity comparable to that of water. Spectral analysis of the signal fluctuations enabled an accurate determination of when the stable laminar regime became unstable. Furthermore, using an electrochemical transfer function, the spectrum of velocity gradient fluctuations at the micro-electrodes and the velocity gradient fluctuating rate were determined. Transition to a turbulent regime was characterised by stabilisation

of the fluctuating rate of the velocity gradient. The study was aimed at characterising flow regimes in various porous media, from the limit of the laminar flow regime through a transition to the turbulent regime. One significant finding of these authors was that for synthetic reticulated foam, the results obtained at the wall of the column that contained the porous medium and within the porous medium were similar. This finding was attributed to the high porosity of these porous media (with porosity values from 0.9 to 0.98). In the case of low porosity porous media, such as a packed bed of spheres, however, there is a significant difference in the porosity between the column wall/interface (with another medium) and the core of the porous medium. Wall effects can be attributed to the difference in the porosity (Mickley *et al.*, 1965). The structure of synthetic reticulated foams thus allows measurements taken close to the interface or the wall column of a foam sample, to characterise flow in the foam.

For characterising flow regimes within the porous media, Seguin *et al.* (1998a), used a pore Reynolds number defined by

$$\mathrm{Re}_p = \frac{\rho u_p d_p}{\mu} \tag{4.1}$$

where $d_p = \dfrac{4\phi}{(1-\phi)a_{vd}}$ is the pore diameter, (4.2)

and $u_p = u_0 \dfrac{\tau}{\phi}$ is the pore velocity. (4.3)

In Equation (4.1), ρ and μ represent the fluid density and viscosity, respectively. In Equation (4.2), ϕ is the porosity of the porous medium, and a_{vd} is the dynamic specific surface area of the porous medium based on the surface area of the foam in contact with the fluid. In Equation (4.3), u_0 is the superficial velocity of the fluid (this is equivalent to the volume averaged velocity, u_{va}, for flow through porous media presented in Section 2.2.3 of chapter two), and τ represents the tortuosity of the porous medium. Seguin *et al.*'s (1998a) structural parameters are listed in Table 4.1 (which is a duplication of their Table 3).

Table 4.1: Structural parameters of synthetic foam investigated by Seguin *et al.* (1998a). Reproduction of Table 3 of Seguin *et al.* (1998a).

Foam	G10	G20	G45	G100
ϕ	0.971	0.973	0.978	0.973
τ	1.31	1.30	1.32	1.20
a_{vd} (m^{-1})	33,400	55,150	186,000	439,000
d_p (m)	0.004	0.0026	0.00095	0.00033

These parameters are converted to the familiar permeability, K, and Forchheimer coefficient, c_F. The conversion was carried out by using the pressure drop to velocity relationship provided by Seguin *et al.* (1998a) in their Equation (16), given below as Equation (4.4), and matching the terms with the Forchheimer's equation, given below as Equation (4.5).

According to Seguin *et al.* (1998a),

$$\frac{\Delta P}{H} = \frac{2\mu(1-\phi)^2}{\phi^3} a_{vd}^2 \tau^2 u_0 + 0.0968\tau^3 a_{vd} \rho \frac{(1-\phi)^2}{\phi^3} u_0^2 \tag{4.4}$$

where $\frac{\Delta P}{H}$ is the intrinsic pressure drop across the porous foam.

The Forchheimer modified Darcy equation can be represented as,

$$\frac{\Delta P}{H} = \frac{\mu}{K} u_0 + \frac{\rho c_F}{\sqrt{K}} u_0^2 \tag{4.5}$$

From Equations (4.4) and (4.5) and Table 4.1, one can arrive at values for permeability, K, and Forchheimer coefficient, c_F, for different foams. These values are listed in Table 4.2. In the present experiments and numerical simulations, the same ranges of K and c_F are used for comparison.

Table 4.2: Permeability, K, and Forchheimer coefficient, c_F for foam. Converted from structural parameters in Table 4.1 by using Equations (4.4) and (4.5).

Foam	G10	G20	G45	G100
ϕ	0.971	0.973	0.978	0.973
K (m^2)	2.843×10^{-7}	1.229×10^{-7}	1.603×10^{-8}	2.277×10^{-9}
C_F	0.1227	0.1204	0.1232	0.1026

Using the above definition for the pore Reynolds number, Seguin *et al.* (1998b), investigated the flow regimes in foam up to Re_p= 700. At this Reynolds number, transition to turbulent flow was observed only for the highest permeability foam (G10 or 10 ppi foam).

Hall and Hiatt (1996) conducted LDV measurements on air flowing in highly porous ceramic foams of different grades (characterised by pores per centimetre, ppcm). These measurements were carried out either between two specimens of foam spaced 0.005 m apart or in a hole drilled in the ceramic foam of pore sizes of 4, 8 and 12 ppcm. They found that transition to turbulent regime occurred at a pore Reynolds number of approximately 150 only for ceramic foams with 4 ppcm and 8 ppcm. For the 12 ppcm foam, the flow was found to be laminar in the range of pore Reynolds numbers investigated. However, their definition of the pore Reynolds number was different from the one used by Seguin *et al.* (1998a):

$$\mathrm{Re}_p^{'} = \frac{\rho d_p^{'} u_p^{'}}{\mu} \tag{4.6}$$

In Equation (4.6) $d_p^{'}$ is the pore diameter (for the 4 ppcm foam, $d_p^{'}$=0.0025 m) and $u_p^{'}$ is the average pore velocity (which is taken as the stream-wise area mean velocity or the volume averaged velocity, u_{va}, as defined in Section 2.2.3 of chapter two).

To the author's knowledge, no other experiments in the high-speed regime have been carried out with porous foams. The primary objective of the studies of Seguin *et al.* (1998 a and b) was to develop a relationship based on structural parameters as well as to investigate the transition to turbulence in different porous media. Hall and Hiatt (1996), on the other hand, investigated experimentally the transition to turbulence in ceramic foams.

The flow equations in porous media are derived by using the principles of volume averaging (see Whitaker, 1967 and Slattery, 1967). However, the measurements reported in the literature are made at distinct points within the porous medium. Therefore, such experimental results cannot be used for comparison with simulations which use the volume-averaged equations for flow in porous media. The

experiments reported in this thesis (flow visualisations and LDV measurements) have been performed primarily for the purpose of comparison with CFD simulations. In the present experiments, instead of taking measurements at point locations within the porous medium, the flow characteristics within the porous medium are inferred by recording the changes in the flow patterns, mean velocities and turbulence kinetic energy in an adjacent fluid layer. The flow visualisation results have been used mainly to determine critical regions of the flow that are examined further using LDV measurements. They have also been used for a visual comparison with the flow pattern obtained from the numerical simulations presented in chapter five.

4.2 Apparatus and experimental setup

Flow visualisations were carried out using a sheet of light from a 5 W argon ion laser. The visualisations were performed with and without the porous foam. The foam specimens were obtained from Joyce foam products, and they were characterised by the average number of pores per inch of foam. Three different types of foam were used corresponding to 10, 30 and 60 pores per inch (ppi) hereafter referred to as G10, G30 and G60 foams, respectively. Water was used as the fluid in all of the experiments. An impinging jet setup was used to generate turbulence (see Figure 4.1). Two different jet exit velocities of 1 and 1.6 m/s were utilised. The jet exit velocities correspond to Reynolds numbers of around 19,000 and 30,000, respectively, based on the jet diameter. For the highest permeability foam used in the present experiment, a mean velocity of 1.6 m/s translates to a pore Reynolds number of approximately 8600, using Equation (4.1). With Equation (4.6), a pore Reynolds number of approximately 4100 is obtained (the calculations are based on μ=1x10^{-3} Pas and ρ=1000 kgm^{-3} for water). With either calculation, the flow in the porous foam can be expected to be turbulent at least for the highest permeability foam as the jet impinges on the porous foam.

A simple schematic representation of the experimental rig is shown in Figure 4.1. The jet diameter, D_j, is 0.019 m and the cylinder inner diameter, D, is 0.39 m. In between the cylinder and the disc holding the jet, there is an annular clearance of width, w, of 0.005 m. All the water entering the system left through this clearance. The jet outlet was flush with the disc holding the jet. Three different heights of water

column, H, of 0.05, 0.1 and 0.15 m were used with and without the porous foam. The diameter of the foam was the same as the inner diameter of the cylinder. Two different foam heights, h_p, equal to 0.05 and 0.1 m were employed for the experiment. Thus the total height of the system varied between 0.05 to 0.15 m without foam, and, 0.1 to 0.25 m with foam. The light reflecting tracer used in the flow visualisation experiments were small air bubbles with an average bubble diameter of 100 μm. Some air bubbles were trapped in the porous foam and affected the quality of the visualisations with the foam.

The terminal velocity of the air bubbles, v_t, needs to be much smaller than the jet velocity, U_b = 1.6 m/s, to assume that these bubbles follow the path of the fluid. The terminal velocity, v_t, is calculated from the relationships given in Bird *et al.* (pp. 193-194, 1960). The following relationships give the friction factor for a single sphere:

$$\begin{aligned} f &= \frac{24}{\mathrm{Re}} && \mathrm{Re} < 0.1 \\ f &\cong \frac{18.5}{\mathrm{Re}^{3/5}} && 2 < \mathrm{Re} < 5\times10^{2} \\ f &\cong 0.44 && 5\times10^{2} < \mathrm{Re} < 2\times10^{5} \end{aligned} \qquad (4.7)$$

where, $\mathrm{Re} = \dfrac{dv_t\rho}{\mu}$

d is the diameter of the air bubble,

ρ is the density of water,

and μ is the viscosity of water.

Using the above relationships and the relationship between terminal velocity and friction factor given below in Equation (4.8), the terminal velocity, v_t, was determined by a trial and error procedure to be approximately $5.5\text{x}10^{-3}$ m/s which is much smaller than the jet velocity.

$$f = \frac{4}{3}\frac{gd}{v_t^2}\left(\frac{\rho-\rho_a}{\rho}\right) \qquad (4.8)$$

In order to prevent coalescence of bubbles, a small amount of surfactant was added to the water. By taking several photographs for the same experiment, it was

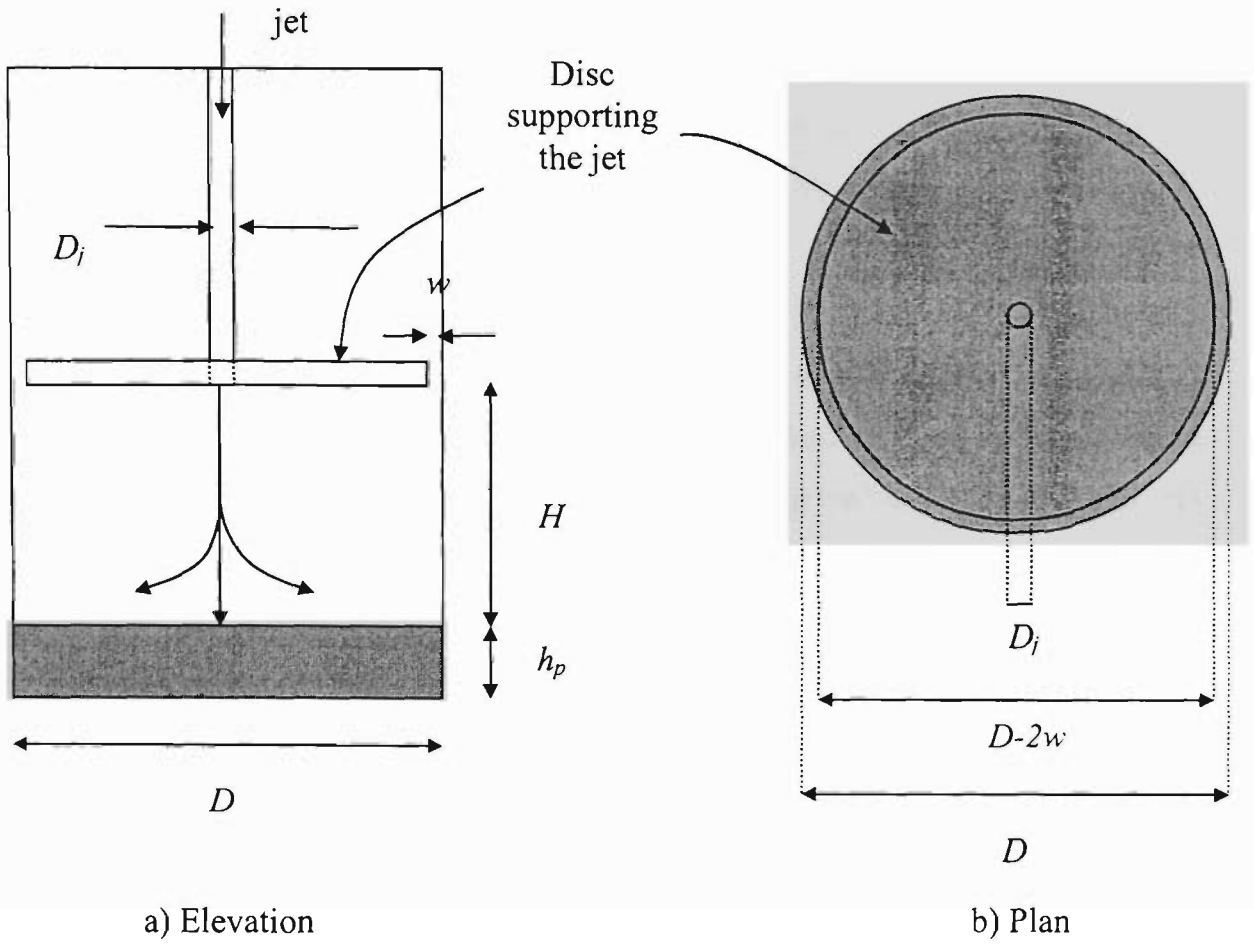

Figure 4.1: Schematic diagram of the inner cylinder along with the impinging jet

found visually that the presence of the air bubbles did not affect the gross flow pattern.

Figure 4.2 shows a schematic representation of the entire setup. As shown in the figure, the position of the laser beam could be adjusted using the beam aligner either in the horizontal or vertical direction. The laser beam was first brought to the centre of the jet, and then, it was aligned with the lower surface of the disc holding the jet. Next, using the beam splitter, the beam was split into a sheet of light. The beam splitter was adjusted to provide maximum intensity of light in the region between the porous fibre and the lower surface of the disc holding the jet. Since the porous fibre is opaque to the laser sheet, visualisation could be carried out only in the fluid layer. However, it is expected that the presence of porous fibre will influence the flow field in the fluid layer.

An overhead tank provided the water to the impinging jet. The overhead tank eliminated any pulsating flow due to changes in the delivery rate of the pump. Two

orifices at the exit of the overhead tank having diameters of 0.0095 and 0.0125 m were used to deliver jet exit velocities of 1 and 1.6 m/s, respectively. The water level in the overhead tank was maintained by pumping water at the desired rate from a bottom tank. The rate of pumping was in turn controlled by a digital speed controller.

The cylinder housing the impinging jet and the impinging jet are made of a transparent acrylic material. This setup is placed in a rectangular glass tank, as shown in Figure 4.2, in order to reduce refraction of the laser sheet thus minimising errors in the flow visualisation. The water level in the rectangular tank and cylinder are maintained with the help of an exit pipe which in turn releases the water back into the bottom tank. Thus there is a constant circulation of water from the bottom tank and to the overhead tank to the experimental setup and back to the bottom tank.

A high speed CCD camera (manufactured by Kodak) was used for recording the flow field. The exposure times were varied between 10 and 500 milliseconds (msec) to capture a range of speeds in the form of bubble streak lines. The flow visualisation was used mainly for determining the gross flow characteristics and not to estimate instantaneous velocities. Instead, LDV measurements (presented in the sixth chapter) have been used to determine mean and root mean square (r.m.s.) velocities. Preliminary visualisations were carried out by taking photographs in different regions of the flow to ascertain the correct exposure time. An example is shown in Figure 4.3 for a fluid height of 0.15 m without foam with exposure times of 10, 20 and 200 msec. No additional information could be gained from the visualisations taken in the jet region, such as in Figures 4.3(a) and (b). Therefore, visualisations have not been reported for images taken at the jet centre. As seen in Figure 4.3, the bubble streak lines could be clearly visualised only with an exposure time of 200 msec or longer. Consequently, only visualisations with exposure times of 200 or 500 msec have been documented, as images with sufficient resolution. The bright lines seen in these visualisations, close to the wall of the cylinder, as well as close to the middle of the cylinder at half plane, arise from reflections in the circular cross section of the cylinder. These could not be eliminated completely, and they occur in all the visualisation photographs documented in this chapter. Since the turbulent time scales are much smaller than the exposure times, the present visualisations can be regarded as representative of the gross flow characteristics of the flow field.

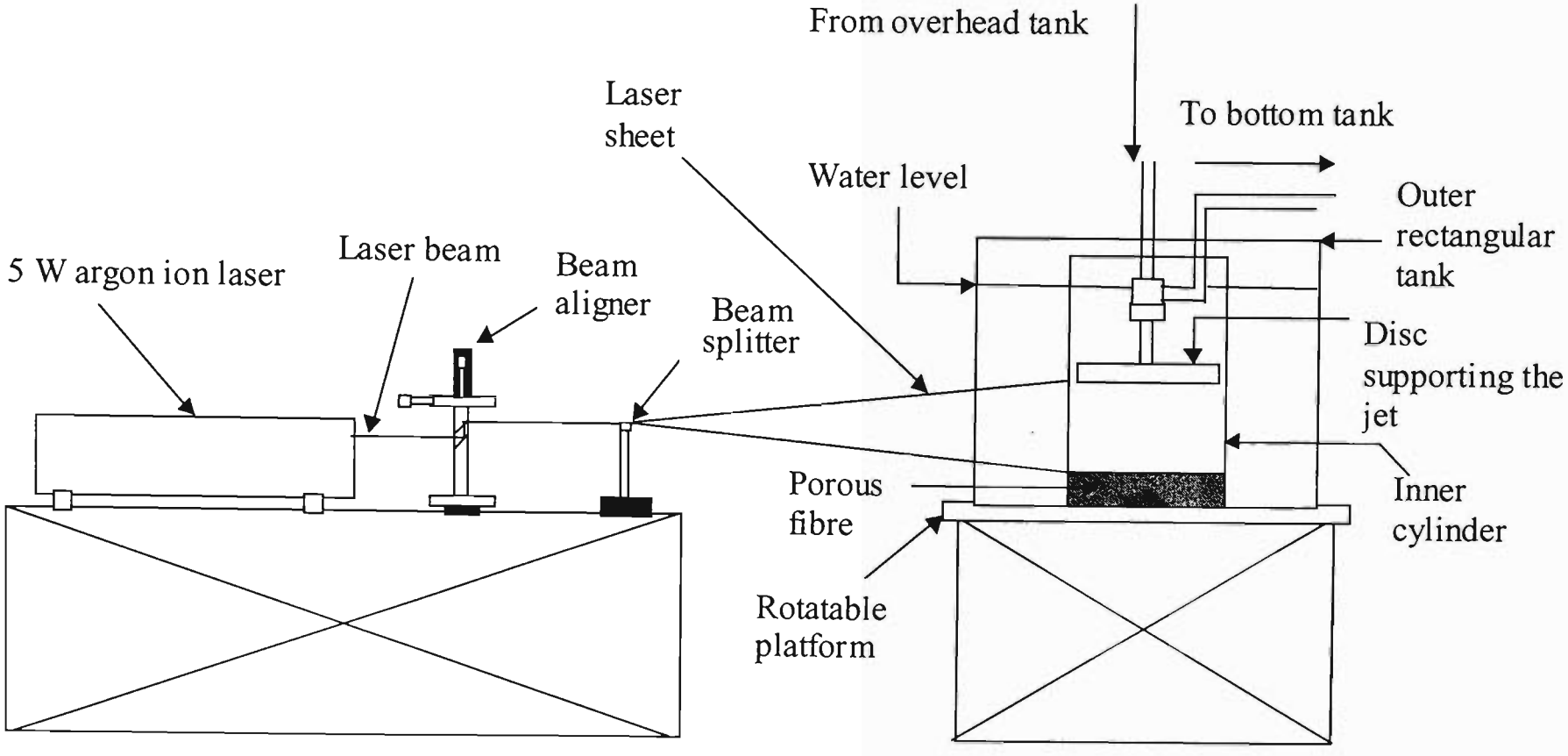

Figure 4.2: Schematic diagram of the experimental setup used for the impinging jet flow visualisations.

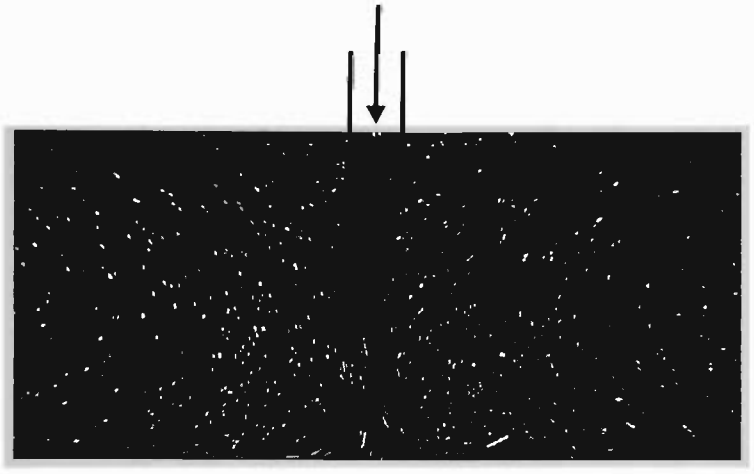

(a) Actual image taken with an exposure time of 10 msec for H=0.15 m, h_p=0.0 m, U_b=1.6 m/s

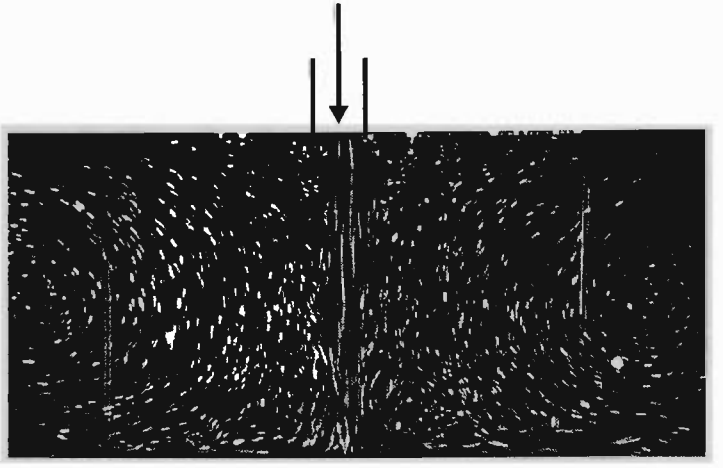

(b) Actual image taken with an exposure time of 20 msec for H=0.15 m, h_p=0.0 m, U_b=1.6 m/s

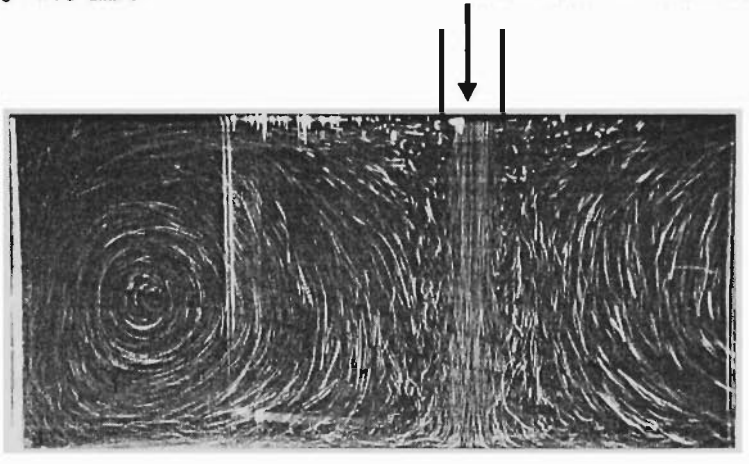

(c) Actual image taken with an exposure time of 200 msec for H=0.15 m, h_p=0.0 m, U_b=1.6 m/s

Figure 4.3: Preliminary flow visualisation results illustrating the central jet region and the effect of change in the exposure times.

4.3 Results and discussion

The visualisations were carried out with three different liquid heights namely H=0.15, 0.1 and 0.05 m and two different porous layer heights, h_p=0.1 and 0.05 m. Two different velocities of water exiting the jet, U_b=1 and 1.6 m/s, were used for each experiment. It was found that there is no apparent difference between the visualisations carried out for the two jet exit velocities. It was concluded that once the flow is in the turbulent regime, there is very little change in the flow characteristics with a change in the Reynolds number. Due to the similarity in the flow patterns for the two Reynolds numbers considered, visualisations are shown only for the higher Reynolds number.

In the next section, flow visualisation results are discussed in detail with reference to Figures 4.4 to 4.21. In these figures, the frames designated as (a) and (b) represent the actual and enhanced images, respectively. Using ***Lview Pro***, an image editing software, which has an option of edge enhancement, the bright bubble streak lines were enhanced. Using this mode, the streak lines can be visualised more clearly. Additional lines have been introduced in the enhanced images in order to put forth the author's impression of the flow visualisation. The dotted lines such as in Figures 4.10 (b) and 4.16(b) represent flow patterns that could not be clearly established through the flow visualisation. For visualisations with foam, such as in Figures 4.7 to 4.21, the shaded region below the fluid layer in the enhanced images represents the porous foam. For the purpose of flow visualisation, axi-symmetry was checked by studying one central plane of the cylinder. Since the two halves of the plane were visually identical, only the left half of the cylindrical tank is shown.

4.3.1 Flow visualisation without foam

In Figures 4.4 to 4.6, three different liquid heights are given without foam. With a liquid height, H, equal to 0.15 m in Figure 4.4, it can be seen that the entire half plane of the cylinder is filled with one large re-circulating cell. There is some evidence of the presence of small re-circulating cells close to the region where the fluid leaves the system, as well as the bottom left corner of the cylinder, although these were not clearly identifiable through the flow visualisations. These two small

cells were observed for all three liquid heights presented in Figures 4.4 to 4.6. As the fluid height is decreased to H=0.1 and 0.05 m, respectively, in Figures 4.5 and 4.6, the single re-circulating cell persists with the position of the centre of re-circulation almost at the vertical centre of the enclosure. However, the centre of the cell moves progressively away from the jet towards the wall of the cylinder as the liquid height decreases. The effect of decreasing liquid height on the horizontal position of the centre of re-circulation for cases without foam is seen in Figure 4.22. Thus, for cases without foam, a single re-circulating cell occupying the half plane dominates the flow pattern.

4.3.2 Flow visualisation with foam

The effect on flow patterns in the fluid layer with variations in the foam grade, the thickness (height) of the porous medium and the height of the overlying fluid layer are investigated in this section. Figures 4.7 through 4.21 represent flow visualisation carried out with foam. For comparison with the visualisations without foam, the same three fluid heights were utilised for all experiments with foam. Figures 4.7 to 4.9, 4.10 to 4.12 and 4.16 to 4.18, respectively, represent flow visualisations carried out with one layer of the G60, G30 and G10 foams (h_p=0.05 m) for varying fluid heights. The effect of changes in the foam grade is studied by comparing images with the same fluid height and foam thickness but different pores per inch gradation. Thus, a comparison is made among Figures 4.7, 4.10 and 4.16. On the other hand, the effect of clear fluid height is studied by comparing Figures 4.7, 4.8 and 4.9 which have the same foam grade and thickness but varying fluid heights. Figures 4.13 to 4.15 and 4.19 to 4.21, respectively, represent flow visualisations carried out with two layers of the G30 and G10 foams (h_p=0.1 m) for the three different fluid heights. These figures in combination with the figures for one layer of the foam have been used to study the effect of the porous layer height. The figures for the flow visualisations are provided at the end of this chapter.

4.3.2.1 The effect of porous layer and its permeability

The visualisations were carried out by using three different grades of foam, G10, G30 and G60, corresponding to 10, 30 and 60 pores per inch. As shown in

Table 4.2, the change in the foam grade is well represented by changes in the permeability. There is little change in the porosity or Forchheimer coefficient in foams in the range G10 to G100. Such an effect is typical for synthetic or metallic foams, which have porosity values close to unity. Thus, the following discussion is limited to the effect of changes in the permeability values of a porous medium. Although there is no information on the permeability of the G30 and G60 foams, they can be expected to have values in the range of the G45 foam given in Table 4.2 which is around 10^{-8} m^2. In this range of permeability, there is no significant change in the flow pattern in the fluid layer as can be seen from a comparison of Figures 4.7, 4.8 and 4.9 with Figures 4.10, 4.11 and 4.12, respectively. Minor differences, such as the enhancement of the small cell at the bottom edge close to the interface in going from a lower to a higher permeability value are discernible from a comparison between Figures 4.7 and 4.10. This can be attributed to the formation of a second minor circulating cell with an increase in the permeability value. A major change in the flow pattern can be observed in going from the G30 to the G10 foam. From Table 4.2, the G10 foam has a permeability that is at least one decade greater than that of the G60 and G30 foams. The G10 foam was also the only foam grade for which Seguin *et al.* (1998b) found a transition to the turbulent regime. From Figures 4.16, 4.17 and 4.18 for the G10 foam, it is evident that for all fluid heights, there is a significant change in the flow pattern from the cases without foam. It is clearly seen from these figures that with the G10 foam, the single circulating cell has been transformed into two cells, the one that is dominant is close to the jet with the second cell forming closer to the wall. The second cell seems to be well established for the two lower fluid heights with evidence of transition to a two-cell pattern for the highest fluid height.

It is interesting to note that for low permeability foams such as the G60 foam, there is little change in the flow pattern in the fluid layer from the cases without foam. This result indicates that although the fluid penetrates the foam, at low permeability values, its interaction with the fluid layer after exiting the foam is negligible. For such permeability values (less than 10^{-8}), the interface between the fluid layer and porous medium can be treated as a wall in numerical simulations for turbulent quantities such as the turbulence kinetic energy, k, and its rate of dissipation, ε. In

such systems, the fluid layer and the porous medium could be regarded to be operating in the turbulent and laminar regimes, respectively. These observations are made use of in the industrial case study presented in chapter seven.

4.3.2.2 The effect of height/thickness of the porous layer

Since the G60 and G30 foams do not show any significant differences in the flow pattern, the effect of porous layer thickness was studied only for the G30 and G10 foams. For the G30 foam, there is no significant change in the flow pattern in the fluid layer with an increase in the foam thickness, as can be seen from a comparison of Figures 4.10, 4.11 and 4.12 for h_p=0.05 m with Figures 4.13, 4.14 and 4.15 for h_p=0.1 m. However, a comparison between Figures 4.10 and 4.13 shows some evidence of a delay in the development of the minor cell close to the interface and at the bottom edge. The effect of the porous layer height is seen more clearly from the visualisations for the G10 foam. Figure 4.16 (for h_p=0.05 m) and 4.19 (for h_p=0.1 m) show a significant difference in the flow pattern. Thus, an increase in the porous layer thickness leads to a delay in the transition to a two-cell pattern in the fluid layer. One can consider that the fluid leaving the porous layer interacts with the fluid layer. This interaction results in a change in the flow pattern in the fluid layer. Thus, a possible explanation is that with a larger foam thickness, the fluid has to travel through more of the porous medium, thus reducing its speed. This reduction in fluid speed reduces the capability of the fluid leaving the porous foam to interact with the fluid layer.

4.3.2.3 The effect of clear fluid layer height

As already mentioned, a comparison between Figures 4.7 to 4.9, 4.10 to 4.12 and 4.16 to 4.18 is used to study the effect of changes in the clear fluid height. For the G60 and G30 foams, a significant change in the flow pattern in the fluid layer is observed only in Figures 4.9 and 4.12 (the lowest fluid height investigated) where the single cell pattern has changed to a two-cell pattern. For the higher fluid heights, Figures 4.7, 4.8, 4.10 and 4.11, the flow pattern is similar to the corresponding cases without foam. At higher liquid levels, the effect of jet penetration into the porous fibre is less because of the spreading of the jet before it impinges the foam. As seen from Figures 4.9 and 4.12, with a decrease in the height of the fluid layer, the jet

penetration into the porous layer is enhanced. This enhancement in turn allows the fluid exiting the foam to interact with the fluid layer thus altering the flow pattern in the fluid layer.

In the case of the G10 foam, one can see that the second cell is present for all three liquid heights. The presence of the second cell for the higher fluid heights can be attributed to the higher permeability of the G10 foam, which allows a better penetration into the foam. As mentioned earlier in Section 4.3.2.1, the two cells have different intensities, the dominant or primary cell is closer to the jet with a secondary cell formed closer to the wall of the cylinder. The position of the centre of circulation of the dominant cell can be useful for comparison with the LDV measurements and CFD simulations. For all three fluid heights (Figures 4.16, 4.17 and 4.18, h_p=0.05 m), the centre of the dominant circulation is approximately at one third the fluid height (H_c=1/3H) from the interface between the fluid and porous layers. However, as can be seen from Figure 4.23, the centre moves closer to the jet with a decrease in the fluid height. This decrease is in contrast with the cases without foam where the centre moves closer to the wall with a decrease in the fluid height.

The above discussion indicates that the effect of the presence of the porous foam is clearly seen only for the G10 foam. This is also the only foam grade for which Seguin *et al.* (1998 a and b) found a transition to turbulent flow. Since the present experiments have been designed primarily for validation of a numerical investigation into turbulent flow in the porous medium, only the experiments with G10 foam are repeated using the LDV measurements (the LDV measurements are presented in chapter six). The flow visualisation experiments are used for a visual comparison with the numerical simulations in the next chapter.

4.4 Conclusions

A detailed flow visualisation experiment was carried out in order to investigate the effect of a porous layer on flow patterns in an overlying turbulent flow. Synthetic reticulated foams of different grades were used as the porous medium. The turbulent flow was generated with the help of an impinging jet setup. Parameters such as the jet Reynolds number, the permeability of the porous medium, the

thickness of the porous medium and the height of the overlying fluid layer were varied in order to assess their effects on the flow pattern. For the jet Reynolds numbers considered in this study (Re=19,000 and 30,000), the flow pattern does not change significantly, indicating that the gross flow is in the fully turbulent regime. It was found that the permeability of the porous medium and the height of the fluid layer above the porous medium significantly affect the flow pattern, at least in the fluid region. The height of the porous medium affects the flow pattern to a smaller extent. In the case of the highest permeability foam investigated, the flow pattern changes significantly in the fluid layer for all three heights investigated. To verify this result, experiments continue with LDV measurements for the highest permeability foam investigated. The cases without foam are also investigated with LDV measurements for comparison. Numerical simulation for the same set of flow visualisation experiment is presented in the next chapter.

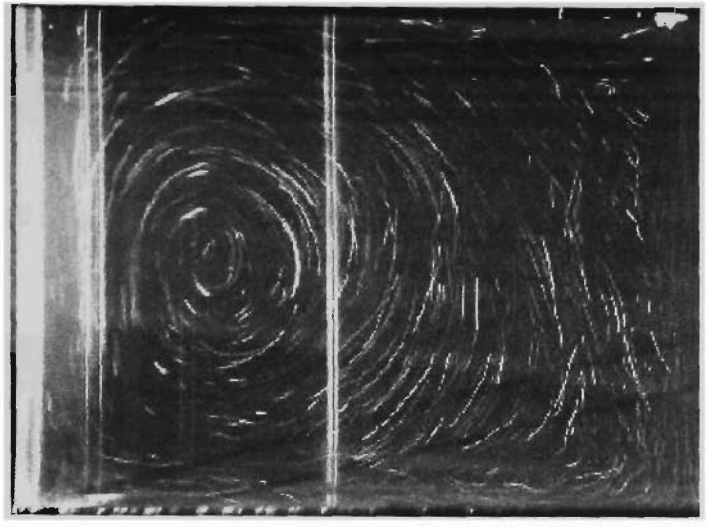

Figure 4.4: (a) Actual image.

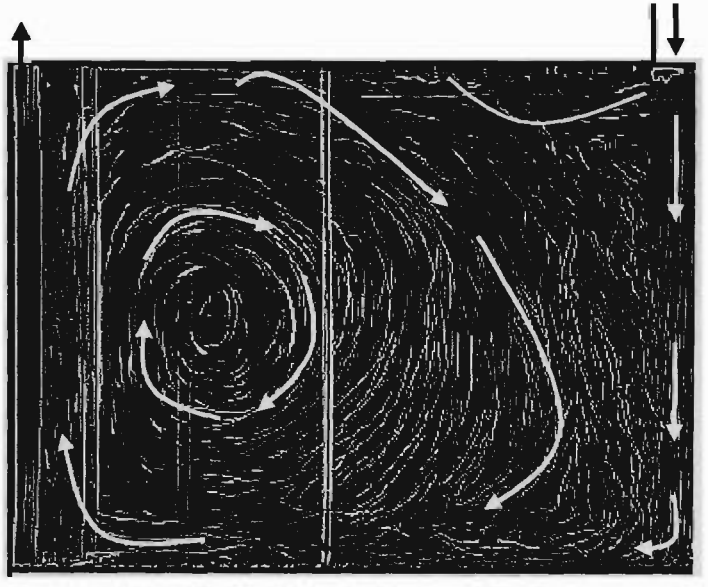

(b) Enhanced image. H=0.15 m, h_p=0 m, U_b=1.6 m/s.

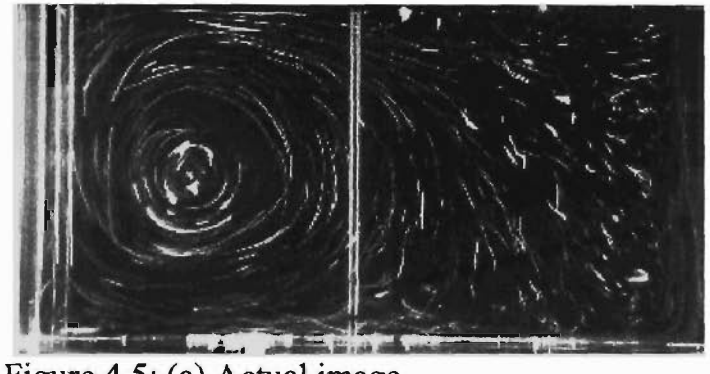

Figure 4.5: (a) Actual image.

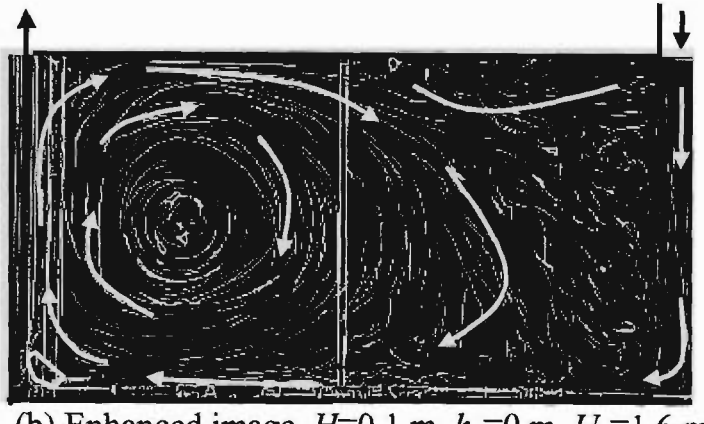

(b) Enhanced image. H=0.1 m, h_p=0 m, U_b=1.6 m/s.

Figure 4.6: (a) Actual image.

(b) Enhanced image. H=0.05 m, h_p=0 m, U_b=1.6 m/s.

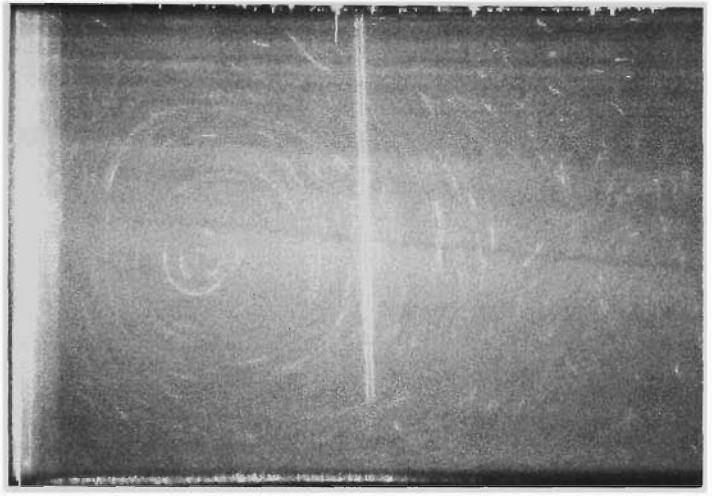

Figure 4.7: (a) Actual image.

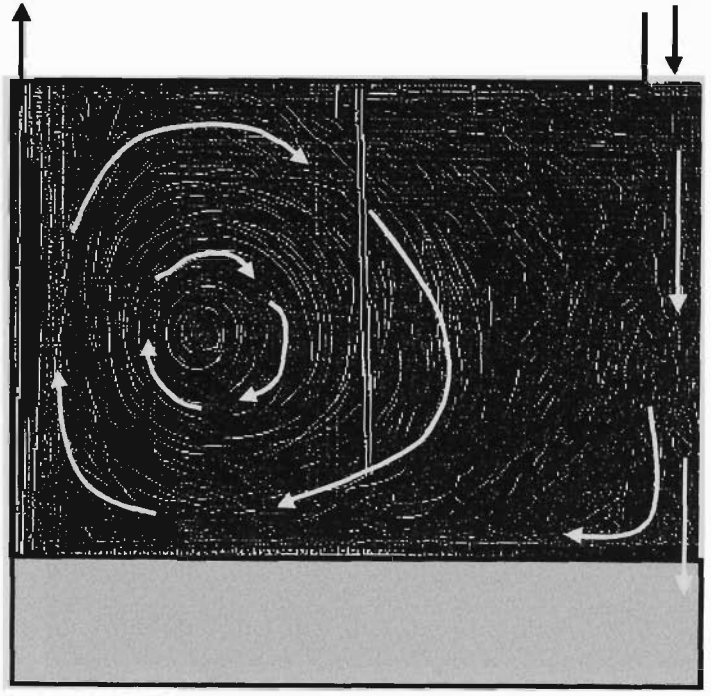

(b) Enhanced image. H=0.15 m, h_p=0.05 m, U_b=1.6 m/s, G60 foam.

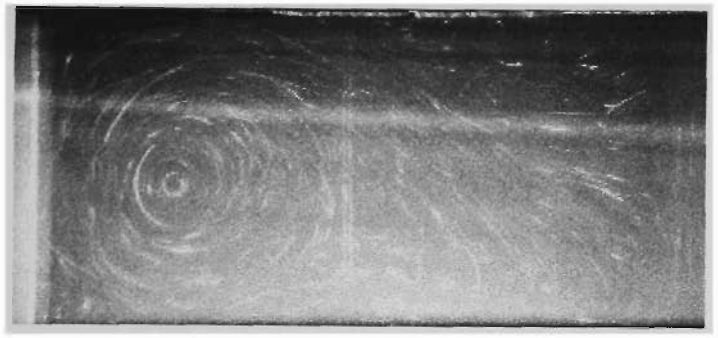

Figure 4.8: (a) Actual image.

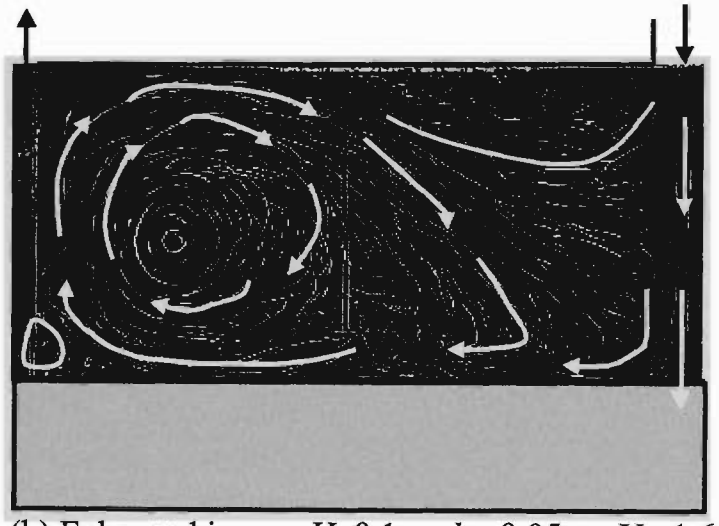

(b) Enhanced image. H=0.1 m, h_p=0.05 m, U_b=1.6 m/s, G60 foam.

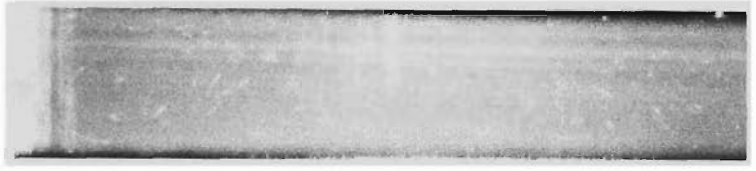

Figure 4.9: (a) Actual image.

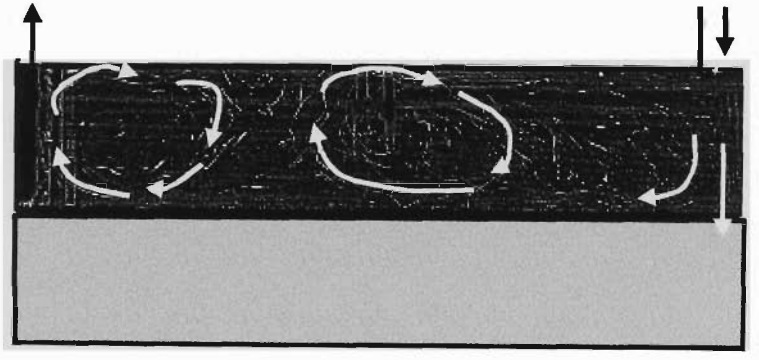

(b) Enhanced image. H=0.05 m, h_p=0.05 m, U_b=1.6 m/s, G60 foam.

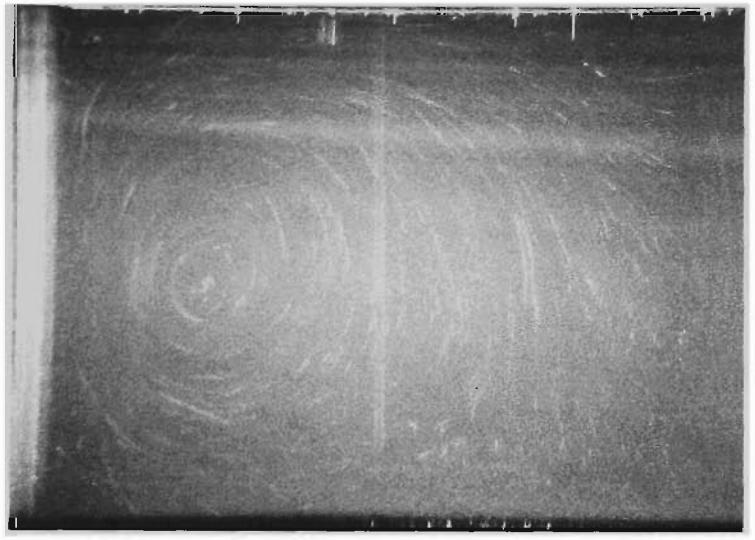

Figure 4.10: (a) Actual image.

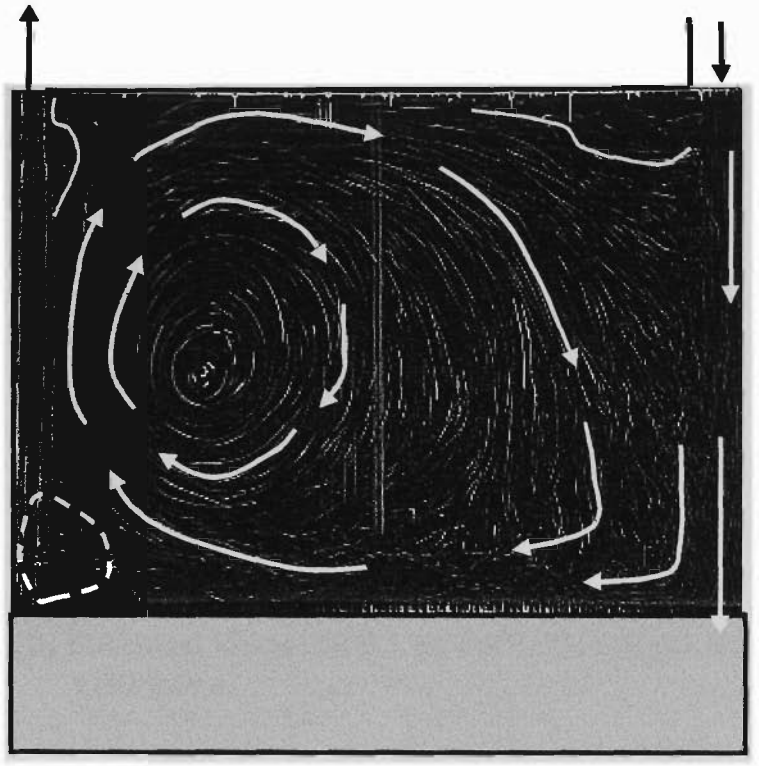

(b) Enhanced image, H=0.15 m, h_p=0.05 m, U_b=1.6 m/s, G30 foam.

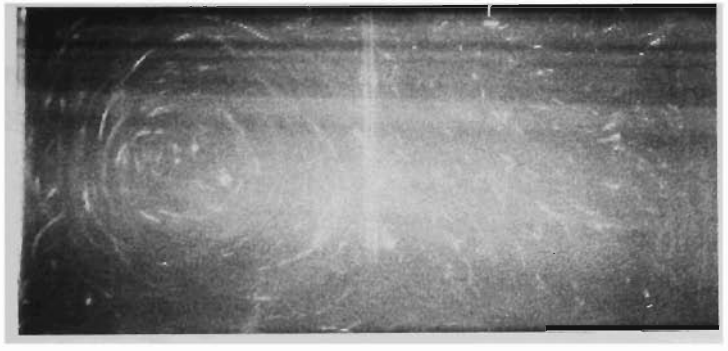

Figure 4.11: (a) Actual image.

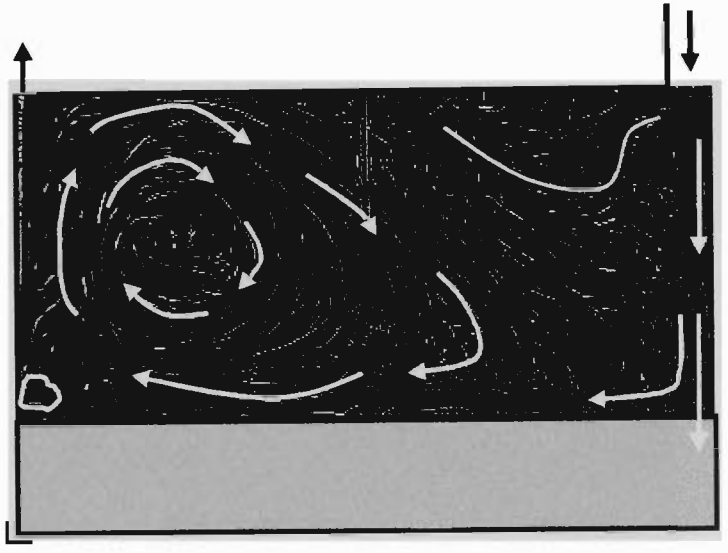

(b) Enhanced image. H=0.1 m, h_p=0.05 m, U_b=1.6 m/s, G30 foam.

Figure 4.12: (a) Actual image.

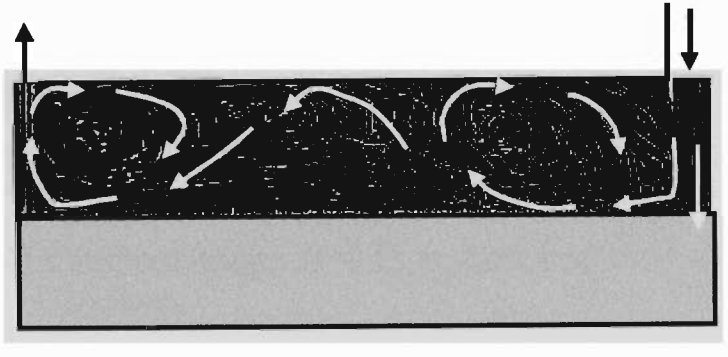

(b) Enhanced image. H=0.05 m, h_p=0.05 m, U_b=1.6 m/s, G30 foam

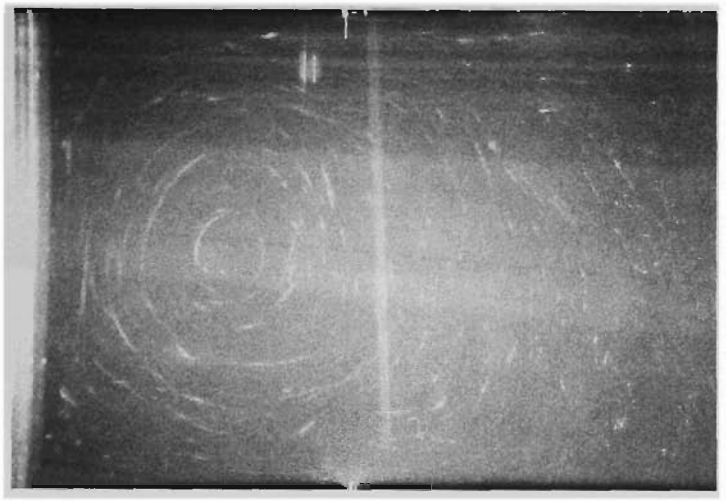

Figure 4.13: (a) Actual image.

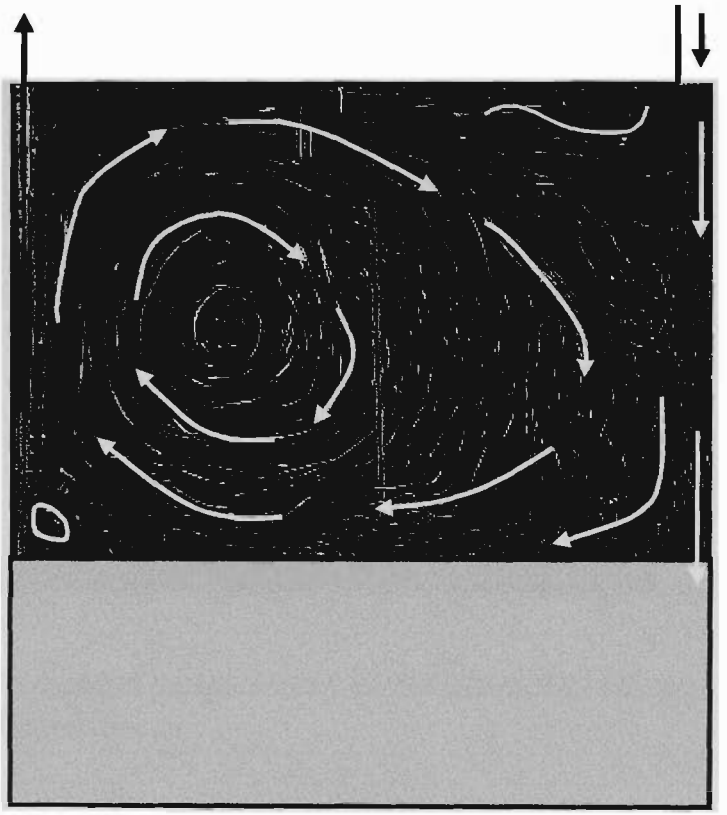

(b) Enhanced image. H=0.15 m, h_p=0.1 m, U_b=1.6 m/s, G30 foam.

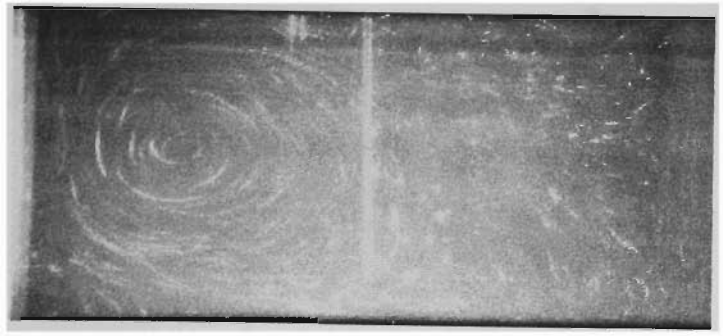

Figure 4.14: (a) Actual image.

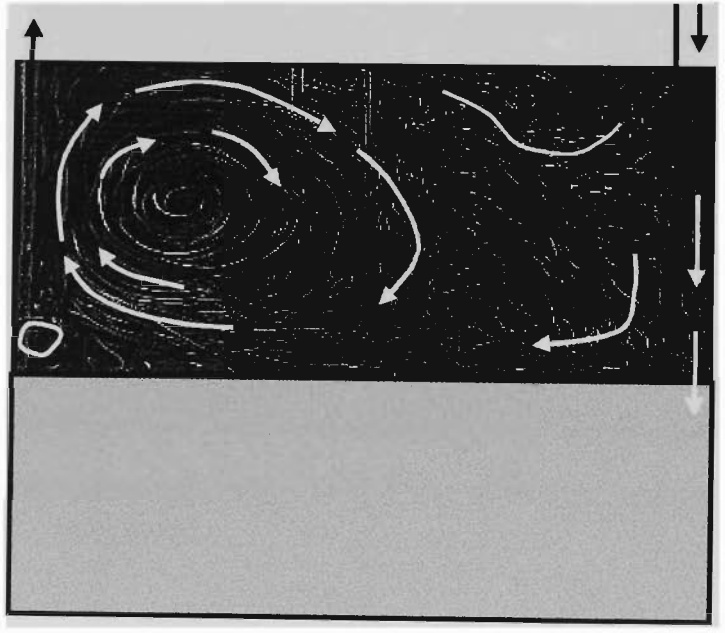

(b) Enhanced image. H=0.1 m, h_p=0.1 m, U_b=1.6 m/s, G30 foam.

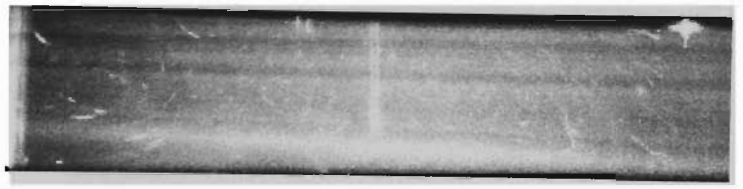

Figure 4.15: (a) Actual image.

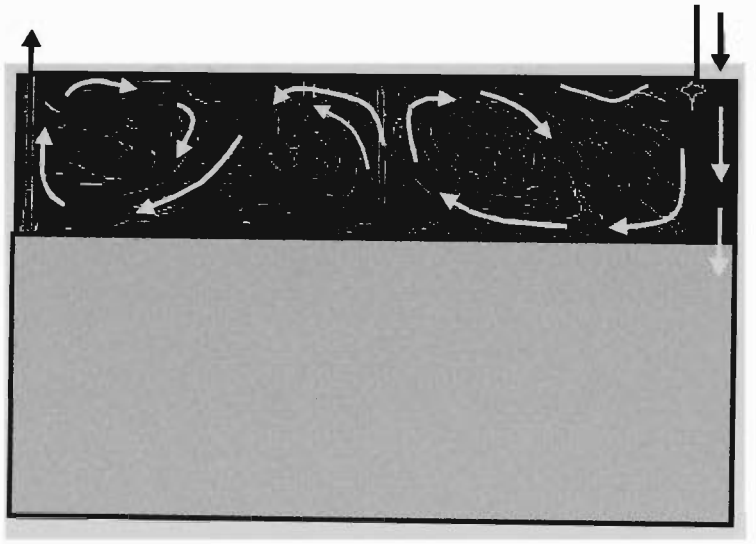

(b) Enhanced image. H=0.05 m, h_p=0.1 m, U_b=1.6 m/s, G30 foam.

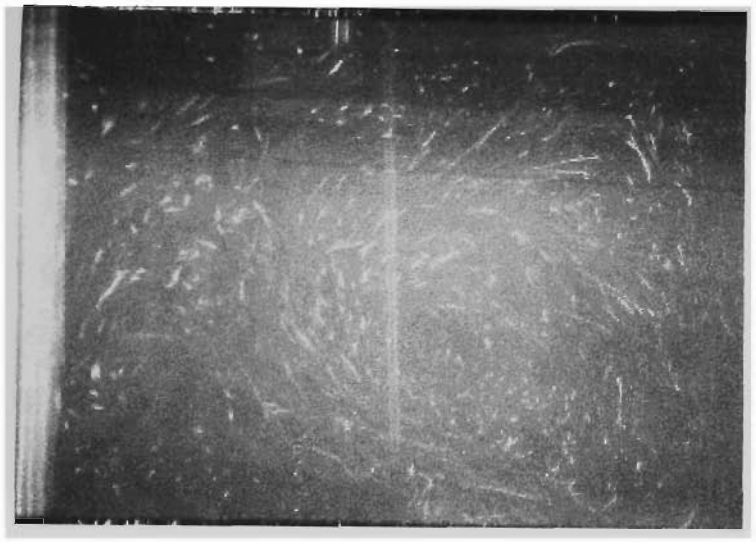

Figure 4.16: (a) Actual image.

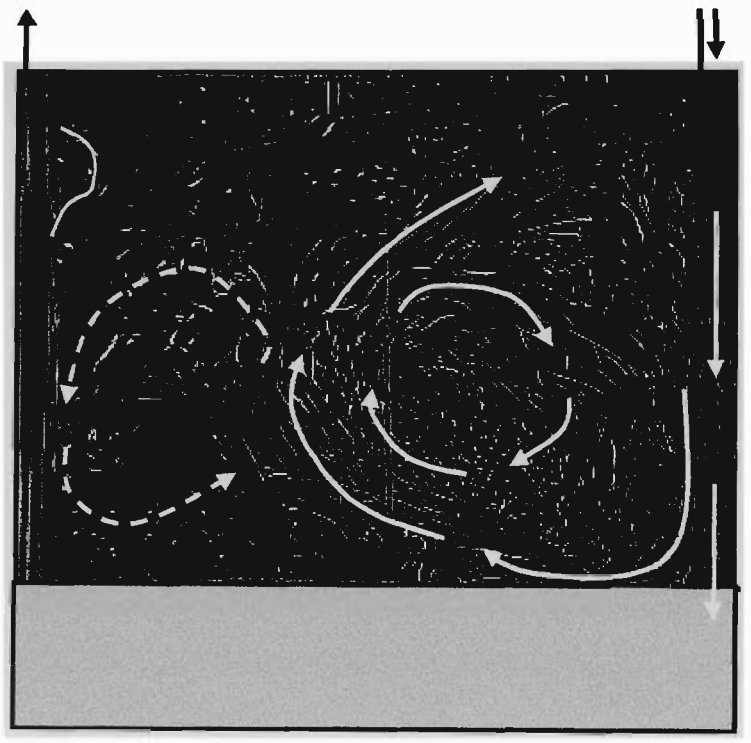

(b) Enhanced image. H=0.15 m, h_p=0.05 m, U_b=1.6 m/s, G10 foam.

Figure 4.17: (a) Actual image.

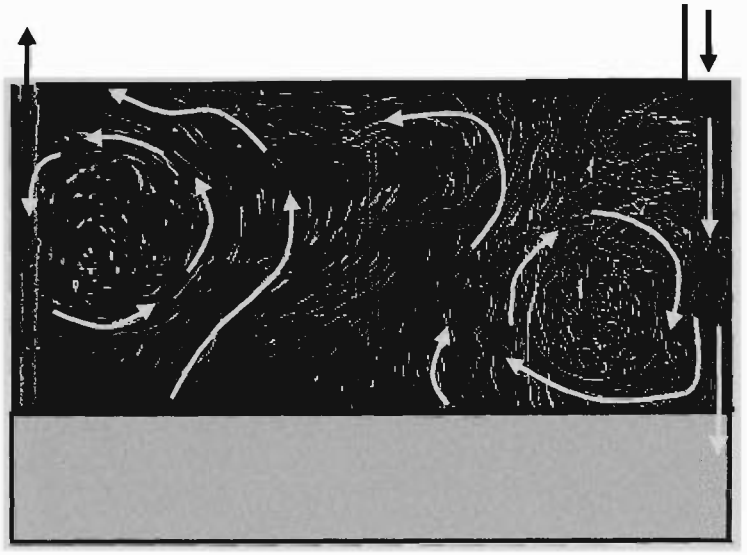

(b) Enhanced image. H=0.1 m, h_p=0.05 m, U_b=1.6 m/s, G10 foam.

Figure 4.18: (a) Actual image.

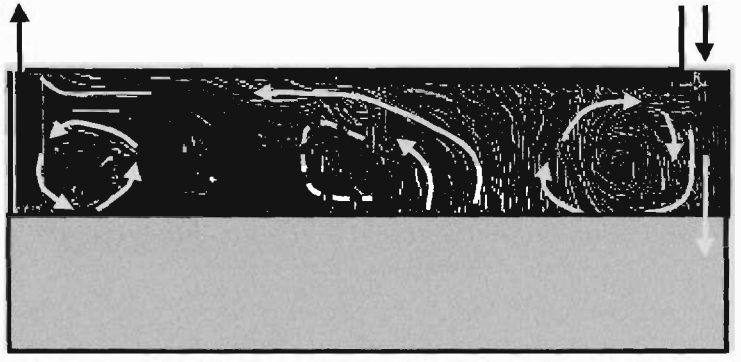

(b) Enhanced image. H=0.05 m, h_p=0.05 m, U_b=1.6 m/s, G10 foam.

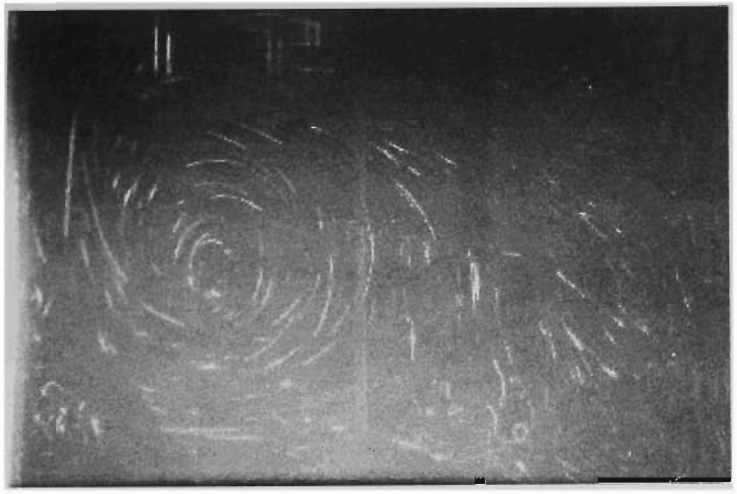

Figure 4.19: (a) Actual image.

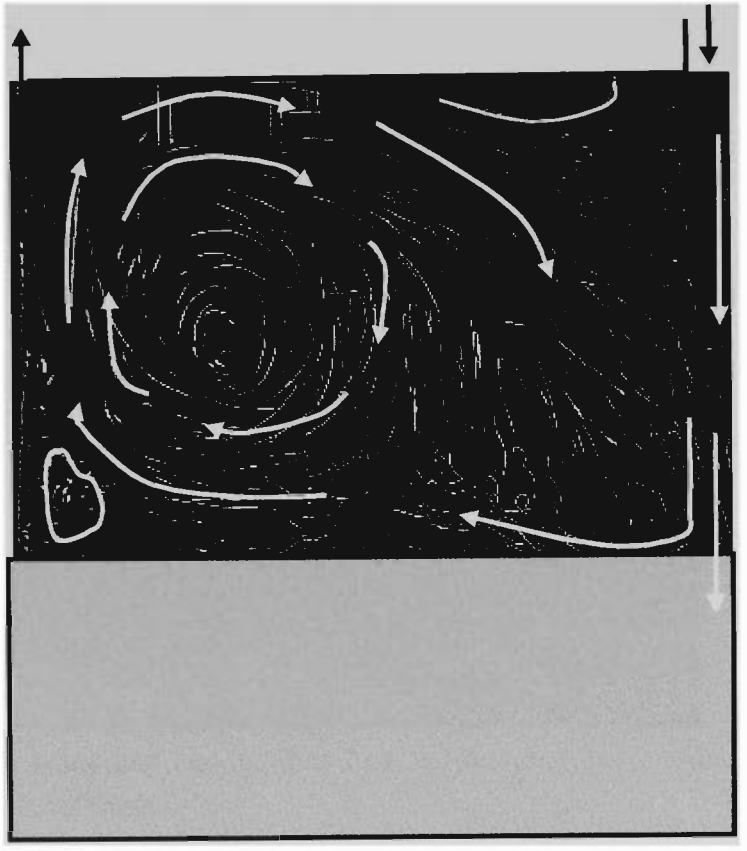

(b) Enhanced image. H= 0.15 m, h_p=0.1 m, U_b=1.6 m/s, G10 foam.

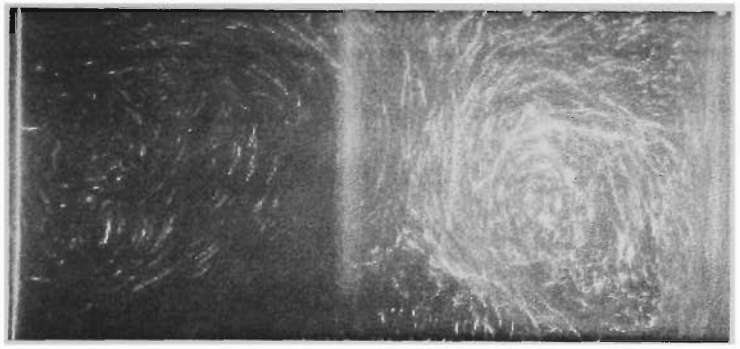

Figure 4.20: (a) Actual image.

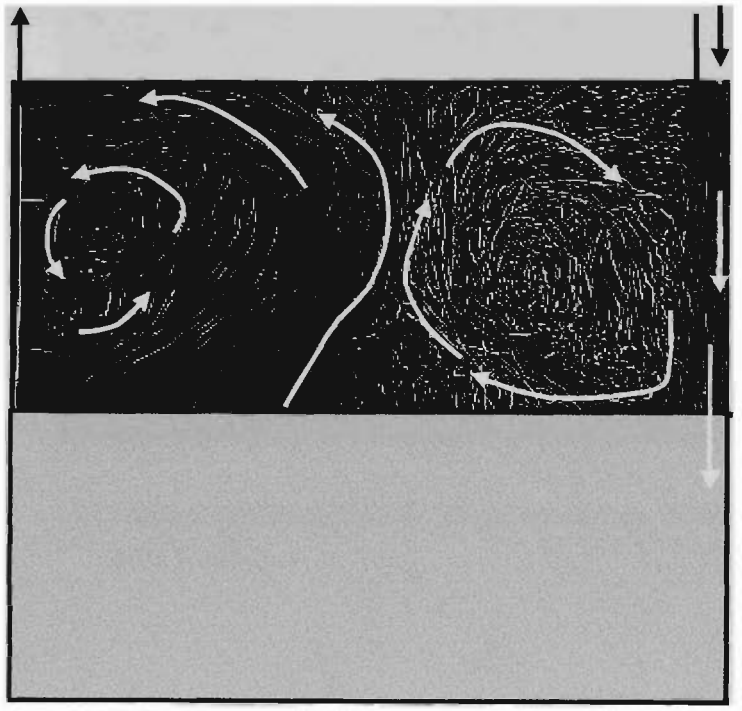

(b) Enhanced image. H=0.1 m, h_p=0.1 m, U_b=1.6 m/s, G10 foam.

Figure 4.21: (a) Actual image.

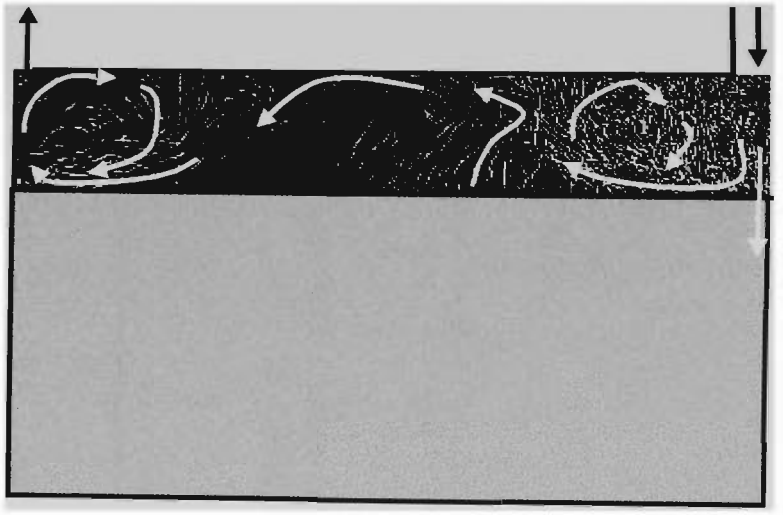

(b) Enhanced image. H=0.05 m, h_p=0.1 m, U_b=1.6 m/s, G10 foam.

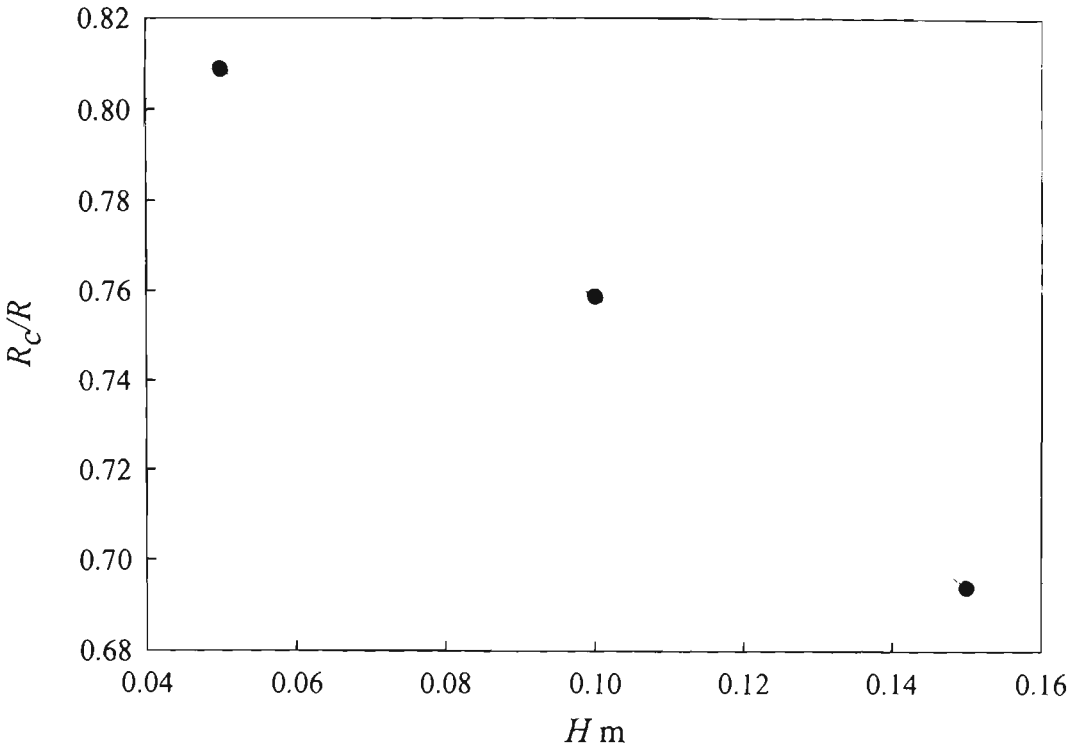

Figure 4.22: Change in the radial position of the centre of re-circulation as a function of the fluid height for cases without foam.

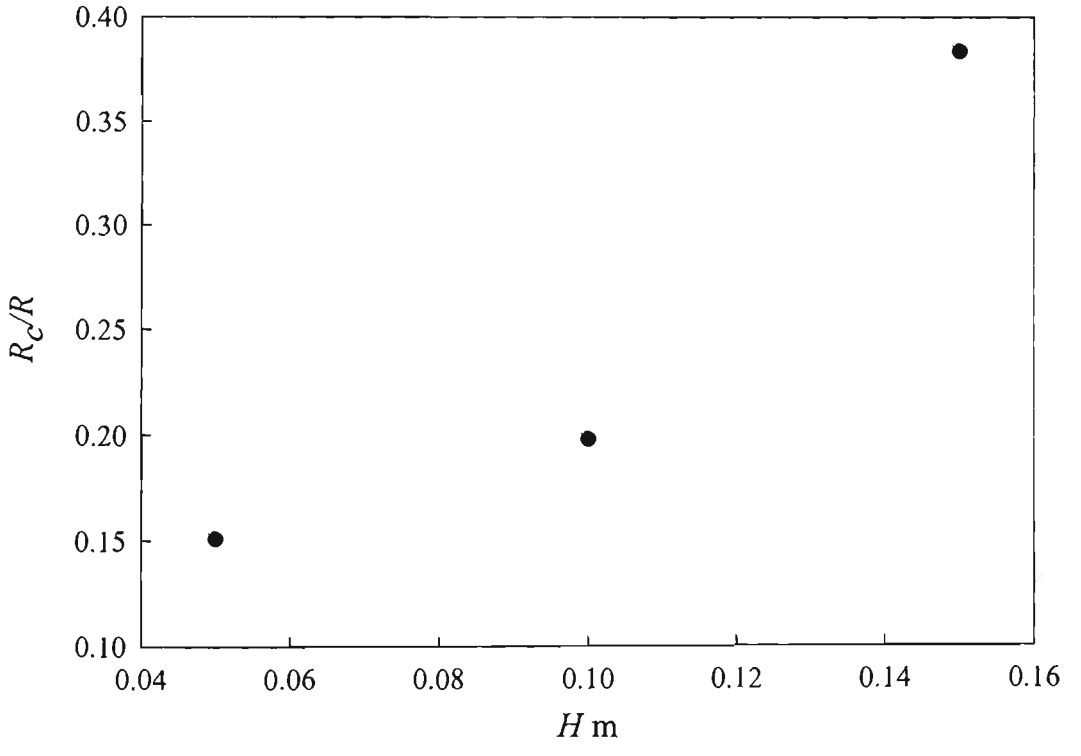

Figure 4.23: Change in the radial position of the centre of the dominant re-circulation as a function of the fluid height for G10 foam with h_p=0.05 m.

Chapter 5

Numerical simulations

5.1 Introduction

The numerical code that was validated against a benchmark natural convection problem in chapter three was written for two-dimensional problems formulated in cartesian co-ordinates. However, the experiments described in chapters four and six were carried out in a system that was essentially axi-symmetric. The code was therefore modified so that it concurs with this geometry. Additional terms were also included in the code to account for the presence of the porous foam used in the experiments. This chapter describes these modifications and the application of the modified code for simulating the experiments of chapter four.

Relatively few attempts have been made to model turbulent flow in porous media as noted in a recent paper by Netto and Guthrie (2000). One reason for the problem is the lack of experimental data that could be used to model such flows. However, a more serious drawback lies in formulating the governing equations, as discussed in Sections 2.2.3 and 2.4.2 of chapter two. The Brinkman Forchheimer extended Darcy (BFD) flow model (Equation (2.21)) has been used successfully by authors such as Beckermann *et al.* (1988), Chen and Chen (1992), Song and Viskanta (1994) and Chen *et al.* (1998) to simulate flow in porous media where inertial effects become important but turbulence effects can be neglected. As described in Section 2.2.3.3 of chapter two, the BFD model also allows the numerical treatment of a composite system, such as that of the present study, as a continuum.

The development of turbulence models of flow within a porous medium was necessitated due to their potential applications in the simulation of metal solidification (Prescott and Incropera, 1995), modelling of turbulent combustion in porous burners (Hall and Hiatt, 1996) and modelling of transport processes in stored produce (Chen and Li, 1998), among others. As mentioned in Section 2.4.2 of chapter two, the derivation of a turbulence model for flow in a porous medium within the framework of the k-ε model, involves the time averaging of the volume averaged BFD model giving rise to a macroscopic turbulence model for the porous medium. Additional

terms in the k and ε equations arise which are the product of the Darcy and Forchheimer terms in the momentum equations. Depending on the characteristics of the flow and the porous medium, these additional terms may either damp or aid turbulence. Such a model was formally derived by Antohe and Lage (1997), although authors such as Lee and Howell (1987) and Prescott and Incropera (1995) had previously used modified forms of the k-ε model to account for turbulence effects in the porous medium in their simulations. These modifications were carried out in an *ad hoc* manner, and little or no comparison with experimental results was presented for the simulations performed with these models. For example, Prescott and Incropera (1995) studied the effect of turbulence on solidification in a binary metal alloy (the solidified region is treated as a porous mushy zone for the simulations) only by comparing the predictions based on a low-Reynolds number k-ε turbulence model with those obtained with a laminar model. Chen *et al.* (1998) showed through simulations in the turbulent natural convection regime that turbulence in an adjacent fluid layer does not penetrate the porous medium for a relatively low permeability $\left(K = O\left(10^{-8}\right)\right)$. These authors used a simplified form of the turbulence model developed by Antohe and Lage (1997) for flow in the porous medium. Netto and Guthrie (2000) used a low-Reynolds number k-ε model and an *ad hoc* viscosity model where the molecular viscosity was boosted 100 times to represent turbulence in a model porous medium. Using a semi-analytical solution to validate the simulations, these authors demonstrated the superiority of the results obtained with the low-Reynolds number k-ε turbulence model. However, no comparisons with experimental results were provided.

The issue of turbulence modelling in a porous medium has been addressed in the present research by comparing the results obtained from simulations with flow visualisation and LDV measurements. As seen in the previous chapter, the experiments involved a two-layer system consisting of a turbulent fluid layer overlying a porous foam layer. The main problem in conducting experiments that are useful for validation of a macroscopic turbulence model for the porous medium is the difficulty in measurements or visualisations within the porous medium. In this work, the issue is addressed by observing the changes in the flow field of a turbulent fluid that is adjacent to porous media that have a range of permeabilities. The interaction

between the fluid and porous medium is enhanced by directing a jet of fluid into the medium. Consequently, the egress of the fluid from the porous medium could be closely observed.

5.2 Governing equations

Before formally presenting the governing equations for axi-symmetric flow, turbulence models of impinging round jet flows are briefly evaluated, because the experiments use an impinging round water jet for generating turbulence.

5.2.1 Evaluation of turbulence models for impinging jet studies

It is well established from studies on impinging round jets (Graham and Bremhorst, 1993; Craft *et al.*, 1993; Durbin, 1996 and Behnia *et al.*, 1999) that the k-ε turbulence model predicts higher than expected levels of turbulence in the stagnation region. Craft *et al.* (1993) have argued that this stagnation point anomaly can be attributed to the eddy-viscosity formulation, Equation (2.26), which is used to represent normal stresses, for example:

$$\overline{v'^2} = \frac{2}{3}k - 2\nu_t \frac{\partial \bar{v}}{\partial y} \tag{5.1}$$

In the irrotational region close to the stagnation point, the above relationship leads to a turbulence kinetic energy generation rate, $P_k = -\overline{u_i' u_j'} \frac{\partial \bar{u}_i}{\partial x_j}$, of:

$$P_k = 3\nu_t \left(\frac{\partial \bar{v}}{\partial y} \right)^2 \tag{5.2}$$

With an increase in the turbulence energy, the value of ν_t increases, which in turn leads to an increase in k.

Several modifications have been suggested to overcome this problem. Changing the value of the constant $c_{\varepsilon 1}$ (Equation (2.35)) from 1.44 to 1.6, (Pope, 1978 and Graham and Bremhorst, 1993), gives rise to an increase in the rate of dissipation of turbulence kinetic energy, ε, thus reducing k. Authors such as Menter (1992) addressed the problem from a more fundamental point of view by using a k-ω

model instead of a k-ε model, which prevents an anomalous growth in k. However, as pointed out by Durbin (1996), these modifications cause an anomalous growth of turbulence kinetic energy in rotating and swirling flows.

The Reynolds stress model used by Craft *et al.* (1993) and the elliptic relaxation turbulence model (v^2-f model) used by Behnia *et al.* (1999) seem to be the only two models which have been validated for impinging round jet flows with heat transfer. However, in the present study, the k-ε model is retained for computations for the following reasons:

1) Since the system being considered is isothermal, heat transfer predictions that greatly depend on the turbulence model used is not an issue.

2) The stagnation region is not of particular interest in the present study. It has been found from preliminary computations that the mean flow patterns are well represented by the k-ε model.

3) For the porous medium, a modified form of the k-ε model has been used. Thus, when simulating systems that contain porous foam, it is suitable to use the k-ε turbulence model in the fluid layer in conjunction with the modified k-ε turbulence model for foam.

Three different versions of the k-ε turbulence model were investigated for the present simulations. These are discussed briefly below.

As described in Section 2.4.1.1.1 of chapter two, the standard k-ε turbulence model uses a wall function to represent the velocity profile close to the wall (Equation (2.38)). The wall function was developed from experiments in a fully developed pipe flow with favourable or negative pressure gradient. Since many flows are not as simple as a pipe flow, low Reynolds number models (Section 2.4.1.2 of chapter two), which solve for velocities and turbulent quantities right up to the wall were developed. In order to account for the no-slip wall boundary condition, the low Reynolds number models incorporated either a wall damping effect or a direct effect

of molecular viscosity, or both, on the empirical constants and functions in the turbulence transport equations.

Since the present experiment has a flow that is significantly more complicated than pipe flow, the wall function approach is not suitable. Therefore, the standard k-ε turbulence model was used without wall functions for the mean velocities, similar to the computations involving turbulent natural convection (Section 3.4.2 in chapter three). With this model, the following values were assigned to k and ε at the first inner grid point. The expressions in Equation (5.3) are obtained from the inertial law (details can be found in Section 2.4.1.1.1 of chapter two):

$$k = \frac{\left(v^*\right)^2}{\sqrt{c_\mu}}, \varepsilon = \frac{\left(v^*\right)^3}{\kappa x} \tag{5.3}$$

The above form of the k-ε turbulence model has been used in Henkes (1990), Lankhorst (1991) and the present study for studying natural convection flows, because the usual wall functions that apply in the case of simple forced convection flows do not apply to natural convection flows. This approach can be considered to be a hybrid of the standard k-ε model (due to the use of wall functions for k and ε) and the low Reynolds number models (due to the practice of solving for mean velocities right up to the wall).

Initial computations using this approach were promising and led to convergent solutions with relative ease. The use of wall functions for k and ε at the first inner grid point is akin to assigning a guess of these quantities. Thus, it was found that an explicit specification for k and ε at the jet exit is unnecessary for this case. However, on grid refinement, the value of ε showed an unbounded increase although the solution converged in all cases. This approach was therefore deemed to be unsuitable for further computations.

The low Reynolds number turbulence model originally proposed by Jones and Launder (1972) (the low-Re turbulence model with code JL in Table 2.1) was used for further computations. Instead of solving for the rate of energy dissipation ε, it was proposed by Jones and Launder (1972) to solve for the pseudo energy dissipation, $\tilde{\varepsilon}$, where

$$\varepsilon = \tilde{\varepsilon} + D \tag{5.4}$$

with $D = 2\nu\left(\frac{\partial\sqrt{k}}{\partial x}\right)^2$

This specification leads to the boundary condition $\tilde{\varepsilon}$ =0 at the wall. With k=0 at the wall, the boundary conditions can be specified conveniently. However, in the present computations, these boundary conditions gave rise to divergence. As shown by Patel *et al.* (1985), the value of $\tilde{\varepsilon}$ varies rapidly near the wall as compared to k and the mean velocities. This rapid growth in $\tilde{\varepsilon}$ can be resolved only if one has sufficiently fine grids close to the wall. Therefore, it was decided to use a boundary condition of $\frac{\partial\varepsilon}{\partial x} = 0$ (where x is normal to the wall), for the rate of energy dissipation as suggested by Patel *et al.* (1985) in connection with the original Jones and Launder (1972) model. The wall value of ε would then be a result of the computations. The additional term in the turbulence kinetic energy equation, D (Equation (2.34)), and in the energy dissipation rate equation, E (Equation (2.35)), would then vanish. Prescott and Incropera (1995) have employed a similar approach in their computations.

5.2.2 Equations for axi-symmetric turbulent flow with modifications for flow through porous media.

Having established the form of the k-ε turbulence model to be used for the impinging jet calculations, the governing equations for the axi-symmetric system in cylindrical co-ordinates are presented with modifications to account for flow through porous media. The macroscopic turbulence model of Antohe and Lage (1997) has been used as the basis for all turbulent flow calculations in the porous medium. Therefore, this model is introduced next in its entirety for an axi-symmetric, incompressible and isothermal system for steady state calculations.

1. Equation of continuity:

$$\frac{1}{r}\frac{\partial(ru_r)}{\partial r} + \frac{\partial u_z}{\partial z} = 0 \tag{5.5}$$

Note that the x and y co-ordinates used for the two-dimensional cartesian equations in chapter two are converted to the radial (r) and axial (z) co-ordinates for axi-symmetric calculations. The notation for the corresponding mean velocities have been changed to u_r and u_z instead of the u and v velocities used earlier.

2. Momentum equation in the radial direction:

$$\frac{\rho u_r}{\phi}\frac{\partial u_r}{\partial r}+\frac{\rho u_z}{\phi}\frac{\partial u_r}{\partial z}=-\frac{\partial p}{\partial r}+\frac{\partial}{\partial r}\left[(\mu J+\mu_t)\left(\frac{1}{r}\frac{\partial}{\partial r}(ru_r)\right)\right]+\frac{\partial}{\partial z}\left[(\mu J+\mu_t)\frac{\partial u_r}{\partial z}\right]-\underbrace{\frac{\mu\phi u_r}{K}}_{\text{Darcy term}}-\underbrace{\rho\frac{c_F\phi u_r Q}{\sqrt{K}}}_{\text{Forchheimer term}} \tag{5.6}$$

where $Q=\sqrt{u_r^2+u_z^2}$.

Momentum equation in the axial direction:

$$\frac{\rho u_r}{\phi}\frac{\partial u_z}{\partial r}+\frac{\rho u_z}{\phi}\frac{\partial u_z}{\partial z}=-\frac{\partial p}{\partial z}+\frac{1}{r}\frac{\partial}{\partial r}\left[(\mu J+\mu_t)\left(r\frac{\partial u_z}{\partial r}\right)\right]+\frac{\partial}{\partial z}\left[(\mu J+\mu_t)\left(\frac{\partial u_z}{\partial z}\right)\right]-\underbrace{\frac{\mu\phi u_z}{K}}_{\text{Darcy term}}-\underbrace{\rho\frac{c_F\phi u_z Q}{\sqrt{K}}}_{\text{Forchheimer term}} \tag{5.7}$$

As mentioned in Section 2.2.3.3 of chapter two, the viscosity associated with the Brinkman term, $\mu_{eff}=\mu J$, for the porous medium could have a value different from the fluid viscosity. In the simulations presented in this thesis, the parameter J is assigned a value of one so that the effective viscosity has a value equal to the fluid viscosity. As discussed in Section 2.2.3.3 of chapter two, such an assumption has some justification due to the analysis of Neale and Nader (1974). For the fluid layer, the porosity, ϕ, is assigned a value of one in the momentum, k and ε equations. The Darcy and Forchheimer terms in the momentum equations vanish for the fluid layer because the permeability, K, tends to infinity.

Note that the variables occurring in the momentum equations above have been volume averaged first to obtain the BFD model (Equation (2.21)) and then time averaged to extract information about the turbulent quantities. The Forchheimer term in the momentum equations was expanded by Antohe and Lage (1997) in their Equation (4) before the time averaging process as:

$$\begin{aligned}\left[u_j u_j\right]^{1/2} u_i &= \left[\left(\overline{u_j}+u_j'\right)\left(\overline{u_j}+u_j'\right)\right]^{1/2}\left(\overline{u_i}+u_i'\right) \\ &= Q\overline{u_i}+Qu_i'+\frac{\overline{u_j u_i}}{Q}u_j'\end{aligned} \tag{5.8}$$

where $Q=\left(\overline{u_k u_k}\right)^{1/2}$ in tensor notation.

These authors retained only the linear terms in the expansion and derived the averaged momentum and turbulence transport equations. Recently Getachew *et al.* (2000) used second-order terms in the expansion to arrive at extra terms in the momentum and turbulence transport equations. Similar to the study of Antohe and Lage, Getachew *et al.* did not provide any numerical or experimental evidence to support their model. Furthermore, the addition of further higher order terms in the k and ε equations resulting from Getachew *et al.*'s expansion lead to terms that is extremely difficult to implement numerically. Getachew *et al.*'s model is not employed for the present computations.

Turbulence kinetic energy equation:

$$\begin{aligned}\frac{\rho u_r}{\phi}\frac{\partial k}{\partial r}+\frac{\rho u_z}{\phi}\frac{\partial k}{\partial z} &= \frac{\partial}{\partial r}\left[\left(\mu J+\frac{\mu_t}{\sigma_k}\right)\frac{\partial k}{\partial r}\right]+\frac{\partial}{\partial z}\left[\left(\mu J+\frac{\mu_t}{\sigma_k}\right)\frac{\partial k}{\partial z}\right]+P_k-\rho J\varepsilon+\rho D \\ &\quad \underbrace{-\ 2\phi\frac{\mu}{K}k}_{\text{Darcy modification (DM)}} \\ &\quad \underbrace{-\ \frac{8}{3}\phi\frac{\rho c_F}{\sqrt{K}}(2Q)k}_{\text{Forchheimer modification A (FMA)}} \\ &\quad \underbrace{+2\phi\frac{c_F}{\sqrt{K}}\mu_t\left(\frac{2}{Q}\right)\left[u_r u_z\frac{\partial u_z}{\partial r}+u_z^2\frac{\partial u_z}{\partial z}+u_r^2\frac{\partial u_r}{\partial r}+u_z u_r\frac{\partial u_r}{\partial z}\right]}_{\text{Forchheimer modification B (FMB)}}\end{aligned} \tag{5.9}$$

The above equation is the same as Equation (32) in Antohe and Lage (1997) written for axi-symmetric systems in cylindrical co-ordinates.

Equation for the rate of energy dissipation:

$$\frac{\rho u_r}{\phi}\frac{\partial \varepsilon}{\partial r}+\frac{\rho u_z}{\phi}\frac{\partial \varepsilon}{\partial z}=\frac{\partial}{\partial r}\left[\left(\mu J+\frac{\mu_t}{\sigma_\varepsilon}\right)\frac{\partial \varepsilon}{\partial r}\right]+\frac{\partial}{\partial z}\left[\left(\mu J+\frac{\mu_t}{\sigma_\varepsilon}\right)\frac{\partial \varepsilon}{\partial z}\right]$$

$$+\left(c_{\varepsilon 1}f_1 P_k-\rho J c_{\varepsilon 2}f_2\varepsilon\right)\frac{\varepsilon}{k}+\rho E$$

$$-\underbrace{2\phi\frac{2\mu}{K}\varepsilon}_{\text{Darcy modification (DM)}}$$

$$\underbrace{-2\phi\frac{c_F}{\sqrt{K}}\left\{\frac{4}{3}(2Q)\rho\varepsilon+\frac{5\mu}{6}\left[2\left(\frac{\partial k}{\partial r}\frac{\partial Q}{\partial r}+\frac{\partial k}{\partial z}\frac{\partial Q}{\partial z}\right)\right]\right\}}_{\text{Forchheimer modification A (FMA)}}$$

$$\underbrace{+2\phi\frac{c_F}{\sqrt{K}}\left\{4\mu\nu_t\left[\begin{array}{l}\frac{\partial}{\partial r}\left(\frac{u_r^2}{Q}\left(\frac{\partial^2 u_r}{\partial r^2}\right)+\frac{u_r u_z}{Q}\left(\frac{\partial^2 u_r}{\partial r\partial z}+\frac{\partial^2 u_z}{\partial r^2}\right)+\frac{u_z^2}{Q}\left(\frac{\partial^2 u_z}{\partial r\partial z}\right)\right)+\\ \frac{\partial}{\partial z}\left(\frac{u_r^2}{Q}\left(\frac{\partial^2 u_r}{\partial r\partial z}\right)+\frac{u_r u_z}{Q}\left(\frac{\partial^2 u_r}{\partial z^2}+\frac{\partial^2 u_z}{\partial r\partial z}\right)+\frac{u_z^2}{Q}\left(\frac{\partial^2 u_z}{\partial z^2}\right)\right)\end{array}\right]\right\}}_{\text{Forchheimer modification B (FMB)...}}$$

$$\underbrace{+2\phi\frac{c_F}{\sqrt{K}}\left\{\frac{4}{Q}\frac{1}{2}\mu_t\nu_t\cdot\left[\begin{array}{l}u_r^2\left(\frac{\partial^3 u_r}{\partial r^3}+\frac{\partial^3 u_r}{\partial r\partial z^2}\right)+\\ u_r u_z\left(\frac{\partial^3 u_r}{\partial z^3}+\frac{\partial^3 u_r}{\partial r^2\partial z}+\frac{\partial^3 u_z}{\partial r\partial z^2}+\frac{\partial^3 u_z}{\partial r^3}\right)+\\ u_z^2\left(\frac{\partial^3 u_z}{\partial z^3}+\frac{\partial^3 u_z}{\partial r^2\partial z}\right)\end{array}\right]\right\}}_{\text{Forchheimer modification B (FMB) continued}} \qquad (5.10)$$

where

$$P_k=\mu_t\left[2\left(\frac{\partial u_r}{\partial r}\right)^2+2\left(\frac{\partial u_z}{\partial z}\right)^2+\left(\frac{\partial u_r}{\partial z}+\frac{\partial u_z}{\partial r}\right)^2+\left(\frac{u_r}{r}\right)^2\right] \qquad (5.11)$$

Note that $\left(\frac{u_r}{r}\right)^2$ in the production term, P_k, arises due to the co-ordinate transformation from two-dimensional plane to axi-symmetric cylindrical co-ordinates.

$$\mu_t=\rho c_\mu f_\mu\frac{k^2}{\varepsilon} \qquad (5.12)$$

and $$\nu_{t^*} = c_{\mu^*} \frac{k^2}{\varepsilon} \tag{5.13}$$

The above equation is the same as Equation (33) in Antohe and Lage (1997) written for axi-symmetric systems in cylindrical co-ordinates. The new constant c_{μ^*} is assumed to possess a value equal to c_μ in the present simulations as suggested by Lage (1998). The terms DM, FMA and FMB occurring in the k and ε equations vanish for the fluid layer because the permeability, K, tends to infinity for the fluid layer. For simulations without foam, the extra terms in the momentum and turbulence transport equations occurring due to the porous medium are dropped and the porosity, ϕ, is set to unity.

From Equations (5.9) and (5.10), it can be seen that the DM term contributes only towards damping turbulence. The Forchheimer modification terms could, however, theoretically damp or aid turbulence depending on the sign of the velocity components and their derivatives. As mentioned earlier, the terms in the k and ε equations (especially the FMB terms) are inconvenient to implement in a numerical code even for the simple axi-symmetric geometry of the present problem.

As discussed in Section 5.2.1, a modified form of the low Reynolds number k-ε model of Jones and Launder (1972) is used for the simulations with the following constants and parameters:

c_μ=0.09, $c_{\varepsilon 1}$=1.44, $c_{\varepsilon 2}$=1.92, σ_k=1.0, σ_ε=1.3

$$f_\mu = exp\left(\frac{-2.5}{1+Re_t/50}\right), f_1=1.0,\ f_2 = 1-0.3exp(-Re_t^2),$$

$D=0,\ E=0$,

where, $$Re_t = \frac{k^2}{\nu\varepsilon}. \tag{5.14}$$

5.2.3 Boundary and interface conditions

The following wall and symmetry boundary conditions were applied for simulations without foam,

$$
\left.\begin{array}{ll}
u_r = u_z = 0 & \\
k = 0, \dfrac{\partial \varepsilon}{\partial x} = 0 & \text{at } r = R \text{ for } 0 \le z \le H \\
 & \text{at } z = 0 \text{ for } 0 \le r \le R \\
 & \text{and at } z = H \text{ for } 0 \le r \le R - w
\end{array}\right\} \text{wall}
$$

$$
\left.\begin{array}{ll}
\dfrac{\partial u_r}{\partial z} = \dfrac{\partial u_z}{\partial z} = 0 & \text{at } z = H \text{ for } R - w \le r \le R \\
\dfrac{\partial k}{\partial z} = \dfrac{\partial \varepsilon}{\partial z} = 0 & \text{at } z = H \text{ for } R - w \le r \le R
\end{array}\right\} \text{outflow} \qquad (5.15)
$$

$$
\left.\begin{array}{ll}
\dfrac{\partial u_r}{\partial r} = \dfrac{\partial u_z}{\partial r} = 0 & \text{at } r = 0 \text{ for } 0 \le z \le H \\
\dfrac{\partial k}{\partial r} = \dfrac{\partial \varepsilon}{\partial r} = 0 & \text{at } r = 0 \text{ for } 0 \le z \le H
\end{array}\right\} \text{symmetry}
$$

where R= radius of the cylinder=0.195 m, w is the width of the clearance (Figure 4.1), and x is normal to the wall. Note that for the portion of the top wall, $z = H$, where the fluid leaves the system through the clearance ($R - w \le r \le R$), axial gradient equal to zero condition was applied for each variable. The same condition was also applied for the symmetry line, at $r = 0$, with the radial gradient.

For the simulations with foam, laminar and turbulent flow models were used for the porous foam. In these simulations, the low Reynolds number k-ε model of Jones and Launder (1972) was used still for the fluid layer. For calculations with a laminar flow model for the foam, the interface between the porous medium and clear fluid was treated like a solid wall for the turbulent quantities k and ε. The motivation for such a treatment of the system came from the visualisation experiments where it was found that the fluid and porous layers could be regarded to be operating in the turbulent and laminar regimes, respectively. This was found to be especially true for the low permeability foams that were investigated (Section 4.3.2.1 of chapter four). Thus, the interface conditions were given as $k=0$ and $\dfrac{\partial \varepsilon}{\partial x} = 0$. The interface conditions for the velocities were satisfied automatically due to the use of the Brinkman-extended Darcy flow model for the porous medium. Note that even with the laminar flow model, inertial effects in the porous medium have been accounted for, through the Forchheimer term in the momentum equation.

For calculations with a turbulent flow model for the foam, two sets of simulations were carried out. In one set of simulations, only the Darcy damping or DM terms in the k and ε equations were retained, and the extra terms due to Forchheimer modification were neglected (this set of simulations will henceforth be referred as simulations with turbulence model TM1). An analogous approach was adopted by Prescott and Incropera (1995) in their simulations of solidification of metals where they assumed that, "*within a coherent mushy zone* (model porous medium), *turbulence is dampened by shear having a characteristic length on the order of dendrite arm spacings (i.e., by Darcy damping)*". These authors used the Darcy damping term only in the k equation without a similar term in the ε equation.

In another set of simulations of the present study, the Darcy and Forchheimer modification terms were retained in the k and ε equations (this set of simulations will henceforth be referred as simulations with turbulence model TM2). Of the two Forchheimer modification terms FMA and FMB, only FMA has been retained for the simulations, as justified in Section 5.4.2. In both sets of simulations, the equations that govern the transport of k and ε for the fluid layer and the porous medium were solved without the need to explicitly account for the interface. Again, the use of the Brinkman-extended Darcy flow model in the momentum equation in the porous medium obviated the need to explicitly use an interface condition for velocities. The boundary conditions were similar to the cases without foam.

5.2.3.1 Mean velocity at the exit of the jet

In the experiments corresponding to the present simulations, the pipe through which the jet issues had a length of approximately 30 nozzle diameters. Craft *et al.* (1993) have found that a pipe length of approximately 50 diameters can be considered to give a fully developed flow at the exit of the jet. Baughn and Shimizu (1989) used a longer pipe length of approximately 72 diameters. For the present investigation, the region of interest is distant from the jet centreline. Preliminary computations with a fully developed profile at the exit of the jet, gave reasonable comparisons with the experimental results in the region of interest of the present study. Thus, one of the profiles at the exit of the jet was chosen as a fully developed profile. Two different jet

exit profiles were specified in the present simulations, a flat profile corresponding to a uniform (bulk, U_b) velocity at the jet exit and a fully developed velocity profile from Bird *et al.* (1960), pg. 155,

$$u_z = u_{z,\max}\left(1-\frac{r}{R_N}\right)^{\frac{1}{7}} \quad with \quad \frac{u_{z,\max}}{U_b} = \frac{60}{49} \tag{5.16}$$

where u_z = axial velocity,

$u_{z,max}$ = centreline axial velocity at the jet exit,

r = radial location,

R_N = radius of the nozzle and

U_b = bulk fluid velocity.

Due to the use of a low Reynolds number turbulence model, some turbulence had to be introduced into the system at the start. For the present simulations, this was achieved by specifying values of k and ε at the exit of the jet (Graham and Bremhorst, 1993),

$$k_{in} = 0.001U_b^2$$
$$\varepsilon_{in} = 0.1643\left(\frac{k_{in}^{1.5}}{0.035D_j}\right) \tag{5.17}$$

The simulations with the two jet exit profiles are compared in Section 5.3.1.

5.3 Numerical methods

As mentioned earlier, the flow was assumed to be axi-symmetric for computations. The flow patterns observed from the flow visualisation experiments and an azimuthal traverse carried out with the LDV probe confirmed the validity of this assumption. Thus, only one half of the actual flow domain needed to be solved. A modified form of the finite volume staggered grid code (modified to include axi-symmetric geometries) that was developed and validated for two-dimensional natural convection flow problems (chapters two and three) was used for all simulations. The SIMPLE algorithm detailed in Patankar (1980) was used for solving the discretised partial differential equations using the control volume formulation. The hybrid, first

order upwind/second order central difference scheme was used to discretise the convection terms, whereas the diffusion terms were discretised using the second order central difference scheme. A steady state approach was adopted for all computations. To avoid divergence, an under-relaxation factor of 0.5 was employed for the mean velocities and pressure, whereas for the turbulent quantities, k and ε, the under-relaxation factors were set to 0.3. All equations were solved in their dimensional form.

The simulation was assumed to have reached a converged solution when the sum of the normalised absolute mass and momentum sources (in the axial and radial directions) for all control volumes was each less than or equal to $1x10^{-8}$. Normalisation of the mass and momentum sources was carried out by dividing them by the total number of control volumes (see Equation (2.72) for an example). Further details about the SIMPLE algorithm and the discretisation procedure can be found in the second chapter.

5.3.1 Grid generation and refinement

For grid refinement for the cases without foam, 100x100, 200x200 and 400x400 non-uniform grids were chosen for H=0.15 m and h_p=0.0 m (refer to Figure 4.1 for nomenclature). As an example of non-uniformity, with the 200x200 grid, 40 vertical grids were uniformly distributed horizontally in the jet region. Thus, 40 grids covered a region equal to half the jet diameter, D_j, or 0.0095 m. Similarly, 20 vertical uniform grids were distributed horizontally across the annular clearance (Figure 4.1) of width, w, 0.005 m. The remaining 140 vertical grids in the horizontal direction were distributed non-uniformly by using the sine function given below in Equation (5.18). All 200 horizontal grids in the vertical direction were distributed non-uniformly by using the sine function given below in Equation (5.19).

$$ru_r(i) = R\left[\frac{i}{imax} - \frac{\alpha}{2\pi}sin\left(2\pi\frac{i}{imax}\right)\right] \qquad i = imin, imax \qquad (5.18)$$

$$zu_z(j) = \left(H + h_p\right)\left[\frac{j}{jmax} - \frac{\alpha}{2\pi}sin\left(2\pi\frac{j}{jmax}\right)\right] \qquad j = jmin, jmax \qquad (5.19)$$

The degree of non-uniformity of the grid generated by Equations (5.18) and (5.19) can be controlled by assigning appropriate values to the variable α ($0 \leq \alpha \leq 1$ with 0 representing a uniform grid distribution). In going from a uniform to a non-uniform grid distribution in the horizontal direction, the size of the control volume should not change drastically, as it would lead to unrealistic solutions. In order to avoid this problem, α was assigned a value of 0.6 in Equation (5.18) for approximately matching the size of the control volume generated by the uniform grid and the first control volume generated by the non-uniform grid. Similar grid distributions were used for the 100x100 and 400x400 grids. Figure 5.1 shows the 200x200 non-uniform grid used for the computations for H=0.15 m and h_p=0.0 m.

In Figure 5.2, the grid refinement study is illustrated for H=0.15 m and h_p=0.0 m. In this figure, frames (a), (b) and (c) represent profiles for the radial velocity, axial velocity and turbulence kinetic energy, respectively. In the figure, CFDFDP refers to simulations carried out with a fully developed profile at the exit of the jet. The profiles have been plotted at three non-dimensional axial locations (y/H locations) which correspond to the locations where LDV measurements were made. As seen in Figure 5.2, the results are grid dependent close to the wall at y/H=0.067. In going from 100x100 grid to 200x200 grid, for example, the maximum variation in the radial velocity is found to be around 15% based on the velocity obtained for the 200x200 grid at y/H=0.067. However, the solutions become almost grid independent in going from 200x200 to 400x400 grid. Therefore, the 200x200 grid was chosen for all computations without foam with the same grid distribution as for H=0.15 m and h_p=0.05 m. Simulations carried out with a flat profile at the exit of the jet gave similar grid independence.

For grid refinement for the cases with foam, 100x100, 200x200 and 400x400 grids were chosen for H=0.15 m and h_p=0.05 m. The vertical grid distribution in the horizontal direction was maintained the same as in the cases without foam. The interface between the foam and clear fluid was resolved by using closely spaced horizontal grids in the vertical direction. This was achieved by using Equation (5.18) in the fluid region as well as in the porous region and matching them at the interface by using appropriate values of α. For the porous layer, α in Equation (5.19) was

assigned a value of 0.2 whereas for the fluid layer a value of 0.5 was assigned. For 200x200 grids, 100 grids were distributed in the fluid layer and 100 in the porous layer. The chosen values of α resulted in similar grid sizes within the fluid and porous layers close to the interface. The distance between two adjacent grids in the vertical direction close to the interface was approximately 0.004 m. The resulting grid for H=0.15 m and h_p=0.05 m is shown in Figure 5.3.

Figure 5.4 gives details of the grid refinement study carried out for H=0.15 m and h_p=0.05 m. In Figure 5.4, frames (a), (b) and (c) represent the radial velocity, axial velocity and turbulence kinetic energy profiles, respectively. The normalised axial positions have been maintained the same as in the cases without foam. The axial velocity and turbulence kinetic energy profiles show little variation with grid refinement from 100x100 to 400x400 grids. The maximum variation in the radial velocity in frame (a) is again around 15% based on the velocity obtained with the 200x200 grid (at y/H=0.067). The radial velocity profile becomes almost grid independent in going from the 200x200 to 400x400 grid. Therefore, the 200x200 grid was again chosen for computations for all cases with foam with the same grid distribution as for H=0.15 m and h_p=0.05 m.

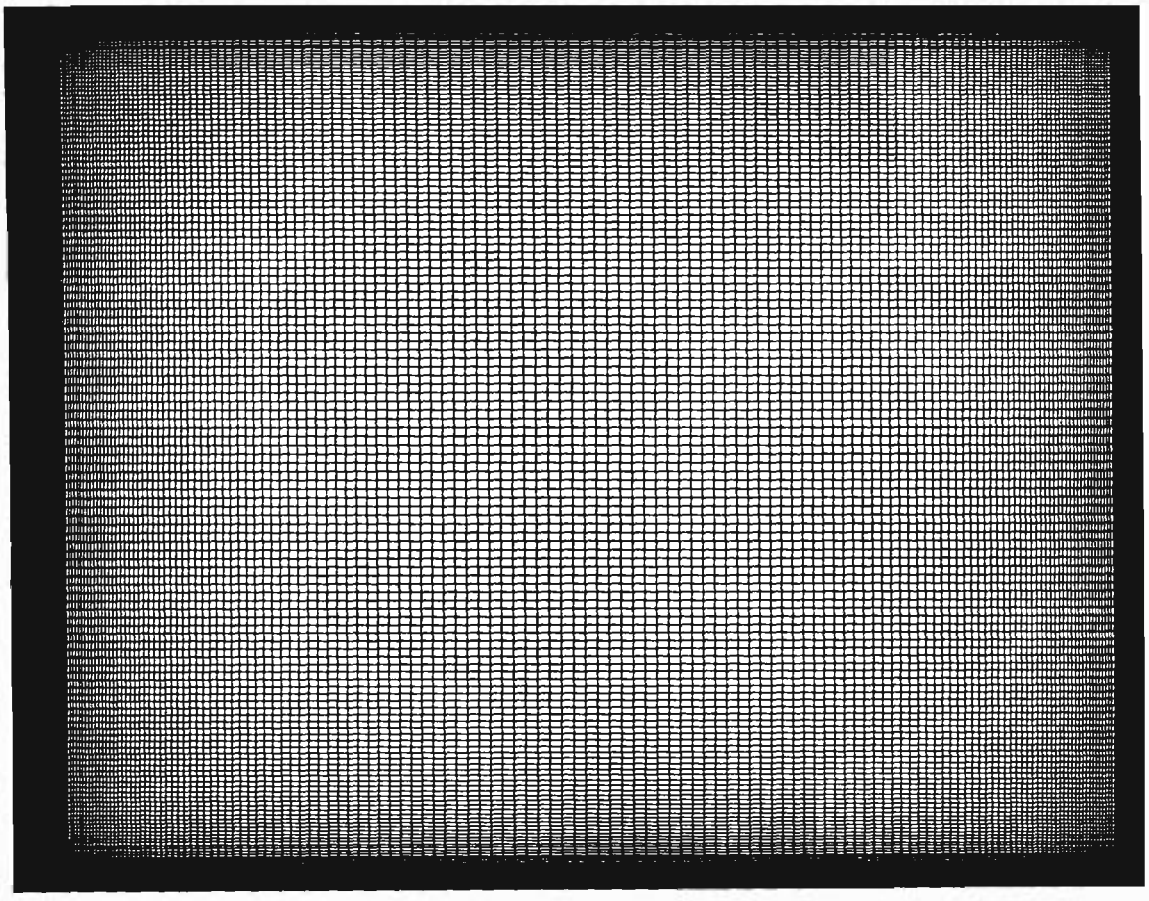

Figure 5.1: Example of the non-uniform grid used for computations. H=0.15 m, h_p=0.0 m.

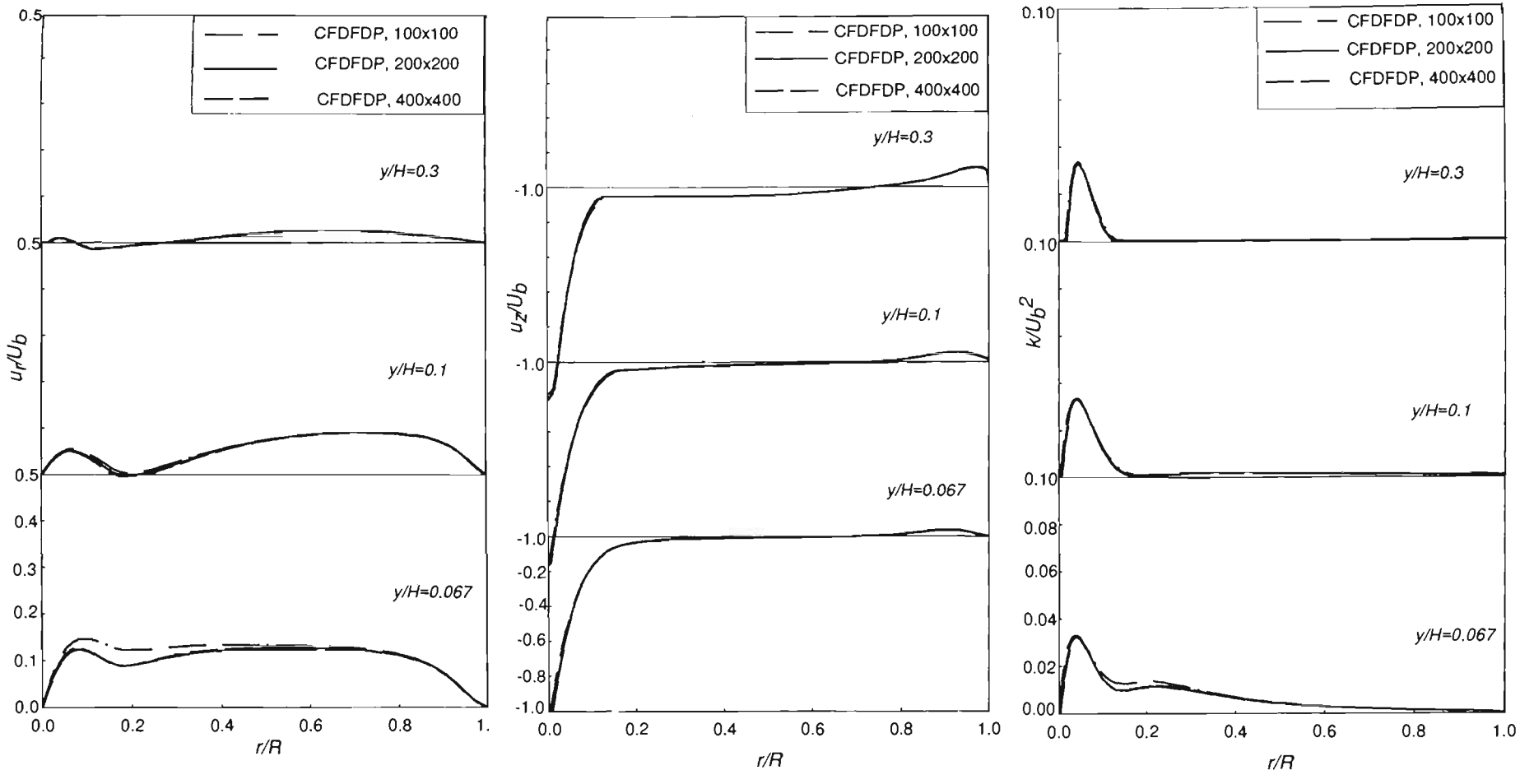

Figure 5.2: Grid refinement study with H=0.15 m, h_p=0.0 m, U_b=1.6 m/s. (a) Radial velocity profiles, (b) Axial velocity profiles. (c) Turbulence kinetic energy profiles.

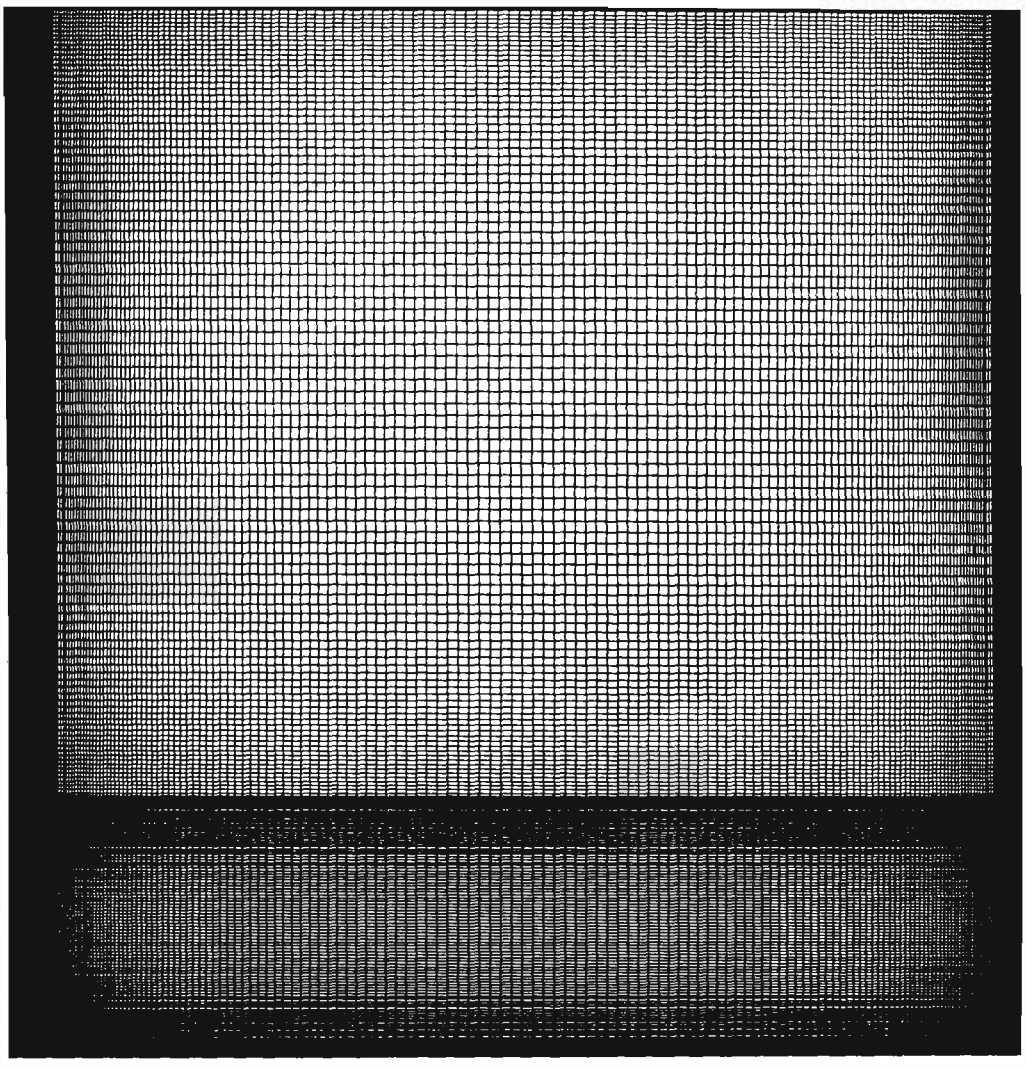

Figure 5.3: Example of the non-uniform grid used for computations. H=0.15 m, h_p=0.05 m.

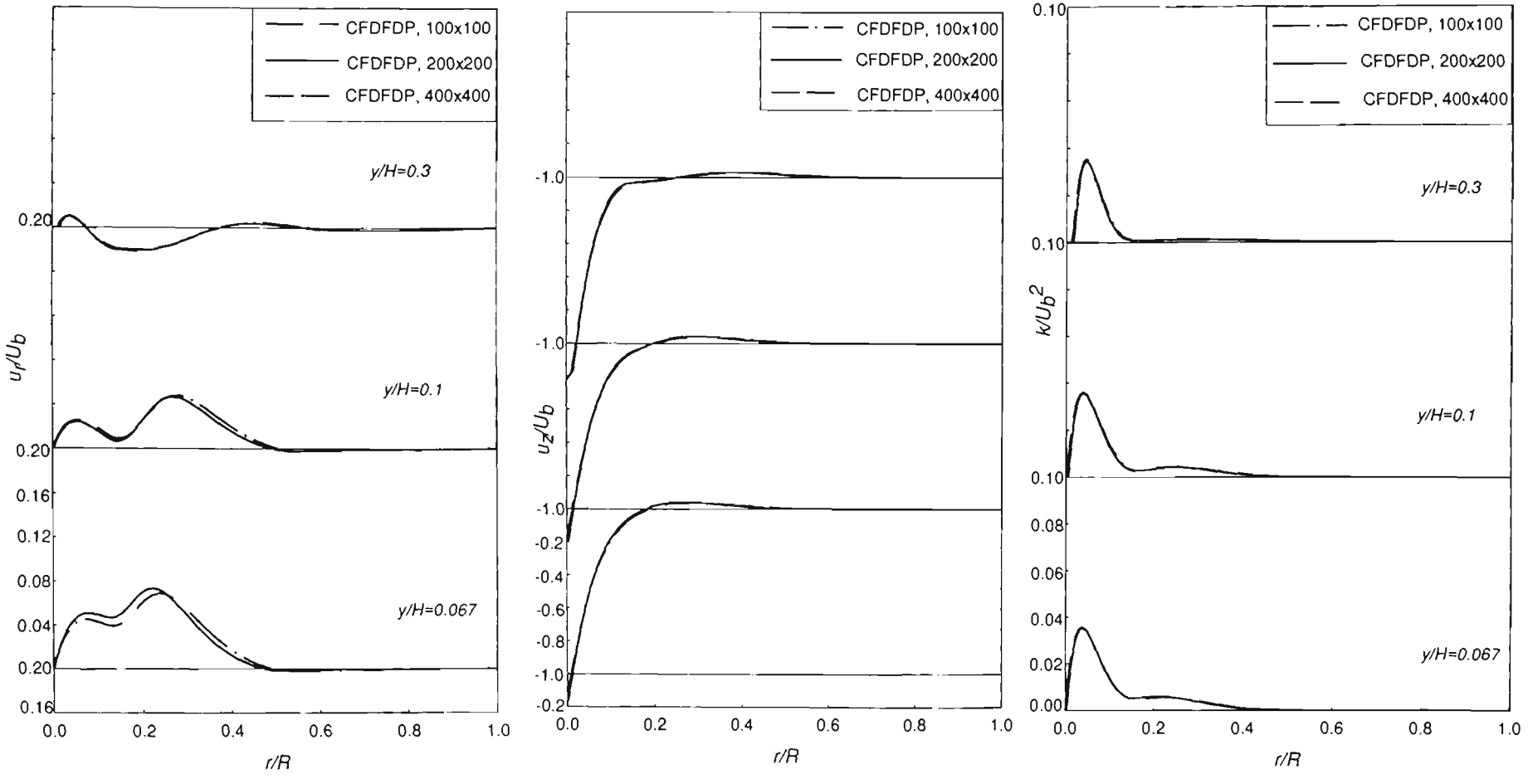

(a) (b) (c)

Figure 5.4: Grid refinement study with H=0.15 m, h_p=0.05 m, U_b=1.6 m/s. (a) Radial velocity profiles, (b) Axial velocity profiles, (c) Turbulence kinetic energy profiles with G10 foam.

5.4 Results and discussion

To evaluate the performance of the CFD simulations for the two-layer system, comparisons have been made between the predicted results and the flow visualisation experiments.

5.4.1 Simulations without foam

Simulations without foam are presented in Figure 5.5 for the three fluid heights, H=0.15, 0.1 and 0.05 m in frames a, b and c, respectively. These frames clearly show the single circulating cell for all three fluid heights as seen in the flow visualisation experiments in Figures 4.4, 4.5 and 4.6. Thus, the CFD model is able to predict the gross flow pattern for the cases without foam quite reasonably.

5.4.2 Simulations with foam

For simulations with turbulence model TM2, preliminary computations were carried out, in order to evaluate the significance of the higher order FMB terms (Equations (5.9) and (5.10)). For these computations, the new constant c_μ^* (Equation (5.13)) was taken to be the same as $c_\mu = 0.09$ as suggested by Lage (1999). These computations did not, however, lead to a converged solution even with a reduction in the under-relaxation factor. The under-relaxation factors were reduced from 0.5 to 0.1 for the mean velocities and from 0.5 to 0.3 for k and ε. The residual for the ε equation in these computations blew up indicating that the extra terms in the ε equation introduced due to the Forchheimer modification could be causing the problem.

In order to understand the significance of the FMB terms, therefore, a new strategy was adopted. Since the FMB terms in the ε equation were potentially causing problems with convergence, these terms were ignored for further computations. Thus, the FMB terms were used only in the k equation. Other terms were used in their original form. It was decided to compare the results obtained from these computations with the results obtained without the inclusion of the FMB terms in

either the k or ε equations. Such a comparison exercise should give an idea about the significance of the FMB terms.

The simulations with the FMB terms only in the k equation converged. Furthermore, the results with and without the FMB terms in the k equation were almost identical with little change in any variable. As an example, the contours of kinetic energy have been compared for the case of the highest investigated permeability G10 foam in Figure 5.6. Frames (a) and (b) in Figure 5.6 represent contours obtained with and without the FMB terms in the k equation for H=0.15 m, h_p=0.05 m and U_b=1.6 m/s. It is clear from Figure 5.6 that the FMB terms have little influence on the turbulence kinetic energy profiles. Similar results were obtained for the other variables as well. Since the FMB terms in the k equation have negligible influence on the final solution, it was decided to neglect this term for further evaluation. The FMA term(s) are therefore the only Forchheimer modification terms used in the k and ε equations for further simulations with turbulence model TM2.

The gross flow patterns with the laminar flow model and with turbulence model TM2 for the porous medium were found to be almost identical. The following figures illustrate the reason for such a result. Figures 5.7, 5.8 and 5.9 give a comparison between the contours of turbulence kinetic energy, rate of energy dissipation and eddy viscosity, respectively, obtained with the two different turbulence models for the G10 foam for H=0.15, 0.1 and 0.05 m with h_p=0.05 m. In the figure, the dashed lines indicate contours obtained with turbulence model TM1 and the solid lines indicate contours obtained with turbulence model TM2 for flow in the porous foam. As seen from these figures, turbulence is damped almost completely at the interface between the fluid layer and the porous foam with turbulence model TM2. Thus, the flow in the porous foam is effectively laminar even for the highest permeability G10 foam due to the damping effect of the Darcy and Forchheimer terms in turbulence model TM2. With turbulence model TM1, however, the turbulence penetrates the porous foam to some extent. The eddy viscosity contours with turbulence model TM1 (contours represented by dashed lines in Figure 5.9) seem to be anomalous due to their relatively large values in the porous foam. This anomaly can, however, be explained by the fact that in the porous foam values of k and ε are almost negligible with the value of ε being much smaller than that of k. Since the

eddy viscosity is defined as, $\mu_t = \rho c_\mu \frac{k^2}{\varepsilon}$, it tends to give an artificially large value even in regions where turbulence is almost non-existent.

Due to the similarity in the flow patterns obtained with the laminar flow model and turbulence model TM2, the remaining results presented in the present chapter are only with the two different turbulent flow models for the porous foam. The comparisons are detailed below in the form of the effect of porous layer and its permeability, effect of height/thickness of the porous layer and the effect of clear fluid layer height. The flow visualisation experiments have shown that for the G30 and G60 foams, the flow pattern in the fluid layer is not significantly different. Thus, for simulations with a lower permeability foam, the parameters for the G45 foam (see Tables 4.1 and 4.2) of Seguin *et al.* (1998a) have been used, as the values for the G30 and G60 foams were unavailable from literature. The values reported by Seguin *et al.* (1998a) for the G10 foam are used in the present study.

5.4.2.1 The effect of porous layer and its permeability

The simulations carried out with the G10 and G45 foams give impressions about the variation in flow pattern with a change in the permeability of the porous foam. Figures 5.10 and 5.11 for the G45 foam and Figures 5.14 and 5.15 for the G10 foam are used to study the effect of permeability of the porous foam to correspond to the observations made in the flow visualisation experiments in Section 4.3.2.1 of chapter four. Figures 5.10 and 5.11, and 5.14 and 5.15, respectively represent simulations carried out with two different turbulence models, TM1 and TM2, for the porous foam with h_p=0.05 m. Frames (a), (b) and (c) in these figures represent simulations carried out for H=0.15, 0.1 and 0.05 m.

For the G45 foam, the flow in the fluid layer is similar to cases without foam for H=0.15 and 0.1 m with both turbulence models as seen from frames (a) and (b) of Figures 5.10 and 5.11, respectively. This result is in agreement with the observations made from the flow visualisations for low permeability porous foams in Figures 4.7 and 4.8 for the G60 foam and Figures 4.10 and 4.11 for the G30 foam. However, for H=0.05 m, the flow pattern in the fluid layer is significantly different with models TM1 and TM2 as seen from frame (c) in Figures 5.10 and 5.11. In Figure 5.10(c),

with model TM1, there is sufficient evidence of the formation of a second cell close to the wall. This result is in agreement with the flow visualisation experiments for the G60 and G30 foams as seen from Figures 4.9 and 4.12, respectively. In Figure 5.11(c), with model TM2, the second cell is not sufficiently developed, and there is no significant change in the flow pattern in the fluid layer from cases without foam. This result indicates that the additional Forchheimer terms introduced in the k and ε equations might be providing excessive damping. This damping reduces the speed of fluid leaving the porous foam, thus reducing its interaction with the flow in the fluid layer.

For the G10 foam, for the two higher fluid heights, a two-cell pattern is produced with both turbulence models for foam as seen from frames (a) and (b) of Figures 5.14 and 5.15. There is, however, some difference in the size and shape of the two cells simulated with the two models. In the corresponding visualisations for the G10 foam in Figure 4.16, the two-cell pattern is not clearly formed for H=0.15 m. This discrepancy could be due to the fact that the flow has unsteady and/or three-dimensional characteristics, which the model does not take into account. However, the two cell pattern can be clearly visualised for H=0.1 m in Figure 4.17. For H=0.05 m, the two simulations predict significantly different flow patterns as seen from Figures 5.14(c) and 5.15(c). In Figure 5.14(c), for model TM1, the two-cell pattern observed for H=0.15 and 0.1 m persists. This result is in agreement with the corresponding flow visualisation in Figure 4.18. In Figure 5.15(c), for model TM2 however, there is no evidence of the second cell, which again demonstrates the inferiority of turbulence model TM2.

Similar conclusions can be drawn from the results obtained with two layers of porous foam given in Figures 5.12 and 5.13 with the G45 foam and 5.16 and 5.17 with the G10 foam.

The above results indicate that turbulence model TM1 is superior in predicting the effect of porous layer and its permeability. Turbulence model TM2 provides excessive damping due to the combined damping effect of the Darcy and Forchheimer terms. As mentioned earlier, results obtained with a laminar flow model and turbulence model TM2 for the porous foam were found to be similar.

5.4.2.2 The effect of height/thickness of the porous layer

For the lower permeability G45 foam, Figures 5.10 and 5.12 using model TM1 and Figures 5.11 and 5.13 using model TM2 are compared for the effect of height/thickness of the porous layer. Figures 5.12 and 5.13 represent simulations with G45 foam with h_p=0.1 m and correspond to Figures 5.10 and 5.11 with h_p=0.05 m. A comparison between frames (a), (b) and (c) of Figures 5.10 and 5.11 with the corresponding frames in Figures 5.12 and 5.13 respectively, reveal that there is no significant change in the flow pattern with a change in the thickness of the porous layer. The flow visualisations for the low permeability G30 foam given in Figures 4.10 to 4.12 for h_p=0.05 m and Figures 4.13 to 4.15 for h_p=0.1 m also showed no significant change in the flow pattern in the fluid layer with a change in the thickness of the porous foam.

For the highest permeability G10 foam, Figures 5.14 and 5.16 using model TM1 and Figures 5.15 and 5.17 using model TM2 are compared for the effect of height/thickness of the porous layer. Figures 5.16 and 5.17 represent simulations with h_p=0.1 m and correspond to Figures 5.14 and 5.15 with h_p=0.05 m. With model TM1, Figures 5.14 and 5.16, there is a significant change in the flow pattern in the fluid layer for H=0.05 m as seen from a comparison between frame (c) in these figures. The two-cell pattern seen for h_p=0.05 m in Figure 5.14(c) is reduced to a single cell pattern for h_p=0.1 m in Figure 5.16(c). However, the flow pattern remains essentially the same for H=0.15 and 0.1 m. With model TM2, Figures 5.15 and 5.17, the flow pattern in the fluid layer is almost unchanged with a change in the thickness of the porous layer for all three fluid heights. The flow visualisation results discussed in Section 4.3.2.2 of chapter four, however, clearly indicate a delay in the transition to a two-cell pattern in the fluid layer with an increase in the thickness of the porous layer for the G10 foam.

The above discussion shows that simulations are not able to effectively capture changes in the flow pattern in the fluid layer with a change in the thickness of

the porous layer. This result was found to be true for simulations with all three models used for the porous foam.

5.4.2.3 The effect of clear fluid layer height

For the lower permeability foams, the effect of height of the clear fluid layer is investigated by comparing individual frames of Figures 5.10 and 5.11 (which use models TM1 and TM2, respectively) for the G45 foam with Figures 4.7 to 4.9 of the G60 foam or Figures 4.10 to 4.12 of the G30 foam. It is clear from the observations made in Section 4.3.2.3 of chapter four that the flow pattern in the fluid layer is essentially a single cell pattern for H=0.15 and 0.1 m for the G60 foam, Figures 4.7 and 4.8 and for the G30 foam, Figures 4.10 and 4.11. This result is predicted accurately by model TM1, Figures 5.10(a) and (b), and model TM2, Figures 5.11(a) and (b). For H=0.05 m, however, the flow pattern changes to a two cell pattern in the visualisations for the lower permeability foams, as seen in Figures 4.9 and 4.12. This result is predicted accurately only by simulations with model TM1 for the porous foam, as seen from Figure 5.10(c). Simulations with model TM2, on the other hand, predicts only a single cell pattern for this case, as seen in Figure 5.11(c).

With the highest permeability G10 foam, the visualisations indicate a two-cell pattern for all three fluid heights investigated for h_p=0.05 m (Figures 4.16 to 4.18). However, for H=0.15 m, the second cell is not completely formed, Figure 4.16. Simulations with model TM1 for the same case, Figure 5.14, show good agreement for all three fluid heights with one dominant re-circulation close to the jet and a second weaker cell close to the wall. Results with model TM2 are also comparable with the visualisations for H=0.15 and 0.1 m, as seen from Figures 5.15(a) and (b). For H=0.05 m, however, the simulations are unable to predict the second cell close to the wall, as seen from Figure 5.15(c).

The above discussion indicates that simulations with turbulence model TM1 are superior in their ability to predict changes in the flow pattern with a change in the height of the fluid layer.

5.5 Conclusions

Simulations of a system consisting of a turbulent fluid layer overlying a porous medium are presented in this chapter. The results obtained are compared with the flow patterns observed through the flow visualisation experiments presented in the previous chapter. Three different flow models are used for the porous foam, a laminar flow model and two turbulence models. One of the turbulence models with only Darcy damping in the k and ε equations is superior in predicting the gross flow patterns, especially the effect of permeability of the porous foam and clear fluid layer height. The higher order terms occurring in the k and ε equations due to the Forchheimer term were found to be negligible through the simulations with the second turbulence model. This model with both Darcy and Forchheimer modifications included in the k and ε equations for the porous foam was found to be similar to the laminar flow model in its predictive capabilities. The similarity in predictions was found to be due to the almost complete damping of turbulence at the interface between the porous foam and clear fluid due to the Darcy and Forchheimer terms. As a result, the flow in the porous foam becomes effectively laminar in nature. None of the three models used to represent flow in the porous foam could adequately predict the effect of changes in the thickness of the porous layer.

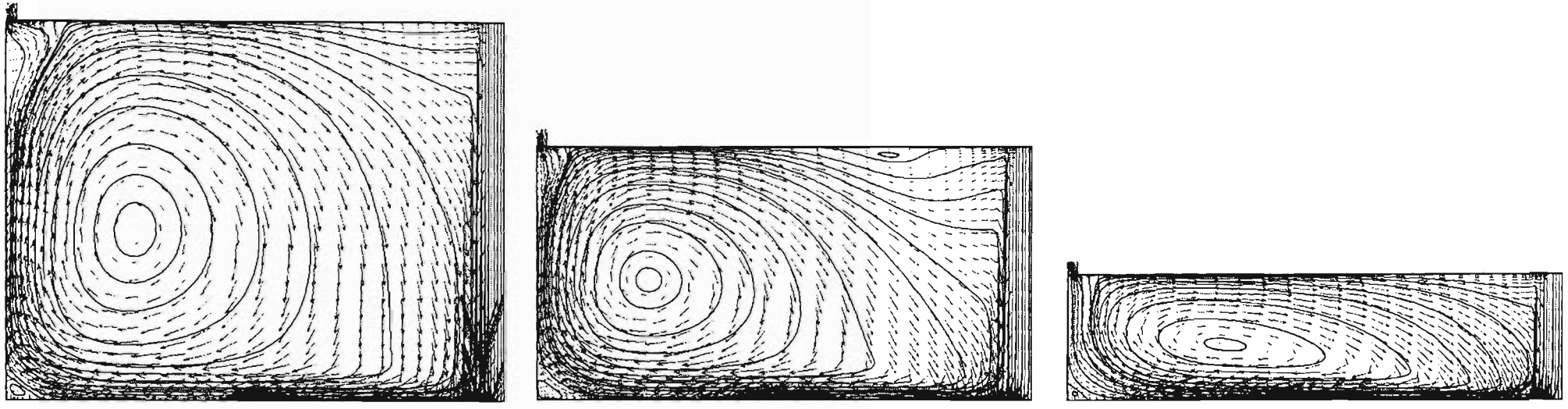

(a) H=0.15 m, h_p=0.0 m, U_b=1.6 m/s

(b) H=0.1 m, h_p=0.0 m, U_b=1.6 m/s

(c) H=0.05 m, h_p=0.0 m, U_b=1.6 m/s

Figure 5.5: Stream traces and vector plots simulations for cases without porous foam.

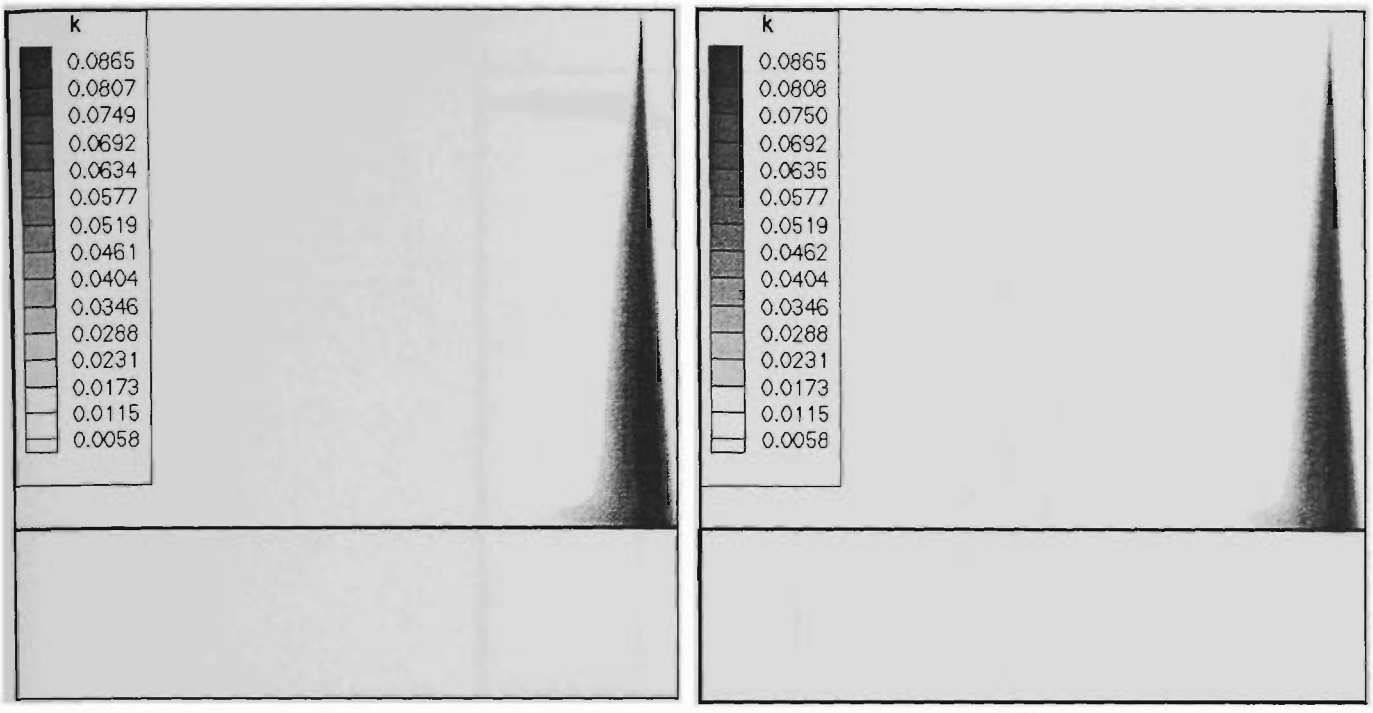

(a) (b)

Figure 5.6: Turbulence kinetic energy contours for G10 foam with H=0.15 m, h_p=0.05 m, U_b=1.6 m/s. a) with FMB terms included in the k equation, b) without FMB terms in the k equation. The figure indicates that the FMB terms have a very small contribution.

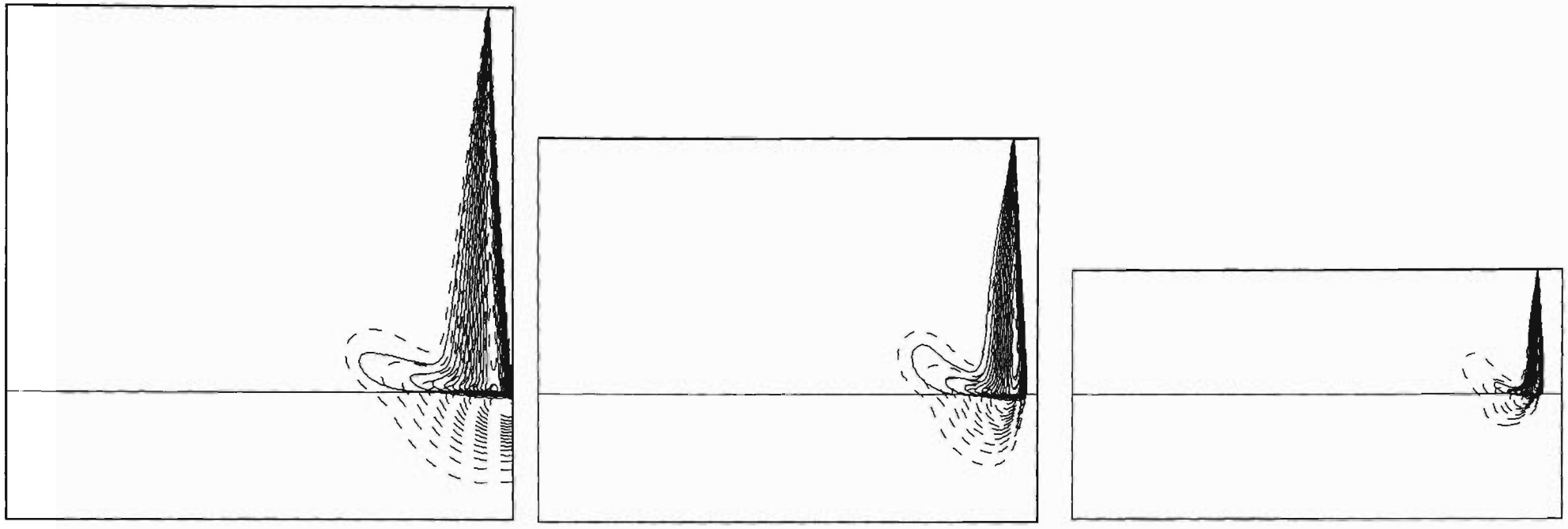

Figure 5.7: Turbulence kinetic energy contours for a) H=0.15 m, b) H=0.1 m, c) H=0.05 m with h_p=0.05 m and U_b=1.6 m/s. Dashed lines indicate contours obtained with simulations using only Darcy damping in the k and ε equations (model TM1). Solid lines indicate contours obtained with simulations using Forchheimer and Darcy modifications in the k and ε equations (model TM2).

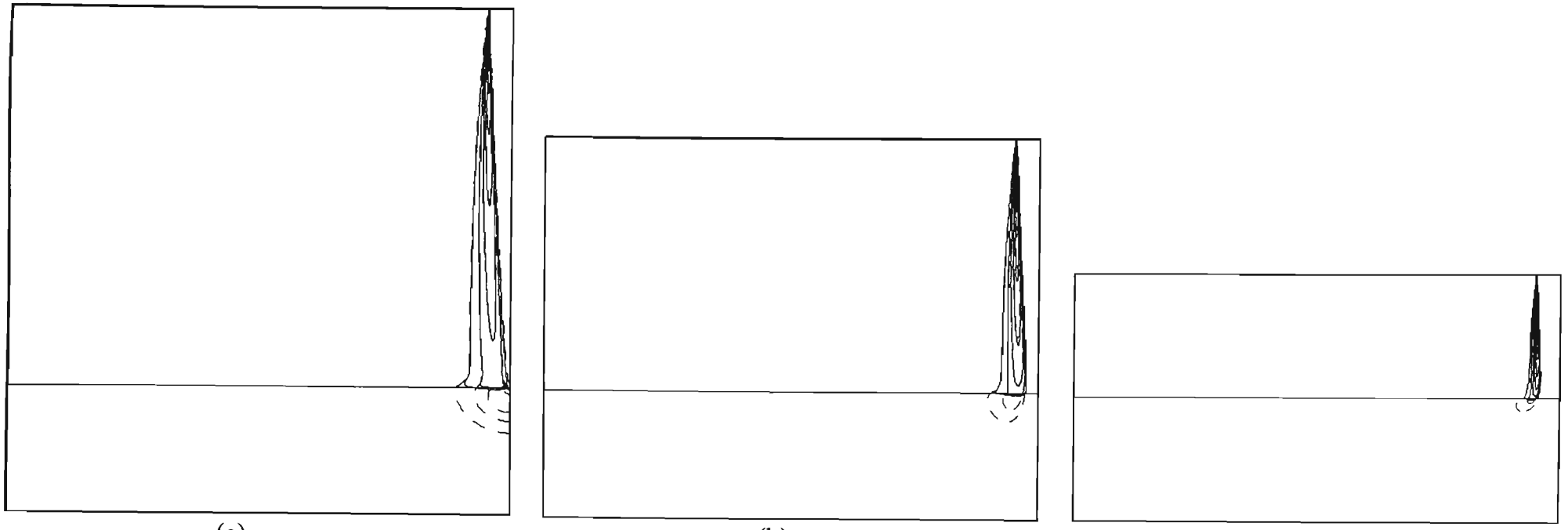

Figure 5.8: Rate of energy dissipation contours for a) H=0.15 m, b) H=0.1 m, c) H=0.05 m with h_p=0.05 m and U_b=1.6 m/s.
Dashed lines indicate contours obtained with simulations using only Darcy damping in the k and ε equations (model TM1).
Solid lines indicate contours obtained with simulations using Forchheimer and Darcy modifications in the k and ε equations (model TM2).

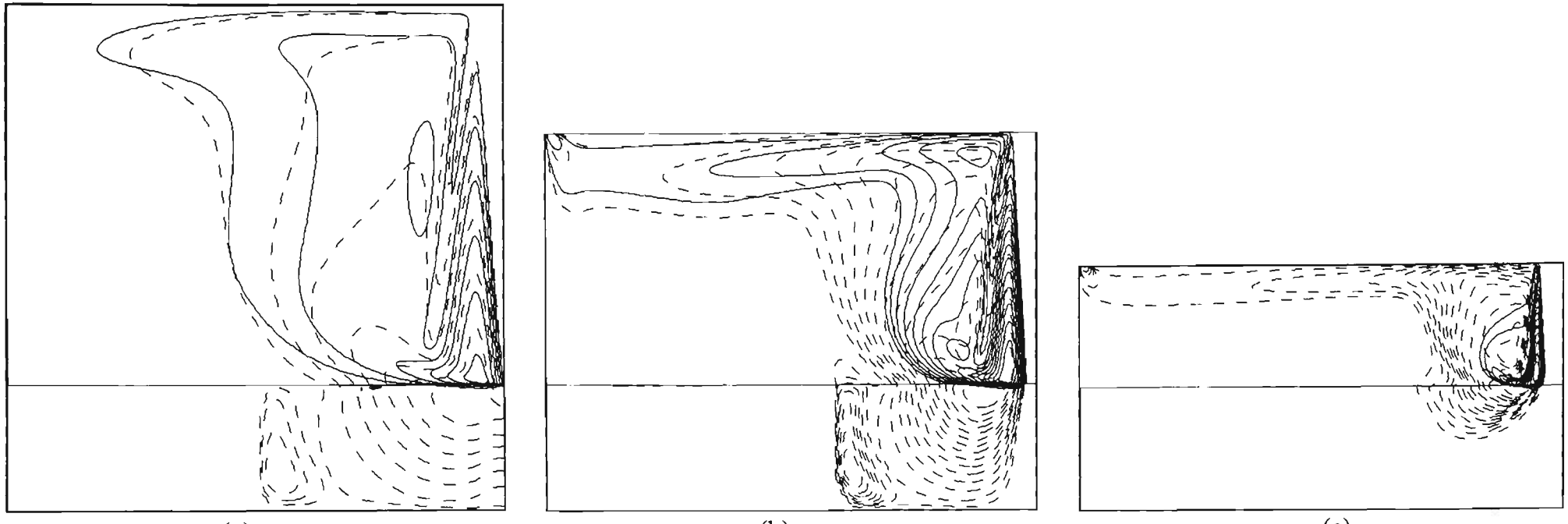

Figure 5.9: Eddy viscosity contours for a) H=0.15 m, b) H=0.1 m, c) H=0.05 m with h_p=0.05 m and U_b=1.6 m/s.
Dashed lines indicate contours obtained with simulations using only Darcy damping in the k and ε equations (model TM1).
Solid lines indicate contours obtained with simulations using Forchheimer and Darcy modifications in the k and ε equations (model TM2).

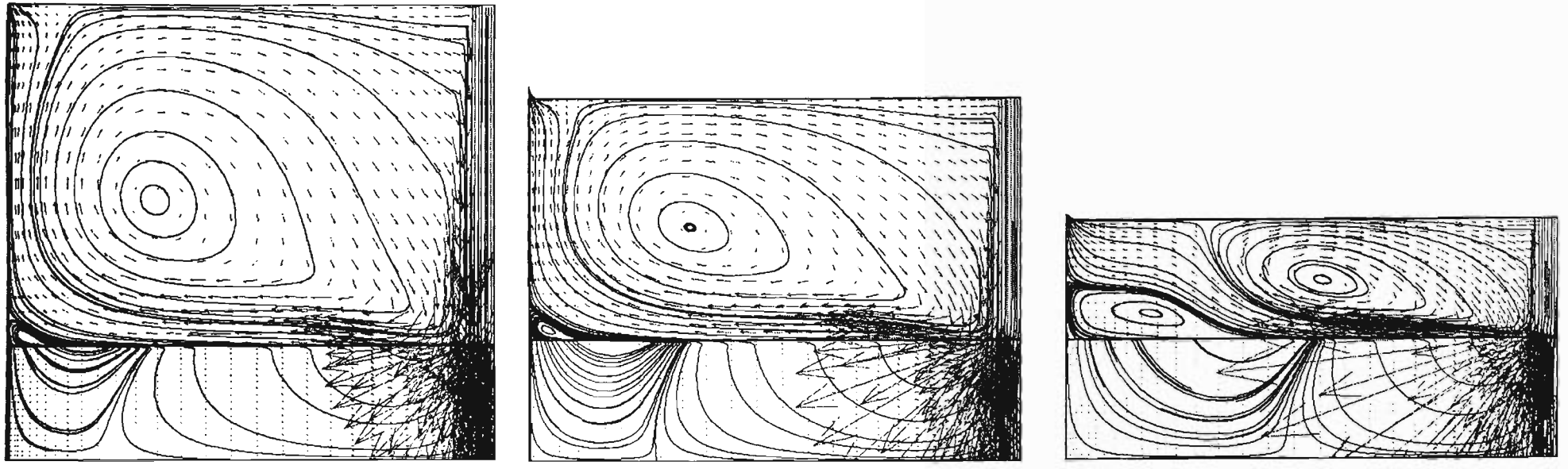

(a) H=0.15 m, h_p=0.05 m, U_b=1.6 m/s (b) H=0.1 m, h_p=0.05 m, U_b=1.6 m/s (c) H=0.05 m, h_p=0.05 m, U_b=1.6 m/s

Figure 5.10: Stream traces and vector plots for cases with porous foam G45 with h_p=0.05 m. Turbulence model TM1 used for the porous foam.

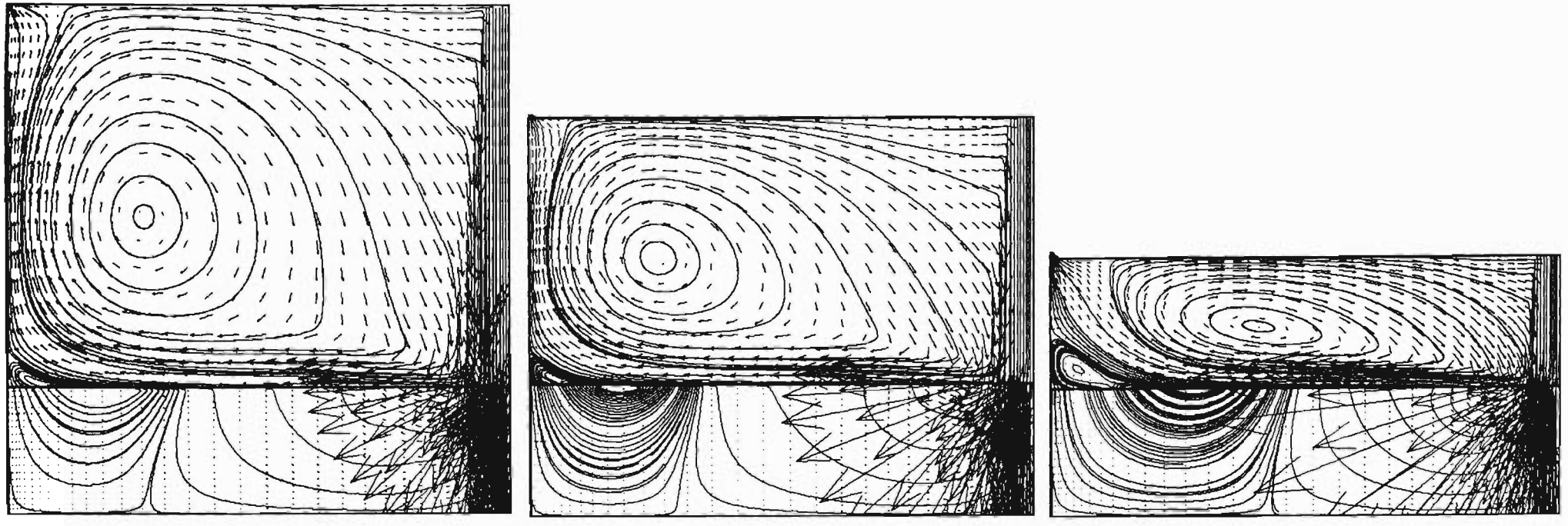

(a) H=0.15 m, h_p=0.05 m, U_b=1.6 m/s (b) H=0.1 m, h_p=0.05 m, U_b=1.6 m/s (c) H=0.05 m, h_p=0.05 m, U_b=1.6 m/s

Figure 5.11: Stream traces and vector plots for the cases with porous foam G45 with h_p=0.05 m. Turbulence model TM2 used for the porous foam.

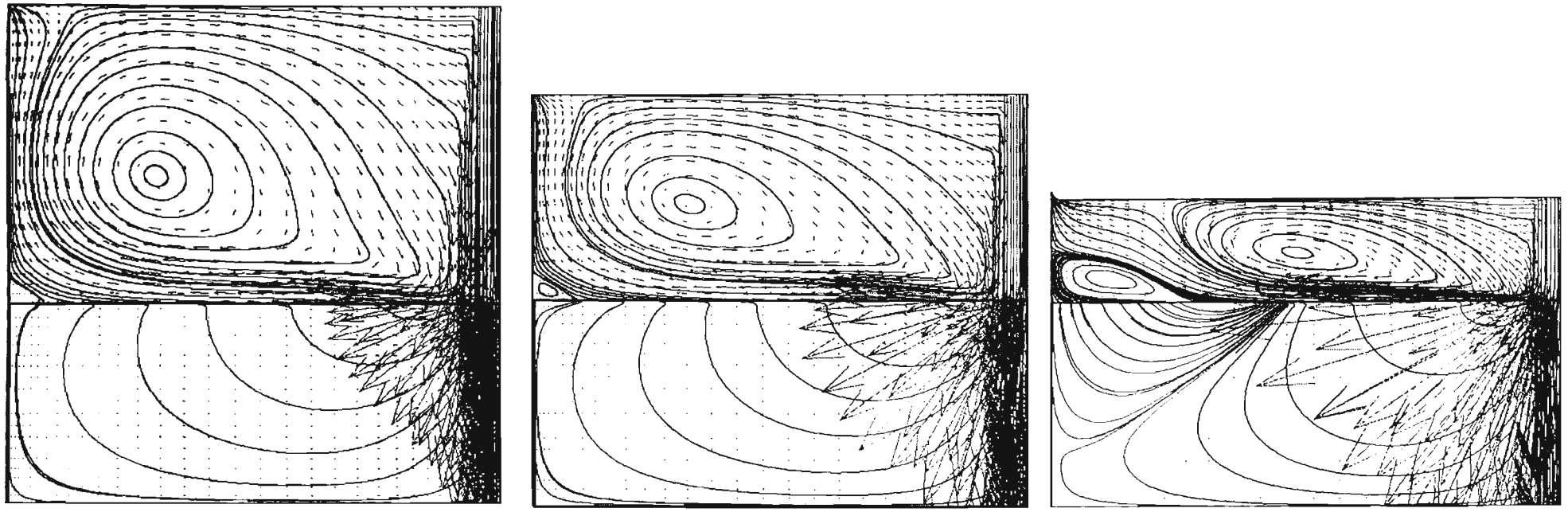

(a) H=0.15 m, h_p=0.1 m, U_b=1.6 m/s (b) H=0.1 m, h_p=0.1 m, U_b=1.6 m/s (c) H=0.05 m, h_p=0.1 m, U_b=1.6 m/s

Figure 5.12: Stream traces and vector plots for the cases with porous foam G45 with h_p=0.1 m. Turbulence model TM1 used for the porous foam.

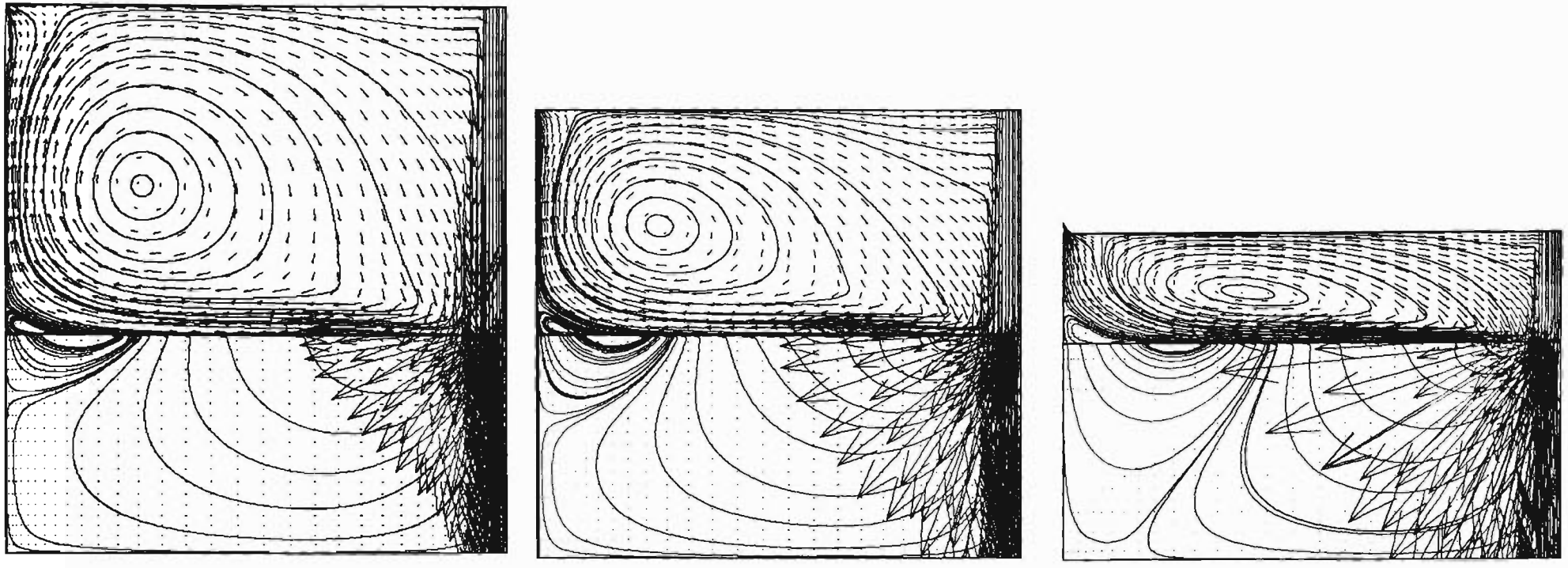

(a) H=0.15 m, h_p=0.1 m, U_b=1.6 m/s (b) H=0.1 m, h_p=0.1 m, U_b=1.6 m/s (c) H=0.05 m, h_p=0.1 m, U_b=1.6 m/s

Figure 5.13: Stream traces and vector plots for the cases with porous foam G45 with h_p=0.1 m. Turbulence model TM2 used for the porous foam.

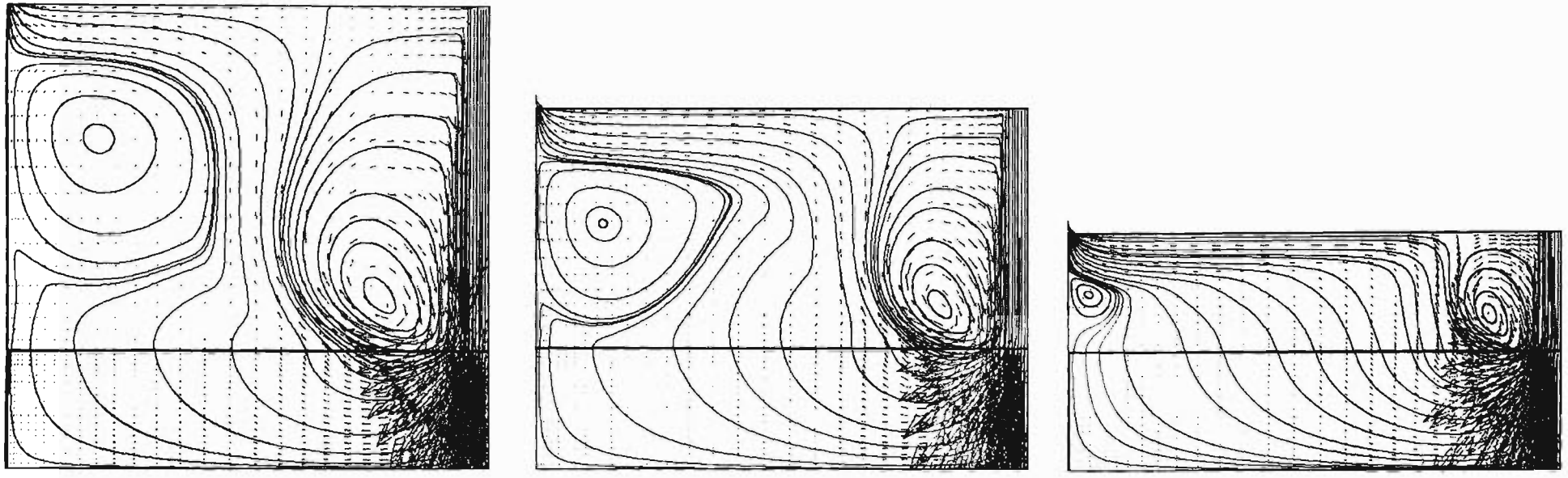

(a) H=0.15 m, h_p=0.05 m, U_b=1.6 m/s (b) H=0.1 m, h_p=0.05 m, U_b=1.6 m/s (c) H=0.05 m, h_p=0.05 m, U_b=1.6 m/s

Figure 5.14: Stream traces and vector plots for the cases with porous foam G10 with h_p=0.05 m. Turbulence model TM1 used for the porous foam.

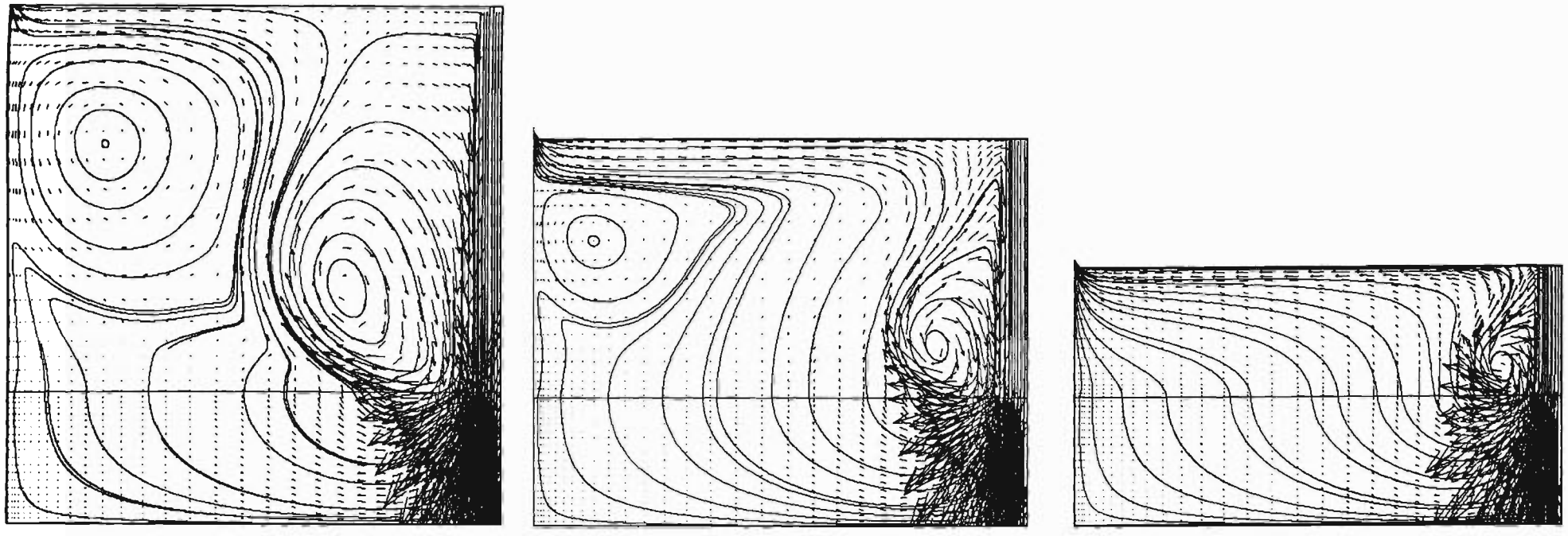

(a) H=0.15 m, h_p=0.05 m, U_b=1.6 m/s (b) H=0.1 m, h_p=0.05 m, U_b=1.6 m/s (c) H=0.05 m, h_p=0.05 m, U_b=1.6 m/s

Figure 5.15: Stream traces and vector plots for the cases with porous foam G10 with h_p=0.05 m. Turbulence model TM2 used for the porous foam.

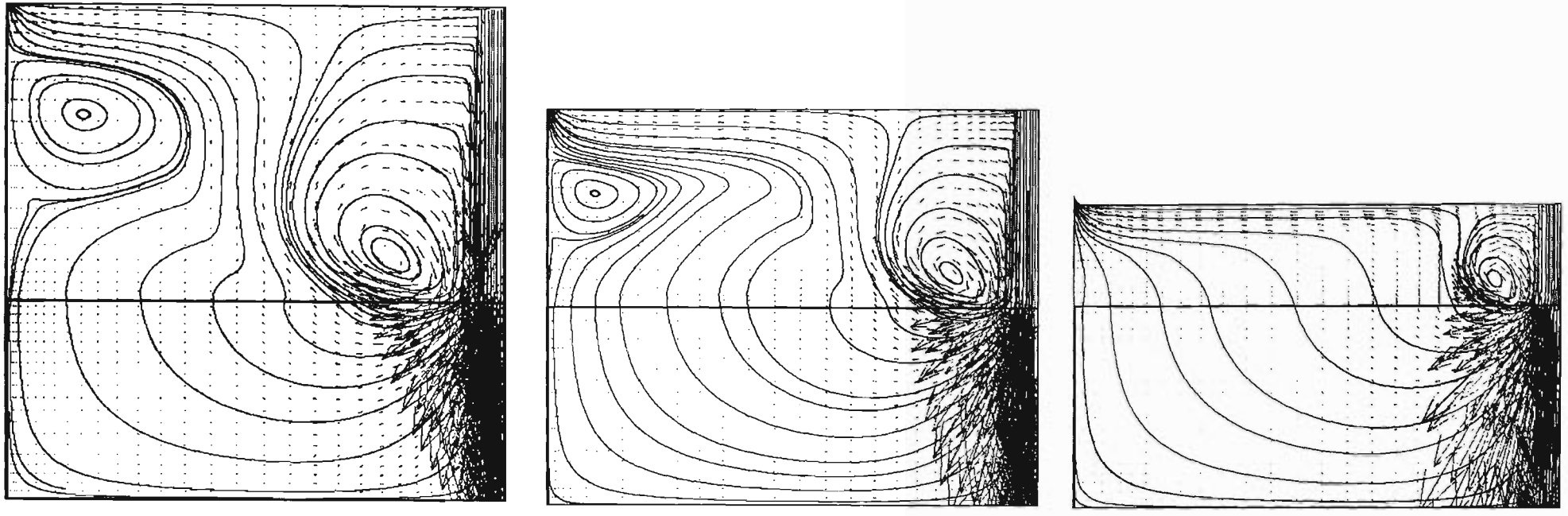

(a) H=0.15 m, h_p=0.1 m, U_b=1.6 m/s (b) H=0.1 m, h_p=0.1 m, U_b=1.6 m/s (c) H=0.05 m, h_p=0.1 m, U_b=1.6 m/s

Figure 5.16: Stream traces and vector plots for the cases with porous foam G10 with h_p=0.1 m. Turbulence model TM1 used for the porous foam.

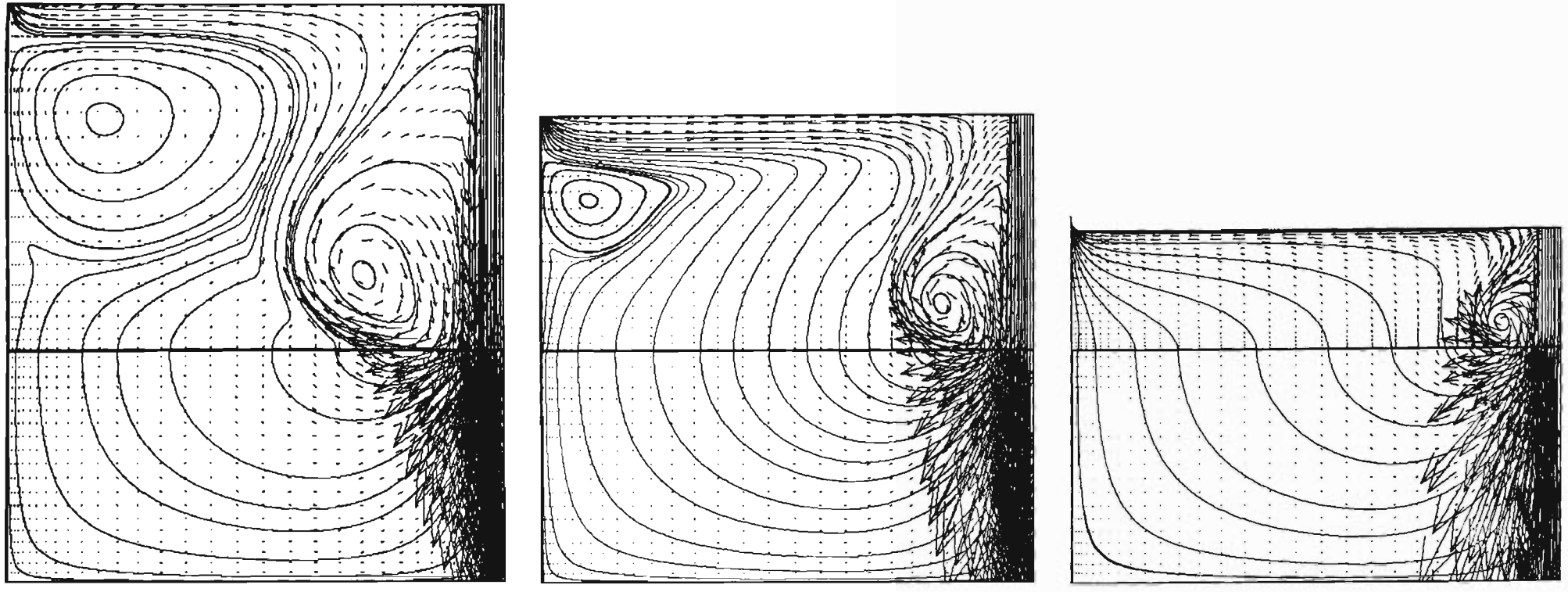

(a) H=0.15 m, h_p=0.1 m, U_b=1.6 m/s (b) H=0.1 m, h_p=0.1 m, U_b=1.6 m/s (c) H=0.05 m, h_p=0.1 m, U_b=1.6 m/s

Figure 5.17: Stream traces and vector plots for the cases with porous foam G10 with h_p=0.1 m. Turbulence model TM2 used for the porous foam.

Chapter 6

LDV measurements and simulations

6.1 Introduction

This chapter presents laser Doppler velocimetry (LDV) measurements and comparisons between CFD simulations and the measurements for the system consisting of a turbulent fluid layer overlying a saturated porous foam. The streaklines that were observed from the flow visualisations in chapter four, highlighted the regions where more detailed experimental investigations were required. Such detail has been achieved by taking LDV measurements. The comparison of the simulations with the flow visualisations in chapter five was qualitative in nature. A quantitative evaluation between the simulated and experimental results is therefore presented in this chapter by comparing the CFD simulations and the LDV measurements.

As noted in chapter four, few experiments have been carried out to evaluate turbulence in porous media. Even the results from the experiments that have been performed cannot be used directly for a comparison with the simulations. The reason is that the experimental results such as the ones by Hall and Hiatt (1996) and Saleh *et al.* (1992) give microscopic or pore scale values, whereas numerically, one is calculating the macroscopic or volume averaged quantities. It has also been recognised by authors such as Antohe and Lage (1997) that macroscopic turbulence may persist only near the interface between a clear fluid and porous medium. Inside the porous matrix, macroscopic turbulence may be attenuated rapidly since the large eddies which transfer energy to the smaller eddies cannot be larger than the pore size (Nield, 1991, and Nield and Bejan, 1992). For these reasons, the present experiment uses a two-layer system consisting of a turbulent fluid overlying a porous medium and infers the effect of the interaction between the two layers on the flow patterns in the fluid layer.

As indicated in chapter four on flow visualisation, it was found that there is a significant change in the flow pattern in the fluid layer of the two-layer system when the highest permeability (G10) foam was tested. For the LDV measurements

therefore, only the cases with the G10 foam have been revisited. All cases without foam were also repeated to ascertain the nature of the flow pattern.

Since the flow in the fluid layer is turbulent, it is expected that this turbulence will persist, on the macroscopic scale, in the foam for some foam height before it is attenuated. It is further believed that a proper representation of the flow in the porous medium will lead to a better prediction of the flow in the fluid layer due to the interaction between the two layers. The CFD simulations presented in chapter five revealed that the simulations with a turbulent flow model for the foam and only Darcy damping incorporated in the k and ε equations (referred as model TM1) gave better predictions of the flow patterns in the fluid layer. Simulations with a laminar flow model and a turbulent flow model with Darcy and Forchheimer modification terms incorporated in the k and ε equations (referred as model TM2) gave identical results for the flow patterns. These two models were inferior to model TM1 in predicting the effect of permeability of porous foam and clear fluid layer height on the flow patterns in the fluid layer. In this chapter, these models are again compared for their ability to quantitatively predict the mean velocity and turbulence kinetic energy patterns in the fluid layer obtained from LDV measurements.

6.2 Principles of LDV

LDV measurements have been carried out to record velocities and turbulence intensities. The principle of this measurement technique has been described in detail in Durst *et al.*(1976). For completeness, a brief description of the technique is presented here.

The LDV is based on the Doppler effect and can be operated in three different optical arrangements, namely, the reference beam mode, the dual beam or fringe mode and the two-scattered beam mode (Durst *et al.*, 1976). The present system uses the fringe mode of operation as illustrated in Figure 6.1. In this mode, two incident light beams of almost equal intensity intersect in space to create an interference fringe. If a scattering particle penetrates the region of intersection of the two light beams, it will scatter light from each of the two beams. The scattered light waves thus produced will have Doppler shifted frequencies given by the relationship:

$$f_{I1} = f_I\left[\frac{c - \boldsymbol{u}.\boldsymbol{e}_1}{c - \boldsymbol{u}.\boldsymbol{l}}\right] \tag{6.1}$$

$$f_{I2} = f_I\left[\frac{c - \boldsymbol{u}.\boldsymbol{e}_2}{c - \boldsymbol{u}.\boldsymbol{l}}\right] \tag{6.2}$$

where f_I is the frequency of the original light source emitted by the laser beam,

c is the speed of light,

$\boldsymbol{u}$ is the instantaneous particle velocity,

$\boldsymbol{e}_1$ and $\boldsymbol{e}_2$ are the unit vectors in the direction from the stationary light source to the moving particle and

$\boldsymbol{l}$ is the unit vector in the direction from the moving particle to the receiver.

The two scattered light waves interfere yielding a beat signal which has a frequency given by the frequency difference $\Delta f_I = f_{I2} - f_{I1}$. For particle velocities much smaller than the velocity of light, this frequency difference can be approximated as:

$$f_{ID} = \frac{1}{\lambda}\boldsymbol{u}.(\boldsymbol{e}_2 - \boldsymbol{e}_1) \tag{6.3}$$

where λ is the wavelength of the emitting light source.

Equation (6.3) is used to approximate the instantaneous fluid velocity. Subsequently, the mean and fluctuating velocities are calculated as follows. The mean velocity refers to the average velocity value of all the velocities measured at a particular point. Thus:

$$u = \frac{\sum_{i=1}^{n}(\boldsymbol{u}.\boldsymbol{e}_1)_i}{n} \tag{6.4}$$

where u= average velocity

$\boldsymbol{u}$ = velocity of the i^{th} particle

and n= number of particles measured (or the number of samples taken per point).

The root mean square (r.m.s.) fluctuating velocity which is also the standard deviation of the velocities measured, is given as

$$\sqrt{u'^2} = \sqrt{\frac{\sum_{i=1}^{n} (u.e_1 - u)_i^2}{n-1}} \qquad (6.5)$$

where $\sqrt{u'^2}$ = the r.m.s. fluctuating velocity.

For all three optical arrangements mentioned above, the LDV can be operated either in the forward scattering or backward scattering mode of operation.

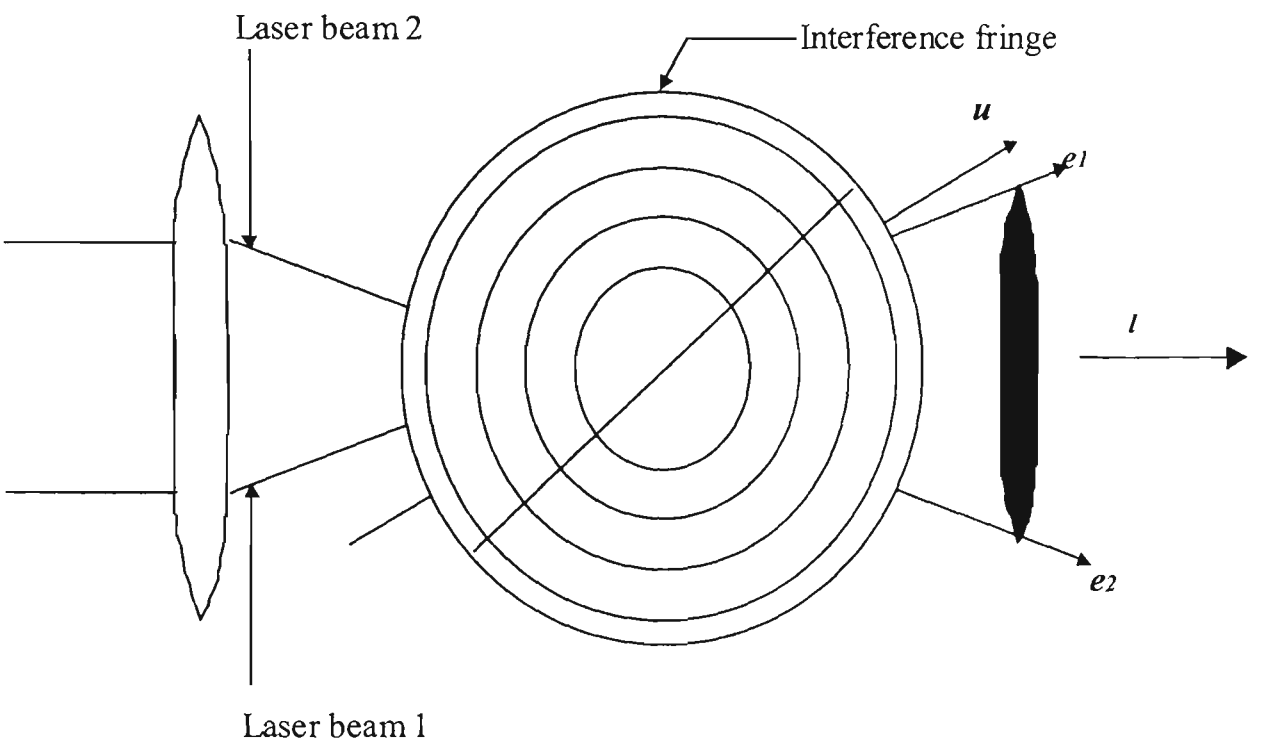

Figure 6.1: An illustration of the LDV operating in the fringe mode.

6.3 LDV setup, traversing mechanism and data acquisition

For the present experiments, the LDV is used in the backward scatter mode. The LDV system was provided by ***Aerometrics*** (1997). It consists of the LDV probe and the ***DataVIEW*** software. The incoming beam has a wavelength of 514.5 nm. A 1 W Argon ion laser is used as the light source for the present experiments, and it is connected to a fibre optic probe through a fibre optic cable. A Bragg cell is used as a beam splitter and frequency shifter. Frequency shifting allows the 180 degree

ambiguity in the direction of the measured velocity to be resolved. The Bragg cell splits the incoming beam into two beams of almost equal intensity ($\pm 5-10\%$). One of the beams is shifted by a frequency of 40 MHz with respect to the frequency of the incident beam. A single channel LDV acquisition system is used for the measurements. Thus, only the normal Reynolds stresses and the mean velocities could be determined.

A high sampling rate leads to an increase in the velocity range that can be measured by the instrument, but decreases the signal quality. On the other hand, a low sampling rate leads to a reduced velocity range that can be measured, but increases the signal quality. Thus, the sampling rate was optimally adjusted to 10 MHz by a trial and error procedure, and a low pass filter of 5 MHz was applied following the Nyquist criterion.

Figure 6.2 shows a photograph of the experimental setup used for the LDV measurements. Measurements could not be taken closer than 0.015 m to the lower wall and 0.01 m to the upper wall for the axial velocity due to the limitations presented by the physical boundaries of the experimental setup. Since it was decided to obtain vector plots by using the axial and radial velocities, the limits on the measurements were set by the ability to measure the axial velocity. A simple schematic diagram of the experimental setup is presented in Figure 6.3 illustrating the traversing mechanism and the data acquisition system. The same impinging jet setup as the one used for flow visualisation experiments presented in chapter four has been used. As shown in Figure 6.3, the LDV probe was attached to a robotic arm. The robotic arm served as the traversing mechanism.

Information about the measurement position was fed to the robot controller through the ***LabView*** software (installed on a Pentium based personal computer, PC1). The ***DataVIEW*** software (installed on a 486 personal computer, PC2) was used to communicate between the LDV system and the ***LabView*** software in PC1. Once a measurement position was assigned to the robotic arm through ***LabView***, the ***DataVIEW*** software was also activated to record measurements. The raw data along with the information about mean velocity (Equation (6.4)) and root mean square

(r.m.s.) fluctuating velocity (Equation (6.5)) were recorded and stored in PC2. After the measurement at a point was completed, the mean and r.m.s. fluctuating velocities were transmitted to PC1. The data acquisition system in PC2 had a facility to specify the maximum number of samples and maximum sampling time. The data acquisition was stopped depending on which of these two events occurred earlier. For the present experiment, a maximum of 10,000 samples was specified for each point measured with a maximum sampling time of 5 minutes. For the measurements, the percentage of valid counts was around 90%. Therefore, for each measurement location, a total of approximately 9000 valid samples were recorded. The data rate varied between 100 and 1000 Hz for all measurements. In regions of high turbulence intensity (> 10%), a data rate of 400 to 1000 Hz could be maintained. In regions of lower turbulence intensity, the data rate fell to values lower than 400 Hz. The minimum data rate could be maintained at about 100 Hz for all measurements that were recorded.

Whole field LDV measurements were carried out for all cases without foam and for the cases with the G10 foam with a foam height, h_p=0.05 m (Figure 4.1). For fluid heights H=0.15 and 0.1 m, a 20x20 grid was used, whereas for a fluid height H=0.05 m, a 20x16 grid was used for the measurements.

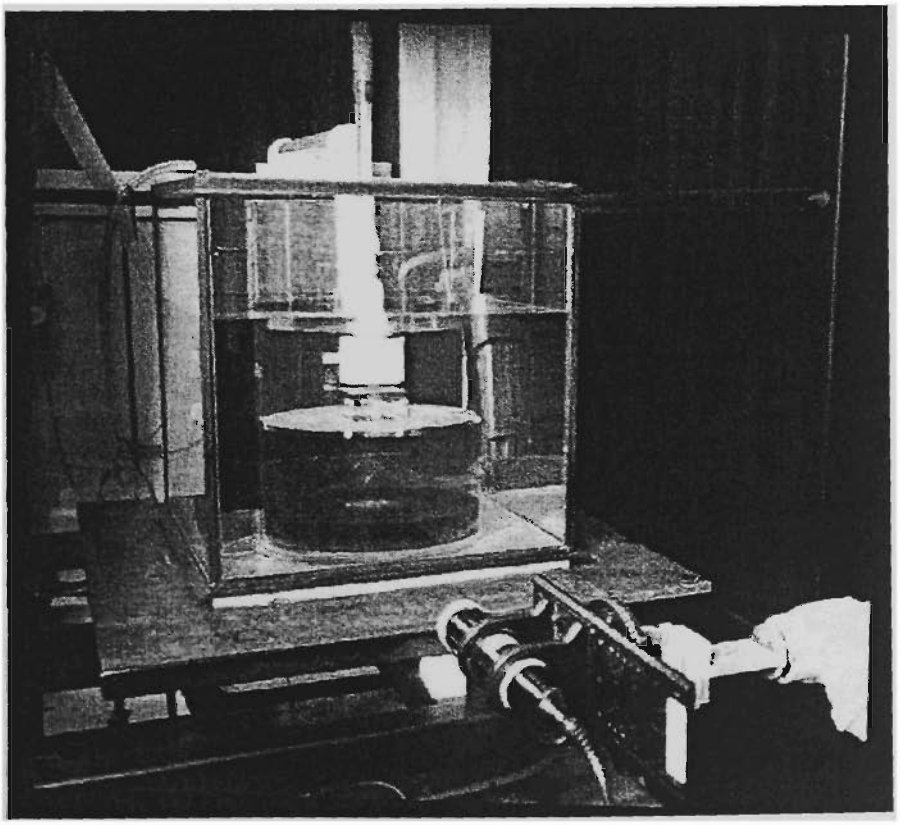

Figure 6.2: Photograph of the experimental setup used for the LDV measurements.

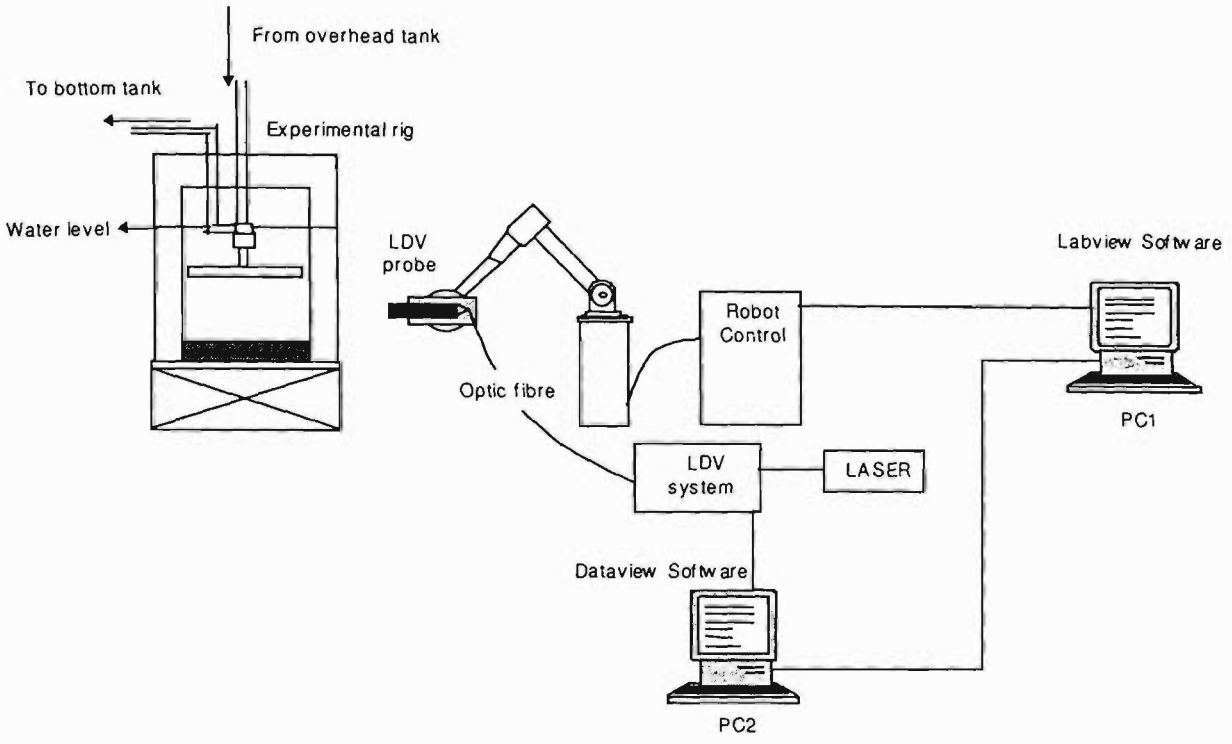

Figure 6.3: Schematic diagram of the experimental setup used for the LDV measurements.

6.4 Seeding particles for LDV measurements

Impurities present in tap water were first removed by passing it through a filter (particulate reduction of 99.96% up to 1-2 μm particles). Finely ground pearl particles, Magna Pearl (average size ~1 μm) supplied by Bronson and Jacobs, were then added to the water as seeding particles. Trial runs were carried out to estimate the optimum amount of seeding particles. It was found that after adding approximately 1 g of seeding particles, the data rate in the majority of the measured domain remained at or above 400 MHz. Additional seeding particles did not change the data rate significantly. Due to the presence of stagnant regions in the flow as the fluid travelled from the bottom tank to the overhead tank and then into the experimental rig, there was a reduction in the concentration of the seeding particles in the flow over a period of time (typically one hour). This reduction necessitated additions of approximately 0.5 g of seeding particles per hour. The tank situated at a lower level than the experimental rig (the bottom tank in Figure 6.3) acted as the reservoir of water. Adding seeding particles to the bottom tank ensured that their addition did not interfere with the flow in the experimental rig itself. Typically,

around 5 hours were required to complete one run of an experiment consisting of 400 data points, corresponding to 20x20 grids for H=0.15 m and 0.1 m.

6.5 Measurement considerations and error estimation

6.5.1 Uncertainty analysis

Using the repeatability of measurements, the uncertainty in the estimation of the mean and fluctuating quantities was checked. In order to check for accuracy in the entire flow domain (from regions of high turbulence intensity to regions of low turbulence intensity), a total of five sweeps was employed in the radial direction to measure the axial mean and r.m.s. velocities. The averaging time varied from 9s to 90s corresponding to data rates of 1000 Hz and 100 Hz, respectively. Figure 6.4 illustrates the repeatability measurements carried out for the mean and r.m.s axial velocities. The mean velocity in Figure 6.4(a) shows considerable overlap among the five different traverses, indicating good repeatability. The r.m.s velocity in Figure 6.4(b), on the other hand, shows a larger scatter. The uncertainty in the mean velocity measurements was found to be within ±2%, and within ±10% in the r.m.s. velocity measurements. The radial mean and r.m.s. velocities were found to have similar repeatability results to the axial ones.

6.5.2 Positioning errors

The positioning error can be attributed to three factors:

1. Spatial accuracy of the traversing mechanism, in this case the robotic arm,
2. The non-cylindrical nature of the container and
3. Inaccuracy in the positioning of the nozzle of the jet exit.

The second and third errors are related, since an accurate positioning of the nozzle at the geometrical centre of the container requires an *apriori* knowledge about the centre.

The spatial accuracy of the traversing mechanism was found to be of the order of $\pm 10\mu m$. The finite size of the measuring volume also contributed to the positioning error. However, these errors were small in comparison with the error in the positioning of the origin of each traverse, corresponding to the cylinder centreline, due to the noncircular cross-section of the cylinder. The origin for each traverse was fixed by assuming the cylinder to have a perfectly circular cross-section. This is not strictly the case because the cylinder was made of acrylic which is not a structural material. For the measurements, it was also assumed that the centre of the jet coincided with the centre of the cylinder. The position of the centre of the jet with respect to the centre of the cylindrical tank has been estimated through measurements as described in the next section.

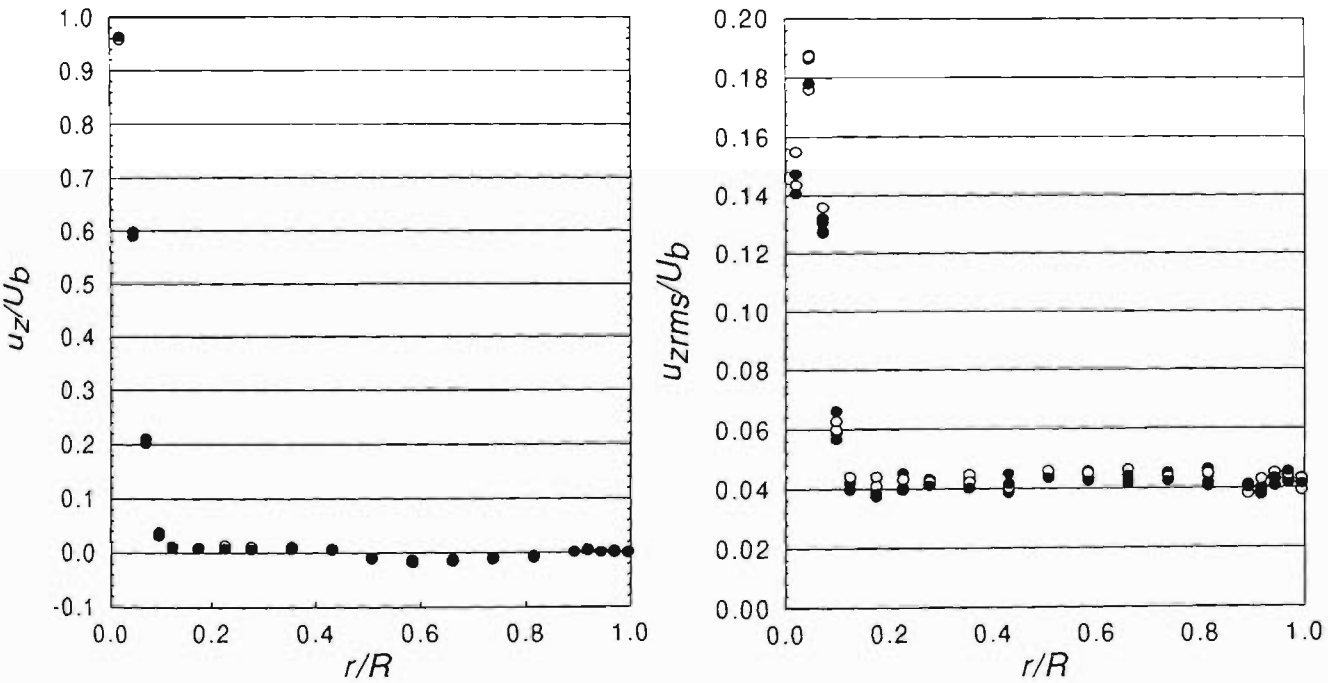

(a) Axial mean velocity (b) Axial r.m.s. velocity

Figure 6.4: LDV measurements representing the magnitude of the uncertainty in the mean and r.m.s. velocities through repeatability tests. A total of five repetitions has been performed at each measurement location. Notice that for the axial velocity measurements in Figure 6.4(a), there is considerable overlap in the measurements indicating excellent repeatability.

6.5.3 Adjustment for deviation of the centre of the jet from the centre of the tank

As mentioned in the previous section, the position of the centre of the jet (or nozzle from which the jet issues) and the centre of the cylindrical tank might not be aligned. In order to evaluate this error, a traverse was carried out through the tank centreline for the case without foam with a fluid height $H = 0.15$ m. In Figures 6.5(a) and 6.5(b), the axial mean and r.m.s. velocity measurements, respectively, are given through the tank centreline at a height of $z = 0.135$ m from the tank base. As shown in these figures, there was a deviation of approximately 3 mm in the case of the axial mean and r.m.s. velocities between the tank and jet centres. This deviation was observed in all experiments that were conducted, and therefore, it can be considered to be a systematic error. Since the origin for the traverses had already been fixed, using the circular tank as the reference, it was decided to first take measurements assuming the origin to be at the apparent tank centre. The results were then adjusted by 3 mm to account for the misalignment.

6.5.4 Location of the measuring volume

The different refractive indices of the media through which the laser beams pass before forming a measuring volume needed to be taken into account to calculate the actual position at which the beams intersect (i.e., to calculate the location of the measuring volume). Otherwise, a shift exists between the actual measuring volume location and its apparent position in air. The information about the actual position thus obtained was entered into the ***LabView*** software (see Section 6.3).

The actual location of the measuring volume was determined by performing a beam path analysis using ***Autocad***. Figure 6.6 illustrates an example of the beam path analysis performed when the two beams are horizontally aligned. This is the case when the radial mean and r.m.s. velocities have to be measured. The figure shows the top view of the experimental setup. For axial velocity measurements, the two beams would be aligned vertically.

One quarter of the acrylic cylindrical tank and the square glass tank is shown in Figure 6.6. The distance from the LDV probe to the centreline of the cylindrical tank is 558.05 mm, whereas the distance of the probe from the outer surface of the square glass tank is 330.45 mm. The external half side length of the square glass tank

is 227.60 mm. These measurements are shown in Figure 6.6. For the analysis, the curved side of the cylindrical tank is approximated as 0.05 degree facets. As a reference for the analysis, the direction of the "Observer" is shown in the figure with an arrow. **X-X** and **Y-Y** represent lines passing through the centreline of the cylindrical tank. For all calculations, the refractive indices, RI, of water, air, acrylic and glass are taken to be equal to 1.330, 1.000, 1.490 and 1.510, respectively. The thickness of the square glass tank and the cylindrical acrylic tank are 12.6 and 5 mm, respectively. The focal length of the beam and the beam separation are 500 and 40 mm, respectively. With these input parameters, the change in the path of the laser beams due to the refractive index changes was calculated using ***Autocad***.

It was decided to take into account the shift in the location of the measuring volume only when it was greater than ± 1 mm. For the vertical beam alignment (axial velocity measurements), the shift was never greater than 1 mm. Therefore, no correction was made for axial velocity measurements.

For the horizontal beam alignment (radial velocity measurements) as shown in Figure 6.6, the shift was found to be greater than 1 mm, but in the direction opposite to that of the "Observer" for positions close to the centre of the cylindrical tank. For example, in Figure 6.6, the shift in the location of the measuring volume is 1.318 mm and in the direction opposite to that of the "Observer". As one goes away from the centre, for the horizontal beam alignment, the shift first decreases and then increases but towards the "Observer". In the case of positions at 175, 180, 185 and 190 mm away from the centre of the tank, for which measurements were recorded, the shift in the location of the measuring volume was found to be greater than 1 mm and in the direction of the "Observer". Thus, in the case of the horizontal beam alignment, five positions corresponding to the centre of the tank and 175, 180, 185 and 190 mm away from the centre of the tank had to be corrected for the shift in the location of the measuring volume. These positions and the corresponding shifts are presented in Table 6.1.

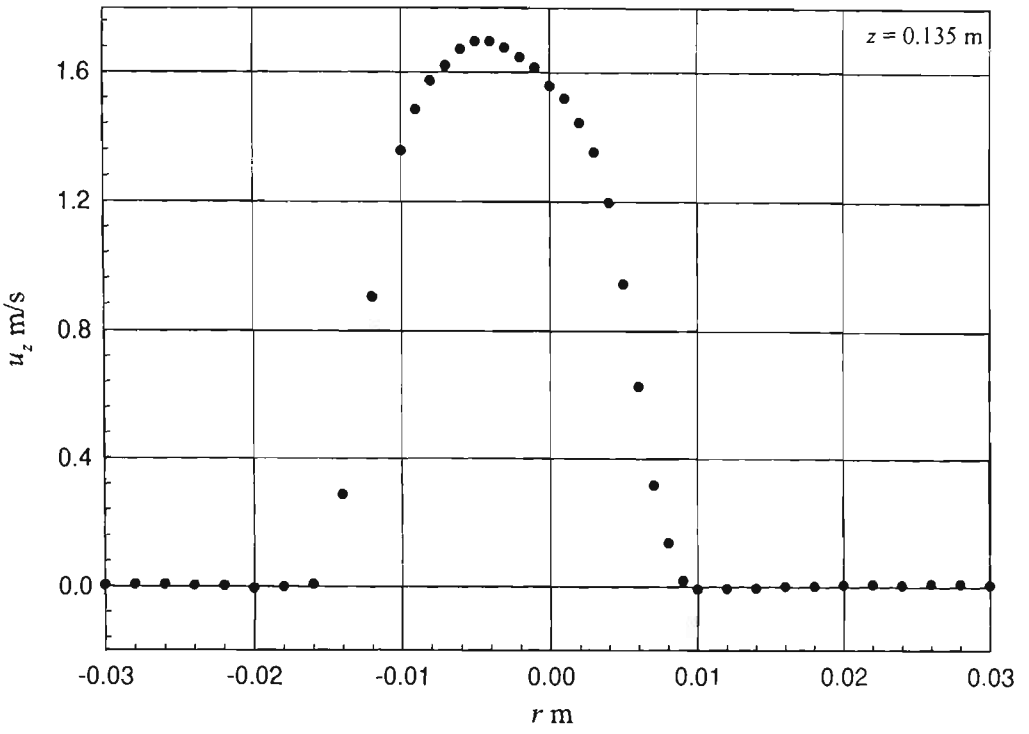

(a): Axial mean velocity profile through tank centreline.
H=0.15 m, h_p=0.0 m, U_b=1.6 m/s

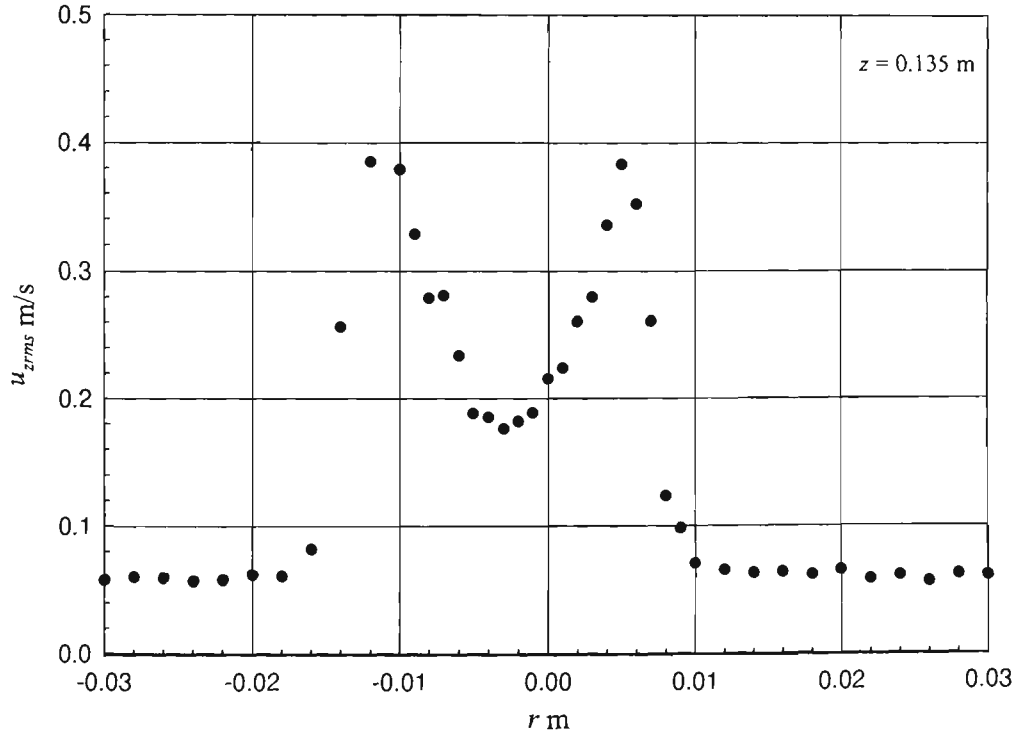

(b): Axial rms velocity profile through tank centreline.
H=0.15 m, h_p=0.0 m, U_b=1.6 m/s

Figure 6.5: LDV measurements indicating the deviation of the centre of the jet from the centre of the tank.

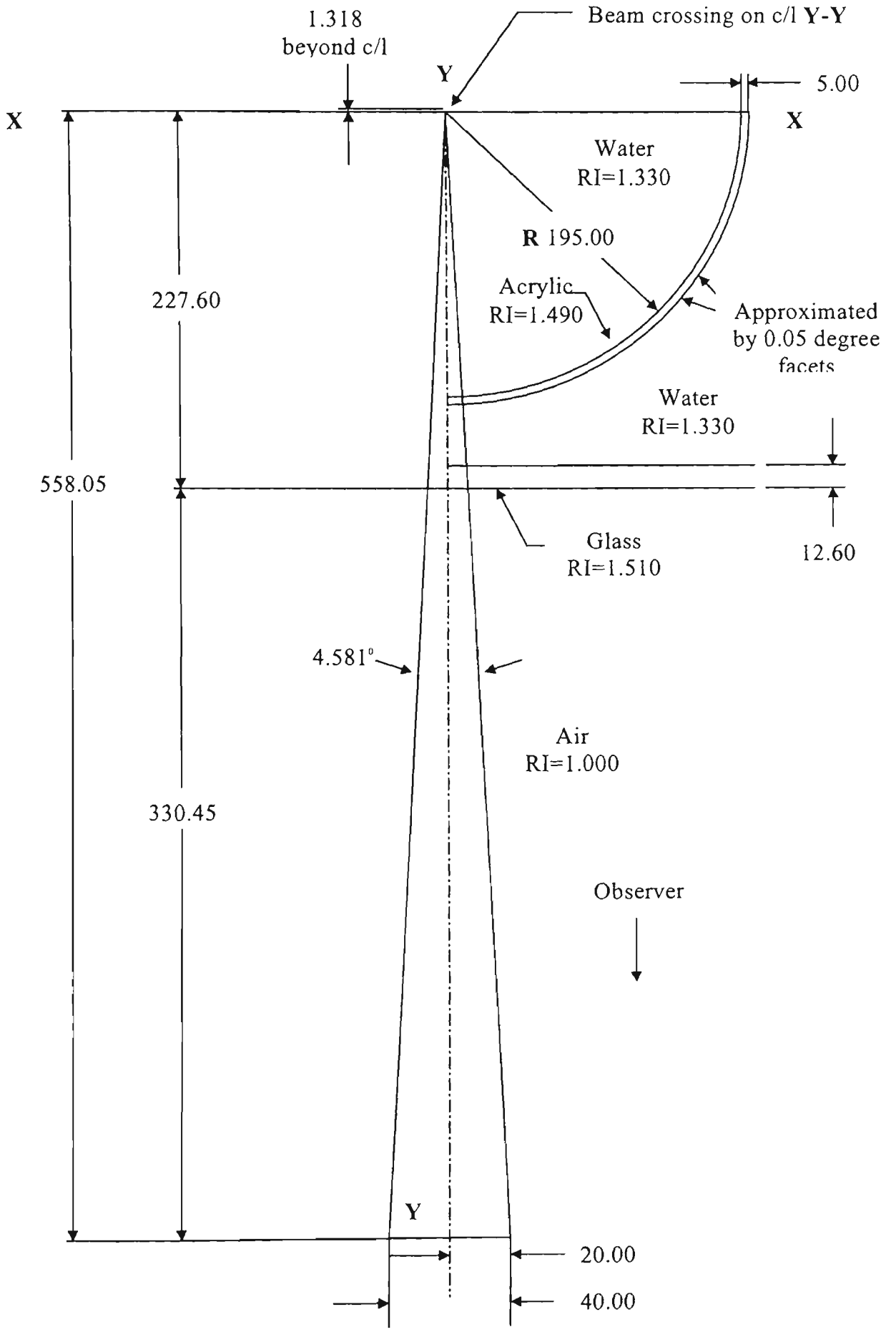

Figure 6.6: Horizontal beam analysis on centreline axis **Y-Y**. All measurements are in mm.

Table 6.1: Shift in the location of the measuring volume in case of the horizontal beam alignment (corresponding to the radial velocity measurements). The positive sign indicates that the apparent shift is away from the observer. The negative sign indicates that the shift is towards the observer. Figure 6.6 indicates the direction of the "Observer".

Position from centreline of tank (mm)	Apparent shift in the position (mm)
0	+1.318
175	-2.813
180	-4.890
185	-6.686
190	-8.633

6.6 Numerical simulations

Details of the governing equations used for the axi-symmetric system with a fluid and porous layer, the boundary and interface conditions and the numerical methods used can be found in chapter five, and they are not repeated here. In the next section, the numerical results are compared quantitatively with the LDV measurements.

6.7 Results and Discussion

6.7.1 Measurements and simulations without foam

As discussed earlier, for the measurements, a 20x20 grid was used for H=0.15 and 0.10 m, whereas a 20x16 grid was used for H=0.05 m. The limits for measurements were set by the ability to measure the axial velocity (see Section 6.3). In the results, comparison with the experimental vector plots and streamtraces give an indication of the ability of the numerical model to predict the gross flow characteristics. The profiles of mean axial and radial velocity as well as the turbulence kinetic energy have also been compared to give a quantitative comparison between the CFD simulations and LDV measurements.

6.7.1.1 Vector plots and streamtraces

Figure 6.7 gives a comparison between the experimental and numerically predicted vector plots. Frames (a), (c) and (e) are the experimental results, whereas frames (b), (d) and (f) are the simulated results for H=0.15, 0.1 and 0.05 m, respectively. The streamtraces have been superimposed on the vector plots for visualising the gross flow pattern. For all the heights considered, there is only a single circulating cell occupying the flow domain. These results are in agreement with the flow visualisations given in Figures 4.4, 4.5 and 4.6 of chapter four. The simulations reproduce the single circulating cell, although the position of the cell is not predicted accurately. This discrepancy could be because the actual flow can have unsteady characteristics. It has been reported that impinging round jet flows in an enclosed cylinder are toroidal (Ngamsirivadhana, 1996). The frequency of oscillations of the cell depends on the aspect ratio and the jet velocity. However, for the present simulations, this aspect of the flow has been ignored, and the flow is approximated to be steady state.

The effect of decreasing liquid height on the horizontal position of the centre of re-circulation for cases without foam is seen in Figure 6.8. The vertical axis, R_c/R, represents the normalised radial position of the centre of the dominant re-circulation from the centreline. The horizontal axis, H, represents the height of the fluid layer in metres. Comparison of results is given in Figure 6.8 as obtained from the visualisations, measurements and simulations. The LDV measurements and visualisation results show a similar trend. The centre of re-circulation moves closer to the wall with a decreasing liquid height. However, the simulations indicate negligible change in the position of the re-circulation with liquid height. As indicated above, this anomaly could be due to the fact that the flow has unsteady and/or three-dimensional characteristics, which the model does not take into account.

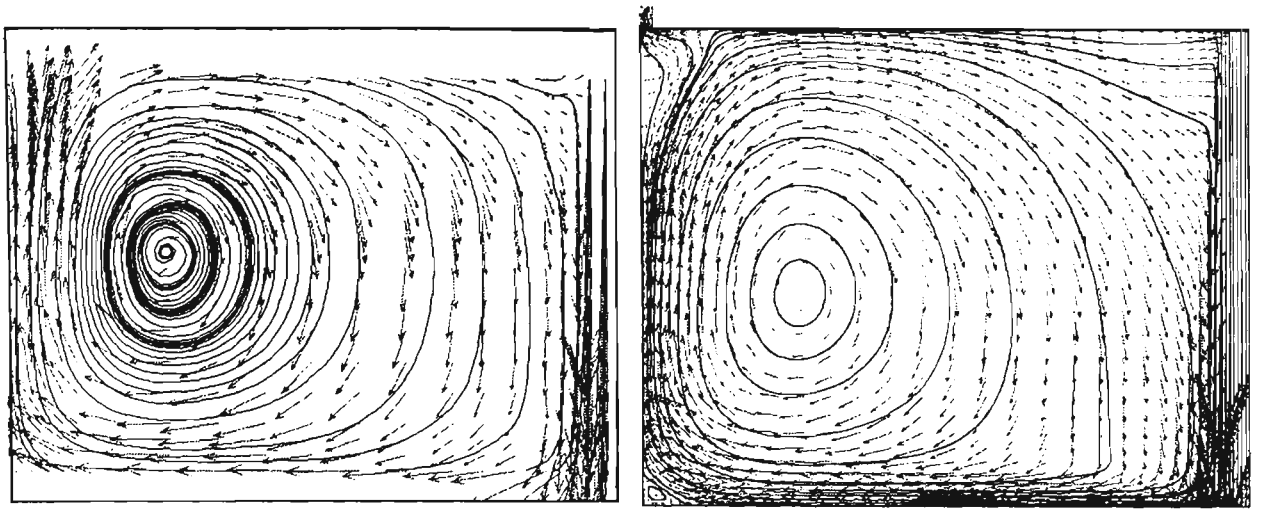

(a) LDV measurements (b) CFD simulation

H=0.15 m, h_p=0.0 m, U_b=1.6 m/s

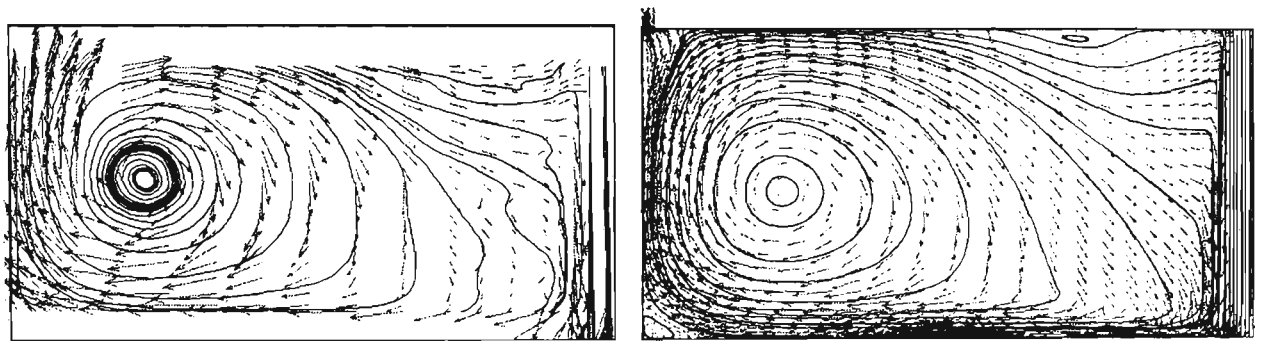

(c) LDV measurements (d) CFD simulation

H=0.1 m, h_p=0.0 m, U_b=1.6 m/s

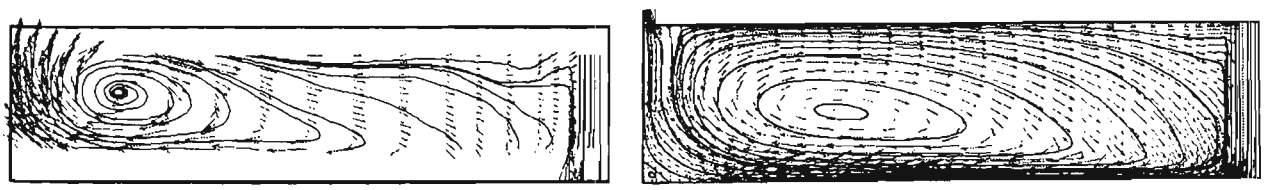

(e) LDV measurements (f) CFD simulation

H=0.05 m, h_p=0.0 m, U_b=1.6 m/s

Figure 6.7: Measurements and simulations for the cases without foam. Vector plots and stream traces.

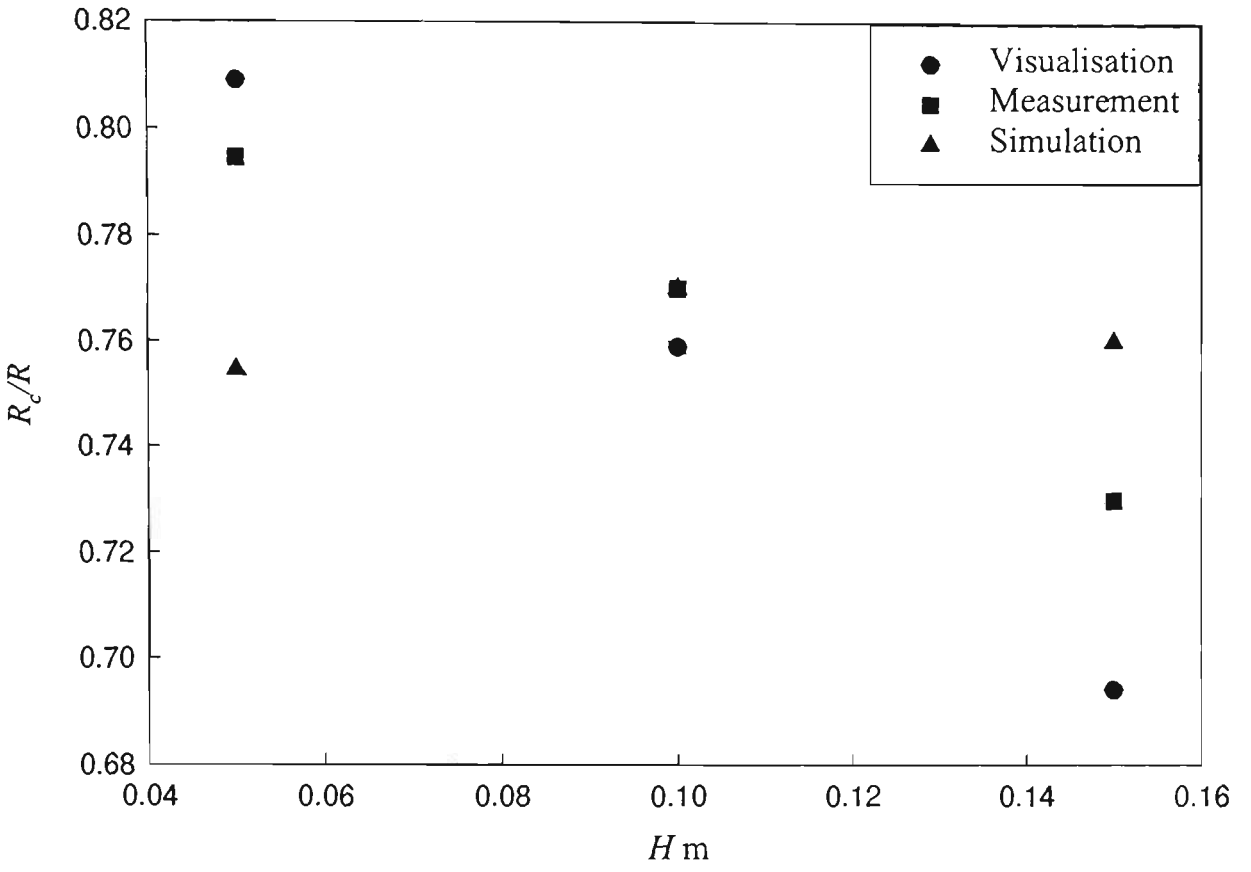

Figure 6.8: Change in the horizontal position of the centre of re-circulation as a function of the fluid height.

6.7.1.2 Mean axial velocity profiles

Figures 6.9, 6.10 and 6.11 show comparisons for the axial velocity profiles for fluid heights of 0.15, 0.1 and 0.05 m, respectively. In these figures, the profiles have been plotted for six different axial locations covering the entire measurement plane. Frames (a) and (b) in each figure present comparisons when a flat profile (CFDFP) and a fully developed profile (CFDFDP), respectively, are used in the predictions at the exit of the jet. Also, in each figure, the effect of grid refinement has been shown.

A comparison between frames (a) and (b) in each figure shows firstly the effect of the two profiles at the exit of the jet. It can be seen that both profiles at the jet exit fail to predict the flow close to the jet and in the region close to the jet centreline. With both flat and fully developed profiles, the reduction in the centreline velocity with axial distance is under predicted. The reason is that the flow in the pipe is still not fully developed, whereas the model assumes a fully developed or flat profile. The actual profile close to the jet exit would be closer to a developing pipe

flow with turbulent boundary layer profiles at pipe walls in the present experiment. With the specification of a flat profile, another problem is with the resolution of the flow close to the jet exit. The sudden change from a flat velocity profile in the jet as it enters the cylinder cannot be resolved numerically with any amount of grid refinement. The resulting discontinuity in the axial velocity at r/R=0.03 and 0.04 for H=0.1 m and H=0.05 m (h_p=0.0 m), respectively, is shown in Figures 6.10(a) and 6.11(a). However, the axial velocity away from the jet centreline is predicted well, regardless of the profile at the exit of the jet indicating that the jet exit profile does not play a significant role in determining the flow characteristics away from the jet centreline. Since the region of interest for the present study, is distant from the centreline of the jet, further investigation on the profile at the exit of the jet was not carried out. However, it is desirable to design future experiments ensuring a fully developed profile at the exit of the jet. Overall, Figures 6.9 to 6.11 indicate reasonable agreement between the measurements and simulations for the axial velocity.

6.7.1.3 Mean radial velocity profiles

Figures 6.12, 6.13 and 6.14 give a comparison of the mean radial velocity profiles. Here again, the frames (a) and (b) in each figure show comparisons made with two different jet exit profiles. From the figures it can be seen that for the mean radial velocity, the two profiles at the exit of the jet, do not have any significant influence on the predictions. There is good qualitative agreement between the measured and predicted profiles although there is some amount of quantitative difference. This can be seen especially after a distance of half the radius from the centreline where the model seems to predict a lower velocity than the measured value. The maximum variation in the radial velocity is approximately 35% between the measured and simulated values and occurs at z/H=0.067 for H=0.15 m in Figure 6.12, z/H=0.09 for H=0.1 m in Figure 6.13 and z/H=0.22 for H=0.05 m in Figure 6.14.

6.7.1.4 Turbulence kinetic energy profiles

Measurements were taken of the r.m.s velocities in the radial and azimuthal directions for the case of H=0.15 m and h_p=0.05 m. These measurements showed that

these two r.m.s. velocities have approximately the same magnitude for the whole flow field. Consequently, only the radial and axial components of the velocities were measured during the remaining experiments, and the measured turbulence kinetic energy was approximated by the following expression,

$$k = \frac{1}{2}\left(\sqrt{\overline{u_z'^2}} + \sqrt{\overline{u_r'^2}} + \sqrt{\overline{u_\theta'^2}}\right) = \frac{1}{2}\left(\sqrt{\overline{u_z'^2}} + 2\sqrt{\overline{u_r'^2}}\right) \tag{6.6}$$

Figures 6.15, 6.16 and 6.17 show a comparison between the measured and predicted turbulence kinetic energy. The predicted distributions agree qualitatively with the measured ones. Quantitatively, important characteristics such as the hump in the profile close to the bottom of the cylinder at z/H=0.067 for H=0.15 m in Figure 6.15 and at z/H=0.09 and 0.11 for H=0.1 m in Figure 6.16 is predicted well regardless of the jet exit profile. However, the predicted turbulence level close to the jet exit depends significantly on the jet exit profile. With a flat profile, the predicted turbulence level at the jet exit is higher than with a fully developed profile and closer to the experimental results. This difference decreases away from the jet exit. For the case of H=0.05 m, the predicted turbulence levels close to the centreline is found to be significantly lower than the measured values. One reason for such high measured values could be due to the approximation given by Equation (6.6) for the turbulence kinetic energy. This assumption may not be true for all the experiments that have been performed. A better prediction could also have been obtained by using a more appropriate profile at the exit of the jet.

Figure 6.18 shows the computed contour plot of turbulence kinetic energy for H=0.15 m, h_p=0.0 m and U_b=1.6 m/s. In Figure 6.18, the k-ε turbulence model is shown to predict higher than expected levels of turbulence in the region where the jet impinges the bottom surface (the stagnation region). This result is in agreement with previous studies carried out by Craft *et al.* (1993) and Behnia *et al.* (1999) for impinging round jet flows. However, for the present study, the region of interest is distant from the stagnation point.

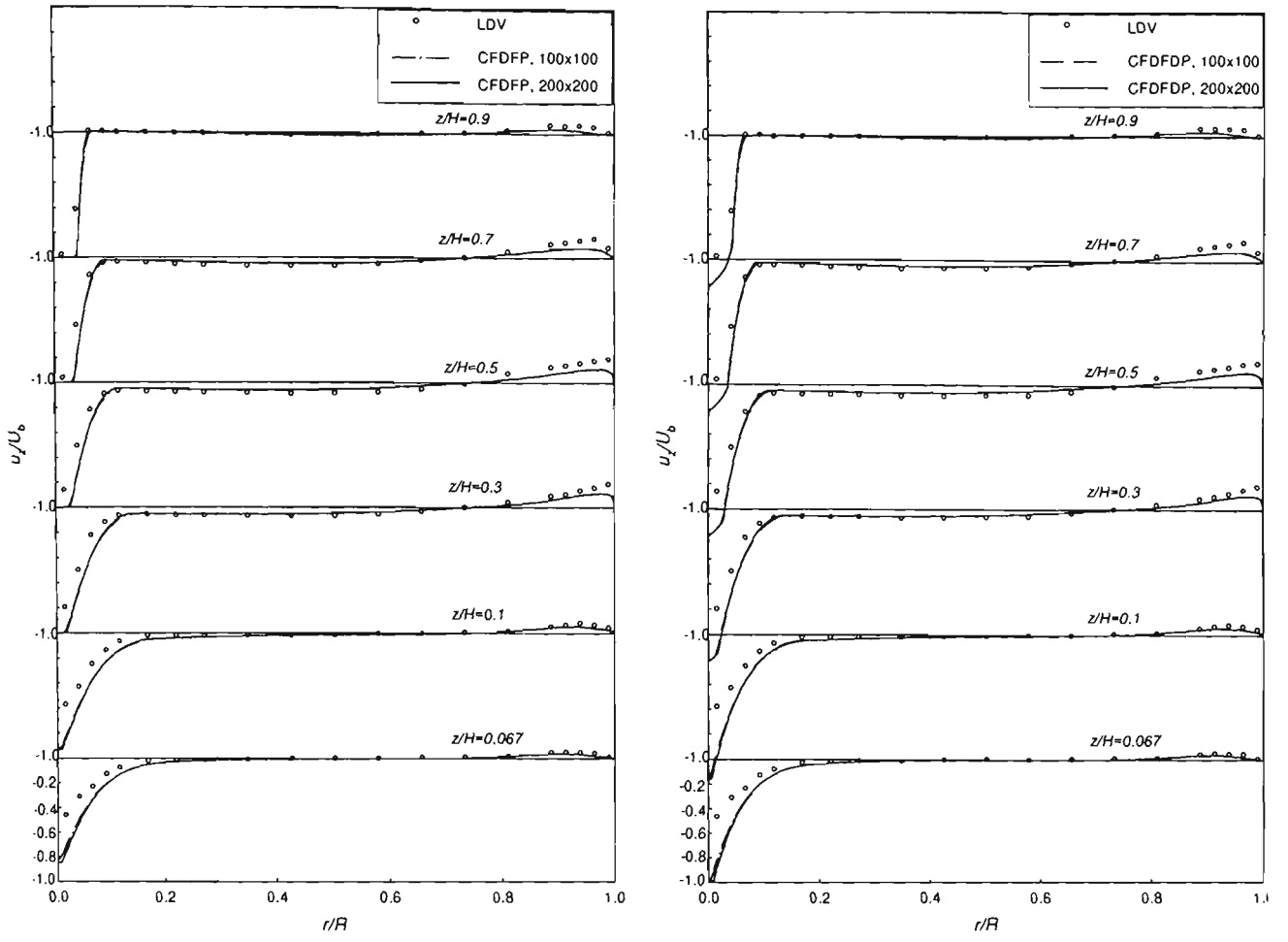

(a) (b)

Figure 6.9: Axial velocity profiles for H=0.15 m, h_p=0.0 m, U_b=1.6 m/s. Frames (a) and (b), respectively, represent simulations with a flat and fully developed profile at the exit of the jet.

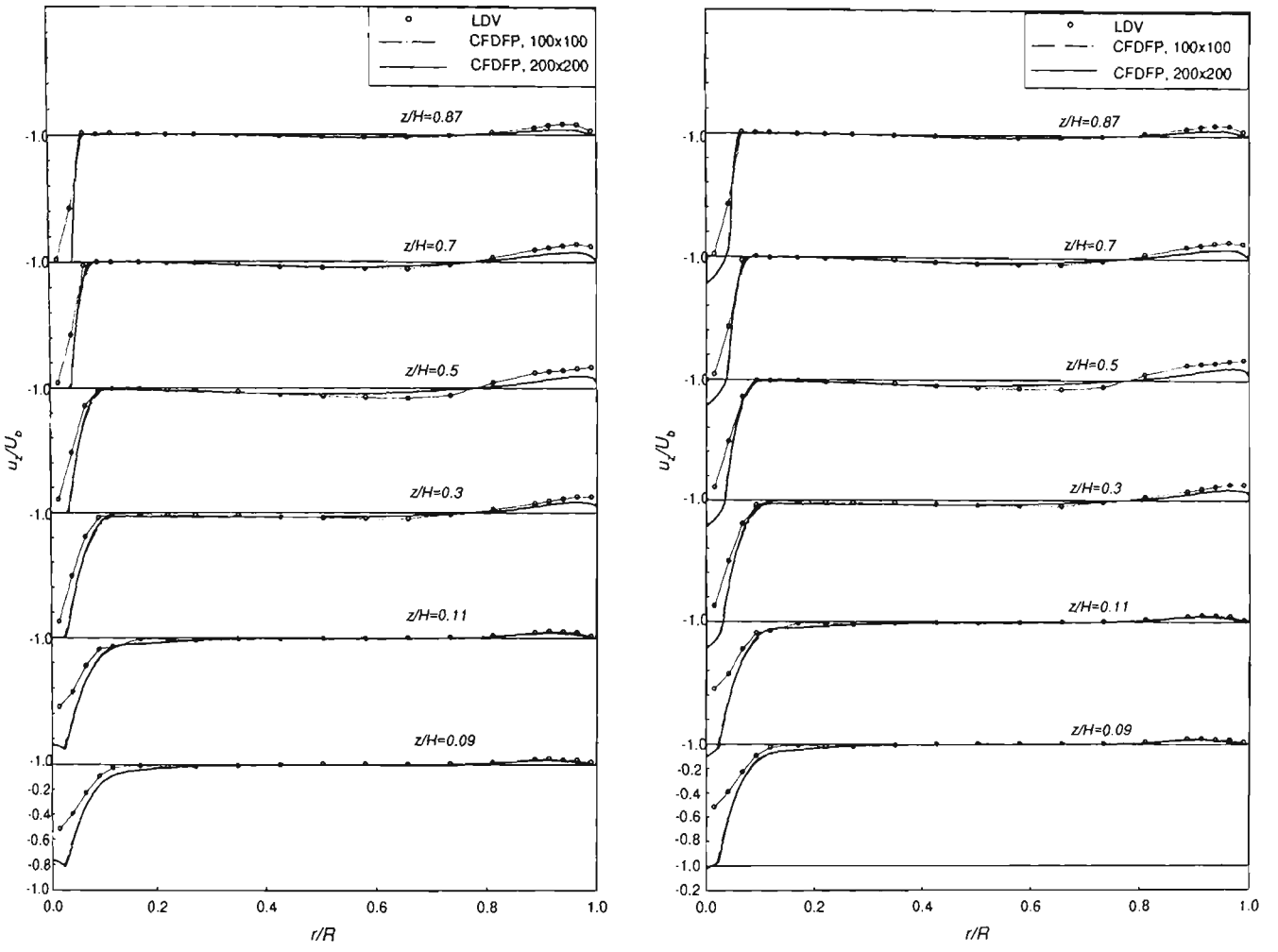

Figure 6.10: Axial velocity profiles for H=0.1 m, h_p=0.0 m, U_b=1.6 m/s. Frames (a) and (b), respectively, represent simulations with a flat and fully developed profile at the exit of the jet.

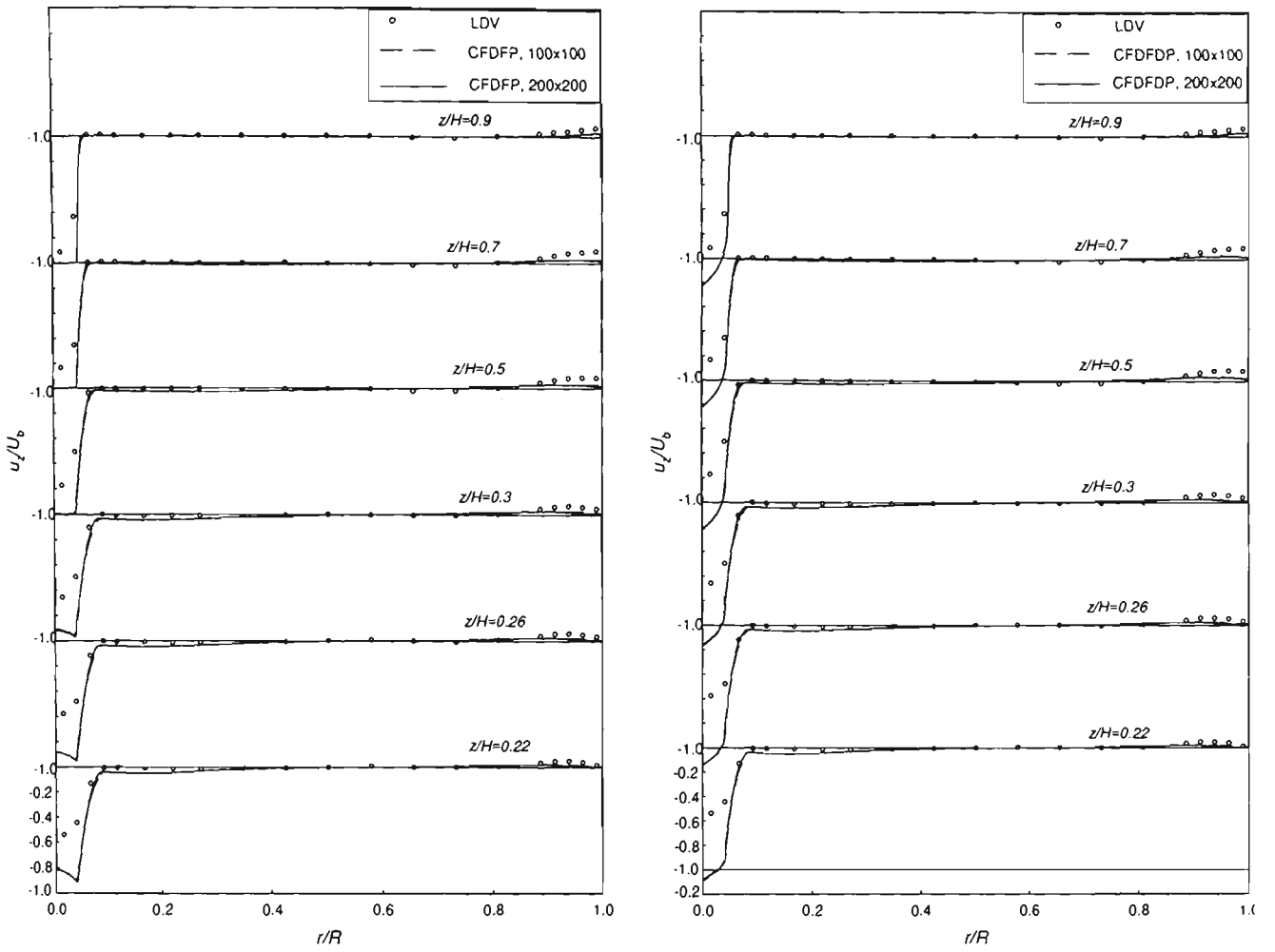

(a) (b)

Figure 6.11: Axial velocity profiles for H=0.05 m, h_p=0.0 m, U_b=1.6 m/s. Frames (a) and (b), respectively, represent simulations with a flat and fully developed profile at the exit of the jet.

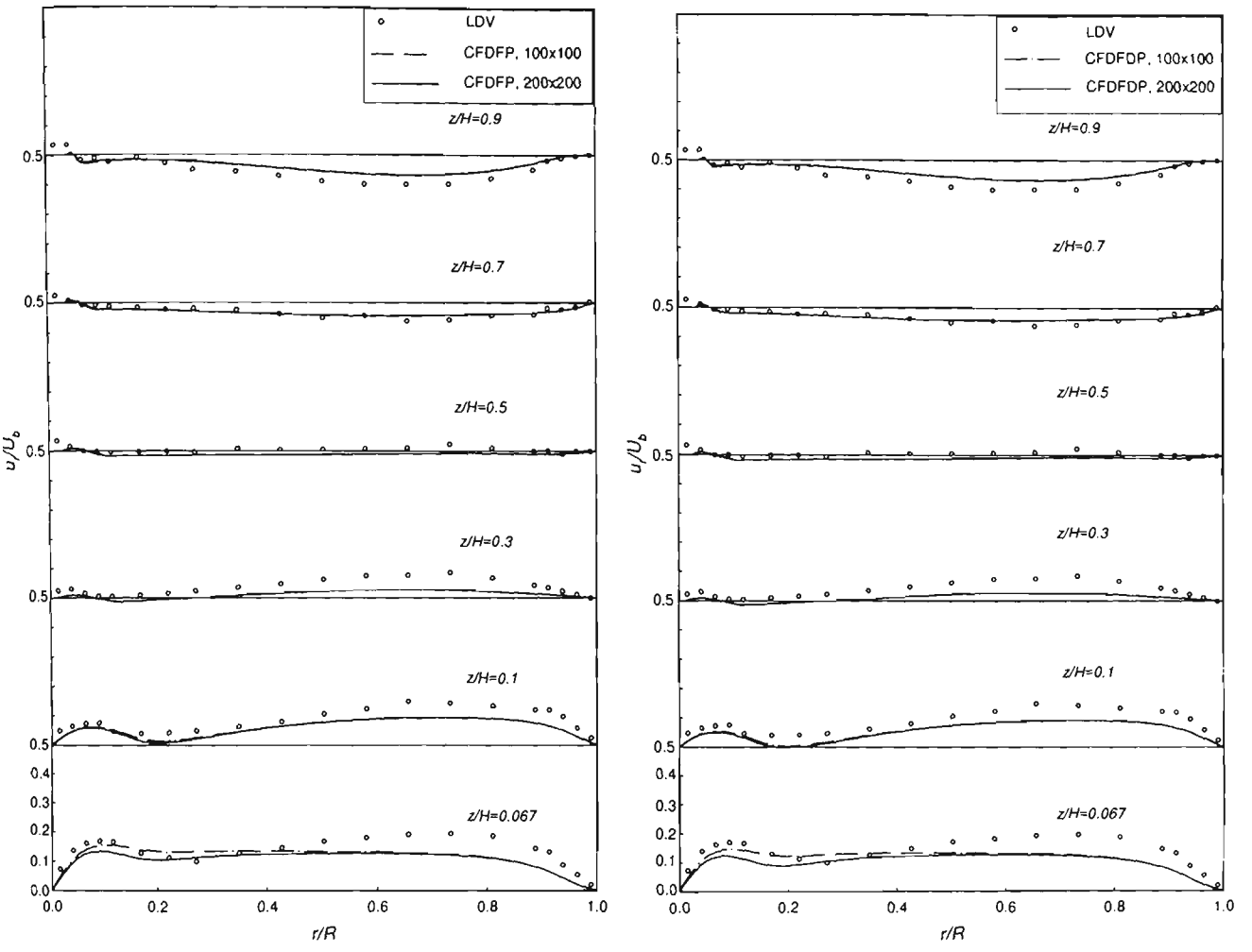

(a) (b)

Figure 6.12: Radial velocity profiles for H=0.15 m, h_p=0.0 m, U_b=1.6 m/s. Frames (a) and (b), respectively, represent simulations with a flat and fully developed profile at the exit of the jet.

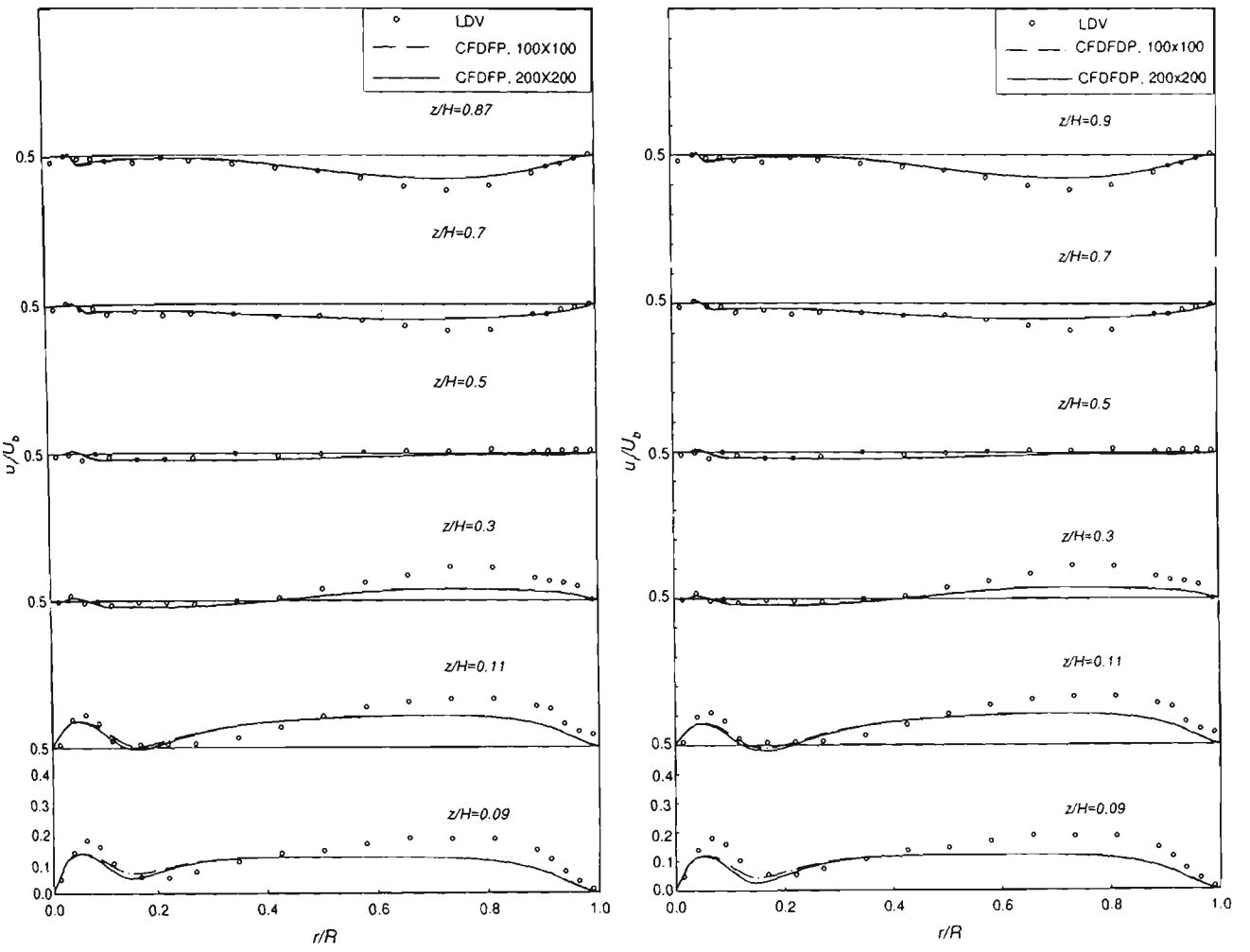

(a) (b)

Figure 6.13: Radial velocity profiles for H=0.1 m, h_p=0.0 m, U_b=1.6 m/s. Frames (a) and (b), respectively, represent simulations with a flat and fully developed profile at the exit of the jet.

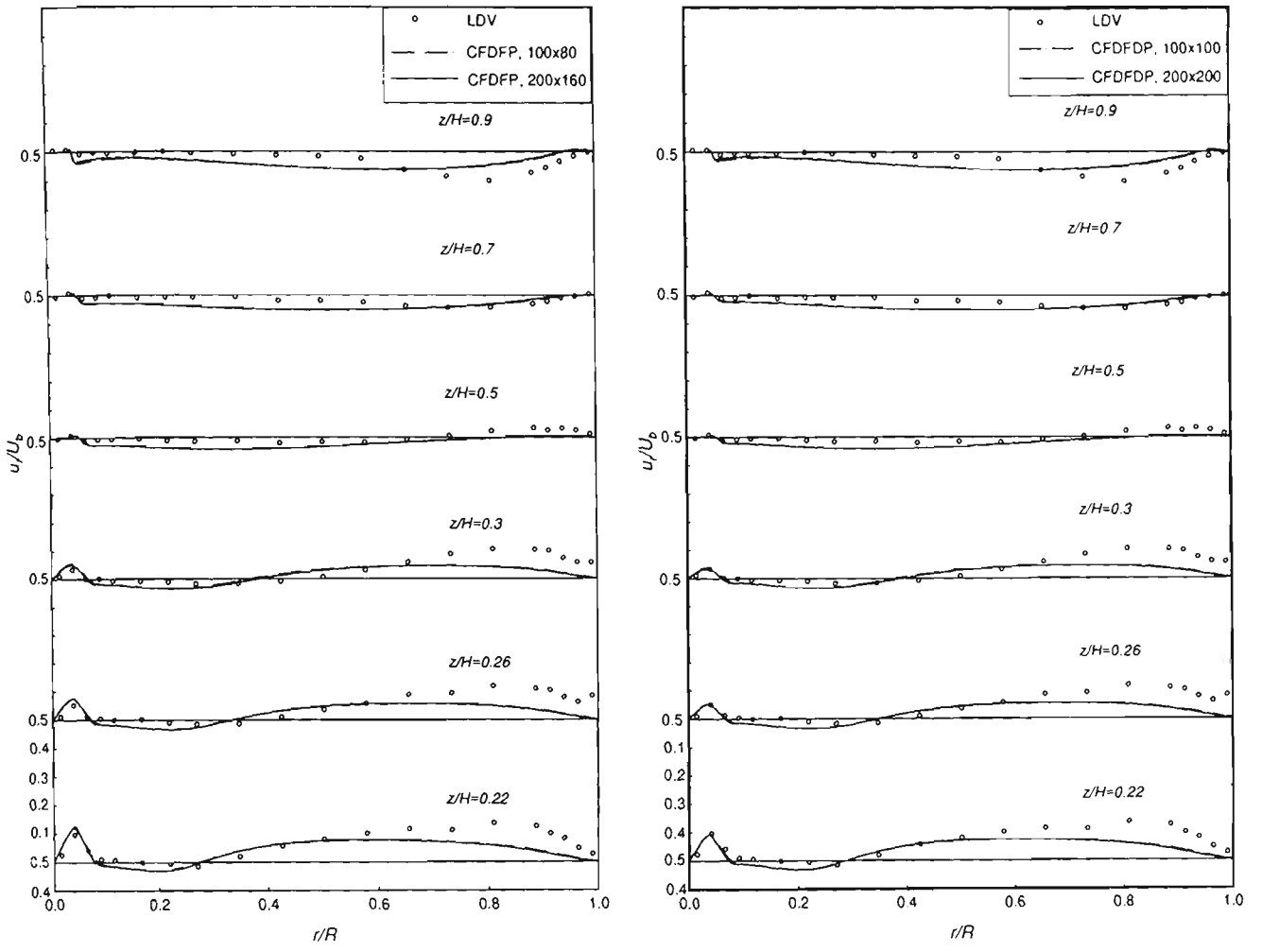

(a) (b)

Figure 6.14: Radial velocity profiles for H=0.05 m, h_p=0.0 m, U_b=1.6 m/s. Frames (a) and (b), respectively, represent simulations with a flat and fully developed profile at the exit of the jet.

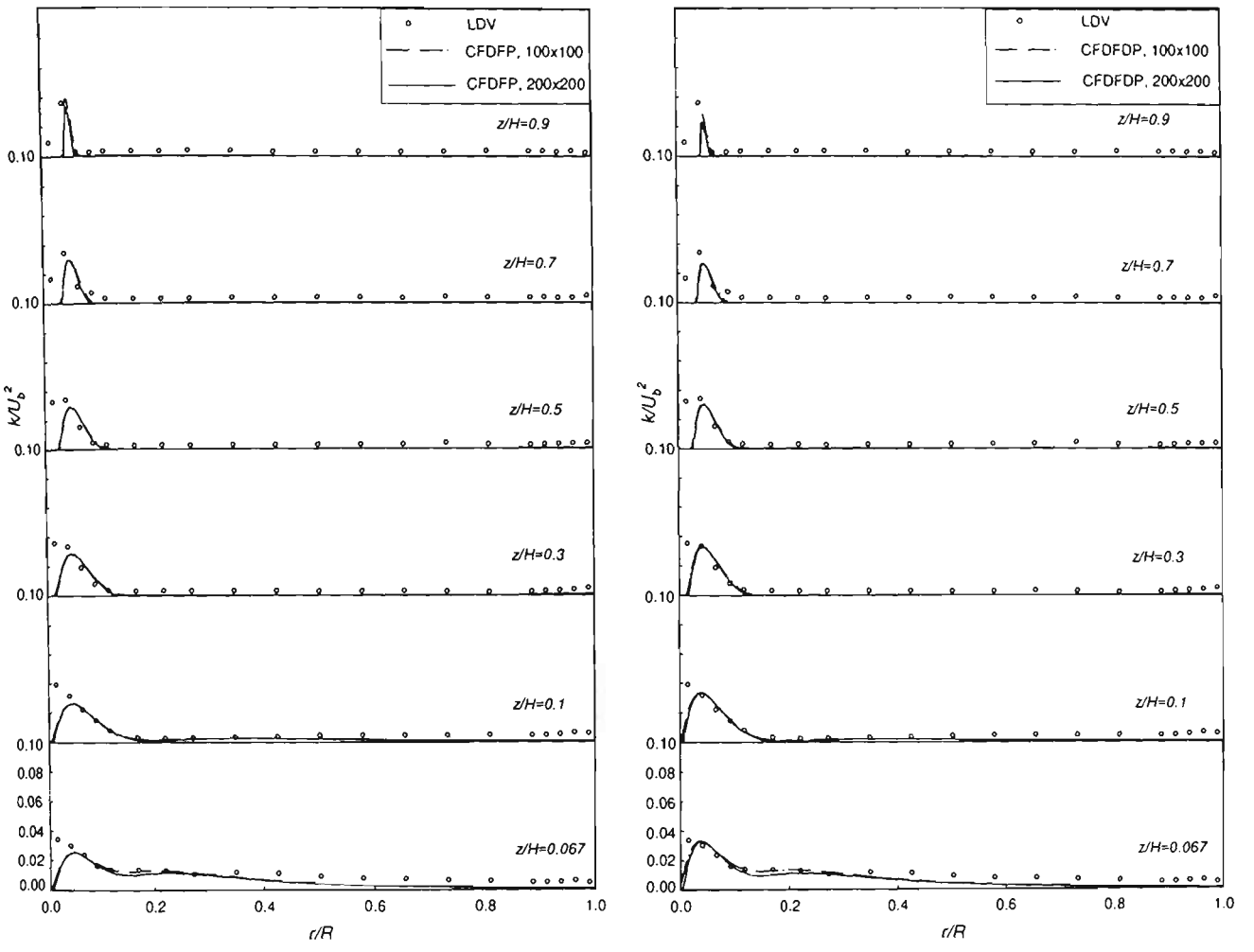

(a) (b)

Figure 6.15: Turbulence kinetic energy profiles for H=0.15 m, h_p=0.0 m, U_b=1.6 m/s. Frames (a) and (b), respectively, represent simulations with a flat and fully developed profile at the exit of the jet.

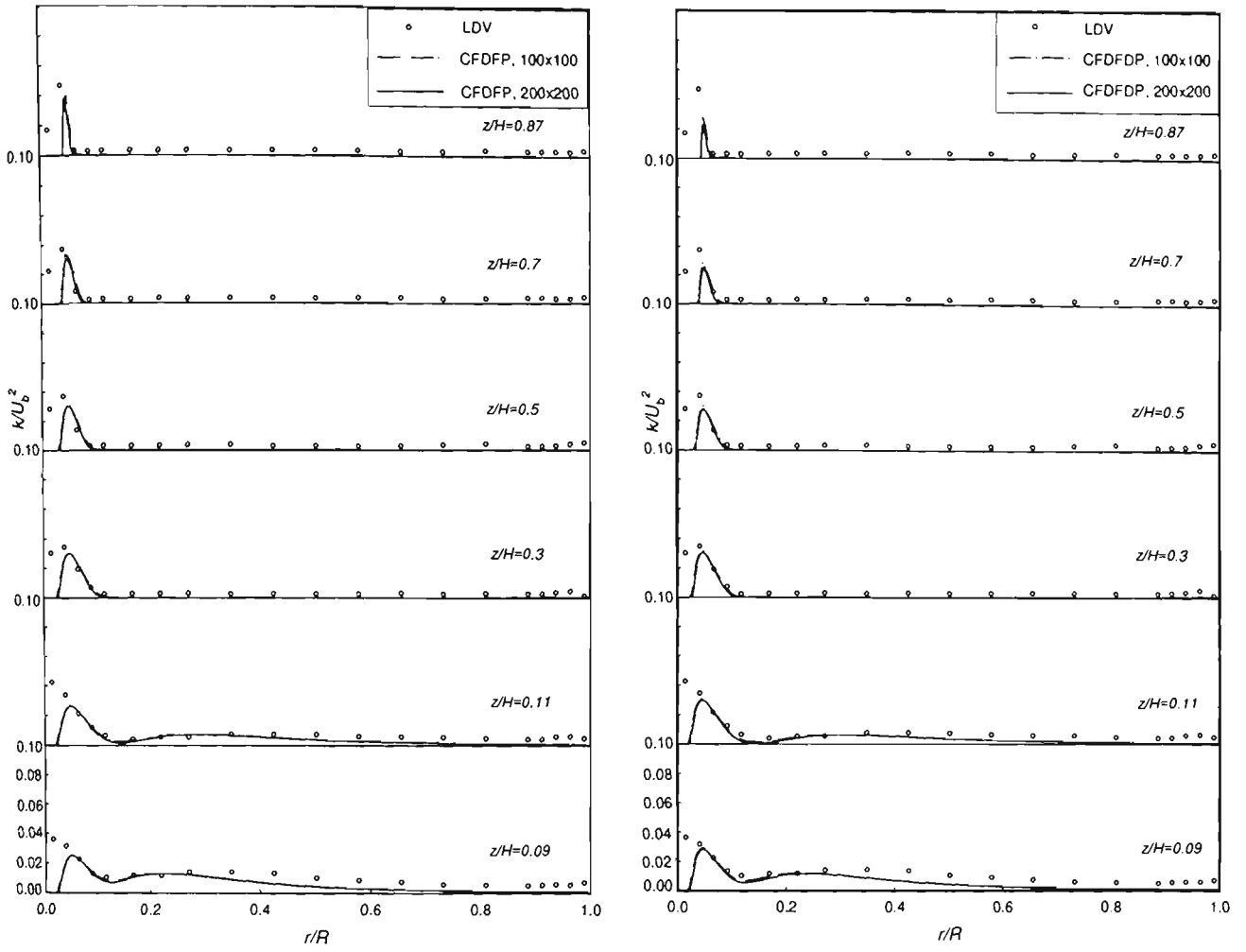

(a) (b)

Figure 6.16: Turbulence kinetic energy profiles for H=0.1 m, h_p=0.0 m, U_b=1.6 m/s. Frames (a) and (b), respectively, represent simulations with a flat and fully developed profile at the exit of the jet.

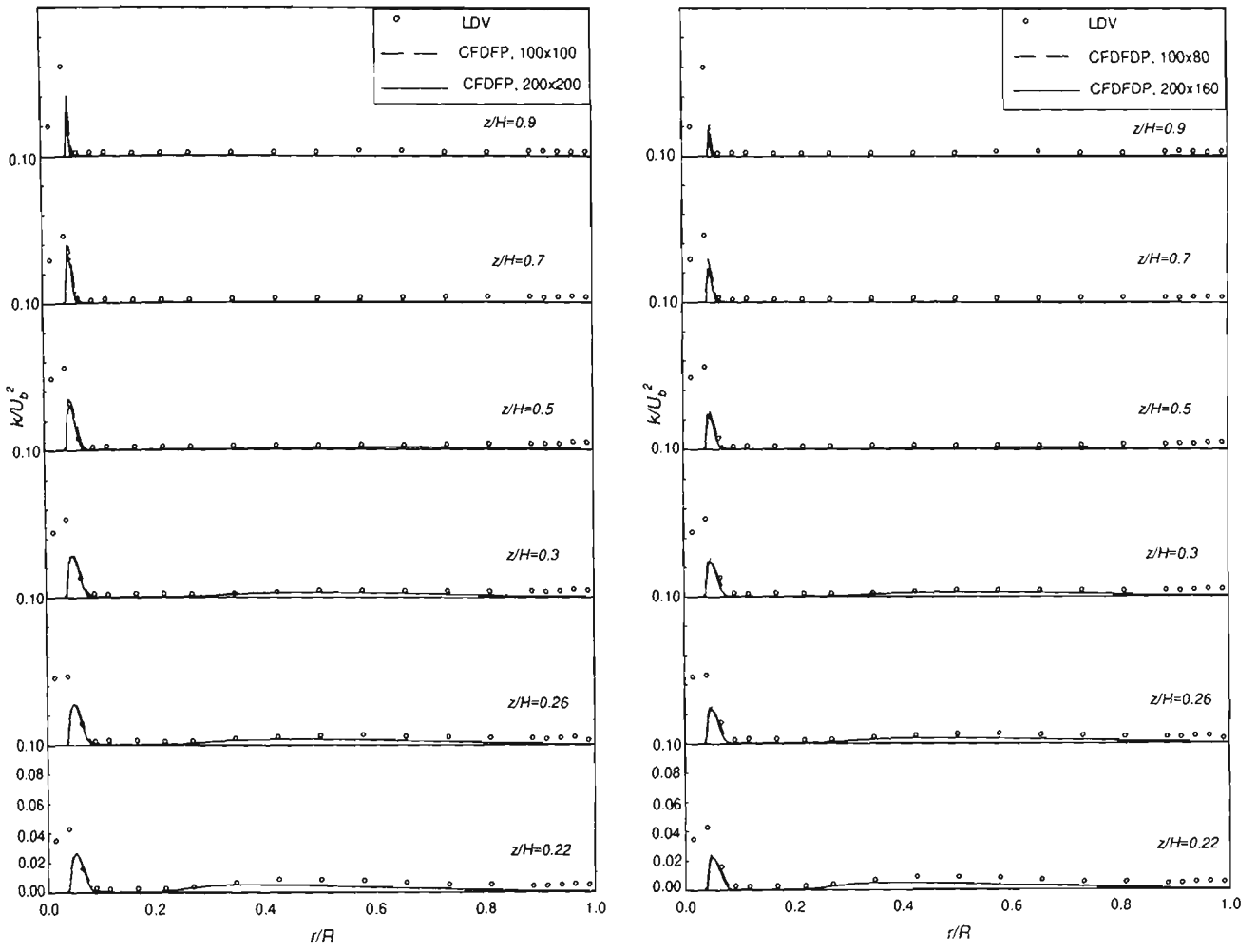

(a) (b)

Figure 6.17: Turbulence kinetic energy profiles for H=0.05 m, h_p=0.0 m, U_b=1.6 m/s. Frames (a) and (b), respectively, represent simulations with a flat and fully developed profile at the exit of the jet.

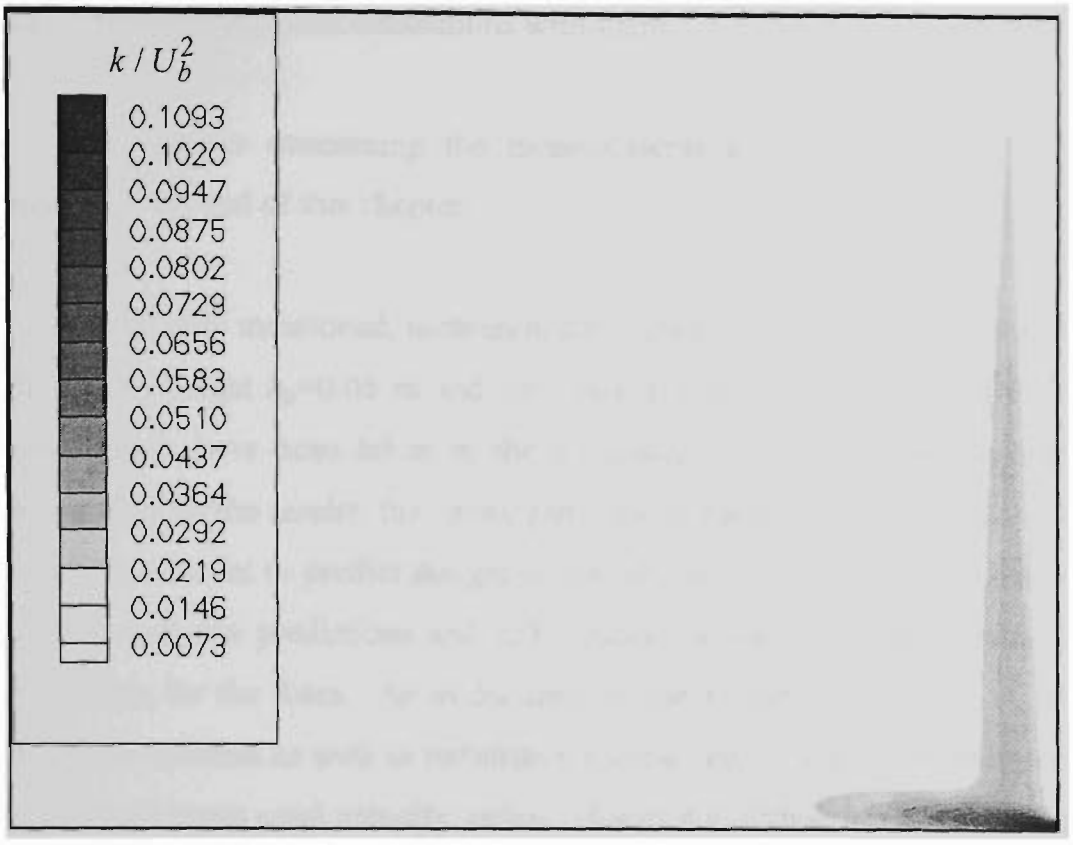

Figure 6.18: Contour plot of turbulence kinetic energy representing the stagnation point anomaly with the k-ε turbulence model.
H=0.15 m, h_p=0.0 m, U_b=1.6 m/s

6.7.1.5 Summary

In this section, comparisons are made between simulations and measurements for the cases without foam. The results presented in Figures 6.7 and 6.9 to 6.14 indicate that the low Reynolds number k-ε turbulence model used for the present simulations, is able to predict the gross flow pattern reasonably well. The turbulence kinetic energy profiles are predicted well away from the stagnation region as seen from Figures 6.15 to 6.17. There is a discrepancy in the prediction of turbulence kinetic energy close to the exit of the jet where the model predicts a lower level of turbulence especially for the lowest fluid height that was examined. However, this discrepancy does not seem to affect the predictions downstream which is the region of interest for the present study. In the next section, the predictions are compared with the measurements for the cases in which the jet of fluid impinges on the G10 foam.

6.7.2 Measurements and simulations with foam

The figures concerning the measurements and simulations with foam are presented at the end of this chapter.

As already mentioned, measurements were carried out only with the G10 foam with a foam height h_p=0.05 m and with liquid heights of H=0.15, 0.1 and 0.05 m. Measurements have been taken in the fluid layer due to the opaque nature of the porous foam. In the results, the vector plots and streamtraces give an indication of the ability of the model to predict the gross flow characteristics. Comparisons have been made between the predictions and LDV measurements with laminar and turbulent flow models for the foam. As in the cases without foam, the profiles of mean axial and radial velocities as well as turbulence kinetic energy have been compared. Also, the predicted mean axial velocity, radial velocity and turbulence kinetic energy in the foam have been reported to give some idea about the effect of turbulence modelling in the porous medium. As mentioned in chapter five, simulations were carried out by using a laminar flow model and two different turbulence models for the porous foam. Since the results with turbulence model TM2 (using Darcy and Forchheimer modification terms in the k and ε equations) and the laminar flow model were found to be identical, the results are presented here with model TM1 (using only Darcy damping in the k and ε equations) and the laminar flow model.

6.7.2.1 Vector plots and streamtraces

Figures 6.19, 6.20 and 6.21 give a comparison for the vector plots and streamtraces obtained from the LDV measurements and CFD predictions for H=0.15, 0.1 and 0.05 m and h_p=0.05 m. In these figures, frames (a), (b) and (c), respectively show the measurements, simulation results with turbulent flow model TM1 and simulation results with a laminar flow model for the foam. The similarity between the results obtained with a laminar flow model and turbulence model TM2 for the foam can be discerned by comparing frame (c) of Figures 6.19, 6.20 and 6.21 with frames (a), (b) and (c) respectively of Figure 5.15 in chapter five.

From the measurements in Figure 6.19(a), one can see a two-cell pattern. However the second cell closer to the wall is not well defined. The flow visualisation result for the same case in Figure 4.16 indicates a similar pattern. The simulations with the turbulent flow model TM1 and laminar flow model for foam in Figures 6.19(b) and (c), however, clearly show two cells. By observing the streamtraces, one can see that the flow pattern with a turbulent flow model for the foam in Figure 6.19(b), is in closer agreement with the experimental pattern of Figure 6.19(a) than the pattern predicted with a laminar model for the foam, Figure 6.19(c). With a turbulent flow model, the size of the second re-circulation is predicted more accurately. Both the laminar and turbulent flow models predict that the dominant cell is closer to the jet than was either measured or visualised.

The two cell pattern is clearly well established for the lower fluid heights of H=0.1 and 0.05 m as seen in Figures 6.20(a) and 6.21(a). There is a remarkable agreement between the patterns obtained with LDV measurements, Figures 6.20(a) and 6.21(a), and with flow visualisation for the same experiments, Figures 4.17 and 4.18 respectively. The predictions carried out with the lower fluid heights clearly indicate the superiority of the predictions with the turbulence model TM1 for the foam. In fact, for the lowest fluid height examined in the present study, the simulation with the laminar flow model is unable to predict the second cell close to the wall, as seen in Figure 6.21(c). The predicted results with the turbulent flow model TM1, on the other hand, shows the size and position of the second cell for the lowest fluid height quite accurately, as seen in Figure 6.21(b). In the case of all three fluid heights examined, the simulations seem to predict the dominant re-circulation to be closer to the jet than is measured or visualised.

Figure 6.22 gives a comparison of the radial position of the dominant re-circulation as a function of the fluid height for the visualisations, measurements and simulations. In Figure 6.22, the vertical axis, R_c/R, represents the normalised radial position of the centre of the dominant re-circulation from the centreline. The horizontal axis, H, represents the fluid height above the porous foam. In this figure, SimulationT and SimulationL refer to the numerical results obtained with the turbulence model TM1 and laminar flow model, respectively, for the porous foam. The horizontal position of the centre of the dominant re-circulation moves closer to

the jet with a decrease in the fluid height for all cases considered, as seen in Figure 6.22. However, the simulations always predict the centre of the dominant re-circulation to be closer to the jet than the visualisations and measurements.

Figure 6.23 gives a comparison of the axial position of the dominant re-circulation as a function of the fluid height for the visualisations, measurements and simulations. In Figure 6.23, the vertical axis, H_c/H, represents the normalised vertical position of the centre of the dominant re-circulation measured from the interface between the porous medium and the clear fluid. The horizontal axis, H, represents the fluid height above the porous foam. The flow visualisations in chapter four (Section 4.3.2.3) indicated that the centre of the dominant re-circulation is approximately at one third of the fluid height (H_c=1/3H). In Figure 6.23, the measurements and predictions show a decrease in the axial position of the centre of re-circulation as the fluid height increases. The discrepancy between the measurements and visualisations for the position of the centre of re-circulation indicates that the centre may not be stationary.

The predictions are able to reasonably reproduce the changes in the gross flow pattern, with the introduction of the porous foam. In particular, the predictions with the turbulent flow model TM1 for the foam give better results than with a laminar flow model and turbulent flow model TM2 for the foam.

6.7.2.2 Mean axial velocity profiles

6.7.2.2.1 Axial velocity profiles in fluid layer

Figures 6.24, 6.25 and 6.26 give the mean axial velocity profiles for H=0.15, 0.1 and 0.05 m, respectively, with h_p=0.05 m for the G10 foam. In these figures, frames (a) and (b) represent comparisons between numerical predictions and experimental results with a flat and fully developed jet exit profile, respectively. The simulated results presented here, are with the 200x200 grid for H=0.15, 0.1 and 0.05 m as the results for this grid were found to be sufficiently grid independent (see Section 5.3.1). In each of these figures, the abbreviations CFDL and CFDT refer to the predicted profiles with the laminar and turbulent flow model TM1 for the foam.

As in the cases without foam, the jet exit profile does not have an influence on the flow away from the jet, as seen from a comparison between frames (a) and (b) of each figure. Observation of the profiles in these figures indicates that the predicted results with the turbulent flow model for the foam are in better agreement with the experimental points. The laminar flow model seems to over-predict the strength of the dominant re-circulation, and this result can be seen more clearly for the lower fluid heights. The damping of the flow away from the jet due to the presence of the porous medium has been well captured by both types of predictions. Overall, with turbulent flow model TM1 for the foam, the predictions are better than those with the laminar flow model.

6.7.2.2.2 Axial velocity profiles in porous foam

The simulated axial velocity profiles in the porous foam are given in Figures 6.27, 6.28 and 6.29 for H=0.15, 0.1 and 0.05 m, respectively, with a constant foam height of 0.05 m. The thickness of the porous foam, h_p, has been used for non-dimensionalising the local depth, z_p, in the foam. The jet exit profiles do not have an influence on the damping effect of the foam, as seen from a comparison between frames (a) and (b) of each figure. In addition, both the laminar and turbulent flow models predict similar profiles in the foam. The axial velocity dies out to values close to zero at around z_p/h_p=0.3 for all three fluid heights investigated.

6.7.2.3 Mean radial velocity profiles

6.7.2.3.1 Radial velocity profiles in fluid layer

Figures 6.30, 6.31 and 6.32 show the mean radial velocity profiles, with frames (a) and (b) representing the predicted results with the two different jet exit profiles. Here again, the jet exit profiles do not have significant influence on the radial velocity profiles. With a laminar flow model for the foam, represented by CFDL in the figures, the peak in the radial velocity at positions such as z/H=0.067 and 0.1 for H=0.15 m in Figure 6.30 and at z/H=0.09 and 0.11 for H=0.1 m in Figure 6.31, is predicted better than with the turbulent flow model TM1. However, the turbulent flow model predicts the spread in the radial velocity, as it approaches zero,

better than the laminar flow model. With a decrease in the fluid height, the predictions of the turbulent flow model are closer to the experimental predictions. As the fluid height decreases, the impingement of the jet into the foam increases, thus increasing the speed of the fluid as it enters the foam. Thus, turbulence effects in the foam are expected to become more important for a lower fluid height. For all fluid heights, the predictions with a turbulent flow model are better than those with a laminar model, away from the foam (see for example the profiles at z/H=0.5 and 0.7 in Figures 6.30, 6.31 and 6.32).

6.7.2.3.2 Radial velocity profiles in porous foam

Figures 6.33, 6.34 and 6.35 represent radial velocity profiles in the foam for H=0.15, 0.1 and 0.05 m with h_p=0.05 m. There is a significant difference in the predicted profiles between the laminar and turbulent flow models at the interface at z_p/h_p=1.0. The difference in the predictions at the interface diminishes with a decrease in the fluid height from H=0.15 m, Figure 6.33, to H=0.05 m, Figure 6.35. However, this difference is not seen in the profiles in the foam, with the laminar and turbulent flow models predicting almost identical profiles. From a comparison between the profiles in frames (a) and (b), it can be concluded that the jet exit profile does not have a significant influence on the flow in the foam.

6.7.2.4 Turbulence kinetic energy profiles

6.7.2.4.1 Turbulence kinetic energy profiles in fluid layer

Figures 6.36, 6.37 and 6.38 represent the turbulence kinetic energy profiles for the cases with the G10 foam with fluid heights of H=0.15, 0.10 and 0.05 m. As in the cases without foam (Figures 6.15, 6.16 and 6.17), the turbulence levels predicted close to the jet exit with a fully developed profile (frame (b) in each figure) are lower than the experimental values. Again, the lower levels of turbulence close to the jet exit do not affect the predictions in other regions of the flow. As expected, the hump in the profile without foam for the same fluid heights gets reduced significantly for the cases with foam, as seen from a comparison between Figures 6.15 and 6.36, as well as between Figures 6.16 and 6.37. This is because the development of a wall jet

is prevented due to the damping effect of the porous foam. The resulting pattern has been predicted quite well both with the laminar and turbulent flow model TM1 for the foam.

6.7.2.4.2. Turbulence kinetic energy profiles in porous foam

With a laminar flow model for the foam, no turbulence kinetic energy exists in the foam. Thus, only the profiles with the turbulent flow model TM1 for the foam are shown in frames (a), (b) and (c) of Figure 6.39 for H=0.15, 0.1 and 0.05 m respectively with h_p=0.05 m. In the figures, the abbreviations CFDFDP and CFDFP represent predictions with fully developed and flat profiles, respectively, at the jet exit. For H=0.15 m in Figure 6.39(a), the fully developed profile predicts larger levels of turbulence in the foam. For the lower fluid heights, the turbulence levels predicted is similar with both jet exit profiles. The turbulence is predicted to persist in the foam to a greater extent for the higher fluid heights investigated. This result appears to be an anomaly, since the jet impingement effect should be lower for the higher fluid heights. As indicated from the contour plots of turbulence kinetic energy in Figure 5.7 of chapter five (solid contour lines), the turbulence model TM2 for foam attenuates the turbulence almost completely. As mentioned earlier, this is probably the reason for the similarity between the results obtained with the laminar flow model and turbulence model TM2 for the porous foam.

6.7.2.5 Summary

The simulations predict the gross flow pattern and the mean axial velocity profiles better with the turbulent flow model with only Darcy damping for the foam. For the radial velocity profiles, predictions with the laminar flow model were found to be better at the highest fluid height in a region close to the interface between the fluid layer and porous foam. The turbulent flow model with Darcy damping showed better agreement with the experimental results as the fluid height decreased. At higher fluid heights, the effect of turbulence in the porous medium is expected to be lower, as the penetration of the jet into the foam must be less intensive. The expected reduction of the turbulence intensity in the porous medium with increasing fluid height does not seem to have been effectively captured by any of the two turbulence model. The

turbulence model with only Darcy damping over predicts the turbulence in the porous foam. On the other hand, the model with Darcy and Forchheimer modification terms included in the k and ε equations almost completely damps turbulence in the porous foam for all cases considered thus under predicting the level of turbulence in the foam.

6.8 Conclusions

LDV measurements and CFD simulations were presented for the system consisting of a turbulent fluid layer overlying saturated porous foam for a quantitative comparison between the experimental and numerical results. The following conclusions can be drawn from the investigation.

1) The vector plots obtained from the measurements confirmed the development of the two-cell pattern in the fluid layer for the highest permeability foam that was investigated initially with the flow visualisation experiments in chapter four.
2) In chapter five, it was revealed that the turbulence model incorporating only Darcy damping in the turbulence transport equations lead to a better qualitative prediction of the flow patterns in the fluid layer. Comparisons of the simulations with LDV measurements in this chapter ascertained the above conclusion.
3) Quantitatively, the simulations predict the gross flow pattern and the mean axial velocity profiles better with the turbulent flow model with only Darcy damping for the foam. For the radial velocity profiles, predictions with the laminar flow model and turbulence model with Darcy and Forchheimer modification terms were found to be better at the highest fluid height in a region close to the interface between the fluid layer and porous foam. The turbulent flow model with Darcy damping showed better agreement with the experimental results as the fluid height decreased.
4) The turbulence kinetic energy profiles in the fluid layer showed relatively good agreement with predictions by laminar and turbulent flow models for the foam.

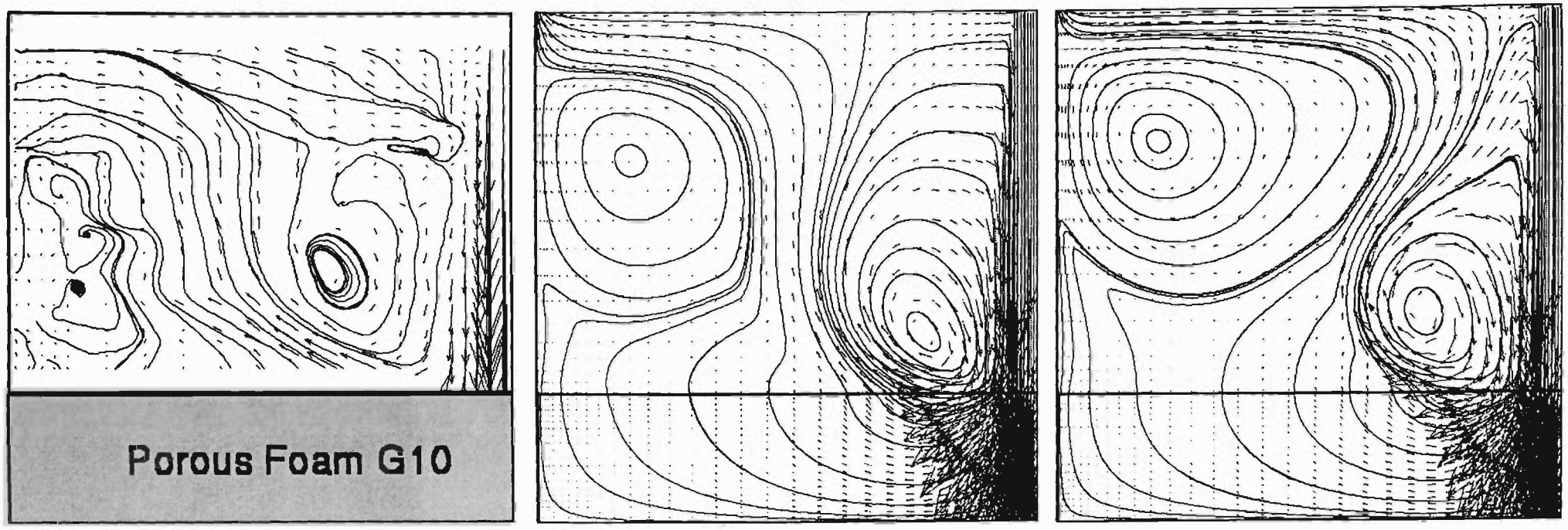

(a) LDV measurement

(b) Numerical simulation, Turbulent flow model with Darcy damping for the foam

(c) Numerical simulation, Laminar flow model for the foam

Figure 6.19: Comparison between measured and simulated vector plots and stream traces. H=0.15 m, h_p=0.05 m, U_b=1.6 m/s.

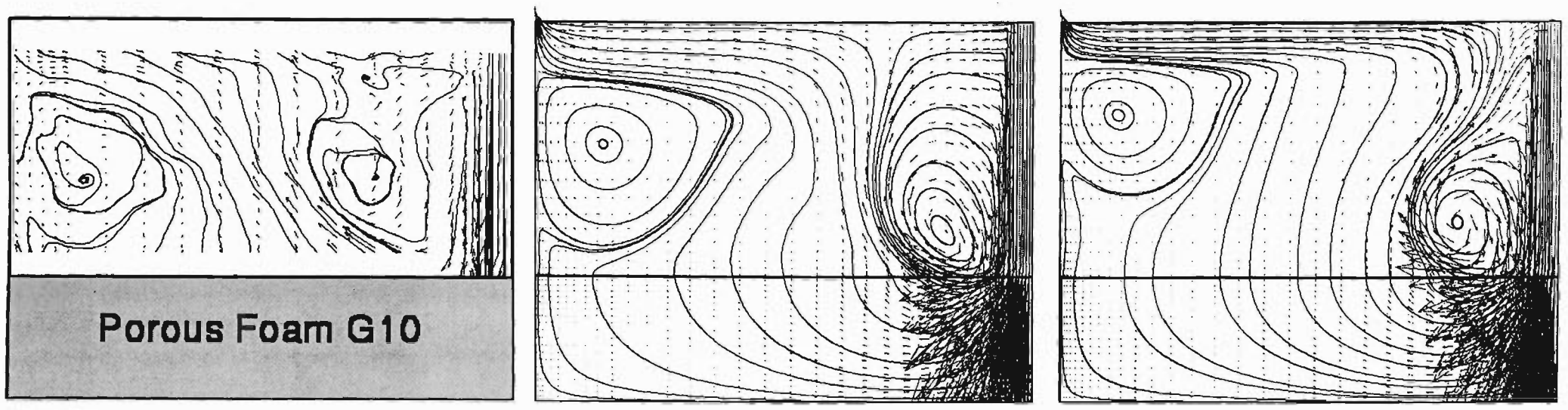

(a) LDV measurement

(b) Numerical simulation, Turbulent flow model with Darcy damping for the foam

(c) Numerical simulation, Laminar flow model for the foam

Figure 6.20: Comparison between measured and simulated vector plots and stream traces. H=0.1 m, h_p=0.05 m, U_b=1.6 m/s.

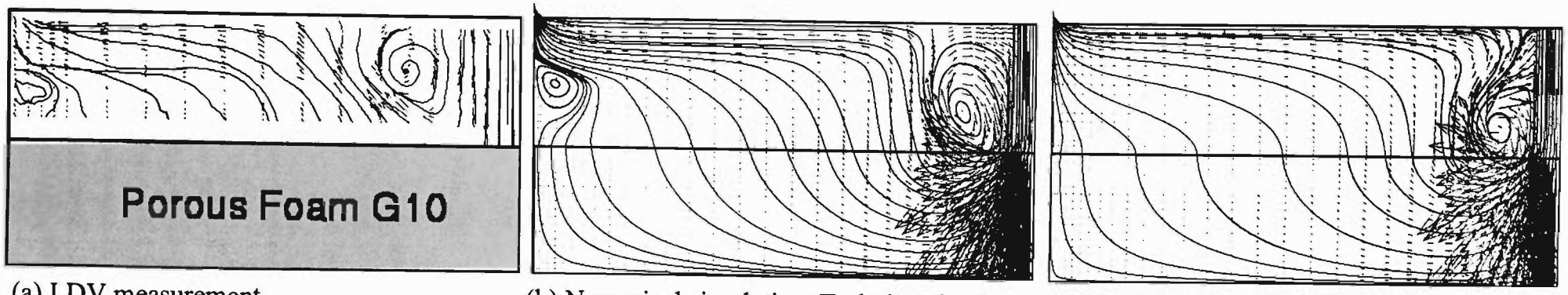

(a) LDV measurement

(b) Numerical simulation, Turbulent flow model with Darcy damping for the foam

(c) Numerical simulation, Laminar flow model for the foam

Figure 6.21: Comparison between measured and simulated vector plots and stream traces. H=0.05 m, h_p=0.05 m, U_b=1.6 m/s

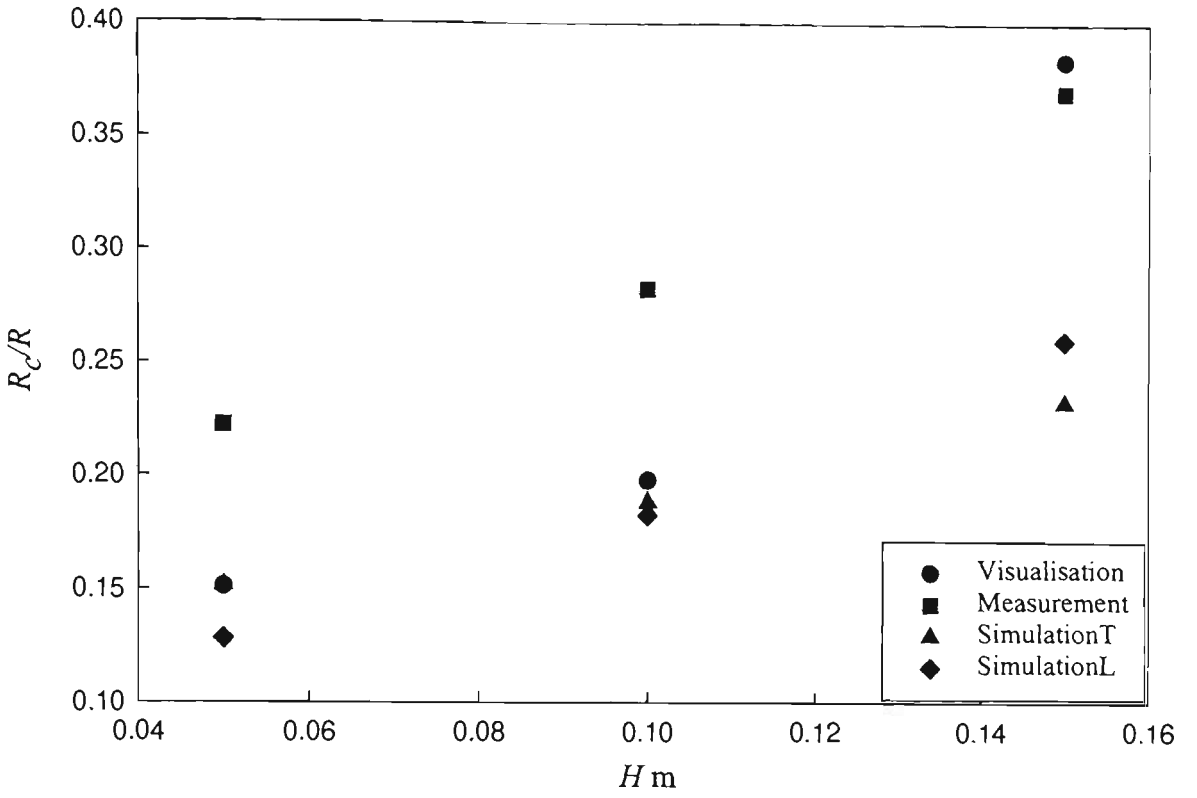

Figure 6.22: Change in the radial position of the centre of the dominant re-circulation as a function of the fluid height for the G10 foam with h_p=0.05 m. R_c/R is the normalised radial distance of the centre of the dominant re-circulation from the centreline. H is the height of the fluid layer above the porous foam.

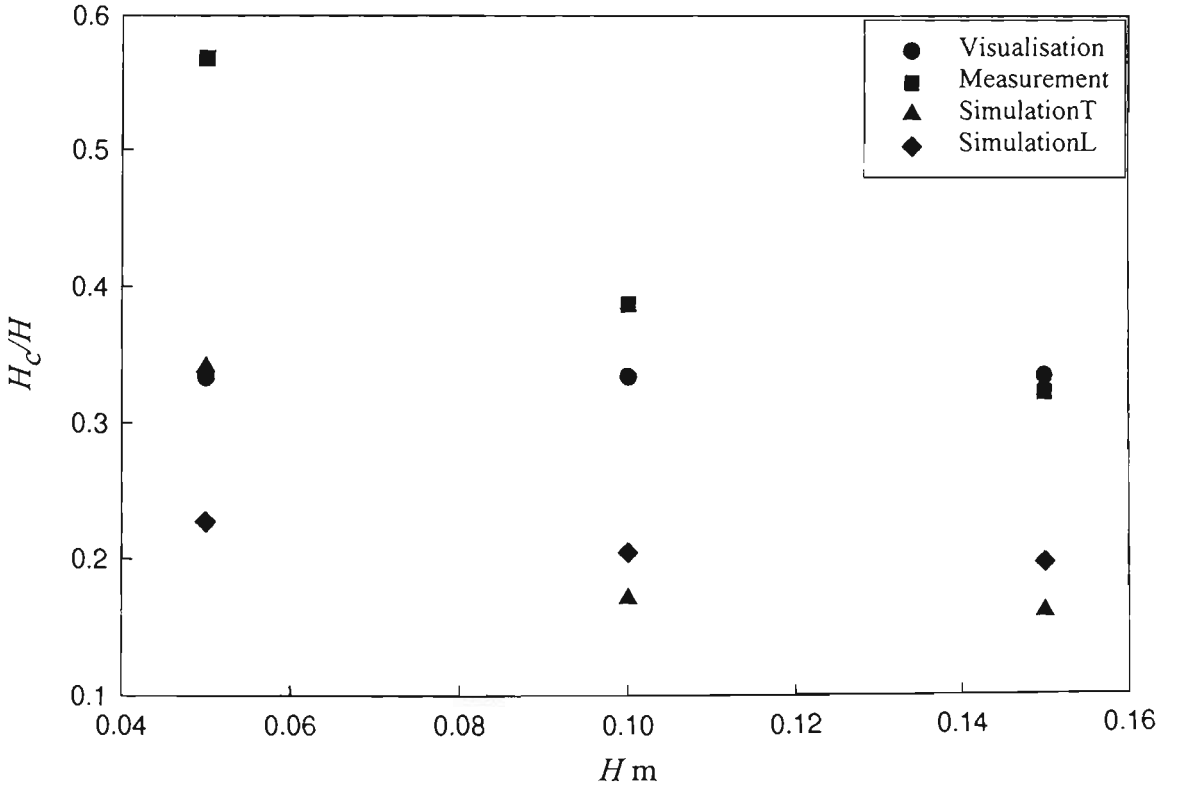

Figure 6.23: Change in the axial position of the centre of the dominant re-circulation as a function of the fluid height for the G10 foam with h_p=0.05 m. H_c/H is the normalised axial distance of the centre of the dominant re-circulation measured from the interface between the fluid and the porous foam. H is the height of the fluid layer above the porous foam.

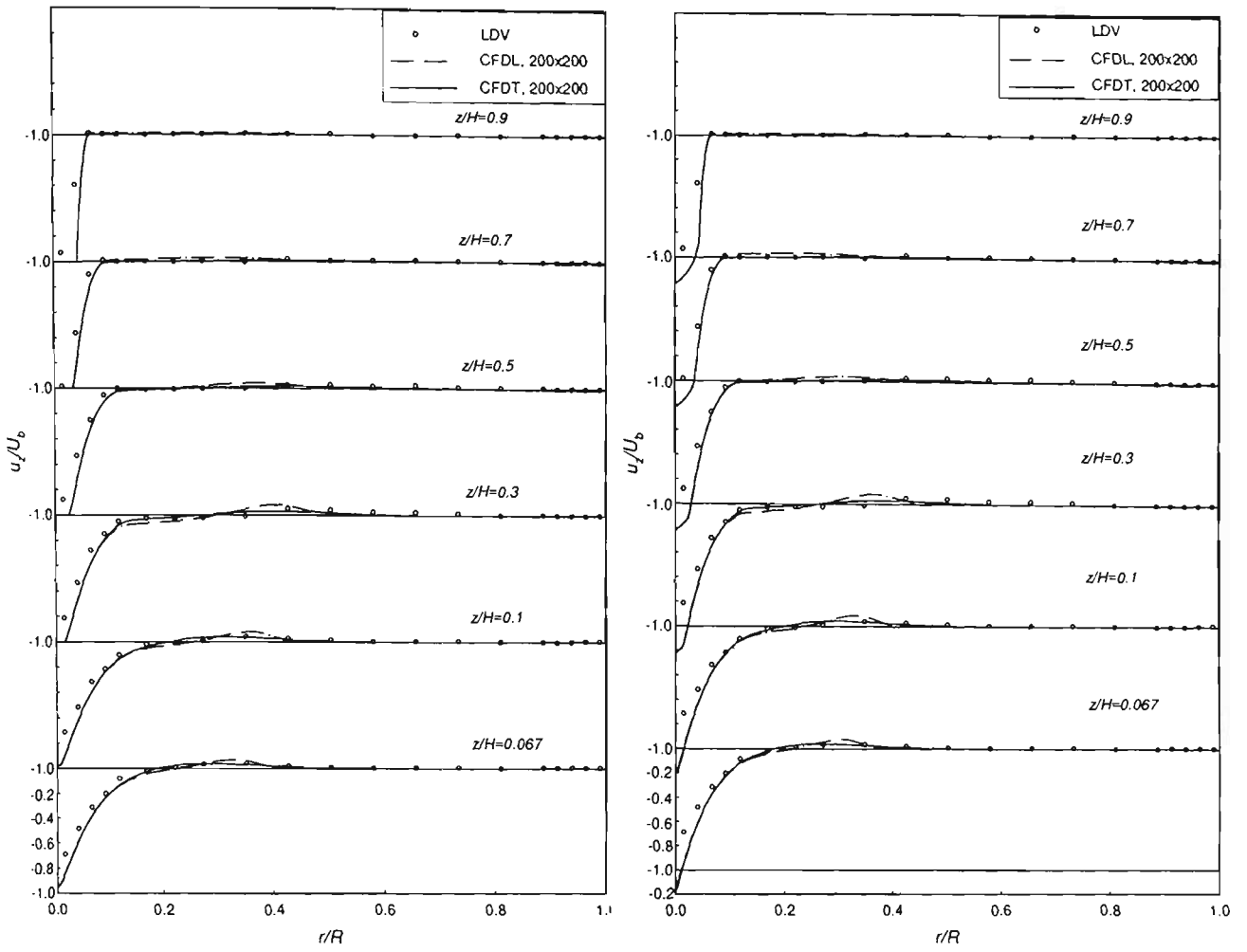

Figure 6.24: Axial velocity profiles in the fluid layer for H=0.15 m, h_p=0.05 m, U_b=1.6 m/s. Frames (a) and (b), respectively, represent simulations with a flat and fully developed profile at the exit of the jet.

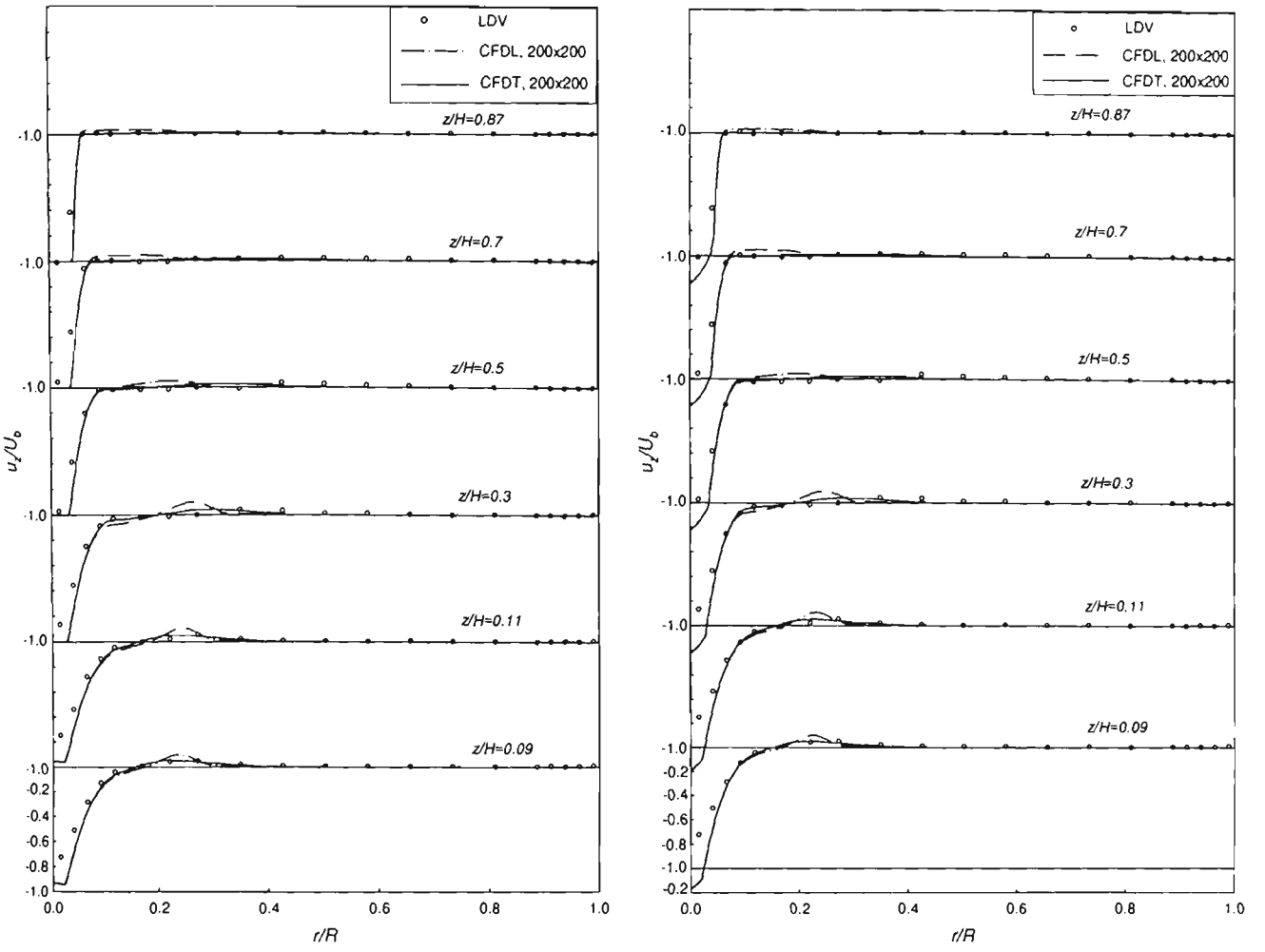

Figure 6.25: Axial velocity profiles in the fluid layer for H=0.1 m, h_p=0.05 m, U_b=1.6 m/s. Frames (a) and (b), respectively, represent simulations with a flat and fully developed profile at the exit of the jet.

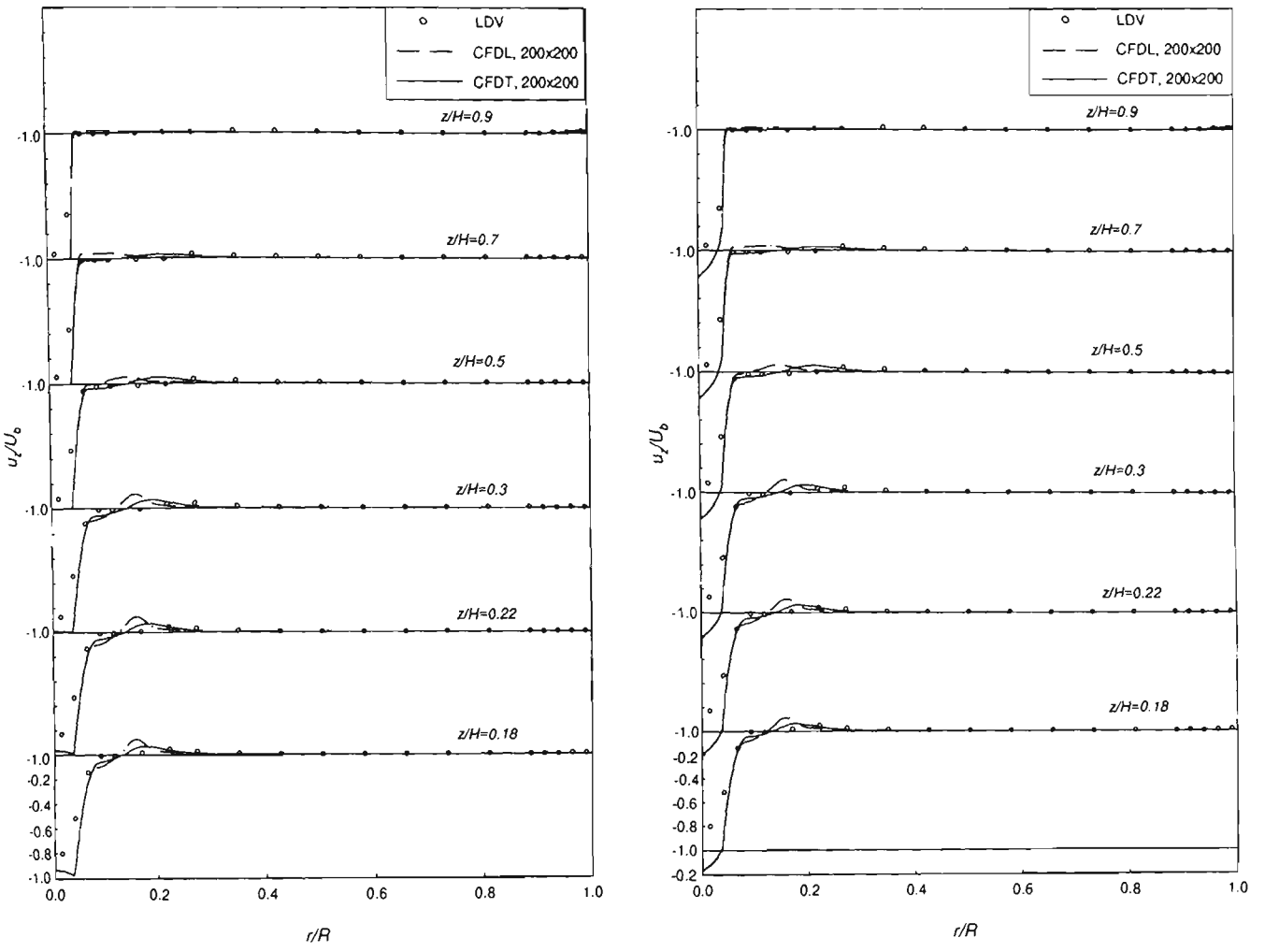

Figure 6.26: Axial velocity profiles in the fluid layer for H=0.05 m, h_p=0.05 m, U_b=1.6 m/s. Frames (a) and (b), respectively, represent simulations with a flat and fully developed profile at the exit of the jet.

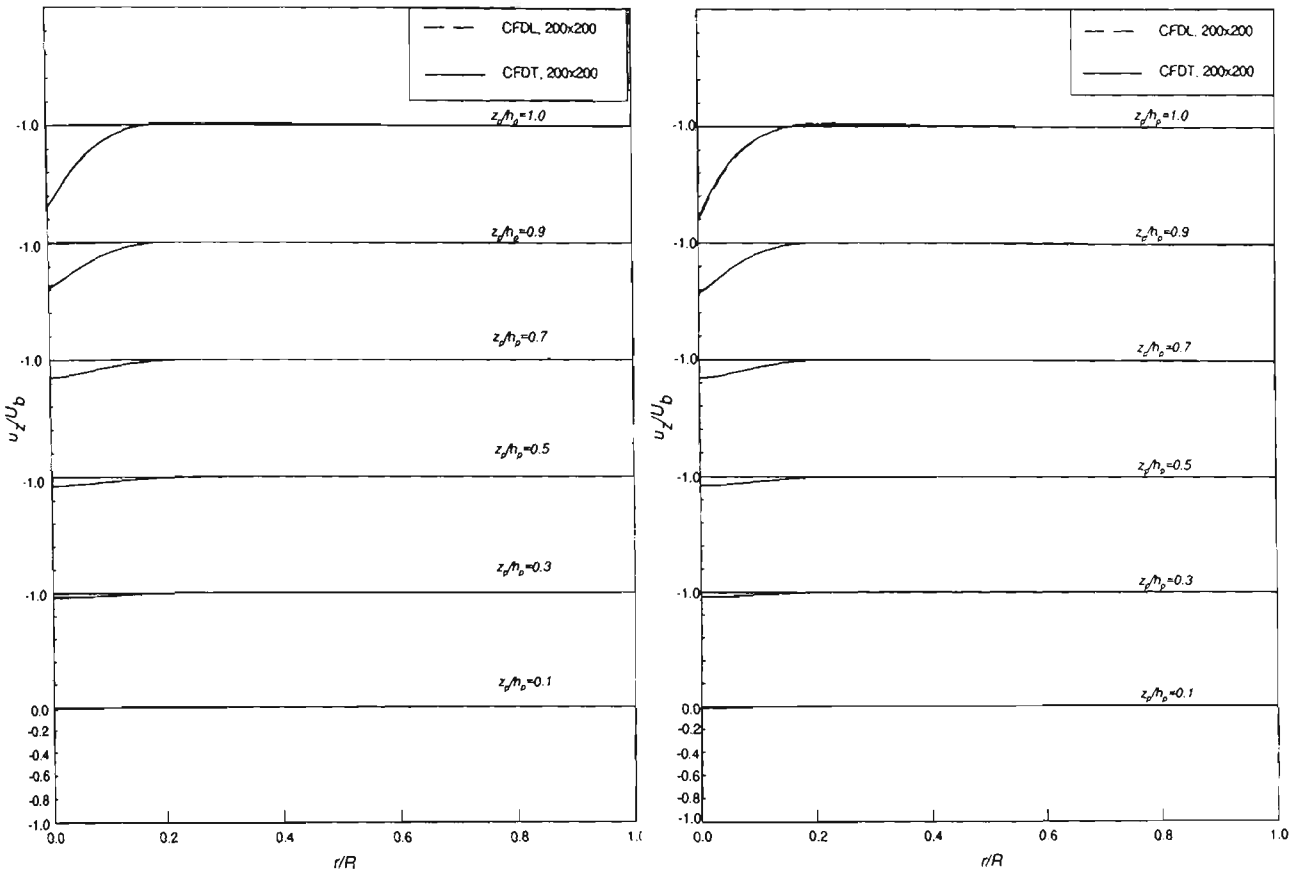

Figure 6.27: Axial velocity profiles in the foam for H=0.15 m, h_p=0.05 m, U_b=1.6 m/s. Frames (a) and (b), respectively, represent simulations with a flat and fully developed profile at the exit of the jet.

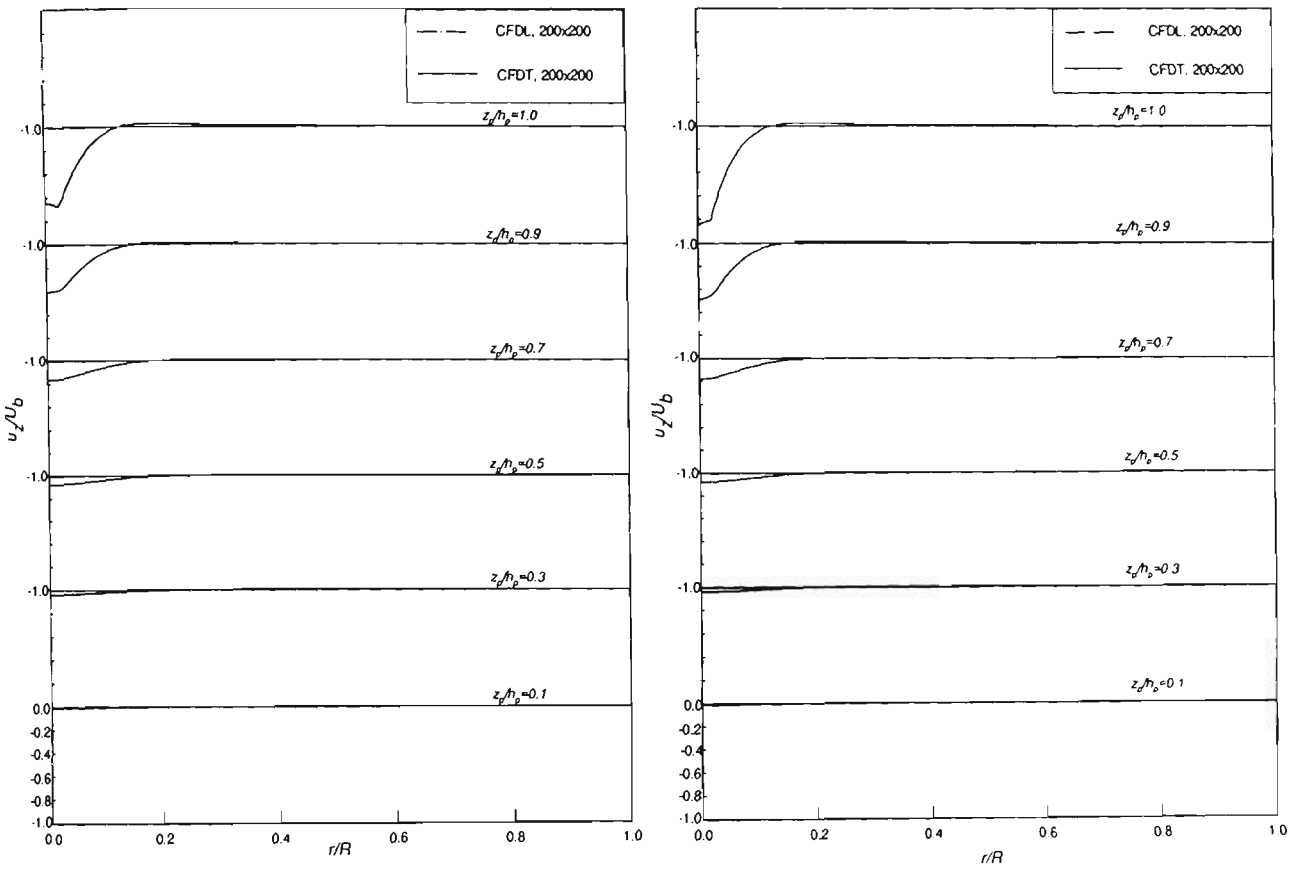

(a) (b)

Figure 6.28: Axial velocity profiles in the foam for H=0.1 m, h_p=0.05 m, U_b=1.6 m/s. Frames (a) and (b), respectively, represent simulations with a flat and fully developed profile at the exit of the jet.

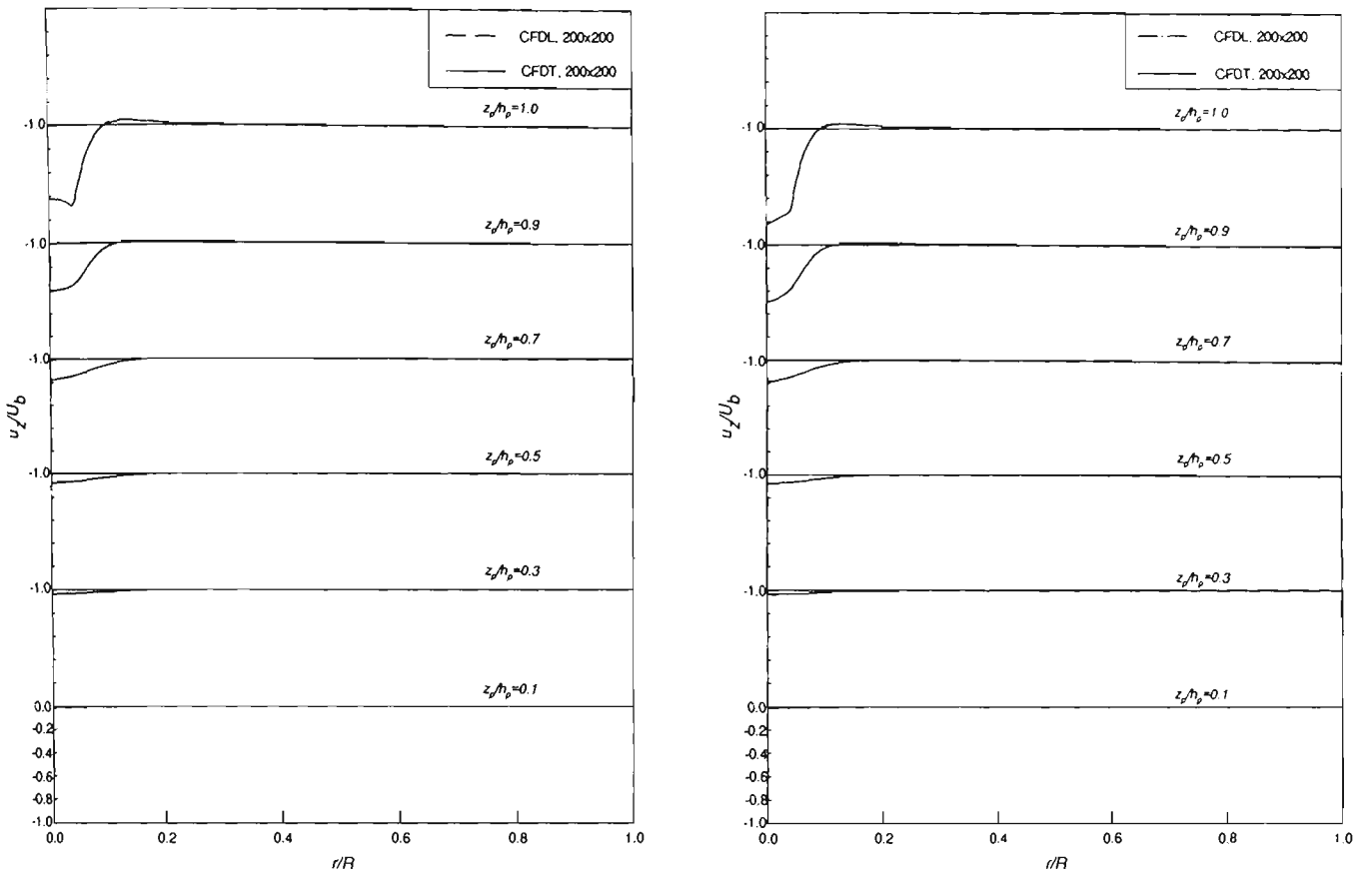

Figure 6.29: Axial velocity profiles in the foam for H=0.05 m, h_p=0.05 m, U_b=1.6 m/s. Frames (a) and (b), respectively, represent simulations with a flat and fully developed profile at the exit of the jet.

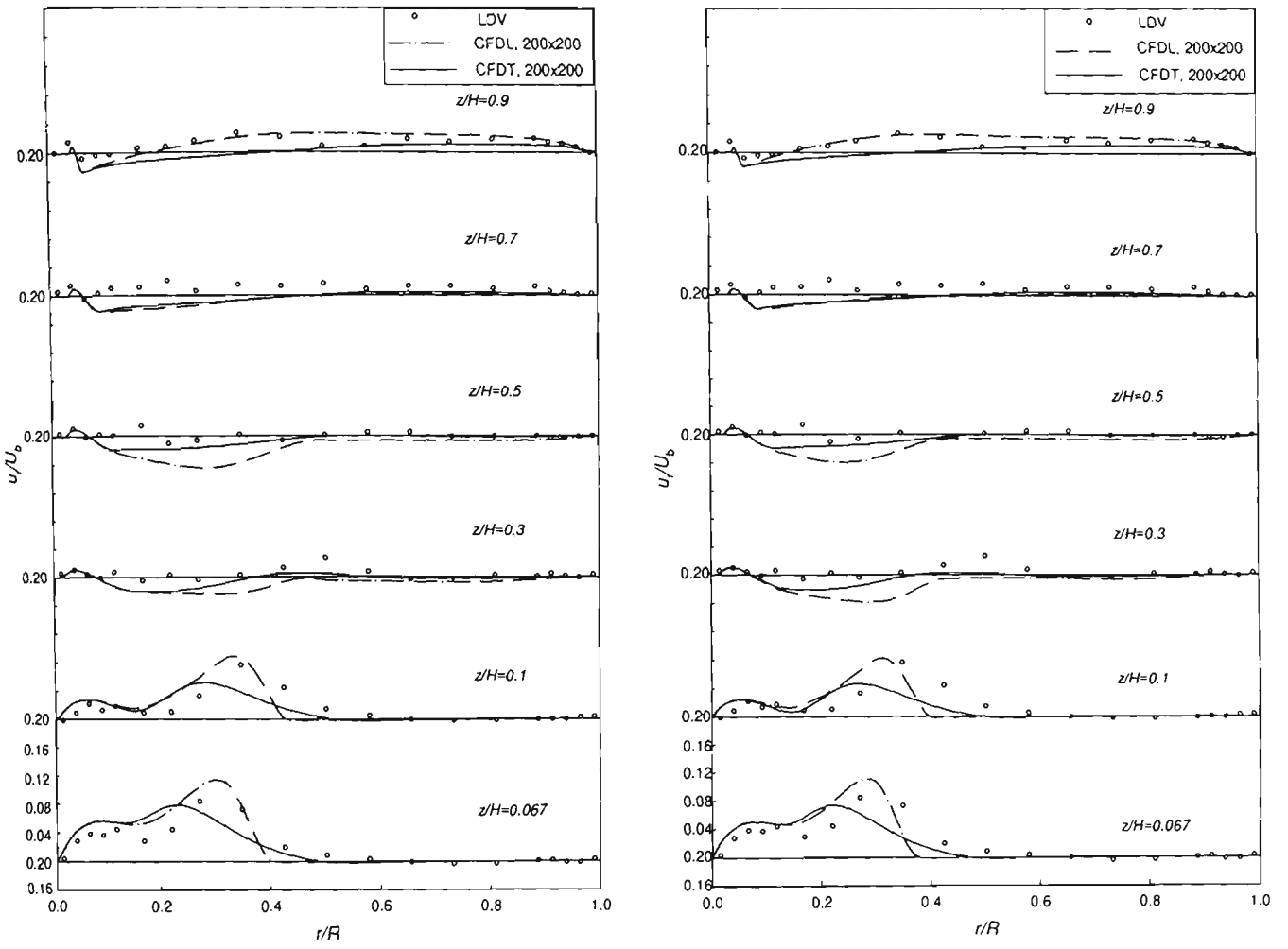

(a) (b)

Figure 6.30: Radial velocity profiles in the fluid layer for H=0.15 m, h_p=0.05 m, U_b=1.6 m/s. Frames (a) and (b), respectively, represent simulations with a flat and fully developed profile at the exit of the jet.

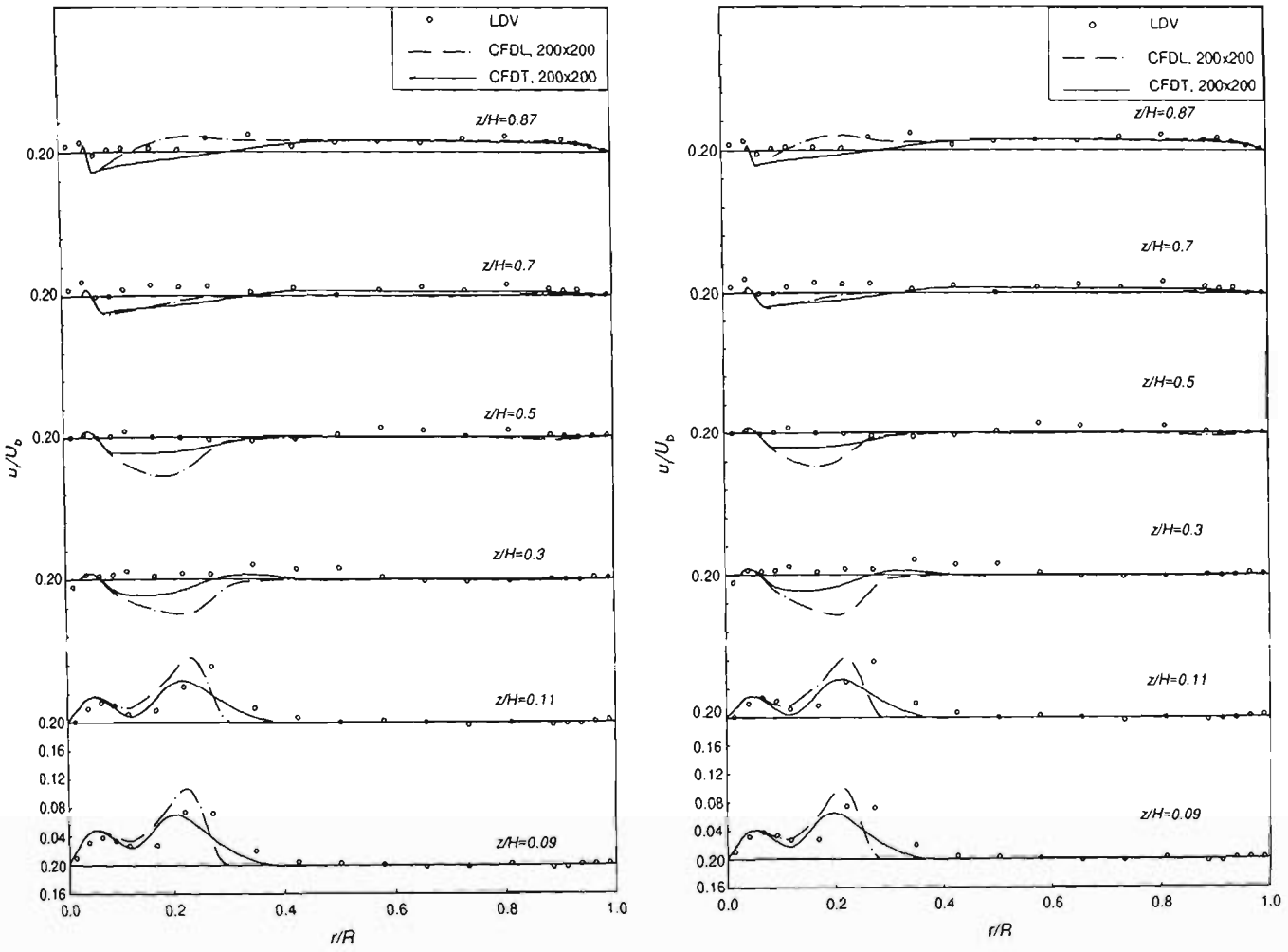

(a) (b)

Figure 6.31: Radial velocity profiles in the fluid layer for H=0.1 m, h_p=0.05 m, U_b=1.6 m/s. Frames (a) and (b), respectively, represent simulations with a flat and fully developed profile at the exit of the jet.

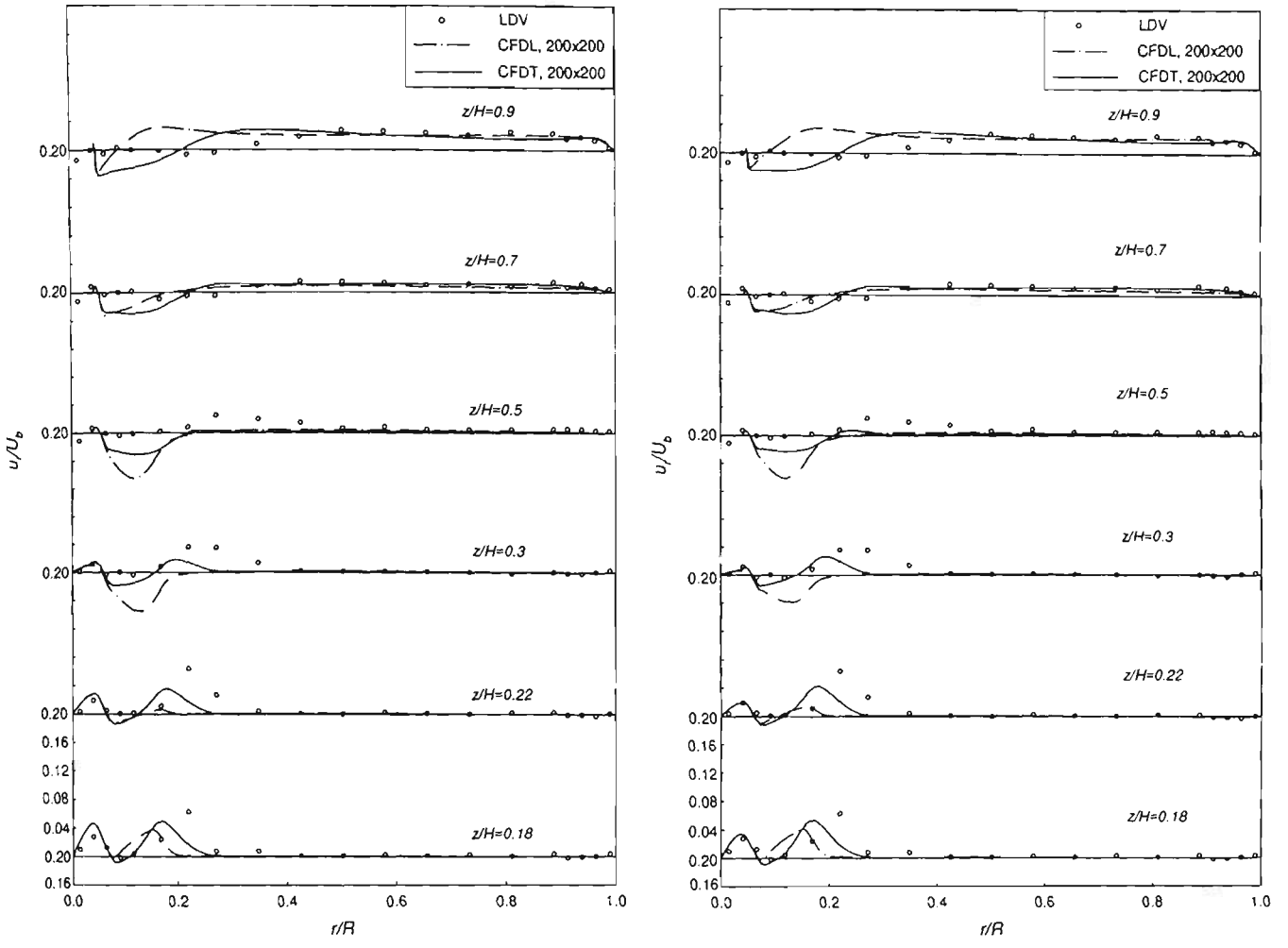

(a) (b)

Figure 6.32: Radial velocity profiles in the fluid layer for H=0.05 m, h_p=0.05 m, U_b=1.6 m/s. Frames (a) and (b), respectively, represent simulations with a flat and fully developed profile at the exit of the jet.

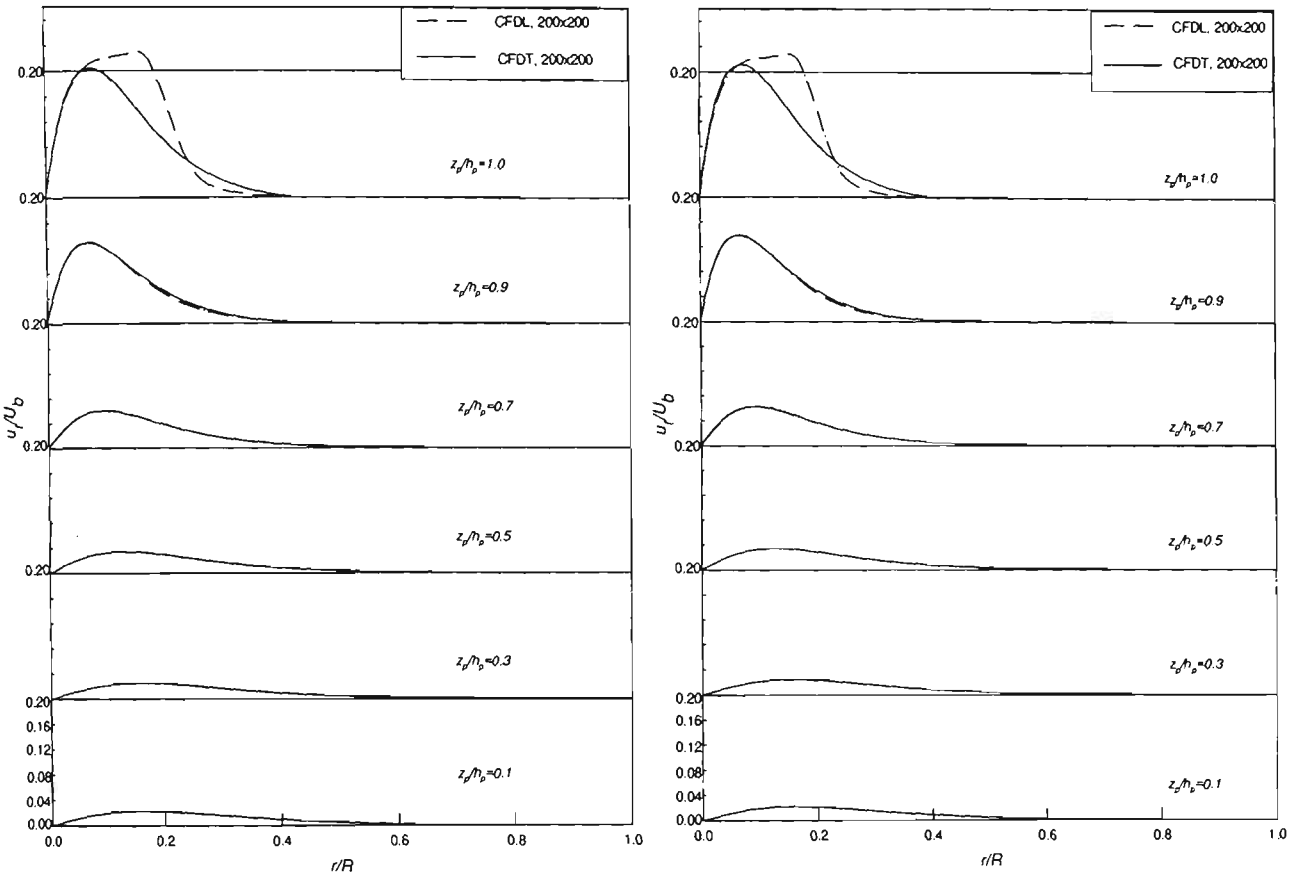

(a) (b)

Figure 6.33: Radial velocity profiles in the foam for H=0.15 m, h_p=0.05 m, U_b=1.6 m/s. Frames (a) and (b), respectively, represent simulations with a flat and fully developed profile at the exit of the jet.

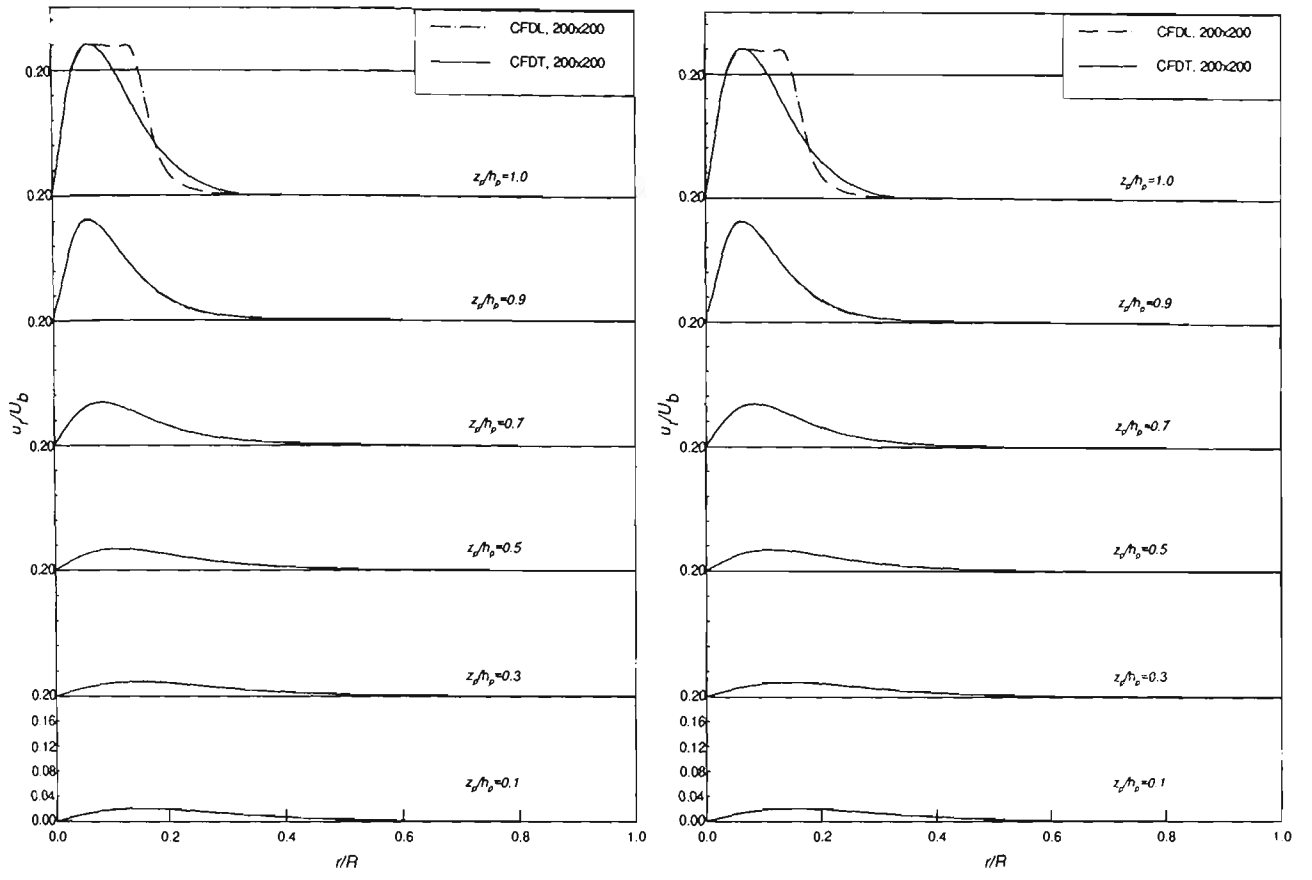

(a) (b)

Figure 6.34: Radial velocity profiles in the foam for H=0.1 m, h_p=0.05 m, U_b=1.6 m/s. Frames (a) and (b), respectively, represent simulations with a flat and fully developed profile at the exit of the jet.

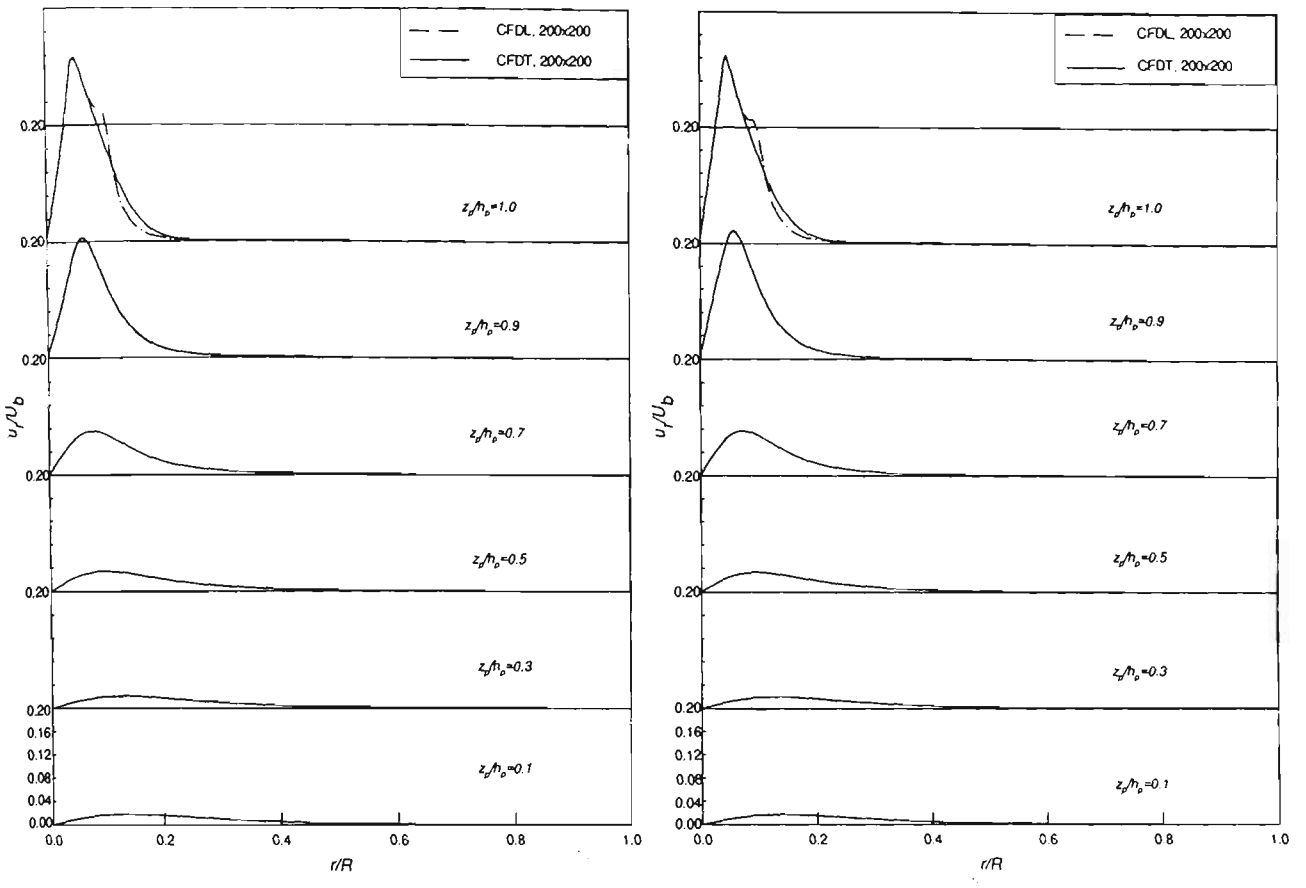

(a) (b)

Figure 6.35: Radial velocity profiles in the foam for H=0.05 m, h_p=0.05 m, U_b=1.6 m/s. Frames (a) and (b), respectively, represent simulations with a flat and fully developed profile at the exit of the jet.

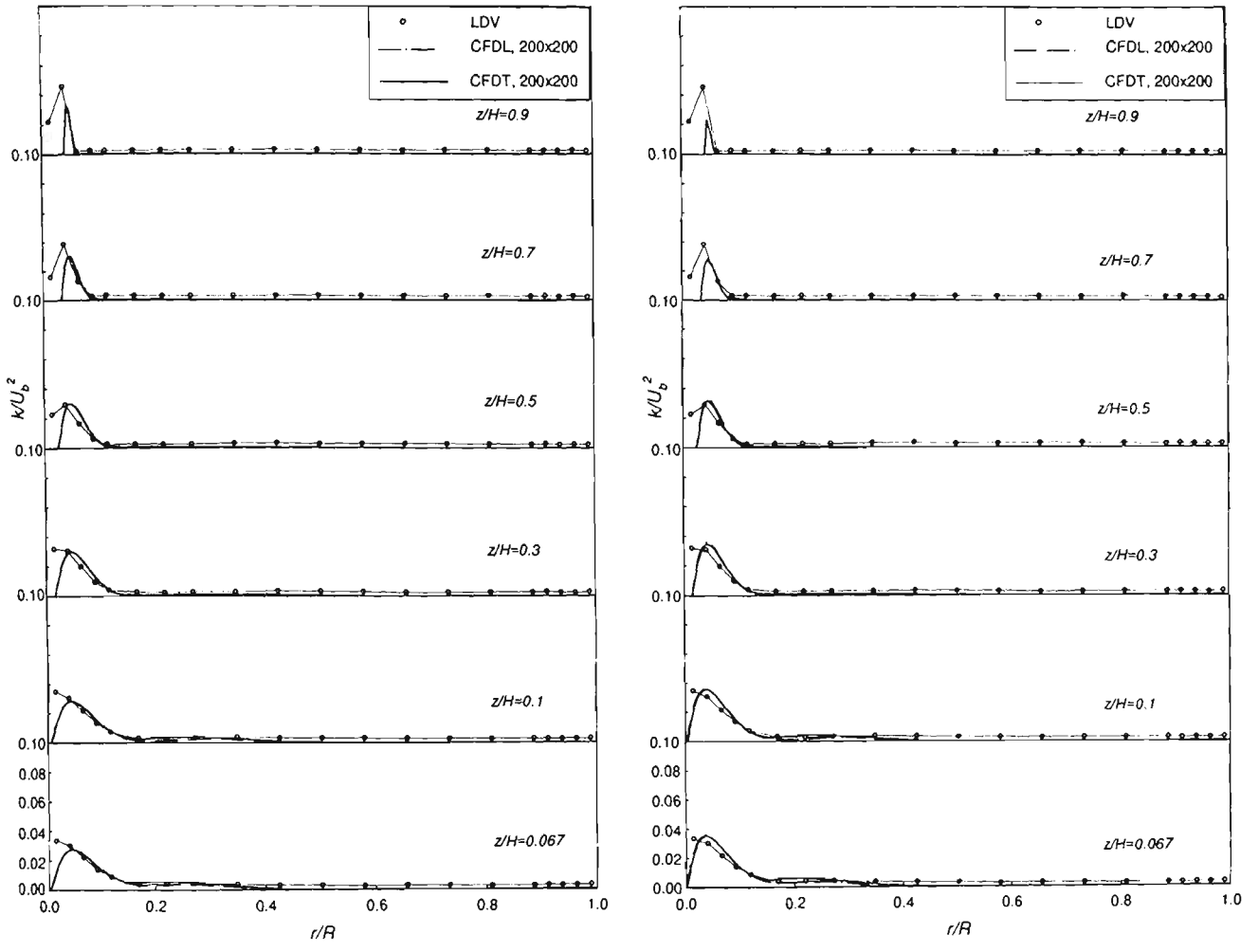

(a) (b)

Figure 6.36: Turbulence kinetic energy profiles in the fluid layer for H=0.15 m, h_p=0.05 m, U_b=1.6 m/s. Frames (a) and (b), respectively, represent simulations with a flat and fully developed profile at the exit of the jet.

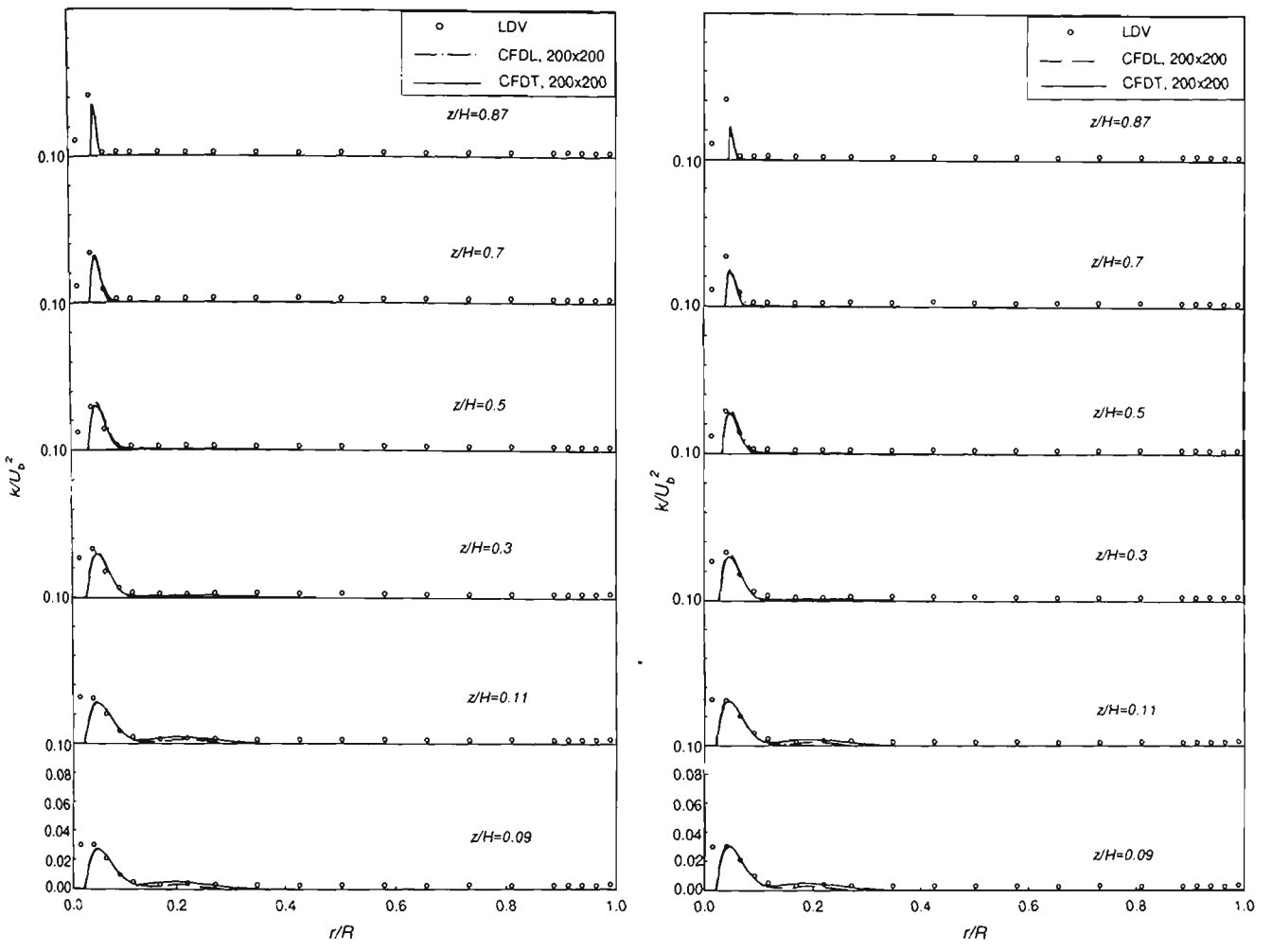

(a) (b)

Figure 6.37: Turbulence kinetic energy profiles in the fluid layer for H=0.1 m, h_p=0.05 m, U_b=1.6 m/s. Frames (a) and (b), respectively, represent simulations with a flat and fully developed profile at the exit of the jet.

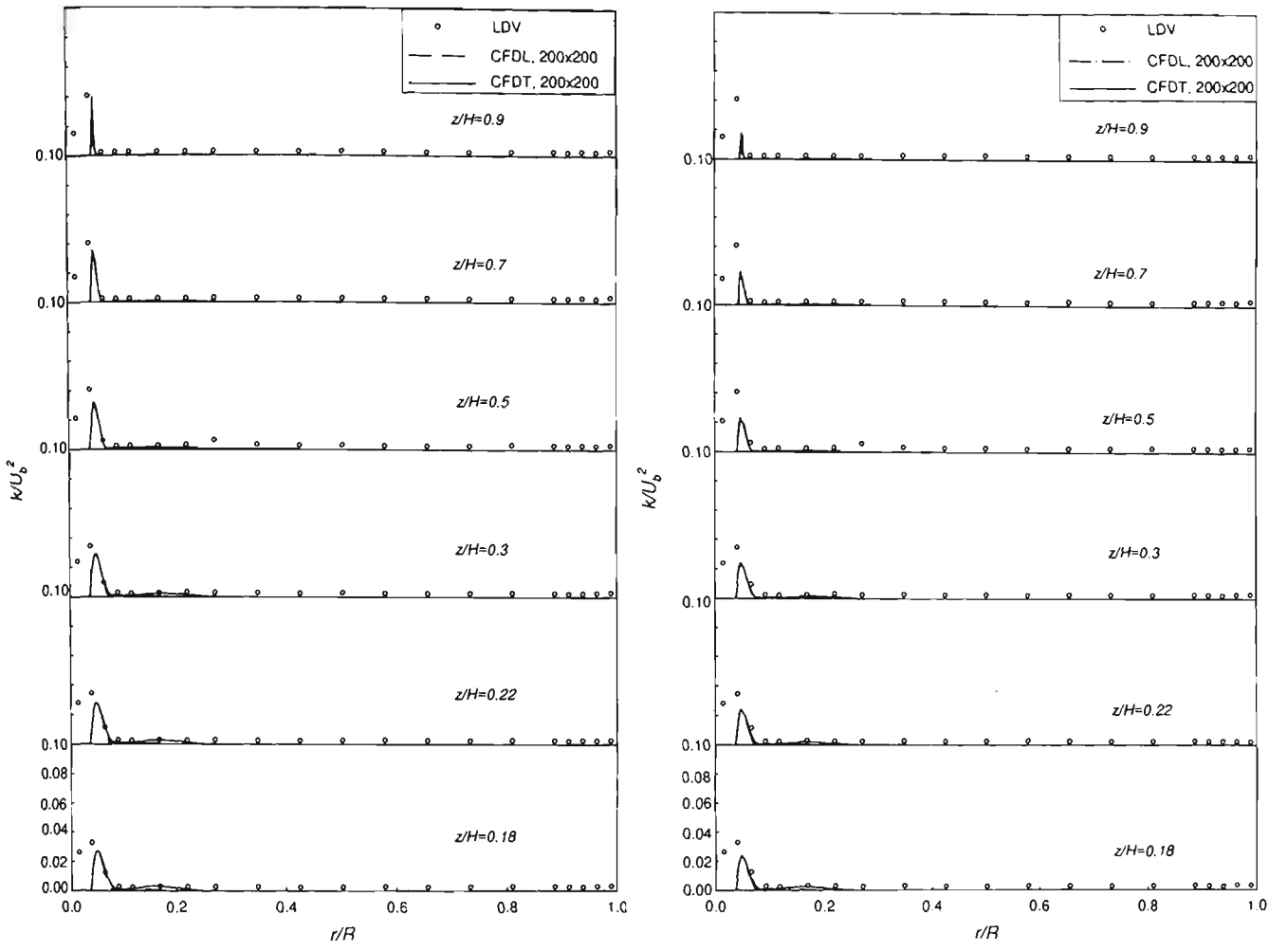

(a) (b)

Figure 6.38: Turbulence kinetic energy profiles in the fluid layer for H=0.05 m, h_p=0.05 m, U_b=1.6 m/s. Frames (a) and (b), respectively, represent simulations with a flat and fully developed profile at the exit of the jet.

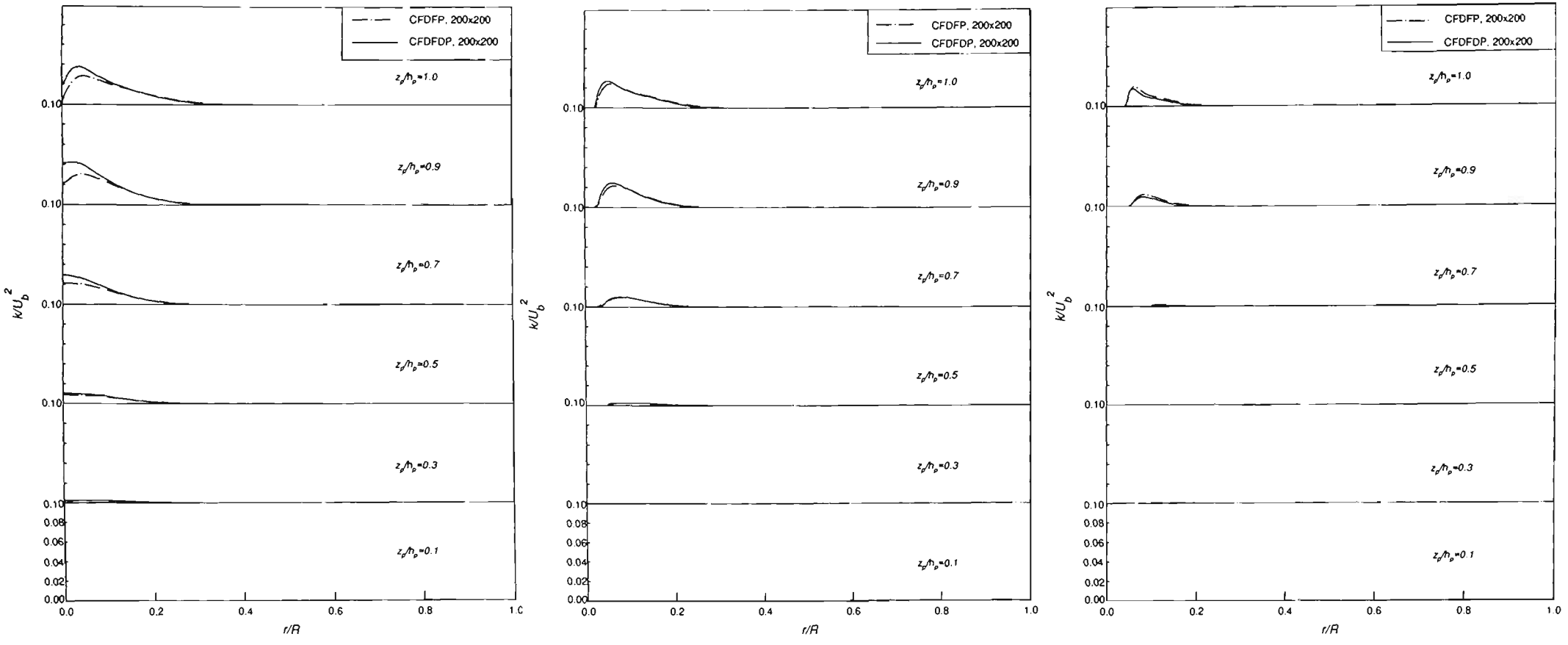

Figure 6.39: Turbulence kinetic energy profiles in the foam with model TM1 for (a) H=0.15 m, (b) H=0.1 m and (c) H=0.05 m with h_p=0.05 m and U_b=1.6 m/s

Chapter 7

Application: Modelling of natural convection heat and mass transfer in hygroscopic porous media

7.1 Introduction

The effect of interaction between a turbulent fluid flow overlying a porous layer was inferred experimentally and numerically in the previous chapters. Having secured the modelling of this interaction on a firm footing, the research was applied to an industrially important problem. The problem involves the interaction of a turbulently flowing fluid and a hygroscopic porous medium.

Previously published experimental and numerical investigations of natural convection flows in a clear fluid overlying a saturated porous medium have been confined to studies in which the flow in the clear fluid is in the laminar regime. In many practical situations, however, one encounters systems in which the heat and mass transfer is significantly affected by turbulence, at least in the fluid region. Such a two-layer system can be encountered in the storage of porous materials such as grains, fruits and catalysts. Thermal insulation in buildings and geothermal reservoirs are also modelled as a two-layer system. In these examples, the fluid (which is generally air), can often be turbulent. It is well established from natural convection studies in clear fluids (the experimental studies of Cheesewright *et al.*, 1986a; Kirkpatrick and Bohn, 1986 and numerical studies of Henkes, 1990 and Kenjeres and Hanjalic, 1995), that the enclosure dimensions contribute to whether the flow is laminar or turbulent. In enclosures the size of typical rooms, the flow of air is normally turbulent due to the large Rayleigh numbers encountered. Thus, one cannot ignore turbulence as a factor which enhances heat transfer, and hence moisture migration in such two layer systems if there is a significantly large fluid layer. In the porous medium, turbulence will not persist if the medium is of a sufficiently low permeability. Thus, one could assume a laminar regime in the porous medium. Flow visualisations presented in chapter four and the corresponding simulations presented in chapter five have revealed that for low permeability porous media with

$K \leq O(10^{-8})$, the fluid layer and the porous medium could be regarded to be operating in the turbulent and laminar regimes respectively.

In the literature, there is a limited number of studies on systems that contain a fluid overlying a porous medium. Numerical and experimental studies of such systems have been concerned with two particular physical configurations. The heating from below case, which is analogous to the Rayleigh-Bénard problem, has been studied by Poulikakos *et al.* (1986), Poulikakos (1986), Chen and Chen (1989) and Chen and Chen (1992) among others. The heating from the side problem has been studied by Beckermann *et al.* (1988), Song and Viskanta (1994) and Singh *et al.* (1993). All of these studies have been carried out for the laminar flow regime.

The present work is a continuation of the study carried out by Nguyen (1987) who presented a method of solving the equations of heat, mass and momentum transport in bulks of stored grains that have peaked geometries. In that paper the effect of turbulence in an overlying fluid layer was not considered probably due to the large computational times required to solve transient problems in natural convection with turbulence. However, with the ready availability of faster computers, such simulations with more realistic physical conditions can be carried out within reasonable times.

A general method of analysing systems with a fluid overlying a hygroscopic porous medium where turbulence in the fluid layer is important is presented in this chapter. A hygroscopic porous medium has been chosen for the present model to be useful in modelling stored agricultural produce such as grains that are hygroscopic in nature. In such systems the commodities in warm regions tend to become dry, and convection currents carry moisture to cooler regions which become moist. Components of the model have been validated with previous experimental and numerical results, which were found to be similar to the present system. An application of moisture migration through a representative hygroscopic porous medium is presented to emphasise the potential application of the model. A two dimensional system has been used so that the salient features of the work are explicated with clarity.

7.2 Governing equations

The governing equations for fluid flow and heat transfer for the case study can be represented as:

Equation of continuity:

$$\frac{\partial u}{\partial x}+\frac{\partial v}{\partial y}=0 \tag{7.1}$$

Momentum equation in the x-direction:

$$\rho_a\frac{\partial u}{\partial t}+\frac{\rho_a u}{\phi}\frac{\partial u}{\partial x}+\frac{\rho_a v}{\phi}\frac{\partial u}{\partial y}=-\frac{\partial p}{\partial x}+\frac{\partial}{\partial x}\left[(\mu+\mu_t)\left(2\frac{\partial u}{\partial x}\right)\right] + \frac{\partial}{\partial y}\left[(\mu+\mu_t)\left(\frac{\partial u}{\partial y}+\frac{\partial v}{\partial x}\right)\right]-\frac{\phi\mu u}{K}-\rho_a\frac{c_F\phi u Q}{K^{1/2}} \tag{7.2}$$

Momentum equation in the y-direction:

$$\rho_a\frac{\partial v}{\partial t}+\frac{\rho_a u}{\phi}\frac{\partial v}{\partial x}+\frac{\rho_a v}{\phi}\frac{\partial v}{\partial y}=-\frac{\partial p}{\partial y}+\frac{\partial}{\partial y}\left[(\mu+\mu_t)\left(2\frac{\partial v}{\partial y}\right)\right] + \frac{\partial}{\partial x}\left[(\mu+\mu_t)\left(\frac{\partial u}{\partial y}+\frac{\partial v}{\partial x}\right)\right]+\rho_a g\beta(T-T_0) -\frac{\phi\mu v}{K}-\rho_a\frac{c_F\phi v Q}{K^{1/2}} \tag{7.3}$$

where, ϕ represents porosity of the porous medium, K is its permeability and c_F is the Forchheimer coefficient. ρ_a is the density of air and $Q=\sqrt{u^2+v^2}$. The variables have the same meaning as in Section 2.4.1.1 of chapter two. The difference in the above momentum equations and Equations (5.4) and (5.5) is the presence of the buoyancy term in Equation (7.3).

The eddy viscosity is represented as:

$$\mu_t=\rho_a c_\mu\frac{k^2}{\varepsilon} \tag{7.4}$$

in which $c_\mu=0.09$.

It is assumed that turbulence persists only in the fluid layer, and it is rapidly attenuated in the porous medium due to its low permeability. Thus, the eddy viscosity, μ_t, applies only for the fluid layer. For the porous medium, its value is taken to be zero.

Thus the modelling of the two-layer system for the application is equivalent to the use of a laminar flow model for the porous foam in the numerical simulations presented in the fifth chapter. As seen in chapter five, the Darcy and Forchheimer terms vanish in the fluid layer as the fluid has infinite permeability. The porosity of the fluid layer is taken to be unity, and a step change in porosity and permeability is assumed at the interface between the fluid layer and porous medium.

Thermal energy equation:

Due to the presence of the hygroscopic porous medium, the thermal energy balance assumes different forms for the fluid layer and the porous medium. The partial differential equations for heat, mass and momentum transfer in stored agricultural produce have been derived in Thorpe *et al.* (1992). For the present problem one can write,

$$\left[\frac{(\rho c)_{eff}}{c_a}\right]\frac{\partial T}{\partial t}+\rho_a u\frac{\partial T}{\partial x}+\rho_a v\frac{\partial T}{\partial y}=\frac{\partial}{\partial x}\left[\left(\frac{\mu}{\mathrm{Pr}}+\frac{\mu_t}{\sigma_T}\right)\frac{\partial T}{\partial x}\right]+\frac{\partial}{\partial y}\left[\left(\frac{\mu}{\mathrm{Pr}}+\frac{\mu_t}{\sigma_T}\right)\frac{\partial T}{\partial y}\right]+\frac{\rho_b h_s}{c_b}\frac{\partial W}{\partial t} \tag{7.5}$$

where, $(\rho c)_{eff}=(1-\phi)\rho_s c_s+\phi\rho_a c_a+Wc_w+\dfrac{\partial H_w}{\partial T}$ (7.6)

and $\sigma_T = 0.9$

c_a represents the specific heat of air; c_w is the specific heat of liquid water. c_s is the specific heat of the porous solid and ρ_s is its density. c_b is the bulk specific heat, h_s is the latent heat of sorption and ρ_b is the bulk density. W is the moisture content of the porous medium on a fractional dry basis and Pr is the Prandtl number of air.

The term Wc_w arises due to the presence of moisture in the porous medium. The term H_w represents the integral heat of wetting, the details of which can be found

in Sutherland *et al.* (1971). The last term on the right hand side represents the heat of sorption. It should be noted that for the fluid layer, the integral heat of wetting, H_w, and the heat of sorption, h_s, would vanish since these are terms only associated with the porous medium. Again, for the porous medium the eddy viscosity term is zero, as turbulence is absent in the porous medium

Turbulence kinetic energy equation:

$$\rho_a \frac{\partial k}{\partial t} + \rho_a u \frac{\partial k}{\partial x} + \rho_a v \frac{\partial k}{\partial y} = \frac{\partial}{\partial x}\left[\left(\mu + \frac{\mu_t}{\sigma_k}\right)\frac{\partial k}{\partial x}\right] + \frac{\partial}{\partial y}\left[\left(\mu + \frac{\mu_t}{\sigma_k}\right)\frac{\partial k}{\partial y}\right] + P_k + G_k - \rho_a \varepsilon \tag{7.7}$$

where, σ_k=1.0

Equation for the rate of energy dissipation:

$$\rho_a \frac{\partial \varepsilon}{\partial t} + \rho_a u \frac{\partial \varepsilon}{\partial x} + \rho_a v \frac{\partial \varepsilon}{\partial y} = \frac{\partial}{\partial x}\left[\left(\mu + \frac{\mu_t}{\sigma_\varepsilon}\right)\frac{\partial \varepsilon}{\partial x}\right] + \frac{\partial}{\partial y}\left[\left(\mu + \frac{\mu_t}{\sigma_\varepsilon}\right)\frac{\partial \varepsilon}{\partial y}\right] + \left(c_{\varepsilon 1} f_1 \left(P_k + c_{\varepsilon 3} G_k\right) - \rho_a c_{\varepsilon 2} f_2 \varepsilon\right)\frac{\varepsilon}{k} \tag{7.8}$$

where, σ_ε=1.3, κ= von Karman's constant = 0.41, $c_{\varepsilon 1}$=1.44 and $c_{\varepsilon 2}$=1.92.

For the coefficient $c_{\varepsilon 3}$, the form suggested by Henkes (1990) is used (see Section 2.4.1.1 in the second chapter)

Thus $c_{\varepsilon 3} = \tanh|v/u|$.

Note that Equations (7.7) and (7.8) apply only to the fluid layer since turbulence is assumed to be absent in the porous medium.

Governing equations for moisture migration in porous media

In the following description, the term porous medium implies a bulk of solid particles, which is saturated with air. This bulk is considered to be a continuum according to the principles of volume averaging independently derived by Whitaker (1967) and Slattery (1967) discussed in Section 2.2.3 of chapter two. The term porous solid refers to an individual particle such as grain or silica gel crystal that has micropores within which moisture can be adsorbed.

In case of stored agricultural or horticultural produce and hygroscopic porous media such as silica gel (used as a desiccant), the total moisture content is the sum of

the moisture content of the air and the solid, which is porous. Since the porous solid and the surrounding air carry moisture in them, the total moisture balance involves the concentration of moisture in air as well as in the porous solid. Thus one needs to take into account two moisture balances namely the intra-granular and inter-granular moisture balances.

Intra-granular moisture balance:

$$\frac{\partial W}{\partial t} = D_{as}\left(W_e - W\right) \tag{7.9}$$

where W is the moisture content of the porous medium on a dry basis, W_e is the equilibrium moisture content of the porous medium and D_{as} is a rate coefficient for moisture exchange between air and porous medium.

In the present study, it is assumed that the solid is always in thermodynamic equilibrium with the surrounding air. This assumption is correct when the rate of intra-granular moisture migration is much faster than inter-granular moisture migration. In case of small particles like grains or silica gel crystals, this will be true at the low air flow rates encountered in natural convection (Thorpe and Whitaker, 1992). However, one needs to incorporate the above equation in the solution procedure for large particles such as fruits.

Inter-granular moisture balance

The equation that governs the concentration of moisture in the air has a slightly different form in the fluid and porous layers due to the contribution of the solids to the air moisture balance in the porous medium. The moisture balance for the porous medium can be represented by:

$$\phi\rho_a \frac{\partial w}{\partial t} + \rho_a u \frac{\partial w}{\partial x} + \rho_a v \frac{\partial w}{\partial y} + \rho_b \frac{\partial W}{\partial t} = \rho_a \frac{\partial}{\partial x}\left(\frac{\mu}{Sc}\frac{\partial w}{\partial x}\right) + \rho_a \frac{\partial}{\partial y}\left(\frac{\mu}{Sc}\frac{\partial w}{\partial y}\right) \tag{7.10}$$

where w is the air moisture content on a dry basis and Sc is the Schmidt number of air. The moisture balance in the fluid layer can be written as:

$$\phi\rho_a \frac{\partial w}{\partial t} + \rho_a u \frac{\partial w}{\partial x} + \rho_a v \frac{\partial w}{\partial y} = \rho_a \frac{\partial}{\partial x}\left[\left(\frac{\mu}{Sc} + \frac{\mu_t}{\sigma_m}\right)\frac{\partial w}{\partial x}\right] + \rho_a \frac{\partial}{\partial y}\left[\left(\frac{\mu}{Sc} + \frac{\mu_t}{\sigma_m}\right)\frac{\partial w}{\partial y}\right] \quad (7.11)$$

where, $\sigma_m = 0.65$.

The eddy viscosity, μ_t, has been invoked only in the equation for the fluid layer.

An order of magnitude analysis is now carried out on Equation (7.10) to determine the relative significance of each term for low permeability porous media such as grains. Significant variations in the moisture content occur only over a long period of time, which is on the order of months. When expressed in seconds, a time scale of $t = O(10^6)$ seconds is obtained. During such a time period, there is a variation in the moisture content on the order of $\Delta w = O(10^{-2})$ and $\Delta W = O(10^{-1})$ on a kg of moisture/kg dry basis.

Typical velocities encountered in natural convection flows in porous media of low permeability $(Da = O(10^{-8}))$, is $u = O(10^{-3})$ m/s for relatively high Rayleigh numbers $(Ra = O(10^{10}))$. This value has been verified by carrying out computations for these Darcy and Rayleigh numbers without moisture migration. It is assumed that moisture migration will not significantly alter the velocities. The length scale for such Rayleigh numbers is $l = \Delta x = O(1)$ m. The density of air, $\rho_f = O(1)$ kg/m^3 and the bulk density of the porous medium, $\rho_b = O(10^2)$ kg/m^3 are used.

Thus one can write:

$$\rho_a \frac{\partial w}{\partial t} = O\left(1\frac{10^{-2}}{10^6}\right) = O(10^{-8})$$

$$\rho_a u \frac{\partial w}{\partial x} = O\left(1x10^{-3}\frac{10^{-2}}{1}\right) = O(10^{-5}) \quad (7.12)$$

$$\rho_a \frac{\partial W}{\partial t} = O\left(10^2\frac{10^{-1}}{10^5}\right) = O(10^{-5})$$

The analysis shows that the advection term is balanced by the change in the solids moisture content and that the rate of change in the air moisture content is

negligible in comparison. The molecular diffusion term may be significant close to the walls because the velocity component normal to a wall is small, but steep concentration gradient in this direction could exist. Thus, molecular diffusion cannot be neglected. The result enables one to neglect the first term on the left-hand side of Equation (7.10) thus allowing the computation of W explicitly in the porous medium. One problem encountered in a previous study by Chen *et al.* (1999) was with the transient computation of such systems. These authors had used an implicit solution procedure by including all terms in Equation (7.10). This problem is overcome in the present study by using the above explicit procedure. The present formulation also allows one to take large time steps to study moisture migration once the temperature and velocity fields have evolved almost to a steady state, because the moisture field does not significantly affect the temperature and velocity fields. The ability to take large time steps during the process of computations is important due to the large time scales (days or months) encountered in such systems.

The present calculations start with an initial value for moisture content of the porous medium. This value is used to calculate the moisture content of air in the porous medium using an appropriate sorption isotherm. The moisture content of air in the fluid layer is calculated by using Equation (7.11).

Silica gel is used as the representative hygroscopic porous medium for the study because its properties are quite well established and it can adsorb up to 50% of its dry mass of water, hence any effects due to its hygroscopy will be quite pronounced.

The sorption isotherm of the gel is represented by

$$W = 0.5r \tag{7.13}$$

where, $r = \dfrac{p}{p_{sat}}$ represents relative humidity of air. The saturation pressure, p_{sat}, is given by Hunter's (1987) expression:

$$p_{sat} = \frac{6\times10^{25}}{T_{abs}^{5}} \exp\left(-\frac{6800}{T_{abs}}\right) \tag{7.14}$$

The moisture content of the interstitial air in the porous medium is calculated by using the relationship,

$$w = \frac{0.622p}{0.622P_{atm} - p} \tag{7.15}$$

where P_{atm} is the atmospheric pressure.

7.3 Problem definition, boundary and initial conditions

As a case study for the proposed model, moisture migration in a rectangular cavity of aspect ratio 2 with half the cavity filled with silica gel is chosen. A Rayleigh number, $Ra = 10^{10}$ and a Darcy number, $Da = 10^{-8}$ are chosen for the study. These numbers translate to a total system height, H, of about 2 metres with a width, D, of about 1 metre. The Darcy number chosen is typical for a storage system that contains particles such as wheat with a diameter of about 3 mm. Figure 7.1 shows a schematic diagram of the simple two-dimensional geometry considered for the case study.

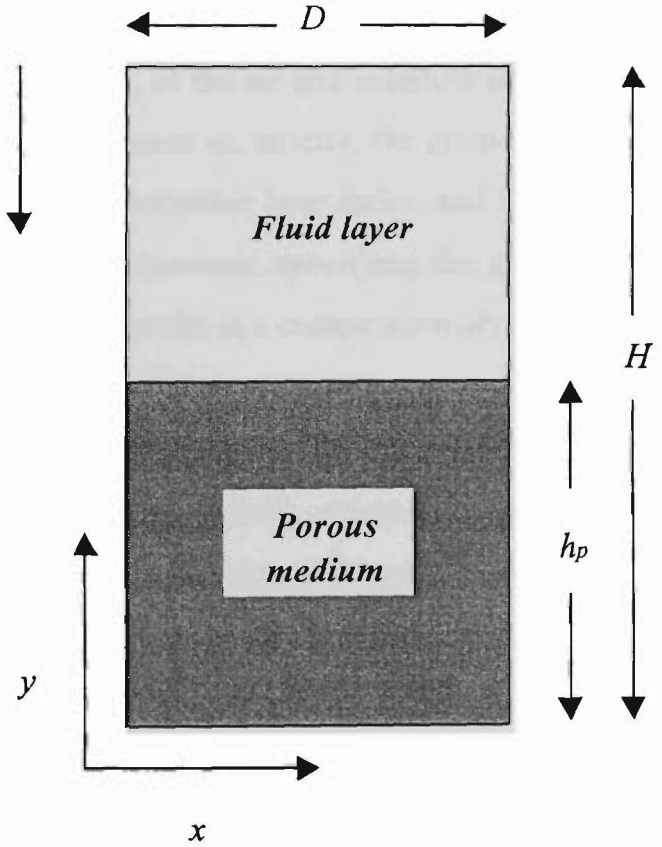

Figure 7.1: Schematic diagram of the system used for the case study.

Typical boundary and initial conditions of a storage vessel are considered for the case study. These can be summarised as follows for the mean quantities:

$$
\begin{aligned}
&u = v = 0 && \text{at } x = 0, D \text{ and } y = 0, H \\
&T = T_c = 10^0 C && \text{at } x = 0, D \text{ and } y = H \\
&\frac{\partial T}{\partial y} = 0 && \text{at } y = 0 \\
&T_{porous} = T_h = 30^0 C && \text{at } t = 0 \\
&T_{air} = \left(\frac{T_c + T_h}{2} \right) && \text{at } t = 0 \\
&\frac{\partial W}{\partial x} = \frac{\partial w}{\partial x} = 0 && \text{at } x = 0, D \text{ and } y = 0, H \\
&\frac{\partial W}{\partial y} = \frac{\partial w}{\partial y} = 0 && \text{at } x = 0, D \text{ and } y = 0, H
\end{aligned}
\tag{7.16}
$$

where T_{porous} and T_{air} are the initial temperatures of the porous medium and air, respectively.

As seen from Equation (7.16), zero gradient boundary conditions are applied to the moisture content, w, of the air and moisture content of the porous medium, W. This over specifies the system as, strictly, the gradient of the moisture content of air should be zero at the impermeable boundaries, and the moisture content of the solids is a dependent variable. However, specifying the gradients of the moisture contents of both air and the solids results in a computationally stable and accurate solution.

The mean variables are solved right up to the wall without using any wall functions. However, for the turbulent variables, k and ε, wall functions obtained from the inertial law are applied at the first inner grid point (see Section 2.4.1.1.1 in chapter two):

$$
k = \frac{\left(v^*\right)^2}{\sqrt{c_\mu}}, \quad \varepsilon = \frac{\left(v^*\right)^3}{\kappa x} \tag{7.17}
$$

where v^* is the friction velocity defined by $v^* = \sqrt{\frac{\tau_{wall}}{\rho}}$

where τ_{wall} is the wall shear stress calculated from $\tau_{wall} = \mu \left(\frac{\partial v}{\partial x} \right)_{wall}$

and x is the normal distance from the wall.

As mentioned before in Section 3.2.2 of chapter three, the above modification to the standard k-ε model has been suggested for natural convection flows, because the wall functions that normally apply for forced convection flows are not applicable for natural convection flows.

The volume-averaged velocities are continuous across the interface since they are continuous across the fluid-solid and fluid-fluid segments of the interface. The temperature, heat flux, moisture content of air and porous medium and the gradient of the air moisture content are continuous at the interface due to the same reason. Due to the use of the Brinkman extended Darcy flow model for the porous medium, the gradients of the velocities or the normal and tangential stresses also become continuous across the interface.

For the turbulent variables, k and ε, at the interface of the fluid and low permeability porous layer turbulence is assumed to be completely damped as implied by the flow visualisation experiments in chapter four. For this reason the conditions at the interface of the fluid and porous layer, for k and ε, are taken to be identical to the conditions at an impermeable wall.

7.4 Validation of the model

For the present problem, two configurations were used to validate components of the model. The simulations and experimental work of Song and Viskanta (1994) were used to validate the Brinkman Forchheimer extended Darcy flow model for a system consisting of a fluid layer adjacent to a porous layer. The schematic diagram in Figure 7.2(a) represents the square cavity adopted by Song and Viskanta (1994) with adiabatic top and bottom walls and differentially heated side-walls. The turbulence model was validated with the experimental results of mixed cavity natural convection reported by Kirkpatrick and Bohn (1986) for their HCCC (Hot-Cold-Cold-Cold) configuration because the boundary conditions used closely resembled the present boundary conditions. Figure 7.2(b) represents a schematic diagram of the HCCC configuration of Kirkpatrick and Bohn (1986) with a square cavity having a hot bottom wall and cold top and side-walls.

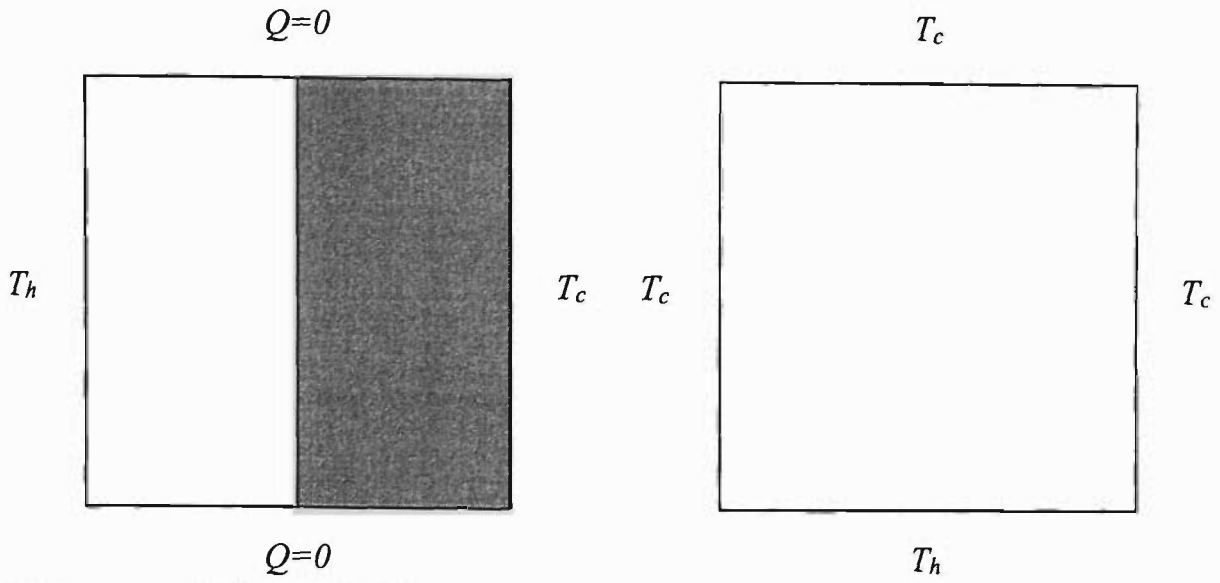

(a) Song and Viskanta (1994) (b) Kirkpatrick and Bohn (1986)

Figure 7.2: Schematic diagram of the configurations used for validation of the model.

7.4.1 Method of solution

As discussed in Section 2.5 of chapter two, the model equations are discretised using the control volume formulation and are solved using the SIMPLE algorithm. The upwind/central hybrid scheme is used for discretising the convection terms. The diffusion terms are discretised using the second order central scheme. Non-uniform grid spacing generated by the sine function given in Equations (3.10) and (3.11) was used to account for the large gradients in velocity and temperature wherever applicable. The simulation is assumed to have reached a converged solution when the sum of the normalised absolute mass, momentum and thermal energy sources for all control volumes have individually reached a tolerance of $1x10^{-8}$ (see Equation (2.72) for an example). The sources were normalised by dividing them by the total number of control volumes.

7.4.2 Results and discussion for model validation

For the prediction of the Song and Viskanta (1994) experiments, an 80x80 grid was found to be sufficiently accurate after carrying out a grid refinement study. Grid points were closely spaced near the walls and at the interface between the fluid

and porous layers to accommodate the steep gradients in these regions. The unsteady terms in the momentum and thermal energy equations were neglected, and a steady formulation was used. Figure 7.3 shows the comparison between the present simulations and experimental and simulated results of Song and Viskanta (1994) for their experiment 3.

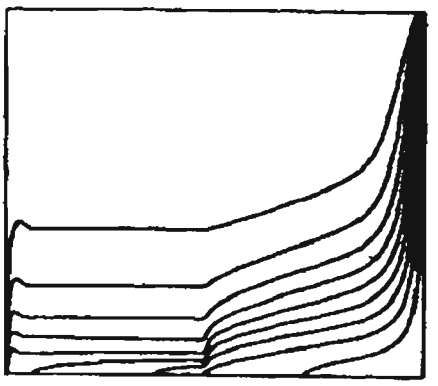

(a) Isotherms

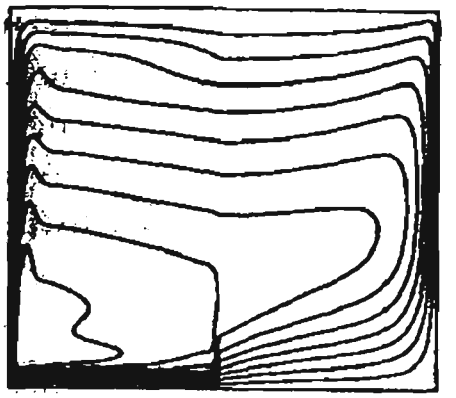

(b) Streamlines

Simulations of Song and Viskanta (1994).
Reproduced from their Figures 4(b) and (c).

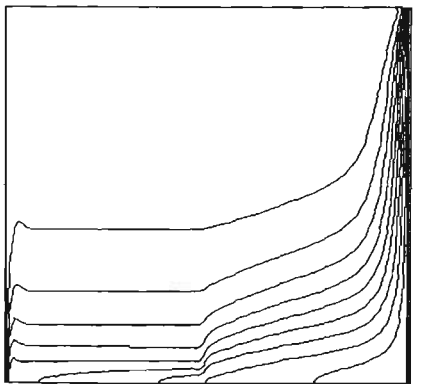

c) Isotherms

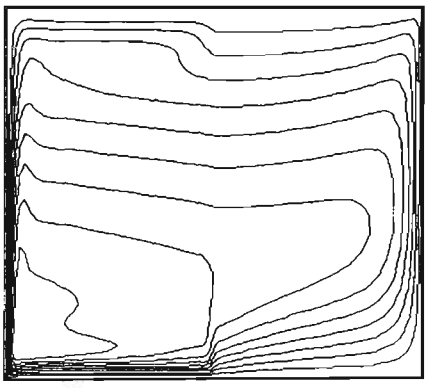

d) Streamlines

Present simulations

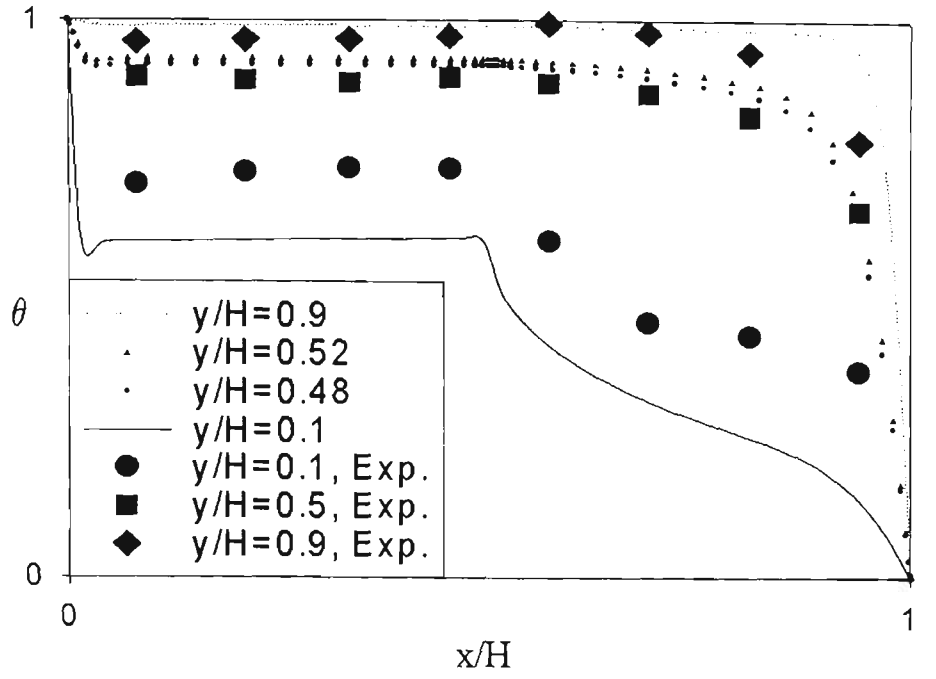

(e) Comparison with experimental temperature profile of Song and Viskanta (1994). Experimental points have been reproduced from Song and Viskanta (1994), Figure 4(d).

Figure 7.3: Comparison of the present simulation with experiment 3 of Song and Viskanta (1994).

The streamlines and isotherms obtained in the present predictions are in good agreement with their predictions as seen from Figures 3(a) to 3(d). The predicted temperature profiles are also similar to the measured results of Song and Viskanta (1994) as seen from Figure 7.3(e). The major discrepancy between the measured and predicted temperature profiles is found at y/H=0.1 in Figure 7.3(e). Song and Viskanta (1994) attributed this discrepancy to the continuum model used. Steeper changes in velocity and temperature are encountered in the lower portions of the cavity (streamlines and isotherms are more closely spaced in the lower portions of the cavity on the fluid side) as one goes from the fluid layer to the porous layer. It is conjectured that the continuum model does not correctly predict these steep changes. However, the general agreement between the modelled and experimental profiles is adequate, as pointed out by Song and Viskanta (1994). Moreover, in the case of the present system one would not have such steep gradients as one goes from the fluid layer to the porous medium. Hence, an even better prediction of the system in Figure 7.1 is expected with the present model.

For the simulations of the experiments of Kirkpatrick and Bohn (1986), 60x60, 120x120 and 240x240 non-uniform grids were used in order to study the effect of grid refinement. For these simulations, a Rayleigh number of 10^{10} was used with the working fluid as water. All the physical properties were taken at the bulk fluid temperature. Table 7.1 gives a comparison of the Nusselt numbers at the four walls for the three grids considered. For all computations the difference between the hot wall and cold wall Nusselt numbers was less than 4% when the convergence criteria were met. Also, the difference between the Nusselt numbers of the vertical walls was less than 1%. It can be seen that with a change in the grid size, the maximum variation in the Nusselt number occurs at the vertical walls. In going from a 120x120 to 240x240 grid, the top and bottom wall Nusselt numbers vary by less than 1%. However, the vertical wall Nusselt numbers vary by almost 10%. Therefore, the solution is still not grid independent for the finest grid used. Finer grids were not used for these simulations as they lead to large computational times. For example, the simulation time required for the 60x60 grid was approximately 30 minutes in a Pentium II 350 MHz machine. In refining the grid from 60x60 to 120x120 the computational effort increases by a factor of about four. This means that even for the 240x240 grid approximately 8 hours is required to complete one run.

Table 7.1: Grid refinement study for the simulations of the experiments of Kirkpatrick and Bohn (1986) using wall Nusselt numbers.

Grid	Left Wall	Right wall	Top Wall	Bottom wall
60x60	64.77	64.34	110.1	238.9
120x120	75.82	75.54	109.4	251.4
240x240	83.82	83.61	109.2	252.4

Kirkpatrick and Bohn (1986) used the average of the four hot/cold wall temperatures as the bulk temperature. The wall to bulk temperature difference was used to evaluate the Nusselt numbers. For the HCCC configuration, they found that the Nusselt number to Rayleigh number relationship collapsed to a single correlation for all four walls, namely:

$$Nu = 0.346 Ra^{0.285} \tag{7.18}$$

The coefficient in this definition of the Nusselt number is calculated for all four walls. These results are given in Table 7.2. The maximum error in the

prediction of heat transfer occurs for the top wall (an over prediction of approximately 78%).

Table 7.2: Coefficient of Nusselt number to Rayleigh number relationship. The exponent for Rayleigh number is taken as 0.285 to match with the relationship given by Kirkpatrick and Bohn (1986), $Nu = 0.346Ra^{0.285}$. The average of the four-hot/cold wall temperatures is taken as the reference temperature for each wall.

Grid	Left wall	Right wall	Top wall	Bottom wall
60x60	0.3660	0.3635	0.6221	0.2531
120x120	0.4284	0.4268	0.6181	0.2663
240x240	0.4736	0.4724	0.6168	0.2674

Studies carried out for the heating from the side configuration (Henkes, 1990; Lankhorst, 1991) show that the heat transfer results for natural convection flows depend significantly on the turbulence model used as well as the near wall treatment. However, it is not the objective of the present study to evaluate different turbulence models. Instead, the comparison exercise gives an estimate of the expected error in the heat transfer prediction of the present model. Figure 7.4 gives the simulations for the HCCC configuration of Kirkpatrick and Bohn (1986). Frames (a), (b), (c) and (d) of Figure 7.4 represent the isotherms, streamlines, eddy viscosity and turbulence kinetic energy contours. The central rising warm plume, which diverges at the top of the cavity and returns along the cold side-walls, observed by Kirkpatrick and Bohn (1986) in their shadowgraph (Figure 12) is predicted accurately by the model, as seen in Figures 7.4(a) and (b). Figures 7.4(c) and (d) also gives the intensity of turbulence predicted by the model through the contours of eddy viscosity and turbulence kinetic energy respectively. The reference viscosity for the eddy viscosity contours is the fluid viscosity. The figure shows that the eddy viscosity can be as high as 100 times the fluid viscosity, thus indicating that turbulence is quite significant at such Rayleigh numbers even for water. Since transition to turbulence occurs at lower Rayleigh numbers in the case of air (Henkes, 1990), a Rayleigh number of 10^{10} is expected to give a turbulent solution for the case study.

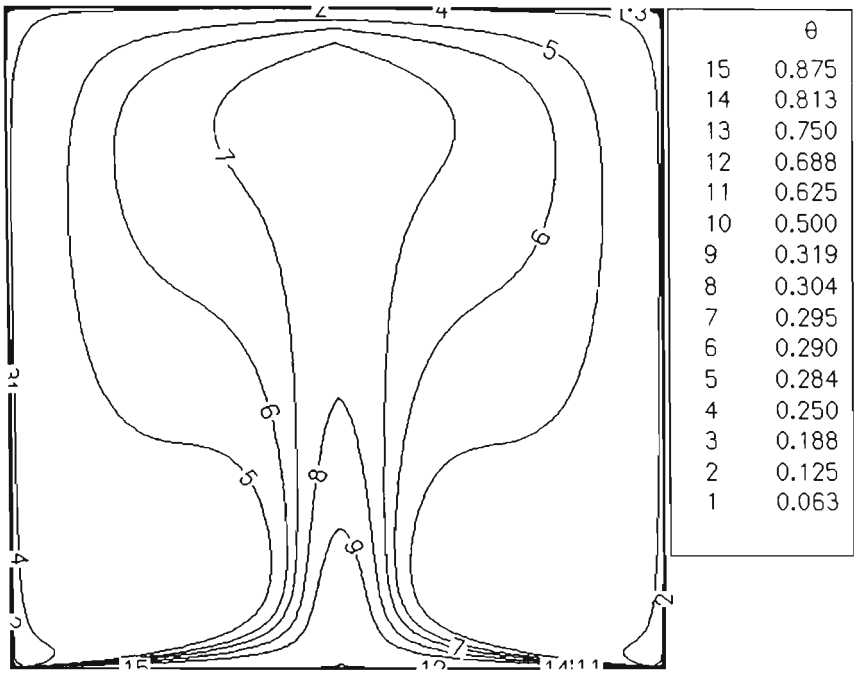

	θ
15	0.875
14	0.813
13	0.750
12	0.688
11	0.625
10	0.500
9	0.319
8	0.304
7	0.295
6	0.290
5	0.284
4	0.250
3	0.188
2	0.125
1	0.063

(a) Isotherms

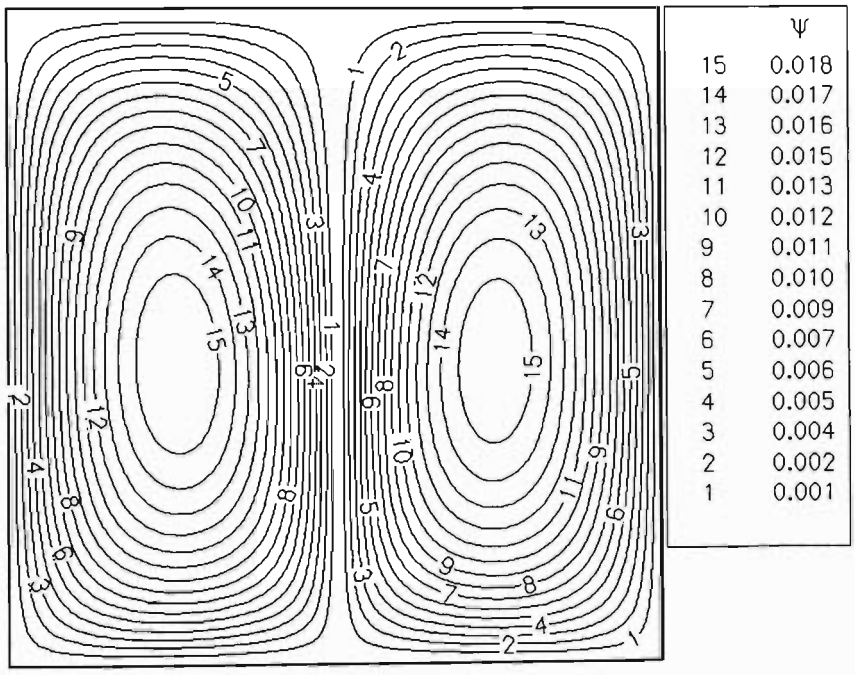

	Ψ
15	0.018
14	0.017
13	0.016
12	0.015
11	0.013
10	0.012
9	0.011
8	0.010
7	0.009
6	0.007
5	0.006
4	0.005
3	0.004
2	0.002
1	0.001

(b) Streamlines

Figure 7.4 (For caption, see next page)

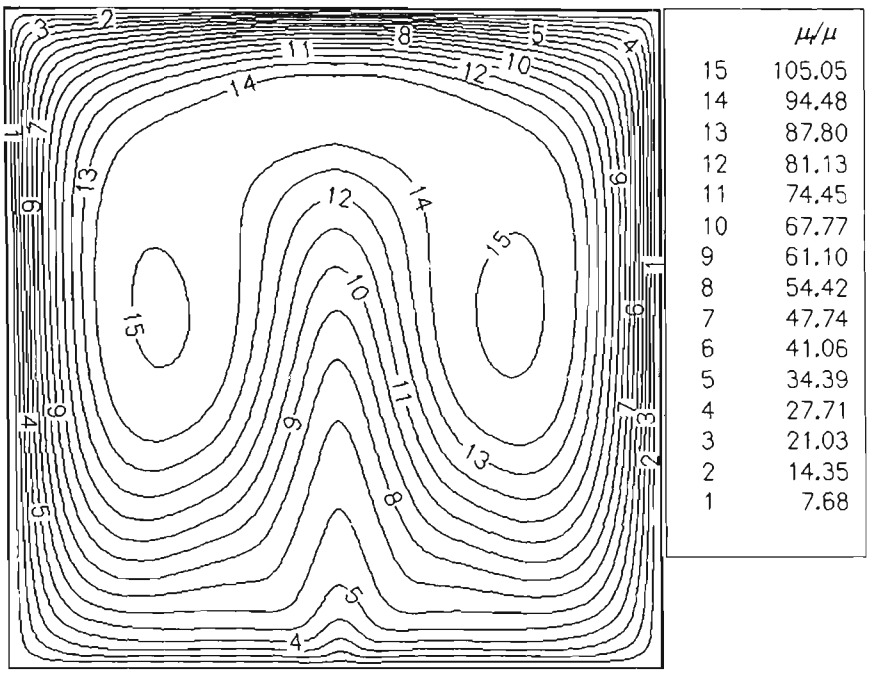

(c) Eddy viscosity contours

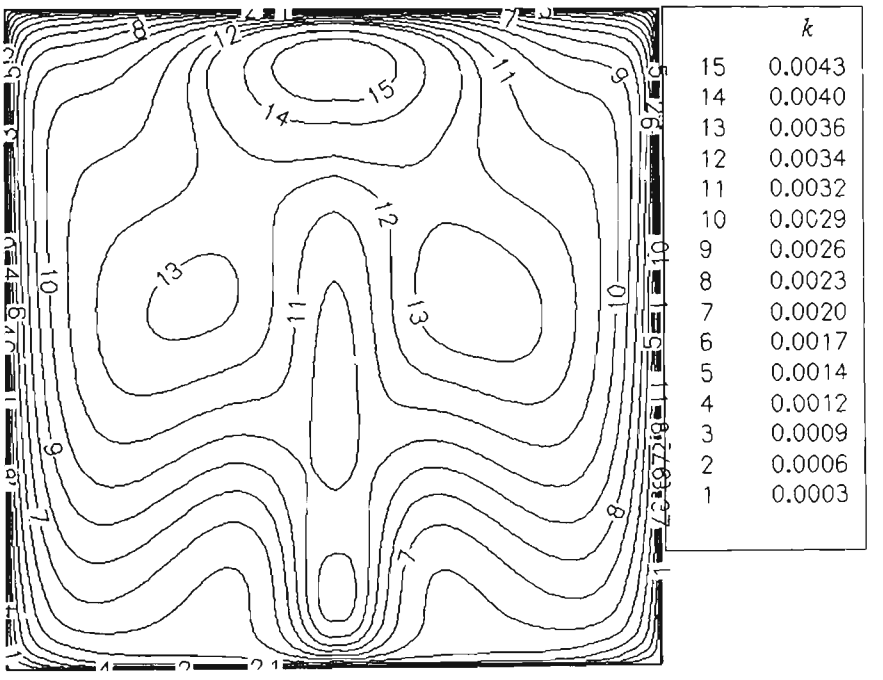

(d) Turbulence kinetic energy contours

Figure 7.4: Simulation for the experiment of Kirkpatrick and Bohn (1986), HCCC configuration. Ra=10^{10} with the working fluid as water.

7.5 Case study

The geometry for the case study is shown in Figure 7.1 above. A 60x60 non-uniform grid was used for the case study since it was found that with a 120x120 grid, the same simulation takes approximately four times longer with no significant change in the accuracy of the solutions. For the unsteady calculations, a time step of 0.1 s was used until the temperature and velocity fields were almost converged in the fluid layer. The convergence was monitored through changes in the wall Nusselt numbers. Approximately 3000 time steps were required. The time step was then increased to 10 s, for monitoring changes in the moisture content and changes in temperature in the porous layer. Any further increase in the time step led to divergence. Due to the small number of space iterations between two time iterations (typically, no more than three to four), computations for significantly large real times can be carried out in relatively short machine times. For the largest real time calculated in the present case study, 50 hours, a CPU time of around 5 hours was required on a Pentium II 350 MHz machine. However, increasing the time step is desirable, as this would lead to shorter computational times. Figure 7.5 indicates the streamlines and isotherms after the initial 3000 iterations.

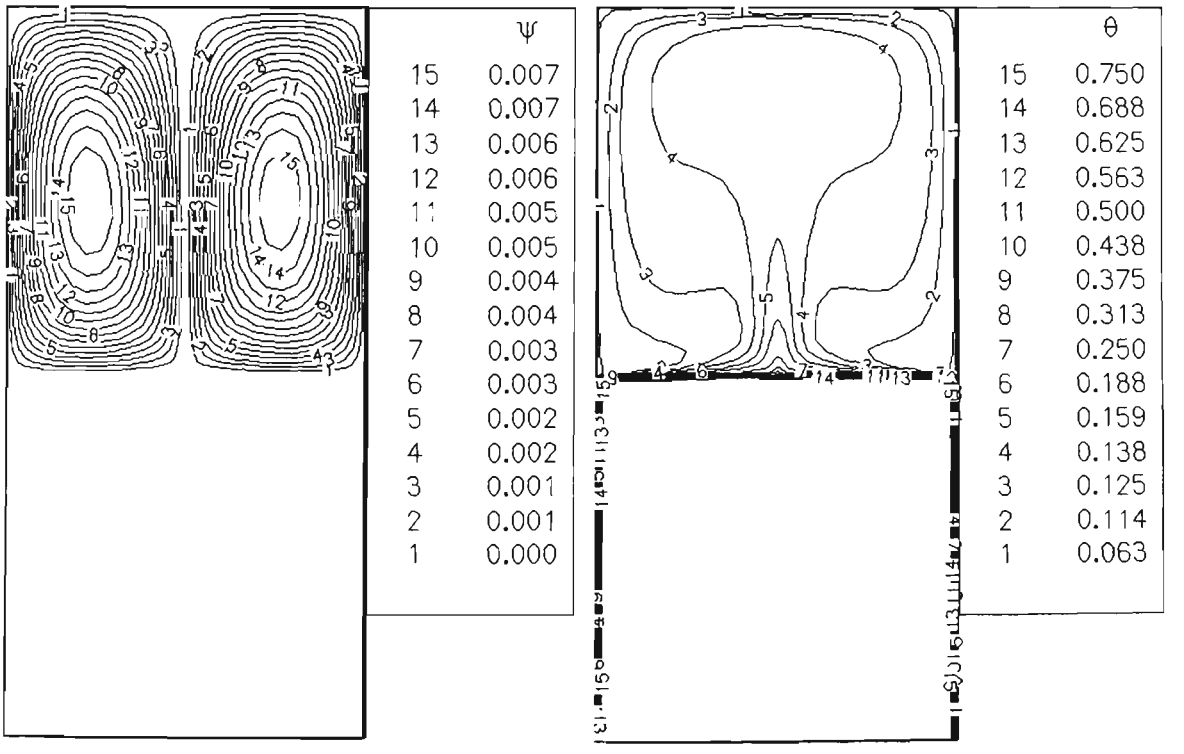

Figure 7.5: Streamlines and isotherms for the case study after the first 3000 time steps, equal to 300 s.

As expected, these do not change significantly for large times in the fluid layer. The eddy viscosity and turbulence kinetic energy profiles in the fluid layer are similar to the profiles obtained for the experiment of Kirkpatrick and Bohn (1986), as presented in Figure 7.4. The changes in the isotherms, moisture content of air and moisture content of the porous medium are shown in Figures 7.6, 7.7 and 7.8, respectively, after 10, 20, 30 and 50 hours. The heat and moisture from the porous medium is driven towards the fluid layer through the central rising plume as seen in Figures 7.6 and 7.7. This plume is expected to enhance the transport of heat and hence moisture from the porous medium. Thus, the choice of a turbulence model is important for the accurate prediction of heat transfer. Due to the heat transfer, the core of the porous medium becomes progressively cooler, as seen in Figure 7.6. Similarly, from Figure 7.7, one can see that the moisture content of the air in the porous medium decreases as time progresses. Figure 7.8 shows changes in the moisture content of the porous medium with time. As the air gets cooler, its ability to hold moisture decreases, and this extra moisture is absorbed by the hygroscopic porous medium. In case of grains, this phenomenon has important implications as it leads to the growth of moulds in these regions, which can eventually destroy the grains. It is clear from Figure 7.8 that close to the side-walls and in the region close to the central rising plume in the porous medium, the moisture content of silica gel increases. This increase becomes significant as time progresses. It is evident from Figure 7.6 that these are regions of relative coolness in the porous medium.

It is emphasised here that the present model does not take into account turbulence within the porous medium due to the low permeability of the porous medium considered for the simulations. However, this would not be the case for porous media of high permeability and turbulence within the porous medium will be an important factor to be considered. As seen in chapter five, one method of doing this would be by solving the turbulence transport equations in the porous medium and accounting for the attenuation of turbulence by incorporating damping terms in the turbulence transport equations for the porous medium.

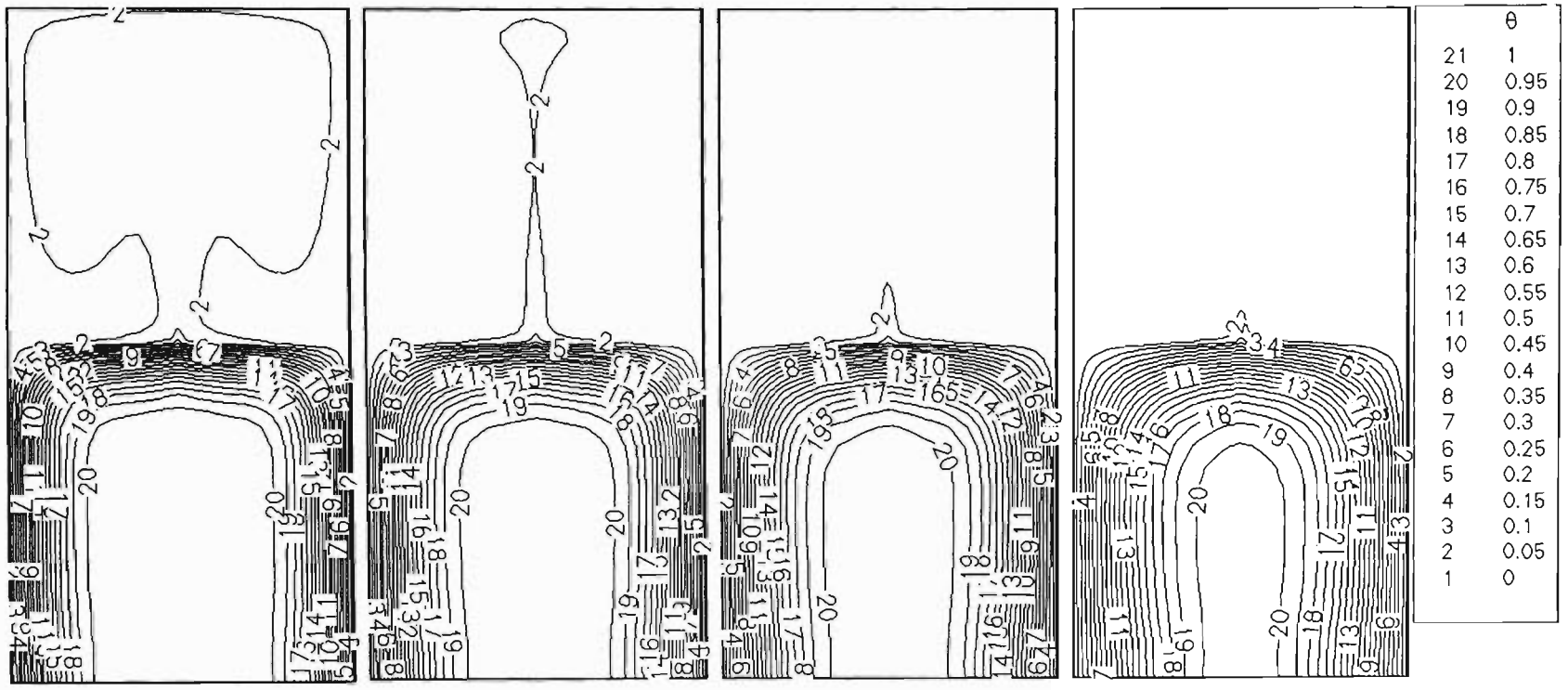

Figure 7.6: Change in isotherms with time in the case study.

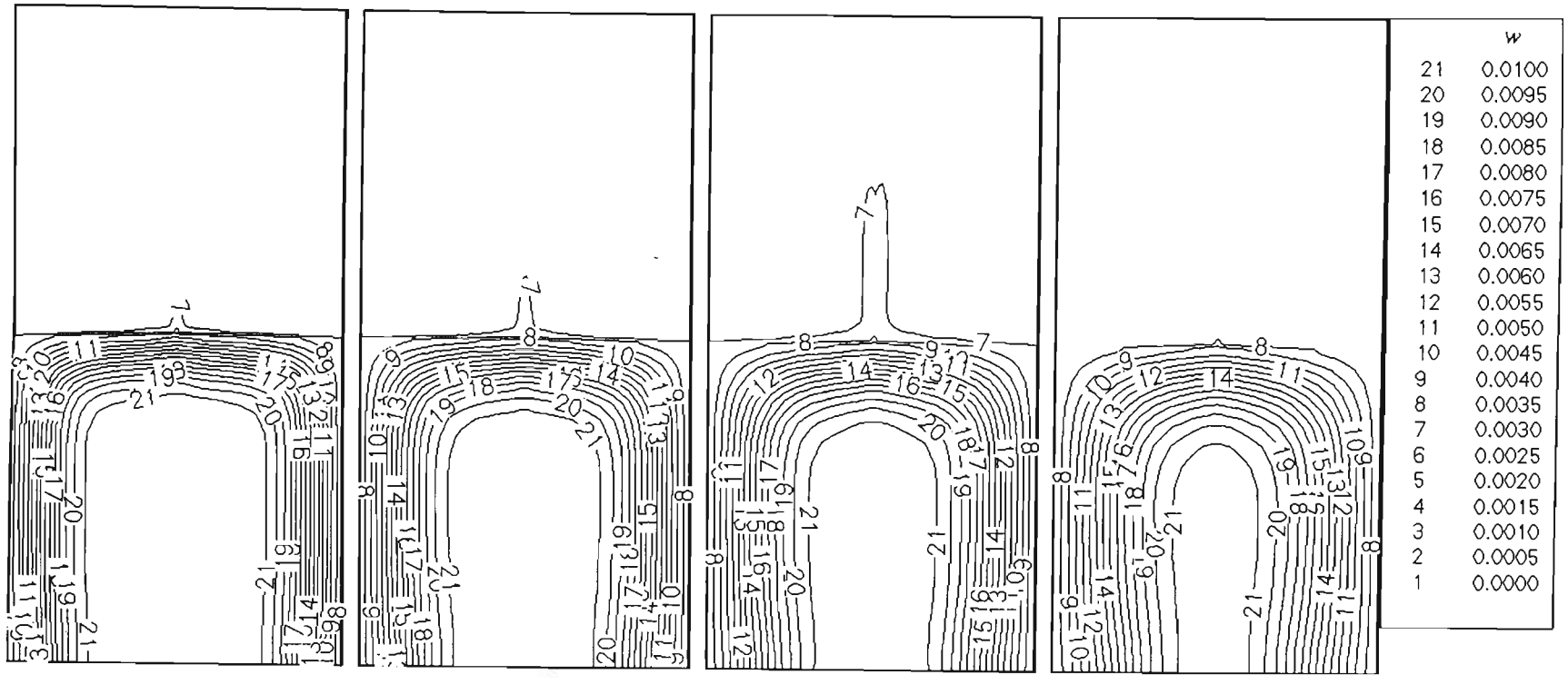

Figure 7.7: Change in moisture content of air with time in the case study.

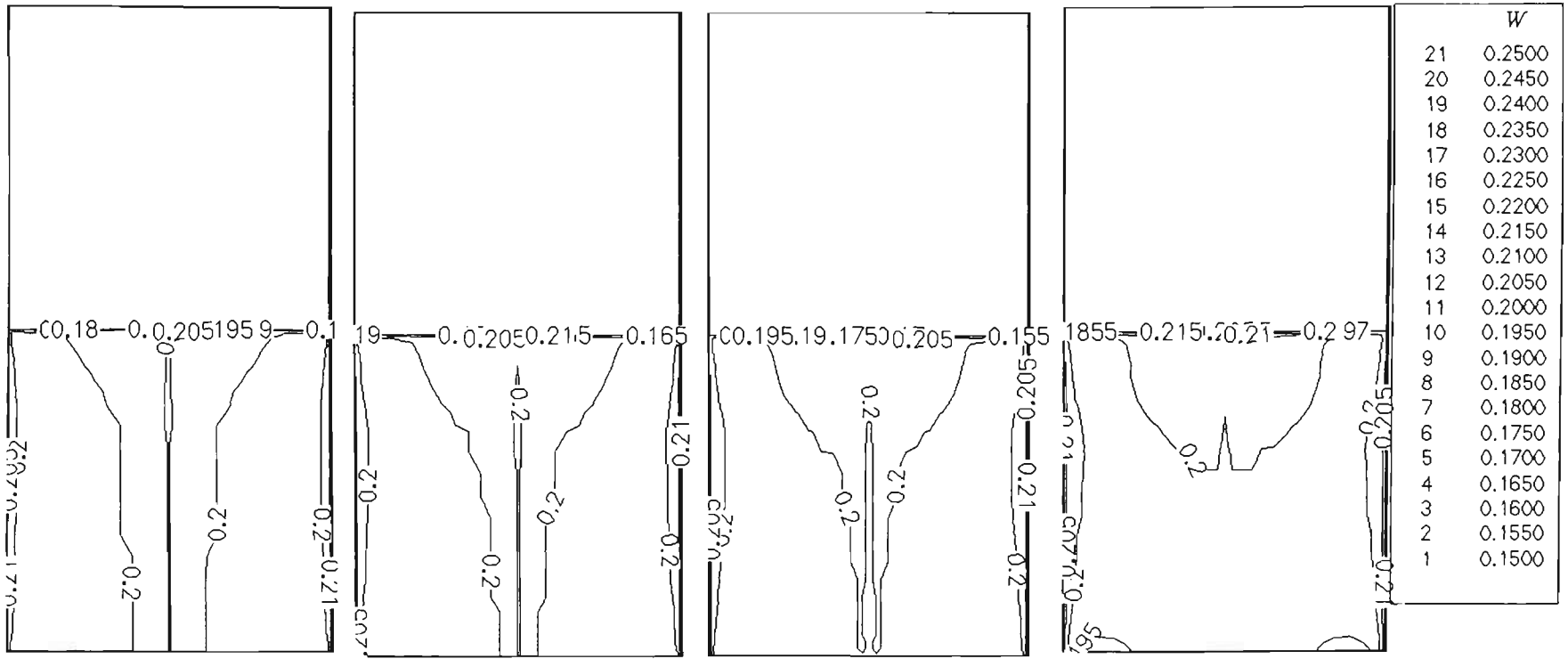

Figure 7.8: Change in the moisture content of the porous medium in the case study.

7.6 Conclusions

A general procedure of simulating systems with a turbulent fluid layer overlying a saturated hygroscopic porous medium has been presented. Emphasis has been placed on using this model for simulating moisture migration in stored agricultural produce. It is believed that such a model is capable of predicting the moisture migration process more accurately as it accounts for turbulence in the fluid layer. The level of sophistication of the turbulence model is however limited by the comparatively large run times encountered to simulate such systems. The model needs to be validated further with realistic experimental data. The present model is capable of simulating flow only when turbulence in the porous medium can be considered to be negligible. However, this would not be the case for porous media of high permeability. This limitation can be overcome by incorporating a turbulence model for the porous medium with appropriate damping terms, as in the simulations presented in the fifth chapter, for the attenuation of turbulence in the porous medium.

7.6 Conclusions

A general procedure of simulating systems with a turbulent fluid layer overlying a saturated hygroscopic porous medium has been presented. Emphasis has been placed on using this model for simulating moisture migration in stored agricultural produce. It is believed that such a model is capable of predicting the moisture migration process more accurately as it accounts for turbulence in the fluid layer. The level of sophistication of the turbulence model is however limited by the comparatively large run times encountered to simulate such systems. The model needs to be validated further with realistic experimental data. The present model is capable of simulating flow only when turbulence in the porous medium can be considered to be negligible. However, this would not be the case for porous media of high permeability. This limitation can be overcome by incorporating a turbulence model for the porous medium with appropriate damping terms, as in the simulations presented in the fifth chapter, for the attenuation of turbulence in the porous medium.

Chapter 8

Conclusions and final remarks

8.1 Conclusions

The following conclusions can be drawn after having investigated the interaction between turbulent flow and saturated porous foams using numerical and experimental methods.

1) Flow visualisation experiments revealed that the permeability of the porous foam and the height of the fluid layer above the porous foam significantly affect the flow pattern, at least in the fluid layer. The thickness of the porous foam affects the flow pattern to a smaller extent. For low permeability porous foams ($K < 10^{-8}$) it was found that there is little change in the flow pattern in the fluid layer from the cases without porous foams. This result led to the concept of treating the interface between the fluid layer and porous medium as a wall in numerical simulations for turbulent quantities such as the turbulence kinetic energy, k, and its rate of dissipation, ε. In such cases, the fluid layer and the porous medium could be regarded to be operating in the turbulent and laminar regimes, respectively. In case of the highest permeability G10 foam investigated, ($K = 2.843 \times 10^{-7}$), the flow pattern changed significantly in the fluid layer with a change from a single cell to a two-cell pattern. This change was observed for all three fluid heights investigated, indicating the strong interaction between the flow in the fluid layer and the adjacent porous medium.

2) Three different models were used to represent the flow in the porous foam namely a laminar flow model and two turbulence models for CFD simulations corresponding to the flow visualisations. The aim was to infer the effect of the presence or absence of macroscopic turbulence in the porous medium by studying the changes in the flow pattern, mean velocities and turbulence kinetic energy in the fluid layer. One of the turbulence models with only Darcy damping in the k and ε equations was found to be qualitatively superior in predicting the gross flow patterns, especially the effect of permeability of the porous foam and clear fluid

layer height. The second turbulence model with Darcy and Forchheimer modifications included in the k and ε equations for the porous foam was found to be qualitatively similar to the laminar flow model in its predictive capabilities. The similarity in predictions was found to be due to the almost complete damping of turbulence at the interface between the porous foam and clear fluid due to the Darcy and Forchheimer modification terms thus making the flow in the porous foam effectively laminar in nature. None of the three models used to represent flow in the porous foam could adequately predict the effect of changes in the thickness of the porous layer.

3) In order to further consolidate on the flow visualisations, LDV measurements were carried out for a quantitative comparison between the CFD simulations and the measurements. The vector plots obtained from the measurements confirmed the development of the two-cell pattern in the fluid layer for the highest permeability G10 foam that was investigated initially with the flow visualisation experiments. It was found that quantitatively, the simulations predict the mean axial velocity profiles better with the turbulent flow model with only Darcy damping for the porous foam. For the radial velocity profiles, predictions with the laminar flow model and turbulence model with Darcy and Forchheimer modification terms were found to be better at the highest fluid height in a region close to the interface between the fluid layer and porous foam. The turbulent flow model with Darcy damping showed better agreement with the measurements for the radial velocity as the fluid height decreased. The turbulence kinetic energy profiles in the fluid layer showed relatively good agreement with predictions by laminar and turbulent flow models for the foam.

4) Having secured the modelling of the interaction between a turbulent fluid flow overlying a saturated porous layer on a firmer footing, the research was applied to an industrially important case study concerning moisture migration in respiring agricultural produce. In this case study a general procedure of simulating systems with a turbulent fluid layer overlying a saturated hygroscopic porous medium was developed. It is believed that such a model is capable of predicting the moisture migration process more accurately as it accounts for turbulence in the fluid layer.

The level of sophistication of the turbulence model is however limited by the comparatively large run times encountered to simulate such systems.

8.2 Final remarks

1) As stated at the beginning of this thesis, the present research was aimed primarily at inferring the effect of turbulence modelling in the porous medium by studying the interaction between a turbulent fluid flow overlying a saturated porous medium. The reason for such an indirect evaluation is due to the inability of using measurements made at point locations in the porous medium for comparison with simulations using volume averaged equations. A more direct approach could have been adopted if there was a method of volume averaging the experimental results obtained by carrying out measurements within the porous medium.

2) The present thesis can be considered to be a first attempt at inferring turbulence in porous media and its interaction between an adjacent turbulent fluid layer using a combination of conventional modelling and experimental techniques. However, the use of conventional turbulence modelling strategies such as in the present research that is analogous to modelling turbulent flow for fluid flow in the absence of porous media might be impracticable for many real porous media. The use of grid based eulerian techniques such as finite volume, finite difference or finite element methods lead to inherent difficulties in modelling flow in real porous media. Instead, grid less lagrangian techniques such as Smoothed Particle Hydrodynamics (SPH) could be used to study the effect of microscopic flow in porous media on macroscopic turbulence.

References

Aerometrics Hardware and Software Manual, 1997, TSI Inc., Minnesota, USA.

Antohe, B. V. and Lage J. L., "A general two-equation macroscopic turbulence model for incompressible flow in porous media", *International Journal of Heat and Mass Transfer*, 1997, **40**, 3013-3024.

Baughn, J. W. and Shimizu, S.," Heat Transfer measurements from a surface with uniform heat flux and an Impinging jet", *ASME Journal of Heat Transfer*, 1989, **111**, 1096-1098.

Bear, J., "Dynamics of fluids in porous media", American Elsevier, New York, 1972, pp.125-128.

Beavers, G. S. and Joseph D. D., "Boundary conditions at a naturally permeable wall", *Journal of Fluid Mechanics*, 1967, **30**, 197-207.

Beckermann, C., Ramdhyani, S. and Viskanta R., "Natural convection flow and heat transfer between a fluid layer and a porous layer inside a rectangular enclosure", *Journal of Heat Transfer*, 1987, **109**, 363-371.

Beckermann, C., Ramdhyani, S. and Viskanta R., "Natural convection in vertical enclosures containing simultaneously fluid and porous layers", *Journal of Fluid Mechanics*, 1988, **186**, 257-284.

Behnia, M., Parneix, S., Shabany, Y. and Durbin, P. A., "Numerical study of turbulent heat transfer in confined and unconfined impinging jets", *International Journal of Heat and Fluid Flow*, 1999, **20**, 1-9.

Betts, P. L. and Dafa'Alla, A. A., "Turbulent buoyant air flow in a tall rectangular cavity", *Proceedings of the ASME Meeting, Heat Transfer Division*, 1986, **60**, 83-91.

Bird, R. B., Stewart, W.E. and Lightfoot, E.N., "Transport phenomena", 1st ed. Wiley New York, 1960.

Brinkman, H. C., "On the permeability of media consisting of closely packed porous particles", *Applied Scientific Research*, 1947, **A1**, 81-86.

Cebeci, T. and Smith, A.M.O., "Analysis of turbulent boundary layers", Academic Press, 1974.

Cheesewright, R. and Ziai, S., "Distributions of temperature and local heat transfer rate in turbulent natural convection in a large rectangular cavity", *Proceedings of the 8th International Heat Transfer Conference*, San Francisco, 1986b, 1465-1470.

Cheesewright, R., King, K. J. and Ziai, S., "Experimental data for the validation of computer codes for the prediction of two-dimensional buoyant cavity flows", *Proceedings of the ASME Meeting, Heat Transfer Division*, 1986a, **60**, 75-81.

Chen, F. and Chen, C. F., "Convection in superposed fluid and porous layers", *Journal of Fluid Mechanics*, 1992, **234**, 97-119.

Chen, F. and Chen, C. F., "Experimental investigation of convective stability in a superposed fluid and porous layer when heated from below, Journal of Fluid Mechanics, 1989, **207**, 311-321.

Chen, L. and Li, Y., "Modelling high Rayleigh number natural convection flows in grain storage", 1999, CSIRO DBCE Research Report, Australia, BCE DOC. 99/0331 (M).

Chen, L. and Li, Y., "Turbulent force flow in an air blast storage room", *Proceedings of the 6th International Conference on Air Distribution in Rooms*, 1998, **1**, 451-458.

Chen, L., Li, Y. and Thorpe, G. R., "High-Rayleigh-number natural convection in an enclosure containing a porous layer", Heat Transfer 1998, J.S. Lee ed., Taylor & Francis, 1998, 423-428.

Chien, K. Y., "Predictions of channel and boundary layer flows with a low Reynolds number turbulence model" *AIAA Journal*, 1982, **20**, 33-38.

Coulaud, O., Morel, P. and Caltagirone, J. P., "Numerical modelling of nonlinear effects in laminar flow through porous media", *Journal of Fluid Mechanics*, 1988, **190**, 393-407.

Cowan, G. H., Lovegrove, P. C. and Quarini, G. L., "Turbulent natural convection heat transfer in vertical single water-filled cavities", *Proceedings of the 7th International Heat Transfer Conference*, 1982, **2**, 195-204.

Craft, T., Graham, L. J. W. and Launder, B., "Impinging jet studies for turbulence model assessment-II. An examination of the performance of four turbulence models", *International Journal of Heat and Mass Transfer*, 1993, **36**, 2685-2697.

De Vahl Davis, G., "Natural convection of air in a square cavity: a bench mark numerical solution", *International Journal for Numerical Methods in Fluids*, 1983, **3**, 249-264.

Durbin, P. A., "On the k-ε stagnation point anomaly", *International Journal of Heat and Fluid Flow*, 1996, **17**, 89-90.

Durst, F., Melling, A. and Whitelaw, J. H., "Principles and practice of laser-Doppler anemometry", Academic Press Inc., London, 1976.

Dutoya, D. and Michard, P., "A program for calculating boundary layers along compressor and turbine blades", Numerical Methods in Heat Transfer, edited by R. W. Lewis, K. Morgan and O. C. Zienkiewicz, John Wiley and Sons, New York, 1981.

Ferziger, J. H. and Peric M., "Computational methods for fluid dynamics", Springer-Verlag, New York, 1996.

Forchheimer, P. H., "Wasserbeuregung durch boden", *Zeit. Ver. Deutsch. Ing.*, 1901, **45**, 1782-1788.

Gebhart, B., "Effects of viscous dissipation in natural convection", *Journal of Fluid Mechanics*, 1962, **14**, 225-232.

Getachew, D., Minkowycz, W. J. and Lage, J. L., "A modified form of the k-ε model for turbulent flows of an incompressible fluid in porous media", *International Journal of Heat and Mass Transfer*, 2000, **43**, 2909-2915.

Givler, R. C. and Altobelli, S. A., "A determination of the effective viscosity for the Brinkman-Forchheimer flow model", *Journal of Fluid Mechanics*, 1994, **258**, 355-370.

Graham, L. J. W. and Bremhorst, K., "Application of the k-ε turbulence model to the simulation of a fully pulsed free air jet", *Journal of Fluids Engineering*, 1993, **115**, 70-74.

Gray, D. D. and Giorgini, A., "The validity of the Boussinesq approximation for liquids and gases", *International Journal of Heat and Mass Transfer*, 1976, **24**, 125-131.

Hall, M. J. and Hiatt, J. P., "Measurements of pore scale flows within and exiting ceramic foams", *Experiments in Fluids*, 1996, **20**, 433-440.

Harlow, F. H. and Nakayama, P., "Turbulence transport equations", *Physics of Fluids*, 1967, **11**, 2323-2332.

Harlow, F. H. and Welch, J. E., "Numerical calculation for time dependent viscous incompressible flow of fluid with free surface", *Physics of Fluids*, 1965, **8**, 2182-2189.

Hassid, S. and Poreh, M., "A turbulent energy model for flows with drag reduction", *Journal of Fluids Engineering*, 1975, **97**, 234-241.

Henkes, R. A. W. M. and Hoogendoorn, C. J., "Comparison of the standard case for turbulent natural convection in a square enclosure", in *a seminar on turbulent natural convection in enclosures: a computational and experimental benchmark study*, ed. Henkes R. A. W. M. and Hoogendoorn, C. J., Delft, Netherlands, 1992, 185-213.

Henkes, R. A. W. M. and Hoogendoorn, C. J., "Numerical determination of wall functions for the turbulent natural convection boundary layer", *International Journal of Heat and Mass Transfer*, 1990, **33**, 1087-1097.

Henkes, R. A. W. M., "Natural-convection boundary layers", PhD Thesis, Technical University of Delft, The Netherlands, 1990.

Hoffman, G. H., "Improved form of the low-Reynolds number k-ε turbulence model", *Physics of Fluids*, 1975, **18**, 309-312.

Hsu, C. T. and Cheng, P., "Thermal dispersion in a porous medium", *International Journal of Heat and Mass Transfer*, 1990, **33**, 1587-1597.

Janssen, R. J. A., "Instabilities in natural-convection flows in cavities", PhD Thesis, Technical University of Delft, The Netherlands, 1994.

Jolls, K. R., and Hanratty, T. J., "Transition to turbulence for flow through a dumped bed of spheres", *Chemical Engineering Science*, 1966, **21**, 1185-1190.

Jones, W. P. and Launder, B. E., "The prediction of laminarization with a two equation model of turbulence", *International Journal of Heat and Mass Transfer*, 1972, **15**, 301-314.

Kenjeres, S. and Hanjalic, K, "On the prediction of thermal convection in horizontal slender enclosures", *Tenth Symposium on Turbulent Shear Flows*, The Pennsylvania State University, USA, 1995.

King, K. J., "Turbulent natural convection in rectangular air-cavities", PhD Thesis, Queen Mary College, UK, 1989.

Kirkpatrick, A. T. and Bohn, M., "An experimental investigation of mixed cavity natural convection in the high Rayleigh number regime", *International Journal of Heat and Mass Transfer*, 1986, **29**, 69-82.

Lage, J. L. *Private communication*, Mechanical Engineering Department, Southern Methodist University, Texas, USA, 1998.

Lage, J. L., "The fundamental theory of flow through permeable media from Darcy to turbulence", *Transport Phenomena in Porous Media*, Eds. D. B. Ingham and I. Pop, Pergamon, Oxford, 1-30, 1998.

Lage, J. L., Antohe, B. V. and Nield, D. A., "Two types of non linear pressure-drop versus flow-rate relation observed for saturated porous media", *Journal of Fluids Engineering*, 1997, **119**, 700-706.

Lam, C. K. G. and Brehmorst, K. A., "Modified form of the k-ε model for predicting wall turbulence", *Journal of Fluids Engineering*, 1981, **103**, 456-460.

Lankhorst, A., "Laminar and turbulent natural convection in cavities: numerical modelling and experimental validation", PhD Thesis, Technical University of Delft, The Netherlands, 1991.

Launder, B. E. and Sharma, B. I., "Application of the energy dissipation model of turbulence to the calculation of flow near a spinning disc", *Letters in Heat and Mass Transfer*, 1974, **1**, 131-138.

Launder, B. E. and Spalding D. B., "Lectures in mathematical models of turbulence", Academic Press Inc. Ltd., London, UK, 1972.

Le Quéré, P. and Behnia, M., "From onset of unsteadiness to chaos in a differentially heated square cavity", *Journal of Fluid Mechanics*, 1998, **359**, 81-107.

Le Quéré, P., " Accurate solution to the square thermally driven cavity at high Rayleigh number", *Computers and Fluids*, 1991, **20**, 29-41.

Le Quéré, P., "Accurate solutions to the square thermally driven cavity at high Rayleigh number", Centre National de la Recherche Scientifique LIMSI (Orsay, France), Notes et Documents 90-2, 1990.

Lee, K. and Howell, J. R., "Forced convective and radiative transfer within a highly porous layer exposed to a turbulent external flow field", *Proceedings of the 1987 ASME-JSME Thermal Engineering Joint Conference*, ASME, Washington, D. C., 1987, **2**, 377-386.

Leonard, B.P., "A stable and accurate convective modelling procedure based on quadratic upstream interpolation", *Computational methods in Applied Mechanical Engineering*, 1979a, **19**, 59-98.

Lim, I. G. and Mathews, R. D., " Development of a model for turbulent combustion within porous inert media", *Transport Phenomena in Thermal Engineering*, ed. J. S. Lee, S. H. Chung and K. Y. Kim, Vol.1. Begell House Inc., New York, 1993, pp.631-636.

MacGregor, R. K. and Emery, A. F., "Free convection through vertical plane layers-moderate and high Prandtl number fluids", *Journal of Heat Transfer*, 1969, 91, 391-403.

Masuoka, T. and Takatsu, Y., "Turbulence model for flow through porous media", *International Journal of Heat and Mass Transfer*, 1996, **39**, 2803-2809.

Menter, F. R., "Improved two-equation k-ω models for aerodynamic flows", 1992, NASA TM 103975.

Mickley, H. S., Smith, K. A. and Korchak, E. I., "Fluid flow in packed beds", *Chemical Engineering Science*, 1965, **20**, 237-246.

Neale, G., and Nader, W., "Practical significance of Brinkman's extension of Darcy's law", *Canadian Journal of Chemical Engineering*, 1974, **52**, 475-478.

Netto, P. G. Q. and Guthrie, R. I. L., "The importance of turbulence modelling in the design of a novel delivery system for a single-belt steel casting process", *International Journal of Heat and Mass Transfer*, 2000, **43**, 21-37.

Ngamsirivadhana, S., "Instabilities in contained toroidal flows", 1996, *Final year project report*, Department of Mechanical Engineering, Monash University.

Nguyen T.V., "Natural convection effects in stored grains: a simulation study", *Drying Technology*, 1987, **5**, 541-560.

Nield, D. A. and Bejan, A., "Convection in porous media", 1st ed. Springer-Verlag, New York, 1992, pp.7-14.

Nield, D. A. Comments on, "Turbulence model for flow through porous media", *International Journal of Heat and Mass Transfer*, 1997, 40, 2499.

Nield, D. A., "The limitations of the Brinkman-Forchheimer equation in modelling flow in a saturated porous medium and at an interface", *International Journal of Heat and Fluid Flow*, 1991, **12**, 269-272.

Nozad I., Carbonell, R. G. and Whitaker S., "Heat conduction in multiphase systems-I: Theory and experiment for two-phase systems", *Chemical Engineering Science*, 1985, **40**, 843-855.

Ochoa-Tapia, J. A. and Whitaker, S., "Momentum transfer at the boundary between a porous medium and a homogeneous fluid-1. Theoretical development", *International Journal of Heat and Mass Transfer*, 1995a, **38**, 2635-2646.

Ochoa-Tapia, J. A. and Whitaker, S., "Momentum transfer at the boundary between a porous medium and a homogeneous fluid-2. Comparison with experiment", *International Journal of Heat and Mass Transfer*, 1995b, **38**, 2647-2655.

Paolucci, S. and Chenoweth, D. R., "Transition to chaos in a differentially heated vertical cavity", *Journal of Fluid Mechanics*, 1989, **201**, 379-410.

Paolucci, S., "Direct numerical simulation of two-dimensional turbulent natural convection in an enclosed cavity", *Journal of Fluid Mechanics*, 1990, **215**, 229-262.

Patankar, S. V. and Spalding, D. B., "A calculation procedure for heat, mass and momentum transfer in three dimensional parabolic flows", International Journal of Heat and Mass Transfer, 1972, **15**, 1787-1806.

Patankar, S. V., "Numerical heat transfer and fluid flow", Hemisphere Publishing Corporation, Washington, 1980.

Patel, V. C., Rodi, W. and Scheuerer G., "Turbulence models for near-wall and low Reynolds number flows: A review", *AIAA Journal*, 1985, **23**, 1308-1319.

Pope, S. B., "An explanation of the turbulent round-jet/plane-jet anomaly", *AIAA Journal*, 1978, **16**, 279-281.

Poulikakos, D., "Buoyancy-driven convection in a horizontal fluid layer extending over a porous substrate", *Physics of Fluids*, 1986, **29**, 3949-3957.

Poulikakos, D., Bejan A., Selimos B. and Blake, K. R., "High Rayeligh number convection in a fluid overlaying a porous bed", *International Journal of Heat and Fluid Flow*, 1986, **7**, 109-116.

Prakash, M., Turan, Ö. F., Li, Y. and Thorpe, G. R., "A CFD study of natural convection heat and mass transfer in respiring hygroscopic porous media", *Proceedings of the 2nd International Conference on CFD in the Minerals and Process Industries*, 1999a, 157-162.

Prescott, P. J. and Incropera, F. P., "The effect of turbulence on solidification of a binary metal alloy with electromagnetic stirring", *ASME Journal of Heat Transfer*, 1995, **117**, 716-724.

Reynolds, W. C., "Computation of turbulent flows", *Annual Review of Fluid Mechanics*, 1976, **8**, 183-208.

Rodi, W., "Turbulence models and their application in hydraulics, a state of the art review", International Association for Hydraulic Research, Delft, The Netherlands, 1980.

Saleh, S., Thovert, J. F. and Adler, P. M., "Measurement of two-dimensional velocity fields in porous media by particle image velocimetry", *Experiments in Fluids*, 1992, **12**, 210-212.

Scheidegger, A. E., "The physics of flow through porous media", 2nd ed., University of Toronto Press, 1963, pp.158-177.

Seguin, D., Montillet, A. and Comiti, J., "Experimental characterisation of flow regimes in various porous media-I: Limit of laminar flow regime", *Chemical Engineering Science*, 1998a, **53**, 3751-3761.

Seguin, D., Montillet, A., Comiti, J. and Huet, F., "Experimental characterisation of flow regimes in various porous media-II: Transition to turbulent regime", *Chemical Engineering Science*, 1998b, **53**, 3897-3909.

Sheng, Y., Shoukri, M., Sheng, G., Wood, P., "A modification to the simple method for buoyancy-driven flows", *Numerical Heat Transfer*, 1998, **33**, 65-78.

Singh, A. K., Leonardi, E. and Thorpe, G. R., "Three-dimensional natural convection in a confined fluid overlying a porous layer", *Journal of Heat Transfer*, 1993, **115**, 631-638.

Slattery, J. C., "Flow of viscoelastic fluids through porous media", *A.I.Ch.E. Journal*, 1967, **13**, 1066-1071.

Song, M. and Viskanta, R., "Natural convection flow and heat transfer within a rectangular enclosure containing a vertical porous layer", *International Journal of Heat and Mass Transfer*, 1994, **37**, 2425-2438.

Sutherland, J. W., Banks, P. J. and Griffiths, H. J., "Equilibrium heat and moisture transfer in air flow through grain", *Journal of Agricultural Engineering Research*, 1971, **16**, 368-386.

Tennekes, H. and Lumley, J. L., "A first course in turbulence", The MIT Press, Cambridge, Massachusetts, USA, 1972.

Thorpe, G. R. and Whitaker S., "Local mass and thermal equilibria in ventilated grain bulks. Part II: The development of constraints", *Journal of Stored Products Research*, 1992, **28**, pp. 29-54.

Thorpe, G. R., Moore, G. A. and Singh, A. K., "Heat, mass and momentum transfer in three-dimensional bulks of stored grains", *Conference on Engineering in Agriculture*, Albury, NSW, Australia, 1992.

To, W. M. and Humphrey, J. A. C., "Numerical simulation of buoyant, turbulent flow-1. Free convection along a heated, vertical, flat plate", *International Journal of Heat and Mass Transfer*, 1986, **29**, 573-592.

Van der Merwe, D. F. and Gauvin, W. H., "Velocity and turbulence measurements of air flow through a packed bed", *A.I.Ch.E. Journal*, 1971, **17**, 519-528.

Van Doormal, J. P. and Raithby, G. D., "Enhancements of the SIMPLE method for predicting incompressible fluid flows", *Numerical Heat Transfer*, 1984, **7**, 147-163.

Wang, H. and Takle, E. S., "Boundary-layer flow and turbulence near porous obstacles", *Boundary Layer Meteorology*, 1995, **74**, 73-88.

Whitaker, S., "Diffusion and dispersion in porous media", *A.I.Ch.E. Journal*, 1967, **13**, 420-427.

Whitaker, S., "Flow in porous media I: A theoretical derivation of Darcy's law", *Transport in Porous Media*, 1986, **1**, 3-25.

Wilcox, D. C., "Turbulence modelling for CFD", DCW Industries, La Canada, 1993.

Publications arising from this research

1) **Prakash M.**, Turan, Ö. F., Li Y. and Thorpe G. R., "A CFD study of natural convection heat and mass transfer in respiring hygroscopic porous media" *Proceedings of the 2nd International Conference on CFD in the Minerals and Process Industries*, 1999, 157-162.

2) **Prakash, M.**, Mahoney, J., Li, Y., Turan, Ö. F. and Thorpe, G. R., "Impinging round jet studies in a cylindrical enclosure with and without a porous layer: Part I-Flow Visualisations", *CSIRO DBCE*, Research Report, 1999.

3) **Prakash, M.**, Mahoney, J., Li, Y., Turan, Ö. F. and Thorpe, G. R., "Impinging round jet studies in a cylindrical enclosure with and without a porous layer: Part II-LDV measurements and CFD simulations", *CSIRO DBCE*, Research Report, 1999.

4) **Prakash, M.**, Mahoney, J., Li, Y., Turan, Ö. F. and Thorpe, G. R., "Experimental and numerical studies of an enclosed turbulent jet impinging a porous layer" *accepted at the 7th International Conference on Air Distribution in Rooms*, 9-12 July 2000, The University of Reading, UK.

5) **Prakash, M.**, Turan, Ö. F., Li, Y. and Thorpe, G. R., "Modelling and simulation of natural convection heat and mass transfer in respiring hygroscopic porous media" *accepted for publication in Drying Technology* (to appear in Vol. 18, No. 10 of the Journal), 2000.

6) **Prakash, M.**, Mahoney, J., Li, Y., Turan, Ö. F. and Thorpe, G. R., "Impinging round jet studies in a cylindrical enclosure with and without a porous layer: Part I-Flow Visualisations and Simulations", *submitted to Chemical Engineering Science*, 2000.

7) **Prakash, M.**, Mahoney, J., Li, Y., Turan, Ö. F. and Thorpe, G. R., "Impinging round jet studies in a cylindrical enclosure with and without a porous layer: Part II-LDV Measurements and Simulations", *submitted to Chemical Engineering Science*, 2000.